THE ρ MESON SPECTRUM AND $K\pi$ SCATTERING WITH PARTIAL WAVE MIXING IN LATTICE QCD

by

Andrew D. Hanlon

B.Sc. in Physics and Computer Science, Michigan State University,

2013

Submitted to the Graduate Faculty of

the Dietrich School of Arts and Sciences in partial fulfillment

of the requirements for the degree of

Doctor of Philosophy

University of Pittsburgh

2017

UNIVERSITY OF PITTSBURGH

DIETRICH SCHOOL OF ARTS AND SCIENCES

This dissertation was presented

by

Andrew D. Hanlon

It was defended on

September 28, 2017

and approved by

Adam Leibovich, Department of Physics and Astronomy, University of Pittsburgh

Colin Morningstar, Department of Physics, Carnegie Mellon University

Eric Swanson, Department of Physics and Astronomy, University of Pittsburgh

Daniel Boyanovsky, Department of Physics and Astronomy, University of Pittsburgh

Vladimir Savinov, Department of Physics and Astronomy, University of Pittsburgh

Dissertation Advisors: Adam Leibovich, Department of Physics and Astronomy, University of Pittsburgh,

Colin Morningstar, Department of Physics, Carnegie Mellon University

THE ρ MESON SPECTRUM AND $K\pi$ SCATTERING WITH PARTIAL WAVE MIXING IN LATTICE QCD

Andrew D. Hanlon, PhD

University of Pittsburgh, 2017

The finite-volume QCD spectrum in the $I = 1$, $S = 0$, parity-odd, G-parity-even channels for zero total momentum is studied using lattice QCD, and the K-matrix for $K\pi$ scattering is investigated to determine the mass and decay width of the $K^*(892)$ from first principles. The recently developed stochastic LapH method has proven to be a valuable tool in lattice QCD calculations when all-to-all quark propagators are needed, as is the case for isoscalar mesons and two-hadron operators. This method is especially important for large volumes where other methods do not scale well. These calculations were done with 412 gauge configurations using clover-improved Wilson fermions on a large anisotropic $32^3 \times 256$ lattice with a pion mass near 240 MeV. The stationary states determined to be single-particle dominated are compared with the experimental resonances and are found to be in reasonable agreement. Additionally, the initial development of tetraquark operators is described.

TABLE OF CONTENTS

LIST OF TABLES

LIST OF FIGURES

PREFACE

I would like to express my very great appreciation to my advisor Prof. Colin Morningstar for his patient guidance and careful critiques of my works. I am also particularly grateful to my co-advisor Prof. Adam Leibovich for all of his helpful support. I finally wish to express my thanks for the many meaningful discussions I have had with Prof. John Bulava, Ben Hörz, and my fellow graduate students Jacob Fallica, Ruairí Brett and Erin Blauvelt that have served to deepen and challenge my understanding of physics. Finally, I am so very appreciative of my family, and especially my parents, who have all done so much to help me get where I am today.

1.0 INTRODUCTION

From the large number of hadrons discovered throughout the 1950s and into the 1960s, a more fundamental understanding of these particles was needed. The first breakthrough in understanding these hadrons came with the quark model, proposed independently by Gell-Mann [1] and Zweig [2], that classified the lightest hadrons into $SU_F(3)$ flavor multiplets. This organization led to the successful prediction for the Ω^- baryon. Over the next decade, proposals of an extra $SU(3)$ degree of freedom for the quarks were made [3, 4]. Finally, in 1973, this extra $SU(3)$ symmetry was proposed as the gauge symmetry underlying the strong interactions, and Quantum Chromodynamics (QCD) was born [5].

Since then, QCD has reproduced many experimental results at high energies using perturbative methods, which were made possible because QCD is asymptotically free [6, 7]. Furthermore, applications of chiral perturbation theory for describing certain low energy hadron interactions have also been successful. From these successes, there is little doubt surrounding the question of QCD being the correct theory for the strong interaction. However, difficulties arise for QCD calculations in the medium energy range where the gauge coupling $\alpha_s(\mu)$ is too large for perturbative QCD and excited hadrons begin to form.

The spectrum of QCD in this regime is rich and much of it is still poorly understood. For instance, the Roper resonance lies below the lightest negative-parity nucleon, which is in contradiction to predictions from a simple quark model [8]. The dire state of our understanding of the nucleon spectrum can be seen in Figure 1.1. Furthermore, controversy still surrounds the nature of the $\Lambda(1405)$: it is the lightest excited spin-1/2 baryon despite containing a strange quark and possessing odd parity [9]. It was suggested long ago that the $\Lambda(1405)$ may in fact be a $N\overline{K}$ molecular state [10, 11]. A recent lattice study also lends support to the molecular nature of this resonance [12], but there is more work to be done

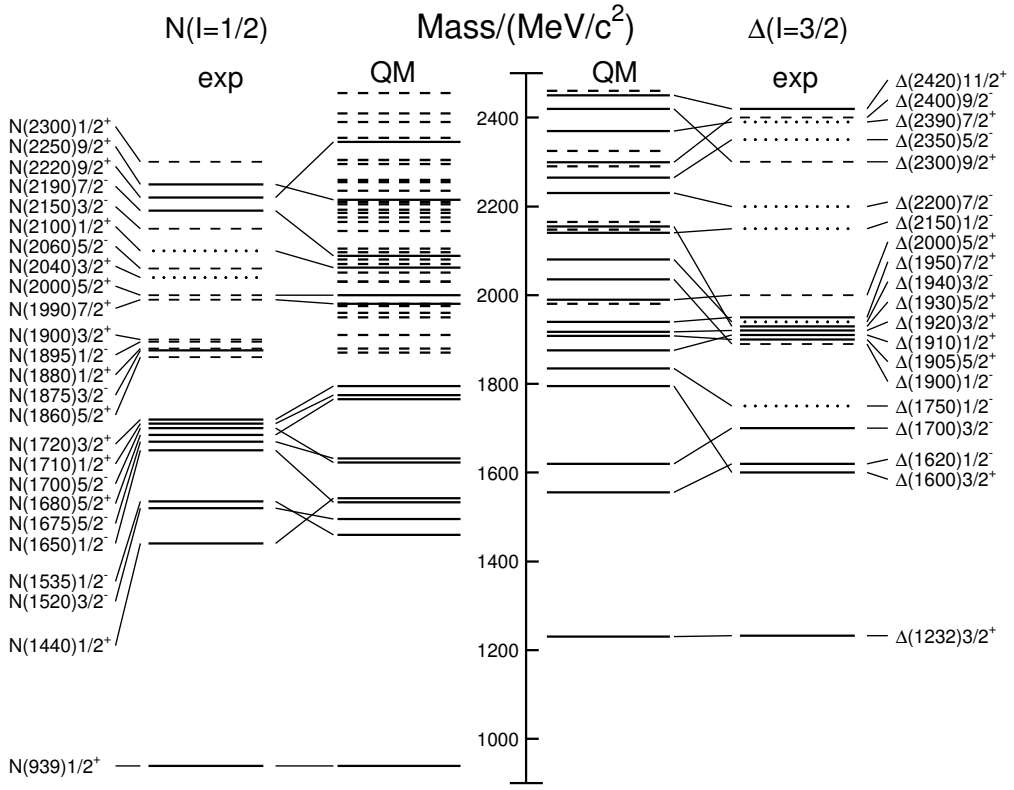

Figure 1.1: The nucleon spectrum. A comparison is made between the experimentally observed nucleon spectrum and the spectrum from a quark model [8]. Figure taken from Ref. [9].

before this classification can be fully established. In the bosonic sector, mesons containing u, d, and s quarks can be qualitatively described by constituent quark models, except for the light scalar mesons (*i.e.* $J^{PC} = 0^{++}$) [13]. This discrepancy is shown in Figure 1.2, which shows a proposed resolution to this problem by using a $qq\overline{qq}$ (*i.e.* a tetraquark) model for these states. Additionally, the discovery of the so-called XYZ mesons [14, 15] also exposes a lack in the understanding of the QCD spectrum.

It is clear that a need for a theoretical understanding of the QCD spectrum from first principles is crucial towards advancing our knowledge of the physics surrounding the strong interaction. Lattice QCD [16] is a non-perturbative method that can help address some of

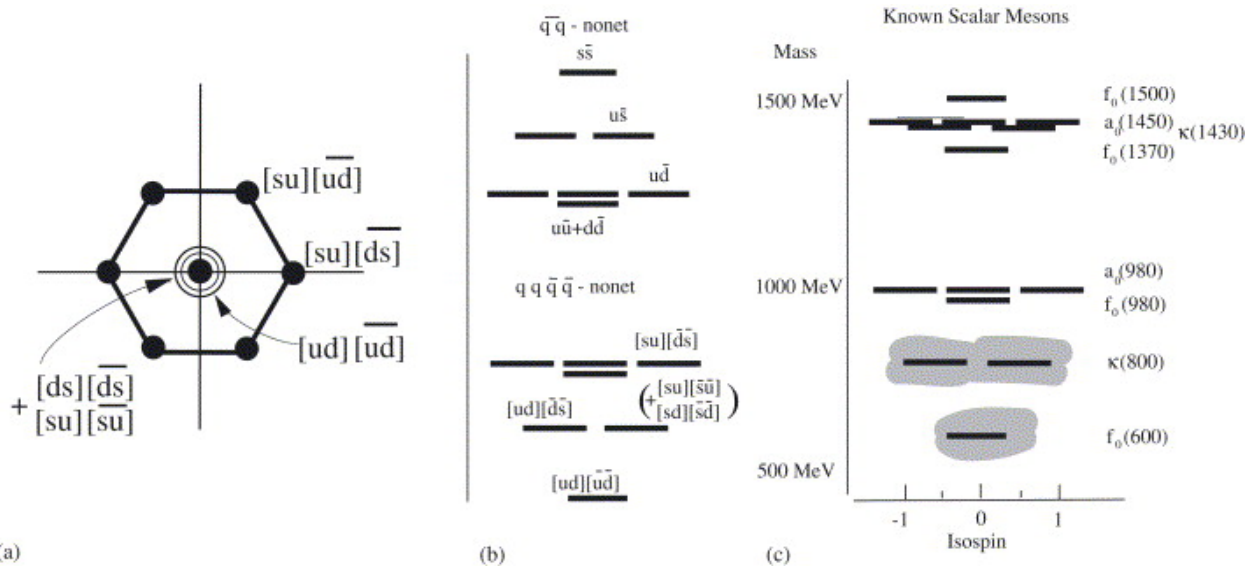

Figure 1.2: The light nonet of scalar mesons. (a) The quark content of the $qq\overline{q}\overline{q}$ nonet. (b) A comparison of the mass orderings from a $q\overline{q}$ nonet vs. a $qq\overline{q}\overline{q}$ nonet. (c) The experimental spectrum of the light scalar mesons [9]. Figure taken from Ref. [13].

the issues raised above. Only recently has lattice QCD been able to extract the excited state spectrum within reasonable error. Considerable progress has been made in lattice QCD due to modern techniques and the continual increase of computational resources. This work makes extensive use of the recently developed stochastic LapH method [17] for estimating quark lines (*i.e.* Wick contractions) and variational methods [18, 19, 20] for extracting stationary-state energies from a large temporal correlation matrix. This has allowed us to extract a significant portion of the excited-state spectrum in finite volume. These calculations should help to elucidate many of these puzzles in spectroscopy, like deciphering the true nature of the controversial resonances, and offer insights into the physics of hadron formation and confinement.

Furthermore, the inclusion of tetraquark operators could shed light on Jaffe's inverted spectrum and the XYZ mesons. Once these operators are used, we can observe how the spectrum is affected. If new stationary states appear, then this would present strong evidence for tetraquarks and the results could help drive experimental searches. If the spectrum seems

undisturbed by the presence of our tetraquark operators, then this would be evidence that there may not be any low-lying tetraquarks.

Of course, the full picture requires an understanding of how the finite-volume spectrum can be related to our infinite world. This was addressed by Martin Lüscher in the 1980s [21, 22], where the finite-volume effects of stable single particle states and scattering states were determined. From this work and in later works by Lüscher in Refs. [23, 24], it was realized that the finite-volume corrections contained information on infinite-volume scattering processes. This was very significant because the Maiani-Testa no-go theorem [25] established that scattering information from Euclidean correlation functions was not possible. However, by working in a finite volume we get around this limitation.

In this work, we extracted the single- and two-particle finite-volume spectrum for the $I = 1$, $S = 0$, parity-odd, G-parity-even channels at zero total momentum on a $32^3 \times 256$ lattice with $m_\pi \approx 240\,\text{MeV}$. To date, these results represent the most comprehensive survey of the finite-volume spectrum for these channels. The use of the stochastic LapH method has made this possible for such a large lattice and small pion mass. The single-hadron dominated states extracted from each channel are compared to those of an earlier study by the Hadron Spectrum Collaboration (HSC) [26], which used a much smaller $24^3 \times 128$ lattice with a much heavier pion mass 391 MeV and which neglected to use two-hadron operators. Comparison with experiment is reasonably good, but some discrepancies are seen. We found a single-hadron dominated state corresponding to either the $\rho_3(1690)$ or the $\rho_3(1990)$, which suggests that one of these resonances may not be a quark-antiquark excitation and instead is something more exotic. We also found a single-hadron dominated state with no corresponding experimental resonance. This state can most likely be designated as a spin-2 resonance. Its energy was found to be $E \approx 3.66\ m_K = 1.814(59)\,\text{GeV}$. A similar state was also extracted from the HSC. We also could not reproduce all of the experimentally excited ρ resonances below $\sim 2\,\text{GeV}$, which means at least one of these excited resonances likely cannot be described as a quark-antiquark excitation. We also used the recently developed strategies in Ref. [27] for including multiple partial waves and/or decay channels in a $K\pi$ scattering analysis based on the formalism introduced by Lüscher. As a first effort toward the extraction of the $K^*(892)$ resonance parameters, we included

$l = 0$, $l = 1$, and $l = 2$ partial waves in our analysis while remaining below the inelastic threshold.

The organization of this work is as follows: Chap. 2 introduces the basics of lattice QCD and sets up the groundwork for our calculations. Chap. 3 introduces our approach to efficiently constructing large sets of operators with the correct transformation properties so that we excite as much of the low-lying spectrum as possible. The estimation of temporal correlation functions from these operators using the stochastic LapH method [17] is described in Chap. 4. The extension of these methods to tetraquarks is then made in Chap. 5. In Chap. 6, the extraction of the finite-volume spectrum from a large temporal correlation matrix is described. Then, Chap. 7 establishes the Lüscher quantization condition and describes recently developed methods for the efficient application of the quantization condition. Finally, Chap. 8 shows results obtained for: 1) the isovector, nonstrange, odd parity, even G-parity bosonic spectra in finite-volume are shown; and 2) the resonance parameters of the $K^*(892)$.

2.0 LATTICE QCD

Lattice QCD, first introduced by Ken Wilson in 1974 [16], offers a non-perturbative approach to QCD by introducing a spacetime lattice which serves to regulate the theory. The fields that comprise this theory, originally having an uncountably infinite number of degrees of freedom, now have finitely many degrees of freedom. This allows correlation functions to be evaluated by a well-defined path integral (*i.e.* an integral of finite dimension).

2.1 CONTINUUM QCD

QCD is a non-abelian gauge theory with an $SU_c(3)$ gauge symmetry group that details the strong interaction between quarks and gluons. The quarks are represented by massive Dirac spinors

$$\psi^{(f)}_{a\alpha}(x), \qquad \overline{\psi}^{(f)}_{a\alpha}(x), \tag{2.1}$$

that transform under the fundamental ($\mathbf{3}$) and antifundamental ($\overline{\mathbf{3}}$) representations of $SU_c(3)$ indicated by the color indices $a = 1, 2, 3$, where $\alpha = 1, 2, 3, 4$ is the Dirac index, and $f = 1, 2, \ldots, N_f$ is the flavor index. Flavor symmetry $SU_F(N_f)$ is broken in nature for $N_f > 2$, but the reduced isospin symmetry $SU_I(2)$ between the up and down quarks is nearly exact and for simplicity is treated as exact in our simulations.

By demanding the Lagrangian be invariant under local gauge transformations, we must introduce a massless vector boson transforming in the adjoint ($\mathbf{8}$) representation of $SU_3(3)$

$$\mathcal{A}^a_\mu(x), \qquad a = 1, 2, \cdots, 8, \tag{2.2}$$

which are the components of a vector $\mathcal{A}_\mu$ in the fundamental representation of the $\mathfrak{su}_c(3)$ Lie algebra. The basis vectors that span $\mathfrak{su}_c(3)$ are the generators of the Lie group $SU_c(3)$ satisfying

$$[T_a, T_b] = if^{abc}T_c, \qquad a, b, c = 1, 2, \ldots, 8, \tag{2.3a}$$

$$\mathrm{Tr}[T_a T_b] = \frac{1}{2}\delta_{ab}, \tag{2.3b}$$

where f^{abc} are the structure constants for the Lie algebra. Conventionally, the Gell-Mann matrices (denoted by λ_a) are used for the fundamental representation of $\mathfrak{su}_c(3)$, which can be shown to satisfy all the necessary properties with $T_a = \frac{1}{2}\lambda_a$ Then, we expand $\mathcal{A}_\mu(x)$ in this basis as

$$\mathcal{A}_\mu(x) = \mathcal{A}^a_\mu(x)\frac{\lambda_a}{2}. \tag{2.4}$$

From these fields, we construct a locally $SU_c(3)$ gauge invariant Lagrangian in the fermionic sector as

$$\mathcal{L}_F = \sum_{f=1}^{N_f} \overline{\psi}^{(f)}_{a\alpha}\Big(i\gamma^\mu_{\alpha\beta}(D_\mu)_{ab} - m^{(f)}\delta_{\alpha\beta}\delta_{ab}\Big)\psi^{(f)}_{b\beta}, \tag{2.5}$$

where D_μ is the gauge-covariant derivative defined as

$$D_\mu = \partial_\mu + ig\mathcal{A}_\mu. \tag{2.6}$$

This Lagrangian reveals the interaction between quarks and gluons, but it is missing a kinetic term for the gluons. This term can be constructed from the gluon field strength tensor via the commutator of the covariant derivative

$$\begin{aligned} G_{\mu\nu}(x) &= \frac{1}{2}G^a_{\mu\nu}\lambda_a \\ &\equiv -\frac{i}{g}[D_\mu, D_\nu] \\ &= \frac{1}{2}\lambda_a(\partial_\mu\mathcal{A}^a_\nu - \partial_\nu\mathcal{A}^a_\mu - gf^{abc}\mathcal{A}^b_\mu\mathcal{A}^c_\nu) \\ &= \partial_\mu\mathcal{A}_\nu - \partial_\nu\mathcal{A}_\mu + ig[\mathcal{A}_\mu, \mathcal{A}_\nu]. \end{aligned} \tag{2.7}$$

The definition of the gluon field strength tensor in terms of the commutator of the covariant derivative makes it easy to show gauge covariance from the fact that D_μ is defined to be gauge covariant. Thus, under a local $SU_c(3)$ gauge transformation

$$\begin{aligned} G_{\mu\nu}(x) &\to -\frac{i}{g}[\Omega(x)D_\mu\Omega^\dagger(x), \Omega(x)D_\nu\Omega^\dagger(x)] \\ &= \Omega(x) - \frac{i}{g}[D_\mu, D_\nu]\Omega^\dagger(x) \\ &= \Omega(x)G_{\mu\nu}\Omega^\dagger(x), \end{aligned} \tag{2.8}$$

where $\Omega(x)$ is an element of $SU_c(3)$. Thus, we can form a gauge invariant object by taking the trace of $G_{\mu\nu}$. Following the generalization from electrodynamics, the gauge Lagrangian is

$$\begin{aligned} \mathcal{L}_G[G] &= -\frac{1}{2}\,\mathrm{Tr}[G_{\mu\nu}G^{\mu\nu}] \\ &= -\frac{1}{2}\,\mathrm{Tr}[G^a_{\mu\nu}\frac{\lambda_a}{2}G^{\mu\nu}_b\frac{\lambda_b}{2}] \\ &= -\frac{1}{2}G^a_{\mu\nu}G^{\mu\nu}_b\,\mathrm{Tr}[T_aT_b] \\ &= -\frac{1}{2}G^a_{\mu\nu}G^{\mu\nu}_b\left(\frac{1}{2}\delta_{ab}\right) \\ &= -\frac{1}{4}G^a_{\mu\nu}G^{\mu\nu}_a. \end{aligned} \tag{2.9}$$

Putting everything together the QCD Lagrangian is then given by[1]

$$\mathcal{L}[\psi, \overline{\psi}, G] = \sum_{f=1}^{N_f} \overline{\psi}^{(f)}_{a\alpha}(i\gamma^\mu_{\alpha\beta}D_{\mu ab} - m^{(f)}\delta_{\alpha\beta}\delta_{ab})\psi^{(f)}_{b\beta} - \frac{1}{4}G^a_{\mu\nu}G^{\mu\nu}_a, \tag{2.10}$$

where γ_μ are the usual gamma matrices.

[1] In general, the QCD Lagrangian can also include a CP violating term $\theta\frac{1}{32\pi^2}G^a_{\mu\nu}G^a_{\rho\sigma}\epsilon^{\mu\nu\rho\sigma}$. However, experiment has shown that θ is consistent with zero, and thus we do not include this term.

2.1.1 Euclidean Spacetime

In lattice QCD calculations, it is necessary to work in a Euclidean spacetime, referred to as the imaginary time formalism, rather than the more commonly used Minkowski spacetime. The reason for this is due to the exponential weighting factor that appears in a path integral. In Minkowski spacetime this weighting factor is e^{iS_M}, where S_M is the action in Minkowski spacetime, which is complex and thus unfit to be used for importance sampling in our Monte Carlo calculations. However, in Euclidean spacetime this weighting factor becomes e^{-S}, where S is the action in Euclidean spacetime, which is real and positive and thus can be used for our numerical calculations.

We define the following relationships between coordinates and derivatives in Minkowski spacetime and Euclidean spacetime:

$$x^4 = x_4 = ix^0_M = ix^M_0, \quad x^j = x_j = x^j_M = -x^M_j, \tag{2.11a}$$

$$\partial^4 = \partial_4 = -i\partial^0_M = -i\partial^M_0, \quad \partial^j = \partial_j = -\partial^j_M = \partial^M_j. \tag{2.11b}$$

From the definition of the covariant derivative in Eq. (2.6), the gluon fields must be similarly defined

$$\mathcal{A}^4 = \mathcal{A}_4 = -i\mathcal{A}^0_M = -i\mathcal{A}^M_0, \quad \mathcal{A}^j = \mathcal{A}_j = -\mathcal{A}^j_M = \mathcal{A}^M_j. \tag{2.12}$$

From this follows the relationship between the Minkowski and Euclidean gluon field strength tensors

$$G^M_{0k} = -G^{0k}_M = iG_{4k} = iG^{4k}, \quad G^M_{ij} = G^{ij}_M = G_{ij} = G^{ij}. \tag{2.13}$$

Finally, we define the Euclidean γ matrices as follows,

$$\{\gamma_\mu, \gamma_\nu\} = 2\delta_{\mu\nu}, \quad \gamma^\dagger_\mu = \gamma_\mu, \quad \gamma_5 = \gamma_4\gamma_1\gamma_2\gamma_3, \tag{2.14}$$

with the following relationship to the Minkowski γ matrices,

$$\gamma^4 = \gamma_4 = \gamma^0_M = \gamma^M_0, \quad \gamma_k = \gamma^k = -i\gamma^k_M = i\gamma^M_k, \quad \gamma_5 = \gamma^5 = \gamma^5_M. \tag{2.15}$$

Three common representations for the Dirac γ-matrices in Euclidean spacetime are the Dirac-Pauli representation, the Weyl chiral representation, and the DeGrand-Rossi chiral

representation. Unless stated otherwise, we will use the Dirac-Pauli representation given by

$$\gamma_k = \begin{pmatrix} 0 & -i\sigma_k \\ i\sigma_k & 0 \end{pmatrix}, \qquad \gamma_4 = \begin{pmatrix} I & 0 \\ 0 & -I \end{pmatrix}, \qquad \gamma_5 = \begin{pmatrix} 0 & I \\ I & 0 \end{pmatrix}, \tag{2.16}$$

where the Pauli spin matrices are given by

$$\sigma_1 = \begin{pmatrix} 0 & 1 \\ 1 & 0 \end{pmatrix}, \qquad \sigma_2 = \begin{pmatrix} 0 & -i \\ i & 0 \end{pmatrix}, \qquad \sigma_3 = \begin{pmatrix} 1 & 0 \\ 0 & -1 \end{pmatrix}. \tag{2.17}$$

In the Dirac-Pauli representation, the γ matrices also have the following properties:

$$\gamma_1^T = -\gamma_1, \quad \gamma_2^T = \gamma_2, \quad \gamma_3^T = -\gamma_3, \quad \gamma_4^T = \gamma_4. \tag{2.18}$$

From the definitions above, we Wick rotate the Minkowski action to determine the action in Euclidean spacetime. Using Eq. (2.10) and suppressing flavor, spin, and color indices, we find

$$\begin{aligned} iS_M &= i \int dx_M^0 \int d^3\mathbf{x}_M \Big[\overline{\psi}(i\gamma_M^0 D_0^M + i\gamma_M^j D_j^M - m)\psi - \frac{1}{4} G_{\mu\nu}^M G_M^{\mu\nu}\Big] \\ &= i \int (-i dx_4) \int d^3\mathbf{x} \Big[\overline{\psi}(i\gamma_4(iD_4) + i(i\gamma_j)D_j - m)\psi - \frac{1}{4} G_{\mu\nu} G_{\mu\nu}\Big] \\ &= -\int d^4x \Big[\overline{\psi}(\gamma_\mu D_\mu + m)\psi + \frac{1}{4} G_{\mu\nu} G_{\mu\nu}\Big] \\ &= -S. \end{aligned} \tag{2.19}$$

It turns out that in order to simultaneously obey both invariance under Euclidean transformations and equivalence of the two-point function in Euclidean space with the two-point function in Minkowski space analytically continued to imaginary time, an identification of $\overline{\psi} = \psi^\dagger \gamma^4$ or $\overline{\psi} = \psi$ cannot be made. Thus, in Euclidean space, the fields ψ and $\overline{\psi}$ will be treated independently. This will not cause any serious issues, especially since we integrate over the quark fields immediately.

In lattice QCD, it convenient to rescale the gauge field as follows:

$$\mathcal{A}_\mu(x) \to \frac{1}{g} \mathcal{A}_\mu(x). \tag{2.20}$$

Then the final form of the QCD action in Euclidean spacetime is

$$S[\psi,\overline{\psi},G]=\int d^4x\Bigg[\sum_{i=f}^{N_f}\overline{\psi}^{(f)}_{a\alpha}\Big((\gamma_\mu)_{\alpha\beta}(D_\mu)_{ab}+m^{(f)}\delta_{\alpha\beta}\delta_{ab}\Big)\psi^{(f)}_{b\beta}+\frac{1}{4g^2}G^a_{\mu\nu}G^a_{\mu\nu}\Bigg] \tag{2.21}$$

where now

$$D_\mu=\partial_\mu+i\mathcal{A}_\mu, \tag{2.22a}$$

$$G_{\mu\nu}=-i[D_\mu,D_\nu]=\partial_\mu\mathcal{A}_\nu-\partial_\nu\mathcal{A}_\mu+i[\mathcal{A}_\mu,\mathcal{A}_\nu]. \tag{2.22b}$$

Notice that the coupling strength g has been taken out of the definition for $G_{\mu\nu}$ and instead is shown explicitly in the gauge action.

2.2 DISCRETIZATION OF THE QCD ACTION

A convenient way to represent the lattice and the points it contains is

$$\Lambda\equiv\left\{n=(n_1,n_2,n_3,n_4)|n_1,n_2,n_3=0,1,\ldots,N_s-1;n_4=0,1,\ldots,N_t-1\right\}, \tag{2.23}$$

where N_s is the number of lattice sites in each spatial direction, N_t is the number of lattice sites in the temporal direction. For the time being, we assume the lattice spacing is a in all directions, but later on we will find it useful to use a different spacing in the temporal direction.

The introduction of a finite spacing a acts as a momentum cutoff which restricts the momenta to the first Brillouin zone

$$p_\mu\in(-\pi/a,\pi/a]. \tag{2.24}$$

The introduction of a finite volume with periodic boundary conditions restricts the momentum further to be discrete

$$\boldsymbol{p}=\frac{2\pi}{L}\boldsymbol{n}, \tag{2.25}$$

where L is the spatial size of the lattice, and $\boldsymbol{n}$ is a vector of integers.

The actual position of any given lattice point is $x = an$. Thus, to define the QCD action on our lattice, we begin with the following replacements

$$x \to n, \tag{2.26a}$$

$$\int \mathrm{d}^4x \to a^4 \sum_{n\in\Lambda}. \tag{2.26b}$$

But the requirement of $SU(3)$ gauge invariance introduces some difficulties in the discretization of the action, and simply applying Eq. (2.26) will not lead to a gauge invariant action.

2.2.1 Fermionic action

As we saw above, in gauge field theory, it is local gauge invariance that forces the introduction of the gauge fields. Thus, if we start from a discretized free fermionic action S_F^0, then the appropriate introduction of the gauge fields emerges from requiring local invariance under local $SU_c(3)$ transformations.[2] In the continuum, the free fermionic action is (ignoring the quark field indices)

$$S_F^0[\psi, \overline{\psi}] = \int \mathrm{d}^4x\, \overline{\psi}(x)(\gamma_\mu \partial_\mu + m)\psi(x), \tag{2.27}$$

which on the lattice becomes,

$$S_F^0[\psi, \overline{\psi}] = a^4 \sum_{n\in\Lambda} \overline{\psi}(n) \left[\sum_{\mu=1}^{4} \gamma_\mu \frac{\psi(n+\hat{\mu}) - \psi(n-\hat{\mu})}{2a} + m\psi(n) \right]. \tag{2.28}$$

Next, we introduce local $SU_c(3)$ gauge transformations on the lattice,

$$\psi(n) \to \psi'(n) = \Omega(n)\psi(n), \tag{2.29a}$$

$$\overline{\psi}(n) \to \overline{\psi}'(n) = \overline{\psi}(n)\Omega^\dagger(n). \tag{2.29b}$$

Then, applying these transformations to Eq. (2.28) gives

$$S_F^0[\psi', \overline{\psi}'] = a^4 \sum_{n\in\Lambda} \overline{\psi}(n) \left[\sum_{\mu=1}^{4} \gamma_\mu \frac{\Omega^\dagger(n)\Omega(n+\hat{\mu})\psi(n+\hat{\mu}) - \Omega^\dagger(n)\Omega(n-\hat{\mu})\psi(n-\hat{\mu})}{2a} + m\psi(n) \right]. \tag{2.30}$$

[2] Without local gauge invariance, significant difficulties arise, including the possible loss of renormalizability.

The second term is gauge invariant, because $\Omega^\dagger(n)\Omega(n) = 1$, but the term involving the discretized derivative is not. To circumvent the issue, we introduce a new field $U_\mu(n)$, the so-called *link variables*, that transforms under $SU_c(3)$ as

$$U_\mu(n) \to \Omega(n)\, U_\mu(n)\Omega^\dagger(n+\hat{\mu}). \tag{2.31}$$

As the name suggests, these objects are not associated with any given site on the lattice but instead with the "link" between n and $n+\hat{\mu}$. Additionally, these link variables obey the following relationship

$$U_{-\mu}(n) \equiv U_\mu^\dagger(n-\hat{\mu}). \tag{2.32}$$

This shows that the Hermitian conjugate reverses the direction of a link variable while retaining the original lattice sites that the link was defined between. Under an $SU(3)$ transformation these oppositely directed link variables transform as

$$\begin{aligned} U_{-\mu}(n) &= U_\mu^\dagger(n-\hat{\mu}) \\ &\to [\Omega(n-\hat{\mu})\, U_\mu(n-\hat{\mu})\Omega^\dagger(n)]^\dagger \\ &= \Omega(n)\, U_\mu^\dagger(n-\hat{\mu})\Omega^\dagger(n-\hat{\mu}) \\ &= \Omega(n)\, U_{-\mu}(n)\Omega^\dagger(n-\hat{\mu}). \end{aligned} \tag{2.33}$$

Inserting these link variables into the fermionic action in the following way

$$S_F[\psi,\overline{\psi},U] = a^4 \sum_{n\in\Lambda} \overline{\psi}(n)\Bigg[\sum_{\mu=1}^{4} \gamma_\mu \frac{U_\mu(n)\psi(n+\hat{\mu}) - U_{-\mu}(n)\psi(n-\hat{\mu})}{2a} + m\psi(n)\Bigg] \tag{2.34}$$

makes the fermionic action gauge invariant. This can be seen explicitly:

$$\begin{aligned} \overline{\psi}(n)\, U_\mu(n)\psi(n+\hat{\mu}) &\to \big(\overline{\psi}(n)\Omega^\dagger(n)\big)\big(\Omega(n)\, U_\mu(n)\Omega^\dagger(n+\hat{\mu})\big)\big(\Omega(n+\hat{\mu})\psi(n+\hat{\mu})\big) \\ &= \overline{\psi}(n)\big(\Omega^\dagger(n)\Omega(n)\big)\, U_\mu(n)\big(\Omega^\dagger(n+\hat{\mu})\Omega(n+\hat{\mu})\big)\psi(n+\hat{\mu}) \\ &= \overline{\psi}(n)\, U_\mu(n)\psi(n+\hat{\mu}), \end{aligned} \tag{2.35}$$

and similarly for the term $\overline{\psi}(n)\, U_{-\mu}(n)\psi(n-\hat{\mu})$.

The next step is to make sure the fermionic action reduces to the continuum action in the limit as the lattice spacing goes to zero. For this to be possible, the link variables need to have some dependence on the gluon field $\mathcal{A}_\mu(x)$. Thankfully, there exists an object in

the continuum that depends on the gluon field and has all the same properties of the link variables discussed above. This object, known as a *gauge transporter*, has the form

$$U(x,y) = P\exp\left(i\int_{\mathcal{C}_{xy}} \mathcal{A}(s)\cdot \mathrm{d}s\right) \tag{2.36}$$

where P is the path-ordering operator and $\mathcal{C}_{xy}$ is a path connecting the points x and y. By choosing $x = an$, $y = a(n+\hat{\mu})$, and $\mathcal{C}_{xy}$ as the straight-line path connecting x and y, the gauge transporter corresponds to the link variable $U_\mu(n)$. Thus, we find the dependence of the link variables on the gluon field to be

$$U_\mu(n) \approx \exp\big(ia\mathcal{A}_\mu(n)\big), \tag{2.37}$$

where the integral in Eq. (2.36) has been approximated by assuming $\mathcal{A}_\mu(s) \approx \mathcal{A}_\mu(x)$ along the path $\mathcal{C}_{xy}$, which is good to $\mathcal{O}(a)$, allowing us to drop the path ordering. In light of Eq. (2.37), we refer to the link variables as the *gauge-link variables*.

For small a, the gauge-link variables become

$$U_\mu(n) \approx 1 + ia\mathcal{A}_\mu(n) + \mathcal{O}(a^2). \tag{2.38}$$

Finally, let us take the limit as $a \to 0$ of Eq. (2.34)

$$\begin{aligned}
\lim_{a\to 0} S_F[\psi,\overline{\psi},U] &= \lim_{a\to 0}\; a^4 \sum_{n\in\Lambda} \overline{\psi}(n)\Bigg[\sum_{\mu=1}^{4}\gamma_\mu\Bigg[\frac{\psi(n+\hat{\mu})-\psi(n-\hat{\mu}))}{2a} \\
&\qquad + \frac{ia\mathcal{A}_\mu(n)\psi(n+\hat{\mu}) + ia\mathcal{A}_\mu(n-\hat{\mu})\psi(n-\hat{\mu})}{2a}\Bigg] + m\psi(n) + \mathcal{O}(a)\Bigg] \\
&= \lim_{a\to 0}\; a^4 \sum_{n\in\Lambda} \overline{\psi}(n)\Big[\gamma_\mu\Big(\partial_\mu + i\mathcal{A}_\mu(n)\Big)\psi(n) + m\psi(n) + \mathcal{O}(a)\Big] \\
&= \int d^4x\,\Big[\overline{\psi}(x)\big(\gamma_\mu D_\mu + m\big)\psi(x) + \mathcal{O}(a)\Big]
\end{aligned} \tag{2.39}$$

which shows that the continuum action is reproduced in the limit $a \to 0$ and that the discretization error is of $\mathcal{O}(a)$. To summarize, so far we have found an action for fermions on the lattice that is gauge invariant and reduces to the continuum action as the lattice spacing goes to zero.

2.2.2 The Fermion Doubling Problem

The Dirac operator on the lattice M is defined by

$$S_F[\psi, \overline{\psi}, U] = \overline{\psi} M[U] \psi. \tag{2.40}$$

Comparing Eqs. (2.40) and (2.34) implies the Dirac operator has the following form

$$M_{a\alpha;b\beta}(n|m) = a^4 \sum_{\mu=1}^{4} (\gamma_\mu)_{\alpha\beta} \frac{U_{\mu,ab}(n)\ \delta_{n+\hat{\mu},m} - U_{-\mu,ab}(n)\ \delta_{n-\hat{\mu},m}}{2a} + a^4 m_f\ \delta_{\alpha\beta}\delta_{ab}\delta_{nm}, \tag{2.41}$$

where m_f is the mass of a quark with flavor f. We find the free lattice quark propagator by inverting M after setting $U_\mu(n) = 1$ for all n and μ. Then, the Dirac matrix in momentum space is given by

$$\widetilde{M}^0(p) = a^4 \sum_{\mu=1}^{4} i\gamma_\mu \frac{\sin(a\ p_\mu)}{a} + a^4 m_f, \tag{2.42}$$

where $p_\mu \equiv \hat{\mu} \cdot p$. Inverting $\widetilde{M}$ gives the free lattice quark propagator

$$a^4 \widetilde{M}^0(p)^{-1} = \frac{-ia \sum_\mu \gamma_\mu \sin(a\ p_\mu) + a^2 m_f}{\sum_\mu \sin^2(a\ p_\mu) + a^2 m_f^2}, \tag{2.43}$$

which is easily verified by computing $\widetilde{M}^0(p)\widetilde{M}^0(p)^{-1}$. As expected, Eq. (2.43) has a physical pole at $p^2 = -m^2$, but there exists 15 extra poles at the edges of the Brillouin zone referred to as fermion doublers.

Wilson proposed adding an extra term to the Dirac matrix that removes the doublers while still retaining the correct continuum limit.[3] The fermions corresponding to this new action are referred to as *Wilson fermions*, and the new Dirac matrix is given by

$$\begin{aligned} M_W(n|m) = a^4 \sum_{\mu=1}^{4} \gamma_\mu \frac{U_\mu(n)\delta_{n+\hat{\mu},m} - U_{-\mu}(n)\delta_{n-\hat{\mu},m}}{2a} + a^4 M \delta_{n,m} \\ - a^4 \sum_{\mu=1}^{4} a \frac{U_\mu(n)\delta_{n+\hat{\mu},m} + U_{-\mu}(n)\delta_{n-\hat{\mu},m} - 2\delta_{n,m}}{2a^2}, \end{aligned} \tag{2.44}$$

where the last term is the Wilson term. This term is the discretized version of $-\frac{a}{2}\partial_\mu\partial_\mu$ with proper insertions of the gauge links to maintain local gauge invariance.

[3] Operators added to the action that vanish in the continuum limit are irrelevant operators. The freedom to add any irrelevant operators we choose will be exploited beyond simply solving the Fermion Doubling problem.

Using Wilson's version of the Dirac operator, we now have a discretized action that reduces to the continuum QCD action in the $a \to 0$ limit, is gauge invariant, and has one physical pole. There is, however, one drawback: we have lost the usual chiral symmetry for massless fermions due to the introduction of the Wilson term. This can be understood by interpreting the Wilson term as a mass term which contributes to the total mass of the fermions, because even in the limit $m_f \to 0$ there still exists a non-zero "mass" which breaks the chiral symmetry.

It may be bothersome that Wilson's Dirac operator does not obey the usual chiral symmetry, and thus many attempts have been made to try and find a solution to the doubling problem without breaking chiral symmetry. But, all other solutions to this problem require some kind of sacrifice. A no-go theorem was proved in 1981 that says a lattice regularization does not exist for local fermions with chiral symmetry such that the action has the correct continuum limit and is free of fermion doublers [28]. Different types of fermions have been proposed in light of this no-go theorem. However, in what follows we will only consider Wilson fermions.

2.2.3 The Wilson Gauge Action

The next step in constructing an action on the lattice is to determine the kinetic term for the gluons. It has become evident from the previous sections that on the lattice we consider the gauge links as the fundamental objects that our quarks interact with rather than the gluon fields themselves. Therefore, we want our gluon action to be dependent on the gauge links only. In addition, we need to use the gauge links in such a way that the gauge action is gauge invariant. In order to allow the cancellation of a significant number of gauge transformation matrices, we should consider using link variables that share their end site with another link variable's starting site (*i.e.* the link variables should be "attached" to one another).

Consider a product of k "attached" link variables that connect the lattice sites n and m

$$L(n|m) = U_{\mu_0}(n)\, U_{\mu_1}(n + \hat{\mu}_0) \ldots U_{\mu_{k-1}}(m - \hat{\mu}_{k-1}). \tag{2.45}$$

Then, using the transformation properties of the gauge-link variables, under a gauge transformation this product of links transforms as

$$L(n|m) \to \Omega(n) L(n|m) \Omega^\dagger(m). \tag{2.46}$$

Many of the gauge transformation matrices have been canceled, and only two remain. Since the trace of any product of matrices is invariant under cyclic permutations, then the trace of $L(n|n)$ is a gauge invariant object. Products of gauge-link variables that start and end on the same lattice site, like $L(n|n)$ will be referred to as closed loops or Wilson loops.

The *plaquette* is the smallest non-trivial closed loop defined as follows

$$\begin{aligned} U_{\mu\nu}(n) &\equiv U_\mu(n)\, U_\nu(n+\hat{\mu})\, U_{-\mu}(n+\hat{\mu}+\hat{\nu})\, U_{-\nu}(n+\hat{\nu}) \\ &= U_\mu(n)\, U_\nu(n+\hat{\mu})\, U_\mu^\dagger(n+\hat{\nu})\, U_\nu^\dagger(n). \end{aligned} \tag{2.47}$$

Wilson used the collection of all plaquettes to form a gauge action [16]

$$S_G[U] = \frac{\beta}{3} \sum_{n\in\Lambda} \sum_{\mu<\nu} \text{Re Tr} \Big[1 - U_{\mu\nu}(n) \Big], \tag{2.48}$$

where $\beta = 2N_c/g^2 = 6/g^2$. Clearly, this action is gauge invariant since the gauge links are only introduced via the trace of plaquettes. We now take the continuum limit to determine the leading order discretization errors in the gauge action [29]:

$$\lim_{a\to 0} U_{\mu\nu}(x) = 1 + ia^2 G_{\mu\nu} - \frac{1}{2} a^4 G_{\mu\nu}^2 + \mathcal{O}(a^6). \tag{2.49}$$

and substituting this into Eq. (2.48) reproduces the correct action in the continuum limit with discretization errors of $\mathcal{O}(a^2)$.

2.2.4 Improved Actions

The required volume that our calculations take place in is determined by the correlation length of the system, which is given by the inverse of the mass of the lightest state in our system. The correlation length of our system must be smaller than the size of the box we work in. In order to increase computational efficiency, we could tune the quark masses to increase the mass of the pion such that the correlation length is small enough. Or, we could increase the coarseness of our lattice (*i.e.* increase a). Both of these methods are usually employed. But, a coarser lattice will induce greater discretization errors. Thus, we make use of so-called improved actions, which decrease the lattice artifacts.

However, the use of a coarse lattice poses two problems in the temporal direction. First, temporal correlation functions, used for energy extraction (see Sec. 2.4), generally have signal-to-noise ratios that decrease as the time separation increases. Therefore, a large a_t gives less viable data points before the time separation in which noise takes over is reached. Second, in order to maintain a positive definite transfer matrix, which in turn guarantees a Hermitian Hamiltonian, we cannot fully exploit improvement in the temporal direction (*e.g.* we cannot use any Wilson loops with lengths greater than one in the temporal direction) [30, 31]. To circumvent these issues, we make use of an anisotropic lattice [32, 33] with $a_s > a_t$, where the anisotropy is defined as $\xi = a_s/a_t$. Now we focus on improvement in the spatial directions.

The main strategy used to remove the lower order lattice artifacts from our action is to employ the Symanzik Improvement program [34]. The idea is to add higher dimensional operators to our action with coefficients chosen so to cancel the lowest order lattice artifacts. Adding additional operators that vanish in the continuum limit can always be done, because we only require that the continuum QCD action be reproduced as $a \to 0$. This allows for a large class of actions that lead to the same physics. Thus, Symanzik improvement comes down to choosing an action within this large class of equivalent actions that has the most desirable properties.

Further improvement of the lattice artifacts can be made by dealing with divergent tadpole contributions that arise within lattice perturbation theory. Tadpole improvement

can be implemented with a rescaling of the gauge links by tadpole improvement factors [35], *i.e.* $U \to U/u$, where

$$u = \left\langle \frac{1}{3} \operatorname{Re} \operatorname{Tr} U_{\mu\nu} \right\rangle^{1/4}. \tag{2.50}$$

Note that since u is both a parameter in the action and an observable, we have to adjust u until the parameter in the action agrees with the measured observable.

The Wilson gauge action is expected to have $\mathcal{O}(a_s^2, a_t^2)$ lattice artifacts present. The gauge action we use is based on the Symanzik-improved Lüscher-Weisz action [36, 37] with tadpole-improved coefficients used in Refs. [32, 33, 38, 39]

$$S_G^\xi[U] = \frac{\beta}{3\gamma_g}\left[\sum_{x,i\neq j}\left(\frac{5}{6u_s^4}\Omega_{\mathcal{P}_{ij}}(x) - \frac{1}{12u_s^6}\Omega_{\mathcal{R}_{ij}}(x)\right) + \sum_{x,i}\left(\frac{4}{3u_s^2u_t^2}\Omega_{\mathcal{P}_{it}}(x) - \frac{1}{12u_s^4u_t^2}\Omega_{\mathcal{R}_{it}}\right)\right], \tag{2.51}$$

where $\Omega_W \equiv Re\,\mathrm{Tr}(1-W)$, $\mathcal{P}$ is a plaquette, and $\mathcal{R}_{\mu\nu}$ is a 2×1 planar Wilson loop (with the μ direction being of length 2 and the ν direction of length 1). The parameters u_s and u_t are the spatial and temporal tadpole coefficients, and γ_g is the bare gauge anisotropy. This action has leading discretization errors of $\mathcal{O}(a_s^4, a_t^2, g^2a_s^2)$, and has a positive definite transfer matrix, because no length-two gauge links in time are used.

The unimproved fermion action was shown to have discretization errors of $\mathcal{O}(a_s, a_t)$. To improve these errors, we use the anisotropic clover improved quark action [40]

$$\begin{aligned} S_F^\xi[\psi,\overline{\psi},U] = \sum_x \overline{\psi}(x)\frac{1}{\tilde{u}_t}\Bigg(&\tilde{u}_t\hat{m}_0 + \hat{W}_t + \frac{1}{\gamma_f}\sum_s \hat{W}_s \\ &- \frac{1}{2}\left[\frac{1}{2}\left(\frac{\gamma_g}{\gamma_f}+\frac{1}{\xi}\right)\frac{1}{\tilde{u}_t\tilde{u}_s^2}\sum_s \sigma_{ts}\hat{F}_{ts} + \frac{1}{\gamma_f}\frac{1}{\tilde{u}_s^3}\sum_{s<s'}\sigma_{ss'}\hat{F}_{ss'}\right]\Bigg)\psi(x), \end{aligned} \tag{2.52}$$

where the $\tilde{u}_s$ and $\tilde{u}_t$ are the spatial and temporal tadpole factors in the fermion action, $\hat{m}_0$ is the dimensionless bare quark mass, γ_f is the bare fermion anisotropy, ξ is the desired renormalized anisotropy, $\sigma_{\mu\nu} = \frac{1}{2}[\gamma_\mu,\gamma_\nu]$, $\hat{F}_{\mu\nu} = \frac{1}{4}\operatorname{Im} U_{\mu\nu}$, and

$$\hat{W}_\mu = a_\mu W_\mu = a_\mu\nabla_\mu - \frac{a_\mu^2}{2}\gamma_\mu\Delta_\mu, \tag{2.53a}$$

$$\nabla_\mu f(x) = \frac{1}{2a_\mu}\Big[U_\mu(x)f(x+\mu) - U_\mu^\dagger(x-\mu)f(x-\mu)\Big], \tag{2.53b}$$

$$\Delta_\mu f(x) = \frac{1}{a_\mu^2}\Big[U_\mu(x)f(x+\mu) + U_\mu^\dagger(x-\mu)f(x-\mu) - 2f(x)\Big]. \tag{2.53c}$$

This action now has leading discretization errors of $\mathcal{O}(a_t^2, g^2 a_s^2, a_s^4)$. Although it is possible to further improve the fermion action, most improvements will involve extra quark fields, and we want it to remain quadratic in the fermion fields.

The use of these actions shows scaling violations on the order of 1% for $a \sim 0.1\,\text{fm}$ [38], which means a continuum extrapolation is generally not necessary when using these improved lattices.

2.2.5 Tuning the Lattice and Setting the Scale

The remaining bare parameters in the action, the bare quark masses, the bare anisotropies, and the inverse coupling β are determined by setting desired physical results (*i.e.* a set of renormalization conditions).

The bare gauge anisotropy γ_g and bare fermion anisotropy γ_f are determined by adjusting their values until the desired renormalized anisotropy is measured. In this work a renormalized anisotropy of $\xi \approx 3.5$ was determined. More specifically, the bare gauge anisotropy was set by requiring $R_{ss}(x, y) = R_{st}(x, \xi t)$, where $R_{ss}(x, y)$ and $R_{st}(x, t)$ are ratios of Wilson loops defined by

$$R_{ss}(x, y) = \frac{W_{ss}(x, y)}{W_{ss}(x + 1, y)}, \tag{2.54a}$$

$$R_{st}(x, t) = \frac{W_{st}(x, t)}{W_{ss}(x + 1, t)}, \tag{2.54b}$$

and $W_{\mu\nu}(x_\mu, x_\nu)$ is the expectation value of the trace of a product of gauge links forming a closed two-dimensional loop with length x_μ in the $\hat{\mu}$ direction and length x_ν in the $\hat{\nu}$ direction. The bare fermion anisotropy was set by requiring the mesons satisfy the dispersion relation

$$a_t^2 E^2(\boldsymbol{p}) = a_t^2 m^2 + \frac{a_s^2 \boldsymbol{p}^2}{\xi^2}. \tag{2.55}$$

From these requirements, the bare anisotropies were found to be

$$\gamma_g = 4.3, \qquad \gamma_f = 3.4. \tag{2.56}$$

The bare quark masses, m_l and m_s, were tuned by setting the ratios

$$s_\Omega = \frac{9(m_K^2 - m_\pi^2)}{4m_\Omega^2}, \qquad l_\Omega = \frac{9m_\pi^2}{4m_\Omega^2}, \tag{2.57}$$

to be as close to their experimentally measured values as possible. These ratios were chosen, because they are proportional to m_s and m_l in chiral perturbation theory to first order, where m_π is the mass of the pion, m_K is the mass of the kaon, and m_Ω is the mass of the omega baryon. The mass of the pion determines the largest correlation length in our system. Requiring that the correlation length always remain smaller than our lattice length L, m_π is made as small such that $m_\pi L$ is at least larger than one, but the general rule of thumb in lattice QCD is to keep $m_\pi \gtrsim 4$ or 5. Fortunately, the mass of the kaon can remain physical without causing any issues. On our lattices we set the bare strange quark mass to be $a_t m_s = -0.0743$. We have lattices with $m_\pi \approx 390\,\text{MeV}$ from setting the bare light quark mass to be $a_t m_l = -0.0840$ and with $m_\pi \approx 240\,\text{MeV}$ from setting the bare light quark mass to be $a_t m_l = -0.0860$.

In order to determine the value for a_t, we must choose some physical value. This procedure is known as *setting the scale*. There are different ways of setting the scale, but the one we choose is to use the mass of the kaon. That is, we determine a_t from

$$a_t = \frac{a_t m_K}{m_{K,phys}}, \tag{2.58}$$

where $a_t m_K$ is determined from our lattice calculation, and $m_{K,phys}$ is set to the experimentally observed value for the kaon mass.[4] We found $a_t \approx 0.034\,\text{fm}$, which gives $a_s \approx 0.12\,\text{fm}$ from our anisotropy. However, from the renormalization group equations, the inverse coupling β is a function of the lattice spacing. Thus, we attained this value for a_t by setting $\beta = 1.5$.

[4]More specifically, we use the average of the experimentally observed masses for the K^+ and the K^0, which gives $m_K \approx 495.6\,\text{MeV}$ [9].

2.3 MONTE CARLO INTEGRATION

One criteria for choosing the lattice action improvement is to maintain a fermionic action that was quadratic in the quark fields. This is desirable so that the integration over the quark fields can be performed exactly. Thus, our lattice action is of the form

$$S[\psi, \overline{\psi}, U] = \overline{\psi} M[U] \psi + S_G[U], \tag{2.59}$$

where $M[U]$ is the so-called Dirac matrix, and $S_G[U]$ is the improved gauge action. Then, Euclidean correlation functions are evaluated via a path-integral

$$\langle \mathcal{O} \rangle_T = \frac{1}{Z_T} \int \mathcal{D}[\psi, \overline{\psi}] \mathcal{D}[U] \mathcal{O}[\psi, \overline{\psi}, U] e^{-\overline{\psi} M[U] \psi - S_G[U]}, \tag{2.60}$$

where $\mathcal{O}$ is a generic operator, which can be replaced by any operator or product of operators one wishes, the subscript T is to remind us that we are working with a finite temporal extent of length T,[5] and the partition function Z_T is given by

$$Z_T = \int \mathcal{D}[\psi, \overline{\psi}] \mathcal{D}[U] e^{-\overline{\psi} M[U] \psi - S_G[U]}. \tag{2.61}$$

The integration over the quark fields can now be performed immediately via Wick's theorem

$$\langle \mathcal{O} \rangle_T = \frac{\int \mathcal{D}[U] F(M^{-1}[U]) \det M[U] e^{-S_G[U]}}{\int \mathcal{D}[U] \det M[U] e^{-S_G[U]}}, \tag{2.62}$$

where F is a function of inverse elements of the Dirac matrix determined from the Wick contractions involved.

However, the integration over the gauge-link variables cannot be done exactly. We need some method to accurately approximate this integral. Numerical quadrature is a commonly used technique for approximating integrals numerically, but this method becomes increasingly impractical as the dimension of the integral increases. There is an integral for each degree of freedom of the gauge links, which will generally be very large except for extremely small lattices. This so called *curse of dimensionality* can be overcome using Monte Carlo

[5] The distinction between a vacuum expectation value $\langle 0 | \mathcal{O} | 0 \rangle$ and $\langle \mathcal{O} \rangle_T$, because these only become equal in the limit $T \to \infty$. However, in much of this work it is assumed that T is large enough such that $\langle \mathcal{O} \rangle_T \approx \langle 0 | \mathcal{O} | 0 \rangle$. A discussion on the validity of this assumption and how violations of this assumption are dealt with can be found in Sec. 6.1.

integration: these methods suffer no serious issues when applied to integrals of very high dimension.

The main result of Monte Carlo integration is an estimate for a highly-multidimensional integral of the form

$$I_f = \int \mathcal{D}[U] p(U) f(U), \tag{2.63}$$

where U, meant to be highly suggestive of the gauge links, is a collection of variables (*e.g.* one for each spacetime point), $p(U)$ is a probability density, and $f(U)$ is an arbitrary function of the integration variables U. If one could randomly sample the variables U according to the probability density $p(U)$ to produce an ensemble $\{U_1, U_2, \ldots, U_{N_C}\}$ consisting of N_C configurations, then by the *law of large numbers* an estimate for I_f can be given as

$$I \approx \frac{1}{N_C} \sum_{k=1}^{N_C} f(U_k). \tag{2.64}$$

The error in this estimate is given by the *central limit theorem*

$$\sigma_I = \sqrt{\frac{V(f(U))}{N_C}}, \tag{2.65}$$

where $V(f(U))$ is the variance of $f(U)$ with respect to the probability density $p(U)$.

The integrals over the gauge-link variables that we want to estimate can be put in the form of Eq. (2.63) by setting

$$p(U) = \frac{\det M[U] e^{-S_G[U]}}{\int \mathcal{D}[U'] \det M[U'] e^{-S_G[U']}}. \tag{2.66}$$

Therefore, we need to determine a method for generating the ensemble of gauge-link configurations. In principal we could generate gauge configurations according to a uniform probability distribution. However, this is very inefficient, because of the large number of gauge configurations that lead to exponentially suppressed contributions to the integral. Using a non-uniform probability density in order to pick out the configurations that are most important is known as *importance sampling*.

We instead use a Markov chain. The idea of a Markov chain is to stochastically generate a sequence of gauge configurations

$$U^n \to U^{n+1} \to U^{n+2} \to \cdots, \tag{2.67}$$

where U^n refers to the n-th gauge configuration of the gauge-link variables, and n can range over all possible gauge configurations. A Markov chain requires a transition probability $T(U^m|U^n)$ to go from the configuration U^n to U^m. Then, if this transition probability satisfies detailed balance

$$T(U^n|U^m)p(U^m) = T(U^m|U^n)p(U^n), \qquad \forall\, n, m \tag{2.68}$$

then it can be shown that the transition probability generates configurations closer to the desired distribution at each update in the chain. Thus, if one waits until the Markov chain has reached equilibrium (or thermalized), then from that point on the configurations generated will be distributed according to $p(U)$.

A very popular algorithm for producing a Markov chain is the Metropolis algorithm [41], which uses an accept-reject step after each proposed new configuration. Generally, this method proceeds by proposing local changes to the gauge configuration, because otherwise the probability of acceptance becomes too low. But, due to the non-local nature of the fermion determinant (*i.e.* the determinant of the Dirac matrix), an algorithm that performs global updates to the gauge configuration at each step is preferred. Furthermore, the direct computation of the fermion determinant is prohibitively expensive and is instead calculated using the method of *pseudofermions* in which the fermion determinant is written as

$$\det M[U] = \int \mathcal{D}[\phi^\dagger]\mathcal{D}[\phi] e^{-\phi^\dagger M^{-1}[U]\phi}, \tag{2.69}$$

where ϕ is a non-Grassmann field with the indices of a fermion.

2.3.1 The Hybrid Monte Carlo Algorithm

In order to satisfy the extra care that the fermion determinant requires, we use the Hybrid Monte Carlo (HMC) method [42], which uses global updates with a reasonable Metropolis acceptance rate. The method introduces a set of momenta $\pi_\mu(x)$ that are canonically conjugate to the gauge links $U_\mu(x)$, which results in the fictitious Hamiltonian

$$H = \frac{1}{2}\sum_{x,\mu} \pi_\mu(x)^\dagger \pi_\mu(x) + S_G[U]. \tag{2.70}$$

One then allows the gauge links to update according to Hamilton's equations of motion via molecular dynamics. This produces gauge configurations distributed as desired, because the canonically conjugate momenta only produces an irrelevant prefactor in the classical partition function [29]. Of course, in order to guarantee ergodicity, the conjugate momenta need to be changed periodically, and this is achieved by updating the momenta from a Gaussian distribution after each update [43]. One issue, however, is that numerical integrators will introduce errors based on the time step size used when integrating Hamilton's equations. This issue is solved by introducing the acceptance probability

$$P_{acc} = \min(1, e^{-\delta H}) \tag{2.71}$$

after each update, where δH is the change in the Hamiltonian after the new configuration is proposed.

We still need to deal with the estimation of the fermion determinant using Eq. (2.69). The inverse of the Dirac matrix appears in the integrand, and it must be positive definite Hermitian in order to guarantee convergence of the integral over the pseudofermion fields. But, this is not the case, and instead, so long as the fermion determinant is real and positive, then we can rewrite the determinant as $\det M = \sqrt{\det(M^\dagger M)}$. This is useful when considering two degenerate quarks, because each will produce an identical fermion determinant $\det M$, and we have

$$\begin{aligned} \det M^{(u)} \det M^{(d)} &= \big(\det M\big)^2 \\ &= \det\big(M^\dagger M\big) \\ &= \int \mathcal{D}[\phi^\dagger]\mathcal{D}[\phi] e^{-\phi^\dagger [M^\dagger M]^{-1}\phi}. \end{aligned} \tag{2.72}$$

This time we have $[M^\dagger M]^{-1}$ in the exponential, and this is guaranteed to be Hermitian and positive definite. The introduction of these pseudofermion fields extends our fictitious Hamiltonian to be

$$H = \frac{1}{2}\sum_{x,\mu} \pi_\mu(x)^\dagger \pi_\mu(x) + S_G[U] + \phi^\dagger \big(M^\dagger[U] M[U]\big)^{-1} \phi, \tag{2.73}$$

and the pseudofermion fields need to be refreshed just as the conjugate momenta are. This can easily be achieved by producing a vector χ distributed according to a Gaussian with a variance of $\frac{1}{2}$ and then calculating $\phi = M^\dagger \chi$.

2.3.2 The Rational Hybrid Monte Carlo Algorithm

The HMC method assumes an even number of degenerate quarks. When adding the strange quark (or any other quark), we need to adjust our method. We follow the Rational Hybrid Monte Carlo (RHMC) method [44], which extends (HMC) to single quarks. As before, because M is not Hermitian and positive definite in general, we write

$$\begin{aligned} \det M &= \det(M^\dagger M)^{1/2} \\ &= \int \mathcal{D}[\phi^\dagger]\mathcal{D}[\phi] e^{-\phi^\dagger [M^\dagger M]^{-1/2}\phi}. \end{aligned} \tag{2.74}$$

The extension of the HMC method is in dealing with the $(M^\dagger M)^{-1/2}$ term, for which a low-order rational approximation can be made

$$\begin{aligned} (M^\dagger M)^{-1/2} &\approx r^{-1/2}(M^\dagger M) \\ &= \alpha_0 I + \sum_k \alpha_k \left[M^\dagger M + \beta_k\right]^{-1}, \end{aligned} \tag{2.75}$$

where the coefficients α_k and β_k specify the particular rational approximation. To refresh the pseudofermion fields, a vector χ is again distributed according to a Gaussian with a variance of $\frac{1}{2}$, and then $\phi = (M^\dagger M)^{1/4}\chi$ is calculated. Apart from this added feature, the RHMC algorithm proceeds in the same way as the HMC algorithm.

2.4 ENERGIES FROM TEMPORAL CORRELATION MATRICES

In our lattice calculations, we focus on two-point temporal correlation functions (correlators) of the form

$$\mathcal{C}(t) = \langle 0 | \, T\mathcal{O}(t+t_0)\overline{\mathcal{O}}(t_0) \, | 0 \rangle \,, \tag{2.76}$$

where it has been assumed that temporal wrap around effects are negligible (*i.e.* $t << T$, where T is the temporal length of the box), and $\overline{\mathcal{O}}(t)$ and $\mathcal{O}(t)$ are creation and annihilation operators, respectively. The usefulness of these correlation functions is best seen by

performing a spectral decomposition (*i.e.* insert a complete set of energy eigenstates)[6]

$$\begin{aligned}
\mathcal{C}(t) &= \sum_n \langle 0| \mathcal{O}(t+t_0) |n\rangle \langle n| \overline{\mathcal{O}}(t_0) |0\rangle \\
&= \sum_n \langle 0| e^{H(t+t_0)} \mathcal{O}(0) e^{-H(t+t_0)} |n\rangle \langle n| e^{Ht_0} \overline{\mathcal{O}}(0) e^{-Ht_0} |0\rangle \\
&= \sum_n e^{E_0(t+t_0)} \langle 0| \mathcal{O}(0) |n\rangle e^{-E_n(t+t_0)} e^{E_n t_0} \langle n| \overline{\mathcal{O}}(0) |0\rangle e^{-E_0 t_0} \\
&= \sum_n \langle 0| \mathcal{O}(0) |n\rangle \langle n| \overline{\mathcal{O}}(0) |0\rangle e^{-\Delta E_n t},
\end{aligned} \tag{2.77}$$

where $\Delta E_n \equiv E_n - E_0$. We assume that the energies have been appropriately shifted such that $E_0 = 0$. Thus, from this point on, we write E_n in place of ΔE_n. From the spectral representation of $\mathcal{C}(t)$, we can see that this temporal correlator contains all of the information about the energy spectrum we are after and one could, in principal, perform a fit to this function to obtain the spectrum. One could easily extract the lowest energy state created by our operator by performing a fit to a single- or two-exponential function assuming that the minimum time used in the fit is after most of the terms in the spectral decomposition have fallen away to zero. To assist in determining the time in which this has occurred, we introduce the effective energy given by

$$E^{eff}(t) \equiv -\frac{1}{\Delta t} \ln\Big(\frac{C(t+\Delta t)}{C(t)}\Big), \tag{2.78}$$

where Δt is some time step, usually taken to be 1, 2, or 3.[7] If E_0 is the lowest energy that appears in the spectral decomposition of Eq. (2.77), then we have

$$\lim_{t\to\infty} E^{eff}(t) = E_0. \tag{2.79}$$

If we determine the effective energy for a particular correlator, then we will see a plateau in this function that occurs at E_0. Observing the time at which an effective energy plateaus gives us a measure of the excited state contamination in that operator. Since the signal-to-noise ratio generally decreases as the time separation in the correlator is made large, it

[6]Since we are working in finite volume with periodic boundary conditions, the allowed momentum is discrete. This in turn enforces discrete energy eigenstates. Thus, we insert a complete set of states with a summation, not an integral.

[7]There is a slight abuse in notation here by using $\Delta t = 1$, where we really mean $\Delta t = 1a_t$. However, this is very common, and we will continue to use it throughout this work.

is important to build operators that have effective energies which plateau for as small of a time separation as possible. The methods for constructing such operators involve smearing the quark fields. These methods will be further discussed in Sec. 3.2.

The operators used in Eq. (2.76) in general create states that have some overlap with all energy eigenstates in a given channel.[8] Thus, to extract N energies from one of these correlation functions, you would need to perform a fit to a function involving a sum of at least N decaying exponentials, which quickly becomes impractical. Additionally, a fit to a particular correlator may miss an energy level if the overlap of that energy eigenstate with the state created by the operator used in the correlator is very small. For these reasons, an alternative approach is desired. This approach works by building a correlator matrix of temporal correlators of the form

$$\mathcal{C}_{ij}(t) = \langle 0 | \, T\mathcal{O}_i(t+t_0)\overline{\mathcal{O}}_j(t_0) \, | 0 \rangle \, , \tag{2.80}$$

where $\left\{\overline{\mathcal{O}}_i(t)\right\}$ and $\{\mathcal{O}_i(t)\}$ are sets of creation and annihilation operators, respectively, that all transform in the exact same way. First of all, one could very reliably extract the ground state energy in any particular channel by employing a variational approach where the states created by the set of operators considered are used as the variational basis.

Thus, the linear combination of operators that creates a state with the largest overlap on the ground state is determined. Additionally, this linear combination is just the eigenvector associated with the largest eigenvalue of a generalized eigenvalue problem [18, 19, 20], and in principle one could extract up to N energies from an $N \times N$ correlator matrix. The details of this method will be presented in Chap. 6.

2.4.1 Hermiticity

When constructing the correlator matrices, it is important to make sure they are Hermitian. This is not required, but it makes the subsequent analysis of these matrices much simpler. The Hermiticity of the correlator matrix will be determined by the operators used, and in

[8] A channel refers to a set of quantum numbers that a set of states have in common (*e.g.* isospin, strangeness, momentum, *etc.*)

what follows we discuss what must be done to maintain Hermiticity. We start by considering the correlator matrices in Minkowski space

$$\begin{aligned}\mathcal{C}_{ij}(t) &= \langle 0|\, \mathcal{O}_i(t)\mathcal{O}_j^\dagger(0)\, |0\rangle \\ &= \sum_n \langle 0|\, e^{iHt}\mathcal{O}_i(0)e^{-iHt}\, |n\rangle\, \langle n|\, \mathcal{O}_j^\dagger(0)\, |0\rangle \\ &= \sum_n \langle 0|\, \mathcal{O}_i(0)\, |n\rangle\, \langle n|\, \mathcal{O}_j(0)\, |n\rangle^*\, e^{-iE_nt}.\end{aligned} \tag{2.81}$$

So long as the operators $\mathcal{O}_i(t)$ behave in the expected way under time reversal

$$T\mathcal{O}_i(t)T^\dagger = \mathcal{O}_i(-t), \tag{2.82}$$

where T is the time reversal operator, then showing Hermiticity is simple

$$\begin{aligned}\mathcal{C}_{ij}(t) &= \langle 0|\, \mathcal{O}_i(t)\mathcal{O}_j^\dagger(0)\, |0\rangle \\ &= \langle 0|\, T\mathcal{O}_i(t)T^\dagger T\mathcal{O}_j^\dagger(0)T^\dagger\, |0\rangle \\ &= \langle 0|\, \mathcal{O}_i(-t)\mathcal{O}_j^\dagger(0)\, |0\rangle \\ &= \langle 0|\, e^{-iHt}\mathcal{O}_i(0)e^{iHt}\mathcal{O}_j^\dagger(0)\, |0\rangle \\ &= \sum_n \langle 0|\, \mathcal{O}_i(0)\, |n\rangle\, \langle 0|\, \mathcal{O}_j(0)\, |n\rangle^*\, e^{iE_nt} \\ &= \left(\sum_n \langle 0|\, \mathcal{O}_j(0)\, |n\rangle\, \langle n|\, \mathcal{O}_i^\dagger(0)\, |n\rangle\, e^{-iE_nt}\right)^* \\ &= \mathcal{C}_{ji}^*(t),\end{aligned} \tag{2.83}$$

where we have used the anti-unitary property of T (*i.e.* $TT^\dagger = 1$), and we assumed the vacuum was invariant under time reversal (*i.e.* $T\,|0\rangle = |0\rangle$).

From the requirement that the analytic continuation to imaginary time of a correlator matrix in Minkowski space match the correlator matrix in Euclidean space, we see that the operators in Euclidean space should be formed from the analytic continuation to imaginary time of the operators in Minkowski space. That is, $\mathcal{O}_i$ is the analytic continuation of $\mathcal{O}_i^{(M)}$ to imaginary time, where the superscript M stands for Minkowski space; and $\overline{\mathcal{O}}_j$ is the analytic

continuation of $\mathcal{O}_j^{(M)\dagger}$ to imaginary time. As an example, consider a baryon annihilation operator in Minkowski space given by

$$B^{(M)}(t) = \varepsilon_{abc}\psi_{a\alpha}(x)\psi_{b\beta}(x)\psi_{c\gamma}(x), \tag{2.84}$$

where the flavor indices have been suppressed. Then, the corresponding creation operator is given by

$$\begin{aligned} B^{(M)\dagger}(t) &= \varepsilon_{abc}\psi^\dagger_{c\gamma}(x)\psi^\dagger_{b\beta}(x)\psi^\dagger_{a\alpha}(x) \\ &= \varepsilon_{abc}\overline{\psi}_{c\gamma'}(x)\gamma^0_{\gamma'\gamma}\overline{\psi}_{b\beta'}(x)\gamma^0_{\beta'\beta}\overline{\psi}_{a\alpha'}(x)\gamma^0_{\alpha'\alpha}, \end{aligned} \tag{2.85}$$

where we used $\overline{\psi} \equiv \psi^\dagger\gamma_0$ (which is true in Minkowski space). Then, during the Wick rotation to imaginary time, the following replacements are made: $\psi \to \psi$, $\overline{\psi} \to \overline{\psi}$, and $\gamma^0 \to \gamma_4$. Hence, to make sure our operators in Euclidean space lead to Hermitian correlator matrices, our $\overline{\psi}$ fields must have an associated γ_4 with them. For convenience, we will use the χ field in place of $\overline{\psi}$, which is defined as

$$\chi \equiv \overline{\psi}\gamma_4. \tag{2.86}$$

It can be shown that for other operator types (*e.g.* mesons), using the χ field in place of $\overline{\psi}$ will also ensure Hermiticity.

3.0 CONSTRUCTION OF HADRONIC OPERATORS

There are a number of issues to take into consideration when constructing the operators to be used in our temporal correlation matrices. First, it was emphasized in Sec. 2.4 that the operators we use should couple minimally to the higher lying states (*i.e.* the states they create should have small overlaps with the high-lying energy eigenstates). This can be achieved by smearing the quark fields and gauge links. Second, we expect the hadron resonances to be large objects, and thus we must use spatially-extended operators in order to capture the orbital and radial structure of hadrons. Next, we must be sure our operators transform appropriately according to the irreducible representations (irreps) of the symmetry groups that characterize the stationary states we are after. Finally, it is important to use a method for operator construction that can produce large sets of linearly independent operators for each symmetry channel in order to produce temporal correlation matrices large enough to extract a significant portion of the excited-state spectrum.

The methods we use, which address all of these concerns, are described in Refs. [45, 46]. In this chapter, the details of this method are discussed. An outline of the general transformation properties for operators under the irreps of a symmetry group is presented in Sec. 3.1. All of our hadron operators are composed of gauge-covariantly-displaced LapH-smeared quark fields, deemed the basic building blocks. Our process for constructing these building blocks and their properties are described in Sec. 3.2. An initial set of linearly independent elemental operators that transform reducibly under the symmetry group of the lattice is then identified for each hadron type (*i.e.* baryon, meson, *etc.*), flavor structure, and displacement type that we wish to study. Our procedure for obtaining these elemental operators is explained in Sec. 3.3. We then describe the properties of the symmetry group of the lattice in Sec. 3.4. Due to the reduced symmetry of a cube, our operators cannot

be made to transform under the usual angular momentum irreps and are instead built to transform under the irreps of the lattice symmetry group. The method for projecting our set of elemental operators onto the irreps of this group is discussed in Sec. 3.5. Finally, in order to reliably determine the energy of a particular state, all the energy eigenstates below that state must first be extracted. But, a significant number of two-hadron states exist below many of the hadron resonances we are interested in, and therefore the inclusion of two-hadron operators is essential for our calculations. The construction of these two-hadron operators is described in Sec. 3.6.

3.1 SYMMETRY CHANNEL TRANSFORMATIONS

The particular irreps that a stationary state belongs to determines the quantum numbers or properties of that state. Hadronic states can be identified by: their momentum $\boldsymbol{p}$, their total spin J, their spin projected onto some axis, their parity P, and their flavor structure (*e.g.* isospin I, isospin projection I_3, strangeness S, *etc.*).[1] Additionally, states that are neutral under all charges can be identified by their C-parity. But, this means C-parity is only a good quantum number for a limited number of particles.[2] For our purposes, we use a generalization of C-parity, known as G-parity. The G-parity operator is defined by

$$U_G = \mathcal{C} e^{-i\pi\tau_2}, \tag{3.1}$$

where $\mathcal{C}$ is the charge conjugation operator, and τ_2 is the operator corresponding to the second component of isospin. G-parity is only a good quantum number for bosonic states within an isospin multiplet that has zero average electric charge. Thus, when applicable, we further identify hadronic states with G-parity. Furthermore, the use of G-parity makes

[1] In this work, we only include up, down, and strange quarks.

[2] Also, since we impose exact isospin symmetry in our simulations, we do not make a distinction between particles within the same isospin multiplet. And, in the case of the pions, which form an isotriplet, C-parity is a good quantum number for the neutral pion but not the other pions. Therefore, the use of C-parity is awkward and not useful in situations like these.

C-parity even less useful, because whenever C-parity is a good quantum number, it is simply related to G-parity by

$$\eta_C = \eta_G(-1)^I, \tag{3.2}$$

where η_C is the C-parity of the state, η_G is the G-parity of the state, and I is the isospin of the state.

In order to create states with particular quantum numbers, we demand our hadronic operators transform under the irreps corresponding to those quantum numbers. For each symmetry group, we denote our operators by $\mathcal{O}_i^{\Lambda\lambda F}(t)$ and $\overline{\mathcal{O}}_i^{\Lambda\lambda F}(t)$ for the annihilation and creation operators, respectively, where Λ is the particular irrep of the symmetry group in question, λ is the row of that irrep, F denotes the quantum numbers for all other symmetry groups, and i labels the set of operators in the $\Lambda\lambda F$ symmetry channel. For a given symmetry group element R, our operators transform as

$$U_R\ \mathcal{O}_i^{\Lambda\lambda F}(t)U_R^\dagger = \sum_\mu \mathcal{O}_i^{\Lambda\mu F}(t)\Gamma^{(\Lambda)}_{\mu\lambda}(R)^*, \tag{3.3a}$$

$$U_R\ \overline{\mathcal{O}}_i^{\Lambda\lambda F}(t)U_R^\dagger = \sum_\mu \overline{\mathcal{O}}_i^{\Lambda\mu F}(t)\Gamma^{(\Lambda)}_{\mu\lambda}(R), \tag{3.3b}$$

where U_R is the quantum operator for the symmetry transformation R, and $\Gamma^{(\Lambda)}_{\mu\lambda}(R)$ is the Λ matrix representation for R. To see that these equations are correct, we use the required transformation properties for the states in the particular irrep:

$$\begin{aligned} U_R\,|\Lambda\lambda F\rangle &= \sum_\mu |\Lambda\mu F\rangle\,\langle\Lambda\mu F|\,U_R\,|\Lambda\lambda F\rangle \\ &= \sum_\mu |\Lambda\mu F\rangle\,\Gamma^{(\Lambda)}_{\mu\lambda}(R), \end{aligned} \tag{3.4}$$

along with the fact that $\overline{\mathcal{O}}_i^{\Lambda\lambda F}$ creates states that transform in the same way as $|\Lambda\lambda F\rangle$ when acting on the vacuum. That is

$$\begin{aligned} U_R\overline{\mathcal{O}}_i^{\Lambda\lambda F}(t)\,|0\rangle &= U_R\overline{\mathcal{O}}_i^{\Lambda\lambda F}U_R^\dagger U_R\,|0\rangle \\ &= U_R\overline{\mathcal{O}}_i^{\Lambda\lambda F}U_R^\dagger\,|0\rangle \\ &= \sum_\mu \overline{\mathcal{O}}_i^{\Lambda\lambda F}\,|0\rangle\,\Gamma^{(\Lambda)}_{\mu\lambda}(R), \end{aligned} \tag{3.5}$$

assuming the vacuum is invariant under the action of the symmetry transformation. This result can be used to deduce Eq. (3.3b). Similarly, using the transformation properties for $\langle \Lambda\lambda F|$:

$$\begin{aligned}
\langle \Lambda\lambda F| U_R^\dagger &= \sum_\mu \langle \Lambda\lambda F| U_R^\dagger |\Lambda\mu F\rangle \langle \Lambda\mu F| \\
&= \sum_\mu \langle \Lambda\mu F| U_R |\Lambda\lambda F\rangle^* \langle \Lambda\mu F| \\
&= \sum_\mu \langle \Lambda\mu F| \Gamma^{(\Lambda)}_{\mu\lambda}(R)^*,
\end{aligned} \tag{3.6}$$

along with the fact that $\langle 0| \mathcal{O}_i^{\Lambda\lambda F}(t)$ has the same transformation properties as $\langle \Lambda\lambda F|$:

$$\begin{aligned}
\langle 0| \mathcal{O}_i^{\Lambda\lambda F}(t) U_R^\dagger &= \langle 0| U_R^\dagger U_R \mathcal{O}_i^{\Lambda\lambda F} U_R^\dagger \\
&= \langle 0| U_R \mathcal{O}_i^{\Lambda\lambda F} U_R^\dagger \\
&= \sum_\mu \langle 0| \mathcal{O}_i^{\Lambda\mu F}(t) \Gamma^{(\Lambda)}_{\mu\lambda}(R)^*,
\end{aligned} \tag{3.7}$$

which can be used to deduce Eq. (3.3a).

The importance of using operators that transform under the irreps of the symmetry groups of our system can also be seen from correlation functions using these operators:

$$\begin{aligned}
\langle 0| T\mathcal{O}_i^{\Lambda\lambda F}(t) \overline{\mathcal{O}}_j^{\Lambda'\lambda' F}(0) |0\rangle &= \frac{1}{g_\mathcal{G}} \sum_{R\in\mathcal{G}} \langle 0| T\mathcal{O}_i^{\Lambda\lambda F}(t) \overline{\mathcal{O}}_j^{\Lambda'\lambda' F}(0) |0\rangle \\
&= \frac{1}{g_\mathcal{G}} \sum_{R\in\mathcal{G}} \langle 0| T U_R \mathcal{O}_i^{\Lambda\lambda F}(t) U_R^\dagger U_R \overline{\mathcal{O}}_j^{\Lambda'\lambda' F}(0) U_R^\dagger |0\rangle \\
&= \frac{1}{g_\mathcal{G}} \sum_{R\in\mathcal{G}} \sum_{\mu\mu'} \Gamma^{(\Lambda)}_{\mu\lambda}(R)^* \Gamma^{(\Lambda')}_{\mu'\lambda'}(R) \langle 0| T\mathcal{O}_i^{\Lambda\mu F}(t) \overline{\mathcal{O}}_j^{\Lambda'\mu' F}(0) |0\rangle \\
&= \delta_{\Lambda\Lambda'}\delta_{\lambda\lambda'} \frac{1}{d_\Lambda} \langle 0| T\mathcal{O}_i^{\Lambda\lambda F}(t) \overline{\mathcal{O}}_j^{\Lambda'\lambda' F}(0) |0\rangle ,
\end{aligned} \tag{3.8}$$

where $\mathcal{G}$ is the symmetry group, $g_\mathcal{G}$ is the number of group elements in $\mathcal{G}$, the invariance of the vacuum was invoked, and the so-called great orthogonality theorem was used:

$$\frac{1}{g_\mathcal{G}} \sum_{R\in\mathcal{G}} \Gamma^{(\Lambda)}_{\lambda\mu}(R)^* \Gamma^{(\Lambda')}_{\lambda'\mu'}(R) = \frac{1}{d_\Lambda} \delta_{\Lambda\Lambda'}\delta_{\lambda\lambda'}\delta_{\mu\mu'}. \tag{3.9}$$

Thus, we see from Eq. (3.8) that temporal correlators between operators in different irreps and/or irrep rows vanish, which provides a natural way to divide our calculations into different symmetry sectors/channels. This result also allows us to label our correlators with the irrep and irrep row:

$$C_{ij}^{\Lambda\lambda F} \equiv \langle 0 | \, T\mathcal{O}_i^{\Lambda\lambda F}(t)\overline{\mathcal{O}}_j^{\Lambda\lambda F}(0) \, | 0 \rangle \, . \tag{3.10}$$

Now we can arrive at another useful result for our correlators by using the orthogonality of the correlators found in Eq. (3.8) and once again invoking invariance of the vacuum:

$$\begin{aligned} C_{ij}^{\Lambda\lambda F} &= \langle 0 | \, T\mathcal{O}_i^{\Lambda\lambda F}(t)\overline{\mathcal{O}}_j^{\Lambda\lambda F}(0) \, | 0 \rangle \\ &= \langle 0 | \, TU_R\mathcal{O}_i^{\Lambda\lambda F}(t)U_R^\dagger U_R\overline{\mathcal{O}}_j^{\Lambda\lambda F}(0)U_R^\dagger \, | 0 \rangle \\ &= \sum_{\mu\mu'} \Gamma_{\mu\lambda}^{(\Lambda)}(R)^* \Gamma_{\mu'\lambda}^{(\Lambda)}(R) \, \langle 0 | \, T\mathcal{O}_i^{\Lambda\mu F}(t)\overline{\mathcal{O}}_j^{\Lambda\mu' F}(0) \, | 0 \rangle \\ &= \sum_{\mu\mu'} \Gamma_{\mu\lambda}^{(\Lambda)}(R)^* \Gamma_{\mu'\lambda}^{(\Lambda)}(R) \delta_{\mu\mu'} C_{ij}^{\Lambda\mu F}(t) \\ &= \sum_{\mu} |\Gamma_{\mu\lambda}^{(\Lambda)}(R)|^2 C_{ij}^{\Lambda\mu F}(t). \end{aligned} \tag{3.11}$$

This equation gives us a relationship between the correlators with different irrep rows for each element in the symmetry group. In many cases, this equation can be used to show that the correlators are independent of the irrep row.

3.2 THE BASIC BUILDING BLOCKS

The construction of our operators starts with identifying appropriate building blocks to be used in all hadronic operators. Hadrons are composed of quarks, and therefore quark fields are the main components of these operators. It is at this level where smearing of the gauge links and quark fields is performed. Keep in mind that our choices are generally based on a few criteria: reducing excited state contamination, efficiency, preservation of symmetries, *etc.* Additionally, since we are interested in hadrons which are extended composite objects, we also consider covariant displacements at this point.

3.2.1 Gauge-Link Smearing

Gauge-link smearing is important for a number of reasons. For example, it reduces high energy contamination (to a significant degree for gluonic states), and dramatically decreases statistical errors in the calculation of correlators involving extended hadron operators (see Figure 3.1). Smearing a gauge link $U_\mu(x)$ usually involves a weighted sum of its neighboring gauge links or staples:

$$C_\mu(x) = \sum_{\nu \neq \mu} \rho_{\mu\nu} \Big(U_\nu(x)\, U_\mu(x+\hat{\nu})\, U_\nu^\dagger(x+\hat{\mu}) + U_\nu^\dagger(x-\hat{\nu})\, U_\mu(x-\hat{\nu})\, U_\nu(x-\hat{\nu}+\hat{\mu}) \Big) \quad (3.12)$$

where x is the lattice site, and $\hat{\mu}$ and $\hat{\nu}$ are directional vectors having the length of the lattice spacing. One popular method involves updating every spatial link variable in the following way[3] [47]

$$U_\mu(x) \to U_\mu(x) + C_\mu(x), \qquad \rho_{jk} = \rho,\ \rho_{4\mu} = \rho_{\mu 4} = 0,\ (\rho \in \mathbb{R}). \quad (3.13)$$

However, this smearing procedure requires we project the spatial link back into $SU(3)$, and this results in a loss of differentiability which can make the application of Monte Carlo techniques to these links difficult or even impossible.

Instead, we follow the procedure in Ref. [48], which presents an analytic method for smearing gauge-link variables. The advantage here is we do not need to project back to $SU(3)$ after the smearing process, and thus we retain differentiability. In addition, this algorithm can be applied to any Lie group, and thus we generalize what follows to $SU(N)$. We use Eq. (3.12) to define an $SU(N)$ matrix to apply to the link variable. We start by defining the following

$$Q_\mu(x) = \frac{i}{2}\Big(\Omega_\mu^\dagger(x) - \Omega_\mu(x)\Big) - \frac{i}{2N}\,\mathrm{Tr}\,\Big(\Omega_\mu^\dagger(x) - \Omega_\mu(x)\Big) \quad (3.14a)$$

$$\Omega_\mu(x) = C_\mu(x)\, U_\mu^\dagger(x) \qquad (\text{no summation over } \mu). \quad (3.14b)$$

[3] We use the convention that Latin indices refer to just the spatial directions (*i.e.* $j = 1, 2, 3$), and Greek indices refer to both the spatial and temporal directions (*i.e.* $\mu = 0, 1, 2, 3$).

The key thing to realize is since $Q_\mu(x)$ is a Hermitian, traceless $N \times N$ matrix then it must belong in $\mathfrak{su}(N)$. Therefore, $e^{iQ_\mu(x)}$ must be an $SU(N)$ matrix. Then, we define an iterative mapping as follows

$$U_\mu^{(n+1)}(x) = e^{iQ_\mu^{(n)}(x)} U_\mu^{(n)}(x). \tag{3.15}$$

Closure guarantees that $U_\mu^{(n+1)}$ remains in $SU(N)$. The smearing process is performed n_ρ times, and we designate the resulting link variables as $\widetilde{U}_\mu(x)$, *i.e.*

$$U \to U^{(1)} \to U^{(2)} \to \cdots \to U^{(n_\rho)} \equiv \widetilde{U}. \tag{3.16}$$

We choose the same staple weights used in Eq. (3.13), which smears the spatial links while leaving the temporal links untouched. By restricting ourselves to smearing only the spatial links, we ensure the transfer matrix remains positive definite [38].

3.2.2 LapH Smearing of the Quark Fields

Now, we move on to the smearing of the quark fields. The goal of this process is to reduce the excited state contamination in our correlation functions. We want our smeared quark fields to behave identically under symmetry transformations as our original quark fields. With this in mind, the natural choice is to make use of the covariant Laplacian $\widetilde{\Delta}$, which is defined in the following way

$$\widetilde{\Delta}_{xy}^{ab} = \sum_{j=1}^{3} \Big[\widetilde{U}_j^{ab}(x)\delta_{x+\hat{j},y} + \widetilde{U}_{-j}^{ab}(x)\delta_{x-\hat{j},y} - 2\delta_{x,y}\delta^{ab} \Big]. \tag{3.17}$$

Notice that the covariant Laplacian is defined to use the smeared gauge links, and that the operator has no dependence on Dirac spin indices. It is a simple matter to show that the

covariant Laplacian is indeed gauge covariant: using the gauge transformations for the gauge links shown in Eqs. (2.31) and (2.33) we find

$$\begin{aligned}
\widetilde{\Delta}^{ab}_{xy}(U) &\to \sum_{j=1}^{3}\Big[\big(\Omega(x)\widetilde{U}_j(x)\Omega^\dagger(x+\hat{j})\big)^{ab}\delta_{x+\hat{j},y} + \big(\Omega(x)\widetilde{U}_{-j}(x)\Omega^\dagger(x-\hat{j})\big)^{ab}\delta_{x-\hat{j},y} - 2\delta_{x,y}\big(\Omega(x)\Omega^\dagger(x)\big)^{ab}\Big] \\
&= \sum_{j=1}^{3}\Big[\big(\Omega(x)\widetilde{U}_j(x)\Omega^\dagger(y)\big)^{ab}\delta_{x+\hat{j},y} + \big(\Omega(x)\widetilde{U}_{-j}(x)\Omega^\dagger(y)\big)^{ab}\delta_{x-\hat{j},y} - 2\delta_{x,y}\big(\Omega(x)\Omega^\dagger(y)\big)^{ab}\Big] \\
&= \Omega^{ac}(x)\sum_{j=1}^{3}\Big[\widetilde{U}^{cd}_{j}(x)\delta_{x+\hat{j},y} + \widetilde{U}^{cd}_{-j}(x)\delta_{x-\hat{j},y} - 2\delta_{x,y}\delta^{cd}\Big]\Omega^{\dagger db}(y) \\
&= \Omega^{ac}(x)\widetilde{\Delta}^{cd}_{xy}(U)\Omega^{\dagger db}(y).
\end{aligned} \tag{3.18}$$

We must now determine how we should use this operator to appropriately smear our quark fields. A popular method is to smear the fields in the following way [49]

$$\widetilde{\psi}(x) = \left(\delta_{x,y} + \frac{\sigma_s^2}{4n_\sigma}\widetilde{\Delta}_{xy}\right)^{n_\sigma}\psi(y), \tag{3.19a}$$

$$\widetilde{\overline{\psi}}(x) = \overline{\psi}(y)\left(\delta_{y,x} + \frac{\sigma_s^2}{4n_\sigma}\widetilde{\Delta}_{yx}\right)^{n_\sigma}, \tag{3.19b}$$

where σ_s and n_σ are parameters used to finely tune the smearing of our quark fields. By making use of the covariant Laplacian, it can easily be seen that the quark fields retain their original gauge transformation properties, which is a necessary condition for our smearing scheme. The effect of this smearing procedure on the effective energy is shown in Figure 3.1, where it is clear that quark smearing dramatically reduces the excited state contamination in our operators. It is possible to express the smearing operators defined in Eq. (3.19) by a sum over the eigenvalues and eigenvectors of the covariant Laplacian. This alternative way of viewing the quark smearing may lead to other smearing schemes, or at least to a better understanding of the smearing process. Consider the smearing operator used in Eq. (3.19)

$$K_{ab}(x,y) = \left(\delta_{x,y} + \frac{\sigma_s^2}{4n_\sigma}\widetilde{\Delta}^{ab}_{xy}\right)^{n_\sigma}. \tag{3.20}$$

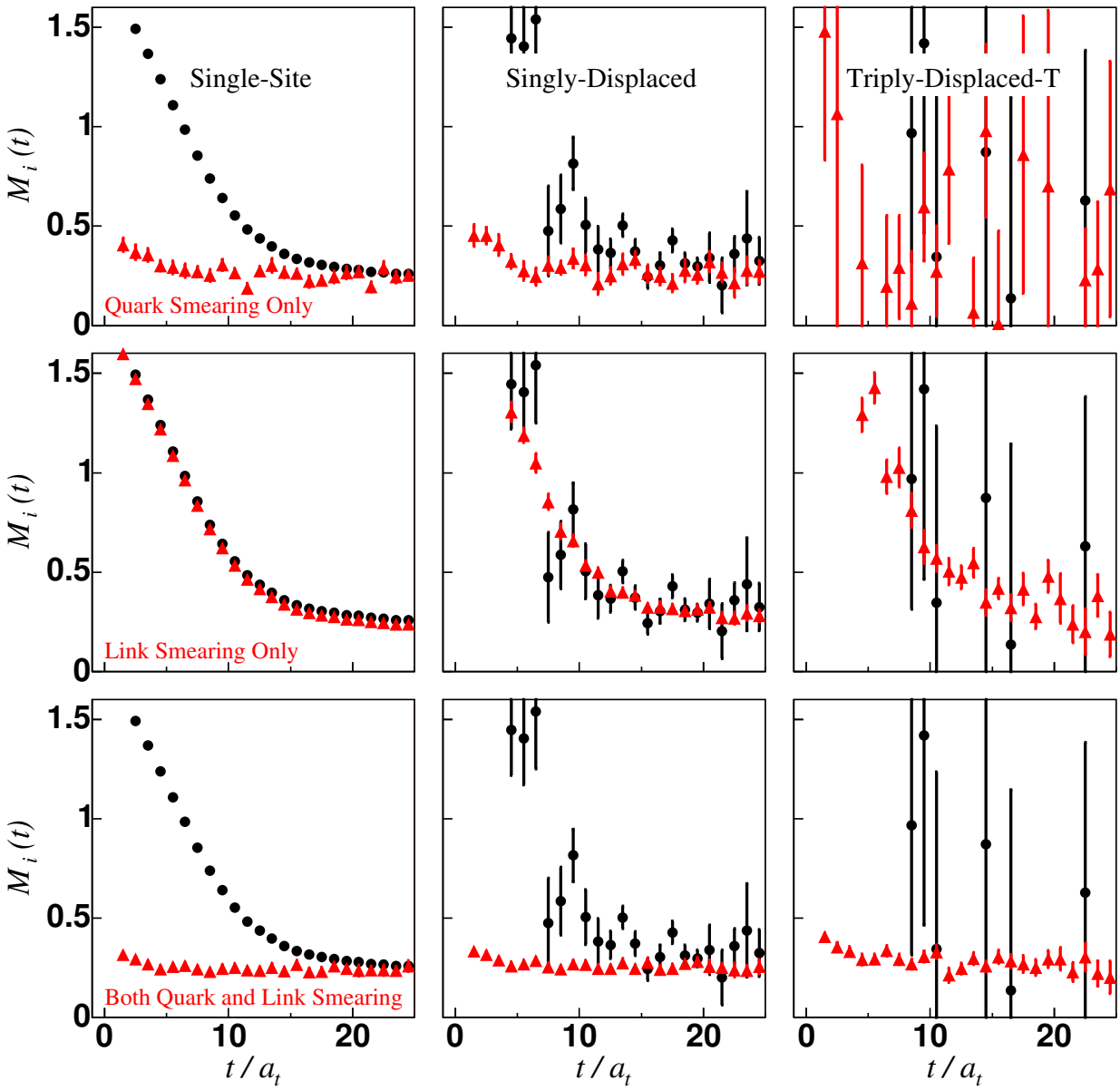

Figure 3.1: The effective energy $M(t)$ (defined in Eq. (2.78)) for unsmeared (black circles) and smeared (red triangles) operators. The three columns correspond to operators displaced in different ways. The quark field smearing is done using Eq. (3.19), and the gauge-link smearing is done using Eq. (3.16). The top row only smears the quark fields. The middle row only smears the gauge links. The bottom row smears the quark fields, and the gauge links. Figure taken from Ref. [43].

Now, we would like to write $K_{ab}(x,y)$ in terms of the eigenvectors and eigenvalues of the covariant Laplacian. It is straightforward to show the covariant Laplacian is Hermitian

$$\begin{aligned}
\widetilde{\Delta}^{\dagger}_{ab}(x,y) &= \widetilde{\Delta}^{*}_{ba}(y,x) \\
&= \sum_{j=1}^{3}\left[\widetilde{U}^{ba}_{j}(y)^{*}\delta_{y+\hat{j},x} + \widetilde{U}^{ba}_{-j}(y)^{*}\delta_{y-\hat{j},x} - 2\delta_{y,x}\delta^{ba}\right] \\
&= \sum_{j=1}^{3}\left[\widetilde{U}^{ab}_{j}(y)^{\dagger}\delta_{x-\hat{j},y} + \widetilde{U}^{ab}_{-j}(y)^{\dagger}\delta_{x+\hat{j},y} - 2\delta_{x,y}\delta^{ab}\right] \\
&= \sum_{j=1}^{3}\left[\widetilde{U}^{ab}_{-j}(y+\hat{j})\delta_{x-\hat{j},y} + \widetilde{U}^{ab}_{j}(y-\hat{j})\delta_{x+\hat{j},y} - 2\delta_{x,y}\delta^{ab}\right] \\
&= \sum_{j=1}^{3}\left[\widetilde{U}^{ab}_{j}(x)\delta_{x+\hat{j},y} + \widetilde{U}^{ab}_{-j}(x)\delta_{x-\hat{j},y} - 2\delta_{x,y}\delta^{ab}\right] \\
&= \widetilde{\Delta}_{ab}(x,y).
\end{aligned} \tag{3.21}$$

From this result, we know all the eigenvalues are real and the eigenvectors can be chosen such that they are orthonormal. It can also be shown that the eigenvalues of $-\widetilde{\Delta}$ are all non-negative. Therefore, we denote the eigenvalues of $-\widetilde{\Delta}$ by $\lambda^{(k)}$ with the understanding that $\lambda^{(k+1)} \geq \lambda^{(k)} \geq 0$, and the eigenvectors of $-\widetilde{\Delta}$ by $\upsilon^{(k)}$. Then, we have

$$\sum_{j}\widetilde{\Delta}_{ij}\upsilon^{(k)}_{j} = -\lambda^{(k)}\upsilon^{(k)}_{i}, \tag{3.22}$$

where the color and spatial indices of $\widetilde{\Delta}$ have been condensed into a single Latin index. Finally, we can write the smearing operator as an eigendecomposition

$$K_{ab}(x,y) = \delta_{x_4,y_4}\sum_{k}\left(1 - \frac{\sigma_s^2}{4n_\sigma}\lambda^{(k)}\right)^{n_\sigma}\upsilon^{(k)}_{a}(x)\upsilon^{(k)}_{b}(y)^{*}. \tag{3.23}$$

From this expression, it is easy to see that the larger eigenmodes of $-\widetilde{\Delta}$ are suppressed since

$$\lim_{n_\sigma\to\infty} K_{ab}(x,y) = \delta_{x_4,y_4}\sum_{k} e^{-\frac{1}{4}\sigma_s^2\lambda^{(k)}}\upsilon^{(k)}_{a}(x)\upsilon^{(k)}_{b}(y)^{*}. \tag{3.24}$$

It is now clear why smearing of the quark fields reduces the excited state contamination. Also, this hints at a simpler strategy: ignore the exponentially suppressed eigenmodes in the sum over k. This is precisely the strategy put forth by Peardon and his collaborators, and

is referred to as Laplacian Heaviside (LapH) smearing [50, 17]. An important advantage of this smearing method for estimating temporal correlators will be discussed in Chap. 4.

In this scheme, the smearing matrix is defined as

$$\begin{aligned}\mathcal{S}_{ab}(x,y) &= \Theta\Big(\sigma_s^2 + \widetilde{\Delta}\Big) \\ &= V_{\widetilde{\Delta}}\Theta\Big(\sigma_s^2 + \Lambda_{\widetilde{\Delta}}\Big)V_{\widetilde{\Delta}}^\dagger,\end{aligned} \tag{3.25}$$

where $\Lambda_{\widetilde{\Delta}}$ is a diagonal matrix diagonalized by $V_{\widetilde{\Delta}}$ (*i.e.* $\widetilde{\Delta} = V_{\widetilde{\Delta}}\Lambda_{\widetilde{\Delta}}V_{\widetilde{\Delta}}^\dagger$). Then, it can be seen that $S_{ab}(x,y)$ only includes the eigenmodes that satisfy $\lambda^{(k)} < \sigma_s^2$. The simplest representation of this operator is by a sum over the eigenmodes of $-\widetilde{\Delta}$. Proceeding as before, the smearing operator can be written as

$$\mathcal{S}_{ab}(x,y) \approx \delta_{x_4,y_4}\sum_{k=1}^{N_\upsilon} \upsilon_a^{(k)}(x)\upsilon_b^{(k)}(y)^*, \tag{3.26}$$

where N_υ depends on the value chosen for σ_s. This representation for $\mathcal{S}$ is only approximately correct since we do not expect N_υ to remain constant for every gauge configuration. Additionally, since $\widetilde{\Delta}$ is block-diagonal in time, then each eigenvector $\upsilon^{(k)}$ has non-zero elements for only one time slice. This means we should also expect some variation in N_υ across different times. However, explicit calculations show that these variations in N_υ are small and that holding N_υ constant has a negligible effect on the final results [50]. The numerical value of σ_s^2 was chosen by calculating the effective energy of three nucleon operators for different values of σ_s^2 until the effective energy on a very early time slice was minimized for the three operators (see Figure 2 of Ref. [17]). The value chosen is $\sigma_s^2 \approx 0.33$.

If we take V_s to be the matrix whose columns are composed of the eigenvectors of the N_υ lowest eigenmodes of $-\widetilde{\Delta}$ for each time slice, then we find[4]

$$\mathcal{S} = (V_s V_s^\dagger) \otimes I_4^d, \tag{3.27}$$

where I_4^d is the identity matrix in the Dirac spin subspace; so we can see that the smearing matrix does not act on the spin indices. Notice that V_s is a $N_s^3 N_t N_c \times N_\upsilon N_t$ matrix, where N_s is the number of spatial sites in each direction, N_t is the number of temporal sites, and

[4]Notice we have dropped the approximation sign for $\mathcal{S}$. This is because we actually use the form in Eq. (3.27) for our simulations, and we assume any errors in this approximation are negligible.

$N_c = 3$ is the number of colors. We take the $N_v N_t N_d$ vectors that comprise $V_s \otimes I_4^d$ to form the so-called LapH subspace, where $N_d = 4$ is the number of Dirac spin indices. In Chap. 4, it will be shown that a drastic reduction in computational effort is achieved by working within the much smaller LapH subspace.

3.2.3 Gauge-Covariant Displacements

An important step in the construction of our operators is to include spatially extended hadron operators. Many hadrons have complicated orbital and radial structure, and we design our operators to capture this extended spatial structure. We consider displacements in multiple directions in order to capture the orbital structure and displacements by different distances in order to capture the radial structure [45]. In order to retain gauge invariance, the displacements are constructed using gauge-link variables to connect the starting point of the quark and the point the quark is displaced to. Thus, the p-link gauge-covariant displacement operator in the jth direction is given by [46, 43, 45]

$$D^{(j)}(x, x') = \widetilde{U}_j(x)\,\widetilde{U}_j(x+\hat{j})\ldots\widetilde{U}_j(x+(p-1)\hat{j})\delta_{x',x+p\hat{j}}, \tag{3.28}$$

where $j = \pm1, \pm2, \pm3$. If we allow $j = 0$, then

$$D^{(0)}(x, x') = \delta_{xx'}, \tag{3.29}$$

which corresponds to no displacement.

Therefore, our basic building blocks used for the construction of all hadron operators are gauge-covariantly-displaced LapH-smeared quark fields defined by

$$q^A_{a\alpha j} \equiv D^{(j)}\widetilde{\psi}^{(A)}_{a\alpha}, \qquad \overline{q}^A_{a\alpha j} \equiv \overline{\widetilde{\psi}}^{(A)}_{a\alpha}\gamma_4 D^{(j)\dagger}, \tag{3.30}$$

where A is the quark flavor, a is the color index, and α is the Dirac spin index.[5] Occasionally we suppress the spatial displacement indices for the basic building blocks, and we sometimes write $u = q^u$, $d = q^d$, $s = q^s$ (and similarly for the barred quarks).

[5]Recall that the γ_4 is a part of the definition of $\overline{q}^A_{a\alpha j}$ in order to ensure the correlator matrices are Hermitian.

3.2.4 Charge Conjugation and G-Parity

In order to determine how our operators transform under G-parity, we first determine how G-parity acts on the basic building blocks shown in Eq. (3.30). Since G-parity involves the charge conjugation operators $\mathcal{C}$, we start by examining the transformation properties of the basic building blocks under charge conjugation. The charge conjugation operator changes quarks into antiquarks and vice versa. One can derive the exact transformation properties under charge conjugation by taking the complex conjugate of the Dirac equation, which must be satisfied by both the quark fields and the charge conjugated quark fields, but with opposite charges. This leads to

$$\mathcal{C}\mathcal{A}_\mu(x)\mathcal{C}^\dagger = -\mathcal{A}_\mu(x)^*, \tag{3.31}$$

which implies

$$\mathcal{C}\,U_\mu(x)\mathcal{C}^\dagger = U_\mu(x)^*, \tag{3.32}$$

by making using the definition of the gauge links in Eq. (2.37). The quark fields must transform as

$$\mathcal{C}\psi_\alpha(x)\mathcal{C}^\dagger = \overline{\psi}_\beta(x)C^\dagger_{\beta\alpha}, \qquad \mathcal{C}\overline{\psi}_\alpha(x)\mathcal{C}^\dagger = -C^\dagger_{\alpha\beta}\psi_\beta(x), \tag{3.33}$$

where the charge conjugation matrix C satisfies

$$C^\dagger = C^{-1}, \qquad C^T = -C, \qquad C\gamma_\mu C^\dagger = -\gamma_\mu^T, \tag{3.34}$$

and is commonly chosen to be

$$C \equiv \gamma_4\gamma_2, \tag{3.35}$$

in the Dirac-Pauli representation. We then have the following transformation properties under charge conjugation for our basic building blocks:

$$\mathcal{C}q^A_{a\alpha j}(x)\mathcal{C}^\dagger = \overline{q}^A_{a\beta j}(x)(\gamma_4 C^\dagger)_{\beta\alpha}, \tag{3.36a}$$

$$\mathcal{C}\overline{q}^A_{a\alpha j}(x)\mathcal{C}^\dagger = -(\gamma_4^T C)_{\alpha\beta}q^A_{a\beta j}(x), \tag{3.36b}$$

where $\gamma_4 C^\dagger = \gamma_4\gamma_2\gamma_4 = -\gamma_2$ and $\gamma_4^T C = \gamma_4\gamma_4\gamma_2 = \gamma_2$ in our representation of the gamma matrices.

Next, we need to apply the isospin rotations that are a part of the G-parity operator. Since isospin only acts on the flavor indices, we can ignore all other indices for these operations. To determine how these isospin operators act on the flavor indices, we need to use the Wigner D-matrix in the $I = 1/2$ representation along with transformation properties for operators transforming irreducibly under isospin shown in Eqs. (3.39) and (3.40). This results in

$$\begin{aligned} e^{-i\pi\tau_2}\overline{u}e^{i\pi\tau_2} &= \overline{d}, & e^{-i\pi\tau_2}ue^{i\pi\tau_2} &= d, \\ e^{-i\pi\tau_2}\overline{d}e^{i\pi\tau_2} &= -\overline{u}, & e^{-i\pi\tau_2}de^{i\pi\tau_2} &= -u, \\ e^{-i\pi\tau_2}\overline{s}e^{i\pi\tau_2} &= \overline{s}, & e^{-i\pi\tau_2}se^{i\pi\tau_2} &= s, \end{aligned} \tag{3.37}$$

which finally gives the transformation of our building blocks under G-parity:

$$\begin{aligned} U_G\overline{u}_{a\alpha j}U_G^\dagger &= -\Gamma^G_{\alpha\beta}d_{a\beta j}, & U_G u_{a\alpha j}U_G^\dagger &= -\overline{d}_{a\beta j}\Gamma^G_{\beta\alpha}, \\ U_G\overline{d}_{a\alpha j}U_G^\dagger &= \Gamma^G_{\alpha\beta}u_{a\beta j}, & U_G d_{a\alpha j}U_G^\dagger &= \overline{u}_{a\beta j}\Gamma^G_{\beta\alpha}, \\ U_G\overline{s}_{a\alpha j}U_G^\dagger &= -\Gamma^G_{\alpha\beta}s_{a\beta j}, & U_G s_{a\alpha j}U_G^\dagger &= -\overline{s}_{a\beta j}\Gamma^G_{\beta\alpha}. \end{aligned} \tag{3.38}$$

3.3 ELEMENTAL OPERATORS

Once the basic building blocks have been designed, the next step is to construct sets of gauge-invariant elemental operators from these building blocks. Each set is identified by the hadron type (*e.g.* baryon, meson, *etc.*), flavor structure, and displacement type. In general, the operators in these sets are not linearly independent, and we remove these linear dependencies within the set. Each set then defines a basis of operators that transform reducibly under the symmetry group of the lattice. Then, in Sec. 3.5, we show how to find the appropriate linear combinations of these basis operators that transform irreducibly under the lattice symmetry group.

3.3.1 Flavor Structure

In our calculations, we only consider the u, d, and s quarks, and thus we could base the flavor structure for our elemental operators on the $SU(3)$ flavor multiplets. However, this

is not necessary since $SU(3)$ flavor symmetry is broken, which allows for the possibility of significant mixing between the different $SU(3)$ flavor irreps (so long as these mixings conserve flavor). This would be somewhat inconvenient, because we would need to include operators that transform in all the irreps that mix in our correlation matrices in order to make sure we find all the stationary states for a given symmetry channel. In our simulations, we work in the approximation that $m_u = m_d$ which gives us exact $SU(2)$ flavor symmetry (also known as isotopic spin or isospin symmetry). Therefore, if we base the flavor structure of our elemental operators on the $SU(2)$ flavor irreps, then no mixing occurs between between the different $SU(2)$ flavor multiplets, which simplifies matters from a computational standpoint. Therefore, we demand our elemental annihilation operators to have flavor structure such that under an isospin rotation R_τ they transform as

$$U_{R_\tau} \mathcal{O}^{II_3S}(t) U^\dagger_{R_\tau} = \mathcal{O}^{II_3'S}(t) D^{(I)}_{I_3'I_3}(R_\tau)^*, \tag{3.39}$$

where I is the isospin, I_3 is the third component of isospin, S is the strangeness, and $D^{(I)}(R_\tau)$ are the Wigner D-matrices. The corresponding elemental creation operators then transform as

$$U_{R_\tau} \overline{\mathcal{O}}^{II_3S}(t) U^\dagger_{R_\tau} = \overline{\mathcal{O}}^{II_3'S}(t) D^{(I)}_{I_3'I_3}(R_\tau). \tag{3.40}$$

Additionally, since we have exact $SU(2)$ flavor symmetry, this means our spectrum is independent of I_3, and the operators we construct are chosen to have maximal I_3 (*i.e.* $I_3 = I$). However, when constructing multi-hadron operators, it is necessary to include all possible values of I_3 for the individual operators in order to exhaust the possible set of multi-hadron operators with a given isospin. But, we still only construct multi-hadron operators with total I_3 that is maximal.

Before we discuss our specific procedure for identifying elemental operators obeying the above transformations, it is useful to list further properties of these elemental operators using the generators τ_1, τ_2, and τ_3 of isospin symmetry, which satisfy $[\tau_i, \tau_j] = i\varepsilon_{ijk}\tau_k$. Any annihilation operator $\mathcal{O}^{(I)}_{I_3}$ transforms appropriately under the isospin irrep I if it obeys the

following:

$$[\tau_3, \mathcal{O}^{(I)}_{I_3}] = -I_3 \mathcal{O}^{(I)}_{I_3}, \tag{3.41a}$$

$$[\tau_+, \mathcal{O}^{(I)}_{I_3}] = -\sqrt{(I - I_3)(I + I_3 + 1)}\mathcal{O}^{(I)}_{I_3+1}, \tag{3.41b}$$

$$[\tau_-, \mathcal{O}^{(I)}_{I_3}] = -\sqrt{(I + I_3)(I - I_3 + 1)}\mathcal{O}^{(I)}_{I_3-1}, \tag{3.41c}$$

where $\tau_\pm = \tau_1 \pm i\tau_2$. These relations also imply the following

$$[\tau_3, [\tau_3, \mathcal{O}^{(I)}_{I_3}]] + \frac{1}{2}[\tau_+, [\tau_-, \mathcal{O}^{(I)}_{I_3}]] + \frac{1}{2}[\tau_-, [\tau_+, \mathcal{O}^{(I)}_{I_3}]] = I(I+1)\mathcal{O}^{(I)}_{I_3}. \tag{3.42}$$

We then use these relations to construct our elemental annihilation operators. During this process it is also necessary to use the commutation relations between the isospin operators and the quark fields. For the barred quark fields, these are

$$\begin{aligned} [\tau_3, \overline{u}] &= \frac{1}{2}\overline{u}, \qquad [\tau_3, \overline{d}] = -\frac{1}{2}\overline{d}, \qquad [\tau_3, \overline{s}] = 0, \\ [\tau_+, \overline{u}] &= 0, \qquad [\tau_+, \overline{d}] = \overline{u}, \qquad [\tau_+, \overline{s}] = 0, \\ [\tau_-, \overline{u}] &= \overline{d}, \qquad [\tau_-, \overline{d}] = 0, \qquad [\tau_-, \overline{s}] = 0, \end{aligned} \tag{3.43}$$

and for the unbarred quark fields, these are

$$\begin{aligned} [\tau_3, u] &= -\frac{1}{2}u, \qquad [\tau_3, d] = \frac{1}{2}d, \qquad [\tau_3, s] = 0, \\ [\tau_-, u] &= 0, \qquad [\tau_-, d] = -u, \qquad [\tau_-, s] = 0, \\ [\tau_+, u] &= -d, \qquad [\tau_+, d] = 0, \qquad [\tau_+, s] = 0. \end{aligned} \tag{3.44}$$

By writing down every possible flavor combination for a given isospin channel, we then find elemental operators that transform under each isospin irrep by applying the relations above. Specific examples are discussed for baryons and mesons in Secs. 3.3.2 and 3.3.3, respectively.

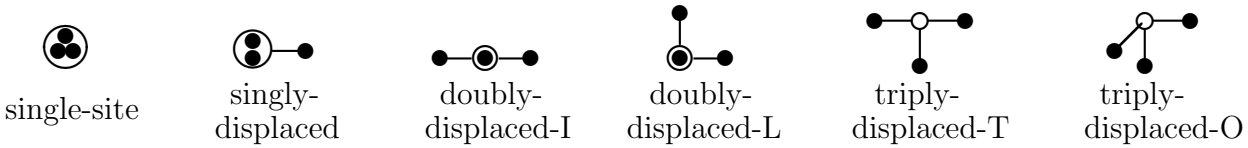

Figure 3.2: The displaced baryon operators we consider. The solid circles depict the quark fields. The line segments show the gauge links making up the displacements. The hollow circle indicates the location of the Levi-Civita tensor from which the quarks are displaced. The displacements are all of the same length. Figure taken from Ref. [43].

3.3.2 Baryons

Constructing baryon operators that are gauge-invariant is easily done with the use of the Levi-Civita symbol ε_{abc}. Our baryon elemental annihilation operators are flavor combinations of [6]

$$\Phi^{ABC}_{\alpha\beta\gamma;ijk}(\boldsymbol{p},t) = \sum_{\boldsymbol{x}} e^{-i\boldsymbol{p}\cdot\boldsymbol{x}} \varepsilon_{abc} q^{A}_{a\alpha i}(\boldsymbol{x},t) q^{B}_{b\beta j}(\boldsymbol{x},t) q^{C}_{c\gamma k}(\boldsymbol{x},t), \tag{3.45}$$

that transform according to the isospin irreps. The corresponding elemental creation operators are flavor combinations of

$$\overline{\Phi}^{ABC}_{\alpha\beta\gamma;ijk}(\boldsymbol{p},t) = \sum_{\boldsymbol{x}} e^{i\boldsymbol{p}\cdot\boldsymbol{x}} \varepsilon_{abc} \overline{q}^{C}_{c\gamma k}(\boldsymbol{x},t) \overline{q}^{B}_{b\beta j}(\boldsymbol{x},t) \overline{q}^{A}_{a\alpha i}(\boldsymbol{x},t). \tag{3.46}$$

We construct elemental operators for each displacement type shown in Figure 3.2, and for simplicity, each displacement is of length $2a_s$. Our choices for these elemental operators are shown in Table 3.1. Some of these elemental operators may be linearly dependent, and therefore we make use of a MAPLE package capable of manipulating Grassmann fields in order to detect these linear dependencies and give us a final set of linearly independent elemental operators.

Our final set of baryon operators are linear combinations of these elemental operators such that they transform appropriately under the lattice symmetry group (see Secs. 3.4 and

[6] Flavor combinations means linear combinations that differ only in the flavor indices. These are needed when a particular isospin cannot be constructed with a single term.

Table 3.1: The chosen set of elemental baryon annihilation operators. Table taken from Ref. [45].

Baryon	$I = I_3$	S	Annihilation operators
Δ^{++}	$\frac{3}{2}$	0	$\Phi^{uuu}_{\alpha\beta\gamma;\,ijk}$
Σ^{+}	1	-1	$\Phi^{uus}_{\alpha\beta\gamma;\,ijk}$
N^{+}	$\frac{1}{2}$	0	$\Phi^{uud}_{\alpha\beta\gamma;\,ijk} - \Phi^{duu}_{\alpha\beta\gamma;\,ijk}$
Ξ^{0}	$\frac{1}{2}$	-2	$\Phi^{ssu}_{\alpha\beta\gamma;\,ijk}$
Λ^{0}	0	-1	$\Phi^{uds}_{\alpha\beta\gamma;\,ijk} - \Phi^{dus}_{\alpha\beta\gamma;\,ijk}$
Ω^{-}	0	-3	$\Phi^{sss}_{\alpha\beta\gamma;\,ijk}$

3.5):

$$B_l(t) = c^{(l)}_{\alpha\beta\gamma}\Phi^{ABC}_{\alpha\beta\gamma}(\boldsymbol{p}, t), \tag{3.47}$$

where l is a compound index that specifies all the quantum numbers for this operator as well as an identifier for the different operators within the same symmetry channel. The corresponding baryon creation operators are then

$$\overline{B}_l(t) = c^{(l)*}_{\alpha\beta\gamma}\overline{\Phi}^{ABC}_{\alpha\beta\gamma}(\boldsymbol{p}, t). \tag{3.48}$$

Notice that we only need to determine these linear combinations for the annihilation operators or the creation operators, because the coefficients are simply related by complex conjugation.

One last interesting point to discuss about our baryon operators is that the creation (annihilation) operators create (annihilate) a particle state with a given parity P and annihilate (create) an anti-particle with same parity P. This means that in our temporal correlators using baryon operators, we are creating a baryon with a given parity that propagates forward in time while also creating an antibaryon with the same parity propagating backwards in time. But, since fermions and their corresponding anti-fermion have opposite parity, then the

backwards propagating antibaryon from our correlator is not the antibaryon of the baryon propagating forward in time. Instead the antibaryon propagating backward in time is the antiparticle of the parity partner of the baryon propagating forward in time [45]. Furthermore, the masses of these two states propagating in different temporal directions differ due to chiral symmetry breaking. We can take advantage of this fact by relating correlators with a given parity for $t > 0$ to correlators with opposite parity for $t < 0$ to increase statistics. This works by first constructing the odd-parity baryon operators from the even-parity baryon operators by utilizing charge conjugation in order to ensure the correlators for these two operators are related by

$$C_{ij}^{g}(t) = C_{ij}^{u}(N_t - t)^*, \qquad (u = \text{odd},\ g = \text{even}), \tag{3.49}$$

where N_t is the temporal extent of the lattice. Then, once the correlators for both the even and odd parity baryons have been calculated, we can average over them in the following way

$$\overline{C}_{ij}^{g/u}(t) = \frac{1}{2}\Big(C_{ij}^{g/u}(t) + C_{ij}^{u/g}(N_t - 1)^*\Big) \tag{3.50}$$

to increase statistics. Note that this procedure can only be applied to baryons at rest, because baryons with non-zero momentum no longer have well-defined parity (since the parity operator flips the momentum).

3.3.3 Mesons

Constructing meson operators that are gauge-invariant can be done by contracting the color indices of the two basic building blocks composing a meson. Hence, every meson elemental annihilation operator is a flavor combination of [7]

$$\Phi_{\alpha\beta;ijk}^{AB}(\boldsymbol{p}, t) = \sum_{\boldsymbol{x}} e^{-i\boldsymbol{p}\cdot(\boldsymbol{x}+\frac{1}{2}(\boldsymbol{d}_\alpha+\boldsymbol{d}_\beta))}\delta_{ab}\overline{q}_{a\alpha i}^{A}(\boldsymbol{x}, t)q_{b\beta jk}^{B}(\boldsymbol{x}, t), \tag{3.51}$$

that transforms according to the isospin irreps, where $\boldsymbol{d}_\alpha$ and $\boldsymbol{d}_\beta$ are the spatial displacements of the $\overline{q}$ and q fields from $\boldsymbol{x}$, respectively. Notice the quark operator has two displacement

[7] For isoscalar mesons with the quantum numbers of the vacuum, it is necessary to subtract off the large vacuum expectation values of the operators. Unless stated otherwise, it will always be assumed that this has been done.

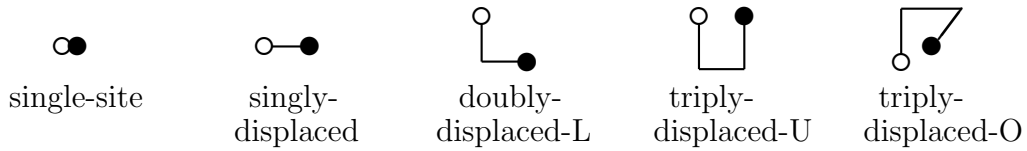

Figure 3.3: The displaced meson operators we consider. The solid circle depicts the quark field, and the hollow circle depicts the antiquark field. The line segments show the gauge links making up the displacements. The displacements are all of the same length. Figure taken from Ref. [43].

indices, because we consider displacements in which the antiquark field is displaced twice. The spatial displacement vectors in the phase factor are necessary for the meson operators to transform appropriately under G-parity. The corresponding elemental creation operator is

$$\overline{\Phi}^{AB}_{\alpha\beta;ijk}(\boldsymbol{p},t) = \sum_{\boldsymbol{x}} e^{i\boldsymbol{p}\cdot(\boldsymbol{x}+\frac{1}{2}(\boldsymbol{d}_\alpha+\boldsymbol{d}_\beta))}\delta_{ab}\overline{q}^B_{b\beta jk}(\boldsymbol{x},t)q^A_{a\alpha i}(\boldsymbol{x},t). \tag{3.52}$$

The different displacement types we consider are shown in Figure 3.3, and for simplicity, we only consider displacement lengths of $3a_s$. Our choices for these elemental operators are shown in Table 3.2. However, when we perform the group theoretical projections to the elemental operators (see Sec. 3.5) we include the G-parity projections at that time as well. Therefore, we actually use the following elemental operators

$$\eta_{\alpha\beta} = \Phi^{uu}_{\alpha\beta} + \Phi^{dd}_{\alpha\beta}, \tag{3.53a}$$

$$\phi_{\alpha\beta} = \Phi^{ss}_{\alpha\beta}, \tag{3.53b}$$

$$\pi_{\alpha\beta} = \Phi^{du}_{\alpha\beta}, \tag{3.53c}$$

$$K_{\alpha\beta} = \Phi^{su}_{\alpha\beta}, \tag{3.53d}$$

$$K^{(c)}_{\alpha\beta} = U_G K_{\alpha\beta} U_G^\dagger = \Phi^{ds}_{\alpha\beta}. \tag{3.53e}$$

As before with the baryons, we expect some of the elemental operators to be linearly dependent, and we make use of the Grassmann field package in Maple to remove these linear dependencies.

Table 3.2: The chosen set of elemental meson annihilation operators. U_G is the quantum operator corresponding to a G-parity transformation. Table taken from Ref. [46].

Hadron	$I = I_3$	S	G	Annihilation operators
f, f', η, η'	0	0	1	$\Phi^{uu}_{\alpha\beta}+\Phi^{dd}_{\alpha\beta}+U_G(\Phi^{uu}_{\alpha\beta}+\Phi^{dd}_{\alpha\beta})U_G^\dagger$
				$\Phi^{ss}_{\alpha\beta} + U_G\Phi^{ss}_{\alpha\beta}U_G^\dagger$
h, h', ω, ϕ	0	0	-1	$\Phi^{uu}_{\alpha\beta}+\Phi^{dd}_{\alpha\beta}-U_G(\Phi^{uu}_{\alpha\beta}+\Phi^{dd}_{\alpha\beta})U_G^\dagger$
				$\Phi^{ss}_{\alpha\beta} - U_G\Phi^{ss}_{\alpha\beta}U_G^\dagger$
b^+, ρ^+	1	0	1	$\Phi^{du}_{\alpha\beta} + U_G\Phi^{du}_{\alpha\beta}U_G^\dagger$
a^+, π^+	1	0	-1	$\Phi^{du}_{\alpha\beta} - U_G\Phi^{du}_{\alpha\beta}U_G^\dagger$
K^+, K^{*+}	$\frac{1}{2}$	1		$\Phi^{su}_{\alpha\beta}$
$\overline{K}^0, \overline{K}^{*0}$	$\frac{1}{2}$	-1		$\Phi^{ds}_{\alpha\beta}$

Our final set of meson operators are linear combinations of these elemental operators such that they transform appropriately under the lattice symmetry group (see Secs. 3.4 and 3.5)

$$M_l(t) = c^{(l)}_{\alpha\beta}\Phi^{AB}_{\alpha\beta}(\boldsymbol{p}, t), \tag{3.54}$$

where l is a compound index that specifies all quantum numbers for this operator, as well as an identifier for the different operators within the same symmetry channel. The corresponding meson creation operators are

$$\overline{M}_l(t) = c^{(l)*}_{\alpha\beta}\overline{\Phi}^{AB}_{\alpha\beta}(\boldsymbol{p}, t). \tag{3.55}$$

Again, as before with the baryons, we need only determine the coefficients for the annihilation operators or the creation operators, because the coefficients for each are related by complex conjugation.

In contrast to the baryons, the backward-propagating mesons have the same energy as the forward-propagating mesons, because bosons have the same parity as their corresponding

antiboson. This then allows for an increase in statistics if we can design our meson operators such that

$$C_{ij}(t) = C_{ij}(N_t - 1), \tag{3.56}$$

which can easily be satisfied if our meson operators satisfy

$$M_i(t) = \eta M_i(N_t - t), \qquad \text{with} \quad |\eta|^2 = 1. \tag{3.57}$$

This was only done for the lightest particles in which temporal wrap-around effects are most significant. This helps in those cases, because a correlator that is symmetric under time reversal can be fit using fewer parameters leading to increased precision in the energy extraction.

3.4 THE LATTICE SYMMETRY GROUP

A commonly used approach for designing operators in lattice QCD has been to use continuum operators that transform according to the quantum numbers specified above, and then to discretize these operators. This strategy has several shortcomings: the efficient construction of spin states larger than the first few J values soon becomes unwieldy; the use of extended hadron operators with the correct transformation properties also quickly becomes burdensome; and, perhaps most importantly, due to the reduced rotational symmetry of the hypercubic box, the discretized operators mix different values of J. Therefore, building operators based on the irreps of $SU(2)$ is ineffective and unnecessary. Instead, our approach is to construct operators that transform under the irreps of the lattice symmetry group, which is a crystallographic space group known as the simple cubic space group and denoted by O_h^1 in Schönflies notation. This group contains: the proper rotations of a cube, which form the octahedral group O; a spatial inversion element denoted by I_s, which can be used to construct the point group O_h using a direct product (*i.e.* $O_h = O \otimes \{E, I_s\}$, where E is the identity element); and the set of allowed translations $T(\boldsymbol{b})$ on a simple cubic lattice with periodic boundary conditions by a vector $\boldsymbol{b}$, which forms an abelian group. Thus, the lattice

symmetry group O_h^1 is the semi-direct product of $T(\boldsymbol{b})$ and O_h, and our operators are made to transform appropriately under irreps of this symmetry group on each timeslice.[8]

The first step in constructing operators with the appropriate transformation properties under O_h^1 is to obtain the irreps of the group of allowed translations $T(\boldsymbol{b})$. Since $T(\boldsymbol{b})$ is an abelian group, all of its irreps are one-dimensional, and we can label these irreps by the total momentum $\boldsymbol{p}$. Next, we use the method of induced representations [51, 52, 53, 54], which is a method used to form the representations of a group from a representation of one of its subgroups, to find the representations of O_h that we demand our operators transform under. The methods for doing this in the general case of transformations with the Poincaré group, known as Wigner's classification [55], have been well known for some time. The idea behind this method is that the irreducible representations of the Poincaré group can be induced from the irreps of the subgroup that leave a chosen reference momentum $\boldsymbol{p}_{ref}$ invariant, known as the little group of $\boldsymbol{p}$.

The simplest case concerns constructing operators that are used to create states at rest (*i.e.* $\boldsymbol{p} = 0$). The representation of the group of allowed translations is trivial in this case. Hence, we need only make sure our operators are translationally invariant and transform according to the irreps of O_h (which is the little group in this case).

Things become more involved when dealing with states that have non-zero total momentum. First, consider how translations affect these types of states:

$$\begin{aligned} T(\boldsymbol{b})\,|\boldsymbol{p}\rangle &= \int \mathrm{d}^3\boldsymbol{x}\; T(\boldsymbol{b})\,|\boldsymbol{x}\rangle\,\langle\boldsymbol{x}\,|\,\boldsymbol{p}\rangle \\ &= \int \mathrm{d}^3\boldsymbol{x}\,|\boldsymbol{x}+\boldsymbol{b}\rangle\, e^{i\boldsymbol{p}\cdot\boldsymbol{x}} \\ &= \int \mathrm{d}^3\boldsymbol{x}\,|\boldsymbol{x}\rangle\, e^{i\boldsymbol{p}\cdot(\boldsymbol{x}-\boldsymbol{b})} \\ &= e^{-i\boldsymbol{p}\cdot\boldsymbol{b}} \int \mathrm{d}^3\boldsymbol{x}\,|\boldsymbol{x}\rangle\, e^{i\boldsymbol{p}\cdot\boldsymbol{x}} \\ &= e^{-i\boldsymbol{p}\cdot\boldsymbol{b}} \int \mathrm{d}^3\boldsymbol{x}\,|\boldsymbol{x}\rangle\,\langle\boldsymbol{x}\,|\,\boldsymbol{p}\rangle \\ &= e^{-i\boldsymbol{p}\cdot\boldsymbol{b}}\,|\boldsymbol{p}\rangle\,. \end{aligned} \tag{3.58}$$

[8] The hadron operators we construct act on single time slices, which is why we are interested in the symmetries of the three-dimensional cubic lattice, rather than the full hypercubic lattice.

Therefore, if an operator $\overline{\mathcal{O}}^{\boldsymbol{p}}$ is to create a state with momentum $\boldsymbol{p}$ by acting on the vacuum, then

$$\begin{aligned} e^{-i\boldsymbol{p}\cdot\boldsymbol{b}}\overline{\mathcal{O}}^{\boldsymbol{p}}\left|0\right\rangle &= T(\boldsymbol{b})\overline{\mathcal{O}}^{\boldsymbol{p}}\left|0\right\rangle \\ &= T(\boldsymbol{b})\overline{\mathcal{O}}^{\boldsymbol{p}}T(\boldsymbol{b})^{\dagger}T(\boldsymbol{b})\left|0\right\rangle \\ &= T(\boldsymbol{b})\overline{\mathcal{O}}^{\boldsymbol{p}}T(\boldsymbol{b})^{\dagger}\left|0\right\rangle \end{aligned} \tag{3.59}$$

which implies that under translations, these momentum creation operators should transform as

$$T(\boldsymbol{b})\overline{\mathcal{O}}^{\boldsymbol{p}}T(\boldsymbol{b})^{\dagger} = e^{-i\boldsymbol{p}\cdot\boldsymbol{b}}\overline{\mathcal{O}}^{\boldsymbol{p}}. \tag{3.60}$$

Similarly, one can show that the momentum annihilation operators should transform as

$$T(\boldsymbol{b})\mathcal{O}^{\boldsymbol{p}}T(\boldsymbol{b})^{\dagger} = e^{i\boldsymbol{p}\cdot\boldsymbol{b}}\mathcal{O}^{\boldsymbol{p}}. \tag{3.61}$$

Next, we need to determine how these operators transform under rotations in the octahedral point group O_h. But, we need to be cautious, because different rotations can bring an initial momentum into the same final momentum, and momentum states are only unique up to the phase introduced by rotations in the little group of the momentum of that state. Therefore, we need to choose a convention for defining our phases in a consistent manner. This is one of the reasons for introducing the reference momentum in Wigner's method. Let us consider a state $\left|\boldsymbol{p},\sigma\right\rangle$, where σ refers to all indices that are affected by a rotation (*e.g.* spin projection). We then pick a reference momentum $\boldsymbol{p}_{ref}$, and a reference rotation $R^{\boldsymbol{p}}_{ref}$ (for each $\boldsymbol{p}$) that uniquely transforms $\boldsymbol{p}_{ref}$ into $\boldsymbol{p}$. Then, we choose our phases to be fixed by

$$\left|\boldsymbol{p},\sigma\right\rangle \equiv U_{R^{\boldsymbol{p}}_{ref}}\left|\boldsymbol{p}_{ref},\sigma\right\rangle. \tag{3.62}$$

Using this convention, we can determine how these states transform under a rotation $R \in O_h$ (*i.e.* including both proper and improper rotations):

$$\begin{aligned} U_R\left|\boldsymbol{p},\sigma\right\rangle &= U_R U_{R^{\boldsymbol{p}}_{ref}}\left|\boldsymbol{p}_{ref},\sigma\right\rangle \\ &= U_{R^{R\boldsymbol{p}}_{ref}} U^{\dagger}_{R^{R\boldsymbol{p}}_{ref}} U_R U_{R^{\boldsymbol{p}}_{ref}}\left|\boldsymbol{p}_{ref},\sigma\right\rangle. \end{aligned} \tag{3.63}$$

We then define the Wigner rotation $R^{\boldsymbol{p}}_W$ as

$$R^{\boldsymbol{p}}_W \equiv (R^{R\boldsymbol{p}}_{ref})^{-1} R R^{\boldsymbol{p}}_{ref}, \tag{3.64}$$

which is an element of the little group of $\boldsymbol{p}_{ref}$. Note, that $R_W^{\boldsymbol{p}}$ explicitly depends on the rotation R chosen, and thus the set of all Wigner rotations forms the full little group of $\boldsymbol{p}_{ref}$:

$$W(\boldsymbol{p}_{ref}) \equiv \left\{ (R_{ref}^{R\boldsymbol{p}})^{-1} R R_{ref}^{\boldsymbol{p}} : R \in O_h \right\}, \tag{3.65}$$

where $\boldsymbol{p}$ is any momentum that can be brought to $\boldsymbol{p}_{ref}$ by a transformation in O_h. Finally, this allows us to determine the effect of an arbitrary transformation in O_h on any momentum state by using the representations of the little group. The representations of the little group can be determined as follows

$$\begin{aligned} U_{R_W^{\boldsymbol{p}}} \left| \boldsymbol{p}_{ref}, \sigma \right\rangle &= \sum_{\sigma'} \left| \boldsymbol{p}_{ref}, \sigma' \right\rangle \left\langle \boldsymbol{p}_{ref}, \sigma' \right| U_{R_W^{\boldsymbol{p}}} \left| \boldsymbol{p}_{ref}, \sigma \right\rangle \\ &= \sum_{\sigma'} \left| \boldsymbol{p}_{ref}, \sigma' \right\rangle \Gamma_{\sigma'\sigma}(R_W^{\boldsymbol{p}}). \end{aligned} \tag{3.66}$$

Thus, continuing with Eq. (3.63):

$$\begin{aligned} U_R \left| \boldsymbol{p}, \sigma \right\rangle &= U_{R_{ref}^{R\boldsymbol{p}}} U_{R_W^{\boldsymbol{p}}} \left| \boldsymbol{p}_{ref}, \sigma \right\rangle \\ &= U_{R_{ref}^{R\boldsymbol{p}}} \sum_{\sigma'} \left| \boldsymbol{p}_{ref}, \sigma' \right\rangle \Gamma_{\sigma'\sigma}(R_W^{\boldsymbol{p}}) \\ &= \sum_{\sigma'} \left| R\boldsymbol{p}, \sigma' \right\rangle \Gamma_{\sigma'\sigma}(R_W^{\boldsymbol{p}}). \end{aligned} \tag{3.67}$$

This allows us to determine how our non-zero momentum creation operators must transform under the group O_h:

$$U_R \overline{\mathcal{O}}_{\boldsymbol{p}}^{\Lambda\lambda} U_R^\dagger = \sum_\mu \overline{\mathcal{O}}_{\boldsymbol{p}}^{\Lambda\mu} \Gamma_{\mu\lambda}^{(\Lambda)}(R_W^{\boldsymbol{p}}), \tag{3.68}$$

where Λ is an irrep of the little group of $\boldsymbol{p}_{ref}$, and λ is the irrep row. Let us combine this with the group of translations to determine how these operators transform under the full space group O_h^1:

$$U_{(R,\boldsymbol{b})} \overline{\mathcal{O}}_{\boldsymbol{p}}^{\Lambda\lambda} U_{(R,\boldsymbol{b})}^\dagger = \sum_\mu \overline{\mathcal{O}}_{\boldsymbol{p}}^{\Lambda\mu} \Gamma_{\mu\lambda}^{(\Lambda)}(R_W^{\boldsymbol{p}}) e^{-iR\boldsymbol{p}\cdot\boldsymbol{b}}. \tag{3.69}$$

Similarly, for the annihilation operators we must have

$$U_{(R,\boldsymbol{b})} \mathcal{O}_{\boldsymbol{p}}^{\Lambda\lambda} U_{(R,\boldsymbol{b})}^\dagger = \sum_\mu \overline{\mathcal{O}}_{\boldsymbol{p}}^{\Lambda\mu} \Gamma_{\mu\lambda}^{(\Lambda)}(R_W^{\boldsymbol{p}})^* e^{iR\boldsymbol{p}\cdot\boldsymbol{b}}. \tag{3.70}$$

Note that these transformation properties for the creation and annihilation operators are completely general. That is, they even apply for zero momentum operators, where the Wigner rotations reduce to normal rotations (*i.e.* $R^{\boldsymbol{p}}_W \to R$) and the exponential factors become unity.

There is one added complication to discuss when considering the group O_h as compared to the Poincaré group: no single reference momentum can be brought to all allowed momenta from transformations within O_h. Hence, we define a reference momentum for each momentum direction we consider.[9] Our choices for these reference momenta are shown in Table 3.3. We only consider three types of momenta: on-axis directions $\pm\hat{x}$, $\pm\hat{y}$, $\pm\hat{z}$; planar-diagonal directions $\pm\hat{x} \pm \hat{y}$, $\pm\hat{x} \pm \hat{z}$, $\pm\hat{y} \pm \hat{z}$; and cubic-diagonal directions $\pm\hat{x} \pm \hat{y} \pm \hat{z}$. We expect these to be sufficient for the energy ranges we are interested in. One last point to be made is that we can simplify this process by first making momentum operators having momentum in the direction of the reference momentum $\boldsymbol{p}_{ref}$ only, and then apply the reference rotations $R^{\boldsymbol{p}}_{ref}$ to these operators to obtain momentum operators for all momentum directions.

3.4.1 The Octahedral Group O

We start by discussing the group of proper rotations that leave a cube invariant, known as the octahedral group O. This group has 24 elements. The proper rotations in this group are denoted by C_{nj}, which produces to a rotation through an angle $2\pi/n$ about the axis O_j. The axes O_j are shown in Figure 3.4. This group has five conjugacy classes, shown in Table 3.4. This implies there must exist five inequivalent irreps with dimensions 1, 1, 2, 3, and 3 (using the fact that the sum of the squares of the dimensions of the irreps equals the order of the group). The five irreps are named A_1, A_2, E, T_1, and T_2.[10]

When we discuss projecting our operators onto the irreps of the little group in Sec. 3.5, we need to obtain explicit matrices for these representations. The set $\{C_{4y}, C_{4z}\}$ is a generating set for O, and therefore we only need the representation matrices for these two group

[9] It does not matter if the lengths of $\boldsymbol{p}_{ref}$ and $\boldsymbol{p}$ differ as long as they can be made parallel by a rotation in O_h. The reason this does not matter, is because the little group is the same regardless of the difference in lengths of these two vectors.

[10] We adopt the Mulliken convention [56, 57] for naming the irreps: The one-dimensional irreps are named A (B) if they are symmetric (antisymmetric) with respect to rotations about the principal axis; the two-dimensional irreps are named E; and the three-dimensional irreps are named T.

Table 3.3: Our choices for the reference momentum directions and the reference rotations for each momentum direction that we use. Table taken from Ref. [46].

$\boldsymbol{p}_{\text{ref}}$ direction	$\boldsymbol{p}$ direction	$R^{\boldsymbol{p}}_{\text{ref}}$
$(0,0,1)$	$(\ 0,\ 0,-1)$	C_{2x}
	$(\ 1,\ 0,\ 0)$	C_{4y}
	$(-1,\ 0,\ 0)$	C_{4y}^{-1}
	$(\ 0,-1,\ 0)$	C_{4x}
	$(\ 0,\ 1,\ 0)$	C_{4x}^{-1}
$(0,1,1)$	$(0,-1,-1)$	C_{2x}
	$(0,\ 1,-1)$	C_{4x}^{-1}
	$(0,-1,1)$	C_{4x}
	$(\ 1,0,\ 1)$	C_{4z}^{-1}
	$(-1,0,-1)$	$C_{2b} = C_{2x}C_{4z}$
	$(\ 1,0,-1)$	$C_{2a} = C_{2y}C_{4z}$
	$(-1,0,\ 1)$	C_{4z}
	$(\ 1,\ 1,0)$	C_{4y}
	$(-1,-1,0)$	$C_{2d} = C_{2z}C_{4y}$
	$(\ 1,-1,0)$	$C_{2c} = C_{4y}C_{2z}$
	$(-1,\ 1,0)$	C_{4y}^{-1}
$(\ 1,\ 1,\ 1)$	$(\ 1,\ 1,-1)$	C_{4y}
	$(\ 1,-1,\ 1)$	C_{4x}
	$(\ 1,-1,-1)$	C_{2x}
	$(-1,\ 1,\ 1)$	C_{4z}
	$(-1,1,-1)$	C_{2y}
	$(-1,-1,\ 1)$	C_{2z}
	$(-1,-1,-1)$	$C_{2d} = C_{2z}C_{4y}$

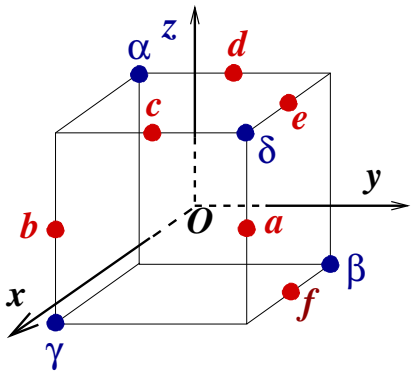

Figure 3.4: The axes denoting the group elements of the octahedral group O. Figure taken from Ref. [46].

elements. Our choice for these matrices is shown in Table 3.5. A very obvious question one might ask is, how do the states transforming in these representations correspond to the physical states we are interested in that transform under $SO(3)$? Since O is a subgroup of $SO(3)$, this question can be addressed by using the subduced representations of $SO(3)$ restricted to O, which are given by $\Gamma^J_{\downarrow O} = \left\{\Gamma^{(J)}(R); R \in O\right\}$. Our goal is to determine the irreps of O contained in $\Gamma^J_{\downarrow O}$, which is in general reducible. The number of times n^J_Γ that the

Table 3.4: The conjugacy classes for the octahedral group O.

$\mathcal{C}_1 = \{E\}$
$\mathcal{C}_2 = \left\{C_{3\alpha}, C_{3\beta}, C_{3\gamma}, C_{3\delta}, C^{-1}_{3\alpha}, C^{-1}_{3\beta}, C^{-1}_{3\gamma}, C^{-1}_{3\delta}\right\}$
$\mathcal{C}_3 = \{C_{2x}, C_{2y}, C_{2z}\}$
$\mathcal{C}_4 = \left\{C_{4x}, C_{4y}, C_{4z}, C^{-1}_{4x}, C^{-1}_{4y}, C^{-1}_{4z}\right\}$
$\mathcal{C}_5 = \{C_{2a}, C_{2b}, C_{2c}, C_{2d}, C_{2e}, C_{2f}\}$

Table 3.5: The choice of matrices used for the representations of O.

Λ	$\Gamma^{(\Lambda)}(C_{4y})$	$\Gamma^{(\Lambda)}(C_{4z})$
A_1	$\begin{bmatrix} 1 \end{bmatrix}$	$\begin{bmatrix} 1 \end{bmatrix}$
A_2	$\begin{bmatrix} -1 \end{bmatrix}$	$\begin{bmatrix} -1 \end{bmatrix}$
E	$\frac{1}{2}\begin{bmatrix} 1 & \sqrt{3} \\ \sqrt{3} & -1 \end{bmatrix}$	$\begin{bmatrix} -1 & 0 \\ 0 & 1 \end{bmatrix}$
T_1	$\begin{bmatrix} 0 & 0 & 1 \\ 0 & 1 & 0 \\ -1 & 0 & 0 \end{bmatrix}$	$\begin{bmatrix} 0 & -1 & 0 \\ 1 & 0 & 0 \\ 0 & 0 & 1 \end{bmatrix}$
T_2	$\begin{bmatrix} 0 & 0 & -1 \\ 0 & -1 & 0 \\ 1 & 0 & 0 \end{bmatrix}$	$\begin{bmatrix} 0 & 1 & 0 \\ -1 & 0 & 0 \\ 0 & 0 & -1 \end{bmatrix}$

irrep Γ of O appears in $\Gamma^J_{\downarrow O}$ is given by

$$n^J_\Gamma = \frac{1}{g_O} \sum_p N_p \chi^J_{\downarrow O}(\mathcal{C}_p) \chi^\Gamma(\mathcal{C}_p)^*, \tag{3.71}$$

where $\chi^J_{\downarrow O}$ is the character vector for the J irrep of $SO(3)$ subduced to O, χ^Γ is the character vector for irrep Γ of O, g_O is the order of the group, the sum is over the classes $\mathcal{C}_p$ of the group, and N_p is the number of elements in class p. The results are shown in Table 3.6. Notice that only integer values of J appear in this table. This is because we only considered the single-valued irreps of O and $SO(3)$. We could find the double-valued (spinor) representations of these two groups as well, but the orthogonality theorems used to derive Eq. (3.71) and the projection formulas to be used in Sec. 3.5 are only valid for the single-valued irreps. However, we can instead use the single-valued irreps in the double covers of O and $SO(3)$, which are known as the double octahedral group O^D and $SU(2)$, respectively. The single-valued irreps of O also occur as single-valued irreps for O^D, and the double-valued irreps of O appear as extra single-valued irreps for O^D. The double octahedral group can be formed by adding a new group generator $\overline{E}$ to O, which performs a rotation by 2π, and has the property that $\overline{E}^2 = E$. This new group generator doubles the number of group elements of O: for each element $R \in O$, there exists a new element $\overline{R} = \overline{E}R \in O^D$. That is $O^D = \{R, \overline{E}R : R \in O\}$. This new group consists of eight conjugacy classes shown in Table 3.7. Therefore, there must exist three new single-valued irreps in O^D that correspond to the double-valued irreps of O, and they must have dimensions 2, 2, and 4. These new irreps are named G_1, G_2, and H. Note that if you choose an irrep such that $\Gamma(\overline{E}) = \Gamma(E)$ and $\Gamma(\overline{R}) = \Gamma(R)$, then this representation corresponds to one of the single-valued irreps from O. To obtain the new irreps, you must choose $\Gamma(\overline{E}) = -\Gamma(E)$ and $\Gamma(\overline{R}) = -\Gamma(R)$. Our choice for these matrices is shown in Table 3.8. We can now use Eq. (3.71) to find the number of times n^J_Γ that the irrep Γ of O^D appears in $\Gamma^J_{\downarrow O^D}$ by replacing O with O^D and $SO(3)$ with $SU(2)$. The results are shown in Table 3.9.

Table 3.6: The number of times n_Γ^J that the irrep Γ of O occurs in $\Gamma^J_{\downarrow O}$.

J	$n^J_{A_1}$	$n^J_{A_2}$	n^J_E	$n^J_{T_1}$	$n^J_{T_2}$
0	1	0	0	0	0
1	0	0	0	1	0
2	0	0	1	0	1
3	0	1	0	1	1
4	1	0	1	1	1
5	0	0	1	2	1
6	1	1	1	1	2
7	0	1	1	2	2
8	1	0	2	2	2
9	1	1	1	3	2
10	1	1	2	2	3
11	0	1	2	3	3
12	2	1	2	3	3

Table 3.7: The conjugacy classes for the double octahedral group O^D.

$\mathcal{C}_1 = \{E\}$
$\mathcal{C}_2 = \left\{C_{3\alpha}, C_{3\beta}, C_{3\gamma}, C_{3\delta}, C_{3\alpha}^{-1}, C_{3\beta}^{-1}, C_{3\gamma}^{-1}, C_{3\delta}^{-1}\right\}$
$\mathcal{C}_3 = \left\{C_{2x}, C_{2y}, C_{2z}, \overline{C}_{2x}, \overline{C}_{2y}, \overline{C}_{2z}\right\}$
$\mathcal{C}_4 = \left\{C_{4x}, C_{4y}, C_{4z}, C_{4x}^{-1}, C_{4y}^{-1}, C_{4z}^{-1}\right\}$
$\mathcal{C}_5 = \left\{C_{2a}, C_{2b}, C_{2c}, C_{2d}, C_{2e}, C_{2f}, \overline{C}_{2a}, \overline{C}_{2b}, \overline{C}_{2c}, \overline{C}_{2d}, \overline{C}_{2e}, \overline{C}_{2f}\right\}$
$\mathcal{C}_6 = \left\{\overline{E}\right\}$
$\mathcal{C}_7 = \left\{\overline{C}_{3\alpha}, \overline{C}_{3\beta}, \overline{C}_{3\gamma}, \overline{C}_{3\delta}, \overline{C}_{3\alpha}^{-1}, \overline{C}_{3\beta}^{-1}, \overline{C}_{3\gamma}^{-1}, \overline{C}_{3\delta}^{-1}\right\}$
$\mathcal{C}_8 = \left\{\overline{C}_{4x}, \overline{C}_{4y}, \overline{C}_{4z}, \overline{C}_{4x}^{-1}, \overline{C}_{4y}^{-1}, \overline{C}_{4z}^{-1}\right\}$

Table 3.8: The choice of matrices used for the double-valued representations of O.

Λ	$\Gamma^{(\Lambda)}(C_{4y})$	$\Gamma^{(\Lambda)}(C_{4z})$
G_1	$\frac{1}{\sqrt{2}}\begin{bmatrix} 1 & -1 \\ 1 & 1 \end{bmatrix}$	$\frac{1}{\sqrt{2}}\begin{bmatrix} 1-i & 0 \\ 0 & 1+i \end{bmatrix}$
G_2	$\frac{-1}{\sqrt{2}}\begin{bmatrix} 1 & -1 \\ 1 & 1 \end{bmatrix}$	$\frac{-1}{\sqrt{2}}\begin{bmatrix} 1-i & 0 \\ 0 & 1+i \end{bmatrix}$
H	$\frac{1}{2\sqrt{2}}\begin{bmatrix} 1 & -\sqrt{3} & \sqrt{3} & -1 \\ \sqrt{3} & -1 & -1 & \sqrt{3} \\ \sqrt{3} & 1 & -1 & -\sqrt{3} \\ 1 & \sqrt{3} & \sqrt{3} & 1 \end{bmatrix}$	$\frac{1}{\sqrt{2}}\begin{bmatrix} -1-i & 0 & 0 & 0 \\ 0 & 1-i & 0 & 0 \\ 0 & 0 & 1+i & 0 \\ 0 & 0 & 0 & -1+i \end{bmatrix}$

3.4.2 The Point Group O_h

By including the spatial inversion operator as a new group generator in O, denoted by I_s, this produces the point group O_h, which is simply a direct product $O_h = O \otimes \{E, I_s\}$. This doubles the number of conjugacy classes: the first five classes are identical to those shown in Table 3.4, and the extra five consist of the first five but with each group element in the classes multiplied by I_s. The irreps of O_h are similarly named to those of O but with the addition of the subscripts g (for the even-parity irreps) and u (for the odd-parity irreps).[11] That is, we now have the irreps A_{1g}, A_{2g}, E_g, T_{1g}, T_{2g}, A_{1u}, A_{2u}, E_u, T_{1u}, and T_{2u}. The choices for the explicit matrix representations shown in Table 3.5 do not depend on this new subscript. But, the matrix representation for I_s is the identity matrix for the even-parity irreps and negative one times the identity matrix for the odd-parity irreps.

As before, if we want to use the double-valued irreps of O_h, we must instead use the

[11] These subscripts are abbreviations for the German words gerade and ungerade, which mean even and odd, respectively.

Table 3.9: The number of times n_Γ^J that the irrep Γ of O^D occurs in $\Gamma^J_{\downarrow O^D}$.

J	$n^J_{G_1}$	$n^J_{G_2}$	n^J_H
$\frac{1}{2}$	1	0	0
$\frac{3}{2}$	0	0	1
$\frac{5}{2}$	0	1	1
$\frac{7}{2}$	1	1	1
$\frac{9}{2}$	1	0	2
$\frac{11}{2}$	1	1	2
$\frac{13}{2}$	1	2	2
$\frac{15}{2}$	1	1	3
$\frac{17}{2}$	2	1	3
$\frac{19}{2}$	2	2	3
$\frac{21}{2}$	1	2	4
$\frac{23}{2}$	2	2	4
$\frac{25}{2}$	3	2	4

double point group O_h^D. The effect of including spatial inversions into O^D to produce O_h^D is exactly analogous to the effect of including spatial inversions into O to produce O_h: the number of elements in O_h^D has doubled as compared to O^D; the first eight conjugacy classes of O_h^D are identical to those shown in Table 3.7, and the extra eight consist of the first eight but with each group element in the classes multiplied by I_s; the double-valued irreps of O_h are denoted by G_{1g}, G_{2g}, H_g, G_{1u}, G_{2u}, and H_u; and the choices for the explicit matrix representations shown in Table 3.8 do not depend on the parity of the irrep, but the matrix representation for I_s is the identity matrix for even-parity irreps and negative one times the identity matrix for the odd-parity irreps.

3.4.3 The Little Groups

When dealing with non-zero momentum operators, we need the irreps of the little groups corresponding to the reference momentum $\boldsymbol{p}_{ref}$. Recall that that we only consider three types of momenta: on-axis directions $\pm\hat{x}$, $\pm\hat{y}$, $\pm\hat{z}$; planar-diagonal directions $\pm\hat{x} \pm \hat{y}$, $\pm\hat{x} \pm \hat{z}$, $\pm\hat{y} \pm \hat{z}$; and cubic-diagonal directions $\pm\hat{x} \pm \hat{y} \pm \hat{z}$. This greatly simplifies matters, and leads to three little groups that we must consider: C_{4v} for on-axis momenta, C_{2v} for planar-diagonal momenta, and C_{3v} for cubic-diagonal momenta. The conjugacy classes and explicit representation matrices used can be found in Ref. [46].

3.4.3.1 The Subductions onto the Little Group Irreps When we are dealing with operators that create states with non-zero momentum it is not always easy to determine the type of particle that might correspond to any particular little group irrep. Whereas, when dealing with particles at rest that transform under the O_h irreps, particle identification is relatively straightforward by considering the other quantum numbers of that particle along with Tables 3.6 and 3.9. We can make the identification of these moving particles easier by considering the number of times that each little group irrep occurs in the subduced representations of O_h restricted to the particular little group in question. The results of these subductions are shown in Table 3.10.

Table 3.10: The subductions $\downarrow$ of the irreps of O_h onto the irreps of the little groups C_{4v}, C_{3v}, and C_{2v}. Table taken from Ref. [46].

$\Lambda\,(O_h)$	$\downarrow C_{4v}$	$\downarrow C_{3v}$	$\downarrow C_{2v}$
A_{1g}	A_1	A_1	A_1
A_{1u}	A_2	A_2	A_2
A_{2g}	B_1	A_2	B_2
A_{2u}	B_2	A_1	B_1
E_g	$A_1 \oplus B_1$	E	$A_1 \oplus B_2$
E_u	$A_2 \oplus B_2$	E	$A_2 \oplus B_1$
T_{1g}	$A_2 \oplus E$	$A_2 \oplus E$	$A_2 \oplus B_1 \oplus B_2$
T_{1u}	$A_1 \oplus E$	$A_1 \oplus E$	$A_1 \oplus B_1 \oplus B_2$
T_{2g}	$B_2 \oplus E$	$A_1 \oplus E$	$A_1 \oplus A_2 \oplus B_1$
T_{2u}	$B_1 \oplus E$	$A_2 \oplus E$	$A_1 \oplus A_2 \oplus B_2$
$G_{1g/u}$	G_1	G	G
$G_{2g/u}$	G_2	G	G
$H_{g/u}$	$G_1 \oplus G_2$	$F_1 \oplus F_2 \oplus G$	$2G$

3.4.4 Transformation of the Building Blocks

In order to determine the effect of an O_h^1 transformation on our operators, we need to know how these transformations effect the basic building blocks, which the operators are made of. From the definition of the gauge links in Eq. (2.37), it is not difficult to show

$$U_{(R,\boldsymbol{b})}\, U_\mu(x) U^\dagger_{(R,\boldsymbol{b})} = U_{R\mu}(R\boldsymbol{x}+\boldsymbol{b},t). \tag{3.72}$$

Unlike the Lorentz group, since O is compact we can find a finite-dimensional unitary irrep of O that the quark fields transform under:

$$S(R) = e^{\frac{1}{8}\omega_{\mu\nu}[\gamma_\mu,\gamma_\nu]}, \tag{3.73}$$

where $\omega_{kl} = -2\pi\varepsilon_{jkl}/n$ and $\omega_{4k} = \omega_{k4} = 0$. Of course, we only need $S(C_{4y})$, $S(C_{4z})$, and $S(I_s)$ to generate all other representation matrices in O_h. These are given by

$$S(C_{4y}) = \frac{1}{\sqrt{2}}(1+\gamma_1\gamma_3), \qquad S(C_{4z}) = \frac{1}{\sqrt{2}}(1+\gamma_2\gamma_1), \qquad S(I_s) = \gamma_4. \tag{3.74}$$

Then using these representation matrices, the basic building blocks transform irreducibly under the lattice symmetry group O_h^1 as

$$U_{(R,\boldsymbol{b})} q^A_{a\alpha j}(\boldsymbol{x}) U^\dagger_{(R,\boldsymbol{b})} = S(R)^{-1}_{\alpha\beta} q^A_{a\beta Rj}(R\boldsymbol{x}+\boldsymbol{b}), \tag{3.75a}$$

$$U_{(R,\boldsymbol{b})} \overline{q}^A_{a\alpha j}(\boldsymbol{x}) U^\dagger_{(R,\boldsymbol{b})} = \overline{q}^A_{a\beta Rj}(R\boldsymbol{x}+\boldsymbol{b}) S(R)_{\beta\alpha}. \tag{3.75b}$$

3.5 GROUP-THEORETICAL PROJECTIONS ONTO SYMMETRY CHANNELS

We now discuss the methods used for obtaining a set of linearly independent operators that transform according to a particular symmetry channel. An essential part of this process involves projecting a set of operators, which initially transform reducibly under the little group, to a set of operators that transform irreducibly under the little group. The formula for performing these projections is given by

$$\mathcal{O}_{Pi}^{\Lambda\lambda F}(t) = \frac{d_\Lambda}{g_{\mathcal{G}^D}} \sum_{R\in\mathcal{G}^D} \Gamma_{\lambda\mu}^{(\Lambda)}(R) U_R \mathcal{O}_i^F(t) U_R^\dagger, \tag{3.76}$$

where $\mathcal{G}^D$ is the double group of the little group $\mathcal{G}$,[12] d_Λ is the dimension of the Λ representation, $g_{\mathcal{G}^D}$ is the order (number of elements) of $\mathcal{G}^D$. The P subscript on $\mathcal{O}_{Pi}^{\Lambda\lambda F}(t)$ just specifies that this is the projection of $\mathcal{O}_i^F(t)$ onto the Λ irrep. This subscript is used, because the set of projected operators from Eq. (3.76) is not our final set of operators: many of these projected operators vanish or are linearly dependent and we choose appropriate linear combinations of these projected operators as our final set of operators. When relevant, projections onto a particular G-parity can also be done. Also, note that the index μ on $\Gamma_{\lambda\mu}^{(\Lambda)}$ can be arbitrarily chosen. However, we make the choice $\mu = \lambda$, because only then does the projection have the property of idempotency (*i.e.* $P^2 = P$). This can be seen by applying the projection formula to a projected operator:

$$\begin{aligned}
\frac{d_\Lambda}{g_{\mathcal{G}^D}} \sum_{R\in\mathcal{G}^D} \Gamma_{\lambda\mu}^{(\Lambda)}(R) U_R \mathcal{O}_{Pi}^{\Lambda\lambda F}(t) U_R^\dagger &= \sum_{\lambda'} \frac{d_\Lambda}{g_{\mathcal{G}^D}} \sum_{R\in\mathcal{G}^D} \Gamma_{\lambda\mu}^{(\Lambda)}(R) \mathcal{O}_{Pi}^{\Lambda\lambda' F}(t) \Gamma_{\lambda'\lambda}^{(\Lambda)}(R)^* \\
&= \sum_{\lambda'} \delta_{\lambda'\lambda}\delta_{\mu\lambda} \mathcal{O}_{Pi}^{\Lambda\lambda' F}(t) \\
&= \delta_{\mu\lambda} \mathcal{O}_{Pi}^{\Lambda\lambda F}(t),
\end{aligned} \tag{3.77}$$

where we invoked the great orthogonality theorem given in Eq. (3.9). From the above result, we see that if $\mu = \lambda$, then idempotency is achieved; otherwise, applying the projection twice

[12] If we are interested only in the single-valued irreps of the little group $\mathcal{G}$ (*i.e.* when creating bosonic operators), then we can use either the little group $\mathcal{G}$ or the double little group $\mathcal{G}^D$ in the projection formula. However, when we are interested in the double-valued irreps of the little group $\mathcal{G}$, we must use the double little group $\mathcal{G}^D$, because $\Gamma^{(\Lambda)}(R)$ is not well-defined since it is a one-to-two mapping. Because of this, we always use the double little group $\mathcal{G}^D$, because it is always be valid.

causes the operator to vanish. It is a nice check to see that the projected operators obey the transformation properties we seek. Consider the transformation of one of the projected operators by the group element $G \in \mathcal{G}^D$:

$$\begin{aligned}
U_G \mathcal{O}_{Pi}^{\Lambda\lambda F}(t) U_G^\dagger &= \frac{d_\Lambda}{g_{\mathcal{G}^D}} \sum_{R \in \mathcal{G}^D} \Gamma^{(\Lambda)}_{\lambda\mu}(R) U_G U_R \mathcal{O}_i^F(t) U_R^\dagger U_G^\dagger \\
&= \frac{d_\Lambda}{g_{\mathcal{G}^D}} \sum_{GR \in \mathcal{G}^D} \Gamma^{(\Lambda)}_{\lambda\mu}(G^{-1}GR) U_{GR} \mathcal{O}_i^F(t) U_{GR}^\dagger \\
&= \frac{d_\Lambda}{g_{\mathcal{G}^D}} \sum_{GR \in \mathcal{G}^D} \Gamma^{(\Lambda)}_{\lambda\mu}(G^{-1}GR) U_{GR} \mathcal{O}_i^F(t) U_{GR}^\dagger \\
&= \frac{d_\Lambda}{g_{\mathcal{G}^D}} \sum_{R \in \mathcal{G}^D} \Gamma^{(\Lambda)}_{\lambda\mu}(G^{-1}R) U_R \mathcal{O}_i^F(t) U_R^\dagger \\
&= \frac{d_\Lambda}{g_{\mathcal{G}^D}} \sum_{\lambda'} \sum_{R \in \mathcal{G}^D} \Gamma^{(\Lambda)}_{\lambda\lambda'}(G^{-1}) \Gamma^{(\Lambda)}_{\lambda'\mu}(R) U_R \mathcal{O}_i^F(t) U_R^\dagger \\
&= \sum_{\lambda'} \Gamma^{(\Lambda)}_{\lambda\lambda'}(G^{-1}) B_{Pi}^{\Lambda\lambda' F}(t) \\
&= \sum_{\lambda'} \mathcal{O}_{Pi}^{\Lambda\lambda' F}(t) \Gamma^{(\Lambda)}_{\lambda'\lambda}(G)^*,
\end{aligned} \tag{3.78}$$

which shows that these projected operators do in fact transform according to the irreps of the double little group.

However, we do not want to apply this projection equation (3.76) for each irrep row within a given irrep. The reason is that the projection equation does not give a consistent phase and normalization convention for each row of a given irrep. There is also the additional possibility that the same irrep occurs more than once within our initial reducible set of operators, and in this case applying the projection equation for each row does not give consistent relative weights between these multiple occurrences of the same irrep. In both of these cases, it may happen that the projected operators do not in fact transform under the little group as in Eq. (3.68), as they must. To circumvent these issues, we only apply Eq. (3.76) to a single irrep row, say $\lambda = 1$, then the other irrep rows can be obtained by

$$\mathcal{O}_{Pi}^{\Lambda\mu F}(t) = \frac{d_\Lambda}{g_{\mathcal{G}^D}} \sum_{R \in \mathcal{G}^D} \Gamma^{(\Lambda)}_{\mu\lambda}(R) U_R \mathcal{O}_{Pi}^{\Lambda\lambda F}(t) U_R^\dagger. \tag{3.79}$$

This result can be proven as follows:

$$\begin{aligned}\frac{d_\Lambda}{g_{\mathcal{G}^D}}\sum_{R\in\mathcal{G}^D}\Gamma^{(\Lambda)}_{\mu\lambda}(R)U_R\mathcal{O}^{\Lambda\lambda F}_{Pi}(t)U_R^\dagger &= \sum_\nu \frac{d_\Lambda}{g_{\mathcal{G}^D}}\sum_{R\in\mathcal{G}^D}\Gamma^{(\Lambda)}_{\mu\lambda}(R)\mathcal{O}^{\Lambda\nu F}_{Pi}(t)\Gamma^{(\Lambda)}_{\nu\lambda}(R)^* \\ &= \sum_\nu \delta_{\mu\nu}\mathcal{O}^{\Lambda\nu F}_{Pi}(t) \\ &= \mathcal{O}^{\Lambda\mu F}_{Pi}(t).\end{aligned} \tag{3.80}$$

In the case of our choices for the representation matrices in each irrep of the little group, it can be shown explicitly that Eq. (3.11) implies

$$C^{\Lambda\lambda F}_{ij}(t) = C^{\Lambda\mu F}(t) \tag{3.81}$$

for all λ and μ. We can use this fact to increase statistics by averaging our final correlators over each irrep row.

We now discuss the detailed steps for applying the above ideas. The first step involves determining the original set of basis operators that transform reducibly. These basis operators are just the linearly independent elemental operators discussed in Sec. 3.3. Let us define these operators by $\mathcal{O}^F_i(t)$, where F specifies the particular basis of linearly independent elemental operators we are considering, and i specifies a particular basis operator within that basis ranging from 1 to M_B. Then, we must find the explicit reducible representation matrices for this basis. That is, we must find a matrix W for each group element R in the little group such that

$$U_R\mathcal{O}^F_i(t)U_R^\dagger = \sum_{j=1}^{M_B}\mathcal{O}^F_j(t)W_{ji}(R), \tag{3.82}$$

but recall that we need only find W for the group generators. Then, in principle, we simply need to find the linear combinations of the original basis operators that block diagonalizes the W matrices. We utilize the projection formulate to obtain the projection operator

$$P^{\Lambda\lambda F}_{ij} = \frac{d_\Lambda}{g_{\mathcal{G}^D}}\sum_{R\in\mathcal{G}^D}[\Gamma^{(\Lambda)}_{\lambda\lambda}(R)W_{ji}(R)]_{\lambda=1}, \tag{3.83}$$

and apply it to each of our basis operators $\mathcal{O}^F_i$, which produces a set of projected operators

$$\mathcal{O}^{\Lambda\lambda F}_{Pi}(t) = \sum_{j=1}^{M_B} c^{\Lambda\lambda F}_{ij}\mathcal{O}^F_j(t). \tag{3.84}$$

Many of the projected operators may vanish or be linearly dependent. The number of linearly independent operators that can be produced from the set of projected operators is the rank r of the projection matrix. We must use the Gram-Schmidt procedure to produce the simplest linearly independent operators from the projected operators to arrive at our final set of operators:

$$\mathcal{O}_i^{\Lambda\lambda F}(t) = \sum_{j=1}^{M_B} c_{ij}^{\Lambda\lambda F} \mathcal{O}_j^F(t), \tag{3.85}$$

where $i = 1, \ldots, r$ with $r \leq M_B$, and $\lambda = 1$. Finally, the coefficients for the other rows can be found from

$$c_{ik}^{\Lambda\mu F} = \sum_{j=1}^{M_B} c_{ij}^{\Lambda\lambda F} \frac{d_\Lambda}{g_{\mathcal{G}^D}} \sum_{R \in \mathcal{G}^D} [\Gamma_{\mu\lambda}^{(\Lambda)}(R) W_{kj}(R)]_{\lambda=1}. \tag{3.86}$$

3.6 TWO-HADRON OPERATORS

Since many of the hadron resonances we wish to study lie above the two-particle thresholds, we must extract every two-particle state below any particular resonance of interest in order to get a reliable estimate for the energy of that resonance. The reason for this is that most of the stationary states above the two-particle threshold have some mixing between single- and two-particle states (*i.e.* these stationary states are linear combinations of single- and two-particle states), and therefore any stationary state containing a single-particle state can be created with our single-hadron operators. However, many of these mixed states may be dominated by the two-particle state and thus should not be compared with the resonances we wish to study, but until we include two-hadron operators we cannot make this determination. Thus the use of two-hadron operators is crucial for a reliable interpretation of the finite-volume spectrum. Our construction of two-hadron operators is similar to the procedures described above, but the main difference is that instead of using the elemental operators as our basis we use the following two-hadron operators as our basis operators

$$\mathcal{O}_{\boldsymbol{p}_a \Lambda_a \lambda_a i_a}^{I_a I_{3a} S_a} \mathcal{O}_{\boldsymbol{p}_b \Lambda_b \lambda_b i_b}^{I_b I_{3b} S_b}, \tag{3.87}$$

where a and b designate the separate hadrons, and i denotes all identifying information about the individual hadrons that is not explicitly labeled (*e.g.* displacement type). These two-hadron operators are constructed from single-hadron operators obtained via the methods described above. Of course, these operators do not transform irreducibly under isospin or the lattice symmetry group. Thus, our first step is to find the correct linear combinations of these basis operators that transform irreducibly under isospin by utilizing the relations in Eqs. (3.41) and (3.42). Then we perform the usual group-theoretical projections as described in Sec. 3.5 to obtain a final set of two-hadron operators that transform irreducibly under the little group of $\boldsymbol{p} = \boldsymbol{p}_a + \boldsymbol{p}_b$. This process is made much simpler due to already knowing exactly how the individual hadron operators transform under the symmetry groups we consider.

3.6.1 Comparison with Local Two-Hadron Operators

The inclusion of two-hadron operators constructed in the way we have described above leads to the need for all-to-all quark propagators (*i.e.* quark propagators from all spatial sites on the lattice to all other spatial sites on the lattice), which is significantly more computationally challenging than just using point-to-all quark propagators (*i.e.* quark propagators from a single site on the lattice to all other sites on the lattice). The reason for this will be discussed further in Chap. 4. But, this motivates the desire to construct two-hadron operators that could make use of point-to-all quark propagators. Such operators are possible. Two examples of such $\pi\pi$ operators in the $I = 2$, A_{1g}^+ and $I = 1$, T_{1u}^+ channels were obtained in [46]:

$$(\pi\pi)^{A_{1g}^+}(t) = \sum_{\boldsymbol{x}} \pi^+(\boldsymbol{x}, t)\pi^+(\boldsymbol{x}, t), \tag{3.88a}$$

$$(\pi\pi)^{T_{1u}^+}(t) = \sum_{\boldsymbol{x}, k=1,2,3} \left[\pi^+(\boldsymbol{x}, t)\Delta_k\pi^0(\boldsymbol{x}, t) - \pi^0(\boldsymbol{x}, t)\Delta_k\pi^+(\boldsymbol{x}, t)\right], \tag{3.88b}$$

where the pion fields are single site operators, the superscripts indicate the electric charges (which specifies I_3), and $\Delta_k\pi(\boldsymbol{x}, t) = \pi(\boldsymbol{x} + \hat{k}, t) - \pi(\boldsymbol{x} - \hat{k}, t)$. These operators are referred to as local operators, because the individual pion operators do not have well-defined momentum and thus correspond to some composite object with some overall momentum. The fact that these operators only involve one spatial sum is what makes them amenable

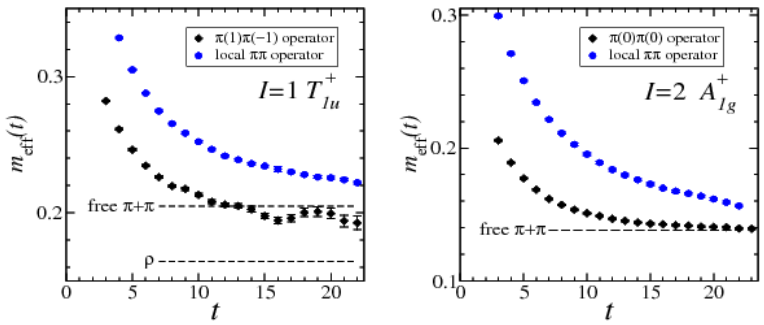

Figure 3.5: These plots of effective energies show how local $\pi\pi$ operators do not quickly plateau as compared to two-hadron operators in which the individual hadrons have well-defined momentum. Therefore these local operators must couple strongly to the unwanted high-lying states. Figure taken from Ref. [46].

to using point-to-all propagators. The individual operators in the two-hadron operators we first described above starting from Eq. (3.87) each have well-defined momentum and their own spatial sums, which makes the point-to-all method impossible to use in this situation. However, recall that we place great importance on removing excited-state contamination from our operators, and in the comparison of the effective masses for these different two-hadron operator constructions we clearly see in Figure 3.5 that the local operators must be coupling[13] to the higher lying states since they have not even begun to plateau for the time separations we consider. In contrast, the operators we have built from Eq. (3.87) perform significantly better in that they plateau very quickly which indicates that these operators couple very weakly to the unwanted high-lying states. One might wonder if this reduction in excited-state contamination outweighs the increase in computational cost associated with needing all-to-all quark propagators. There are two points to be said in regard to this: 1) all-to-all quark propagators are necessary for calculations involving single-meson isoscalars, and therefore all-to-all quark propagators cannot be avoided entirely, and 2) we will see in

[13]The term coupling is a simplification of a more correct statement. Essentially, what is meant when an operator 'couples' strongly to an eigenstate is that the states created by that operator have large overlap with the eigenstate in question.

Chap. 4 that the recently developed Stochastic LapH method has shown to be a very efficient technique for calculating all needed quark propagators.

4.0 THE ESTIMATION OF TEMPORAL CORRELATORS USING STOCHASTIC LAPH

As was discussed in Sec. 2.4, extraction of the finite-volume spectrum can be performed using two-point temporal correlation functions. In order to calculate these correlators, we use a path-integral representation with the discretized action of choice, where the integrations are performed over the quark fields and gauge-link variables. The introduction of the spacetime lattice was necessary to make the path integrals of finite dimension, and thus amenable to numerical evaluation. The actions we use are of the form

$$S[\psi, \overline{\psi}, U] = \overline{\psi} M[U] \psi + S_G[U], \tag{4.1}$$

where M is referred to as the Dirac matrix and $S_G[U]$ is the gauge action. Because the action is quadratic in the quark fields, the integration over the quark fields can be done immediately (see Sec. 2.3). This integration results in a determinant of the Dirac matrix and products of elements of the inverse of M. The inverse M^{-1} is known as the quark propagator. During the generation of gauge configurations via the RHMC algorithm [44] (see Sec. 2.3.2), or other similar algorithms, the determinant of the Dirac matrix was included as part of the probability distribution that the generated gauge links were sampled from. Since this procedure for including the determinant has already been discussed in Sec. 2.3, we focus on the evaluation of the inverse elements of the Dirac matrix. Once these inverse elements have been determined for each gauge configuration the correlators are estimated as simple summations over the gauge configurations.

Performing these needed inversions can be very computationally expensive. Thus, much care should be taken in devising a strategy for efficiently determining the quark propagators. Many calculations can be designed to avoid the direct inversion of the Dirac matrix by

solving the linear system of equations $Mx = y$ for a computationally practical number of source vectors y. Consider a single-hadron operator at rest (*i.e.* $\boldsymbol{p} = \boldsymbol{0}$), which has the form

$$\mathcal{O}(\boldsymbol{p} = \boldsymbol{0}, t) = \frac{1}{V} \sum_{\boldsymbol{x}} \varphi(\boldsymbol{x}, t), \tag{4.2}$$

where $\varphi(\boldsymbol{x}, t)$ is some relevant interpolating field such that the quark fields are all localized about $\boldsymbol{x}$ at time t. Using this operator in a two-point temporal correlator, we have

$$\begin{aligned} C(t) &\equiv \langle 0 | \, \mathcal{O}(\boldsymbol{p} = \boldsymbol{0}, t + t_0) \overline{\mathcal{O}}(\boldsymbol{p} = \boldsymbol{0}, t_0) \, | 0 \rangle \\ &= \frac{1}{V^2} \sum_{\boldsymbol{x}, \boldsymbol{y}} \frac{1}{N_{t_0}} \sum_{t_0} \langle 0 | \, \varphi(\boldsymbol{x}, t + t_0) \overline{\varphi}(\boldsymbol{y}, t_0) \, | 0 \rangle \, . \end{aligned} \tag{4.3}$$

This correlator, in the above form, suggests that we require the evaluation of the quark propagator from all spatial sites $\boldsymbol{y}$ at time $t = 0$ to all spatial sites $\boldsymbol{x}$ at time t,[1] which means that we must find nearly all elements of the inverse of the Dirac matrix, with the only exceptions depending on the source t_0 and sink t times considered in our correlation functions. Normally this would be a formidable task and impractical for most lattice sizes. Specifically, the dimension of the Dirac matrix is $N_s^3 N_t N_d N_c$, where N_s is the number of spatial sites in each spatial direction, N_t is the number of temporal sites, N_d is the number of Dirac spin indices (usually 4), and N_c is the number of color indices (usually 3). Thus, with the largest lattice used in this work (*i.e.* $N_s = 32$ and $N_t = 256$), this means the Dirac matrix is $\approx 100,000,000 \times 100,000,000$, which is far too large to be feasibly inverted. But, we can exploit translation invariance to remove one of the spatial summations. The correlator can then be written as

$$C(t) = \frac{1}{V} \sum_{\boldsymbol{x}} \langle 0 | \, \varphi(\boldsymbol{x}, t) \overline{\varphi}(\boldsymbol{0}, 0) \, | 0 \rangle \, , \tag{4.4}$$

where we have assumed only one source time $t_0 = 0$. We now only need the quark propagator from the origin at time $t_0 = 0$ to all spatial sites $\boldsymbol{x}$ at time t. This drastically reduces the number of inversions that are required. These are referred to as point-to-all propagators.

[1] Note that the quark propagators also have color and spin indices, and we need to evaluate the Dirac matrix inverse elements for all these indices in addition to the spatial and temporal indices. Generally, we use a single compound index on the Dirac matrix to denote all the indices.

Unfortunately, calculations involving isoscalar mesons require more inversions than determined from point-to-all propagators, because these operators involve contractions on the same time slice (also known as internal loops or disconnected diagrams). Although we can still exploit translation invariance to fix the source operator at the origin, the sink operator must still be summed over all lattice sites. Thus, we need to evaluate the quark propagator from all spatial sites at the sink time to the same spatial site at the sink time for all desired sink times. In other words, we need the diagonal elements of the inverse of the Dirac matrix.

In Sec. 3.6 the necessity of two-hadron operators was emphasized along with the need for these operators to be constructed from single-hadron operators that individually have definite momentum. Thus, a typical two-hadron operator with total momentum zero is of the form

$$\mathcal{O}_1(\boldsymbol{p},t)\mathcal{O}_2(-\boldsymbol{p},t) = \frac{1}{V^2}\sum_{\boldsymbol{x},\boldsymbol{y}} \varphi_1(\boldsymbol{x},t)\varphi_2(\boldsymbol{y},t)e^{-i\boldsymbol{p}\cdot(\boldsymbol{x}-\boldsymbol{y})}. \tag{4.5}$$

With two-hadron operators of this form, it is impossible to use translation invariance to remove all the summations over the spatial sites on the source time slice for a temporal correlator. To circumvent this restriction, we could instead use localized multi-particle operators, which create particles that individually do not have definite momentum. A localized two-hadron operator at rest would have the form

$$(\mathcal{O}_1\mathcal{O}_2)(\boldsymbol{p}=\boldsymbol{0},t) = \frac{1}{V}\sum_{\boldsymbol{x}} \varphi_1(\boldsymbol{x},t)\varphi_2(\boldsymbol{x},t). \tag{4.6}$$

When these localized two-hadron operators are used in a temporal correlator the summation over all spatial sites on the source time slice can be removed via translation invariance. However, calculations have shown that these localized operators have significant excited state contamination as compared to two-hadron operators constructed from single-hadron operators of definite momentum and are thus undesirable (see Sec. 3.6.1).

Therefore, we are stuck with the need to calculate the quark propagator from all spatial sites on the source time slice to all spatial sites on the sink time slice, which we refer to as slice-to-slice quark propagators. Additionally, as with isoscalar mesons, the need for sink-to-sink and source-to-source quark propagators will arise for many two-hadron operators that involve disconnected diagrams as shown in Figure 4.1. Due to the significant computational

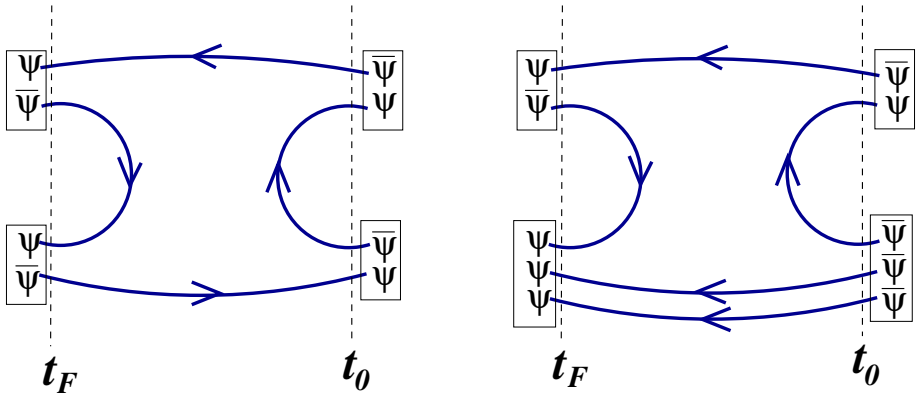

Figure 4.1: Two examples of the type of contractions needed for evaluating correlators of multi-hadron operators. These diagrams require slice-to-slice and sink-to-sink quark lines. Figure taken from Ref. [17].

efforts required for calculating inverse elements of such a large, albeit sparse, matrix, it has become essential to use more efficient methods. In this chapter we discuss the estimation of quark lines using diluted noise vectors in the LapH subspace. This is known as the stochastic LapH method [17], which is just the method we need to efficiently and accurately determine all the necessary quark lines.

We begin the description of the stochastic LapH method by discussing the so-called LapH subspace in Sec. 4.1, which is constructed from the lowest eigenmodes of the covariant Laplacian on each time slice; working in this subspace drastically reduces the number of inverse matrix elements that must be computed. Next, we show how to stochastically estimate the inverse of large matrices using Monte Carlo methods in Sec. 4.2; Then, in Sec. 4.2.1 it is shown how a reduction in variance can be achieved through the dilution of the noise vectors introduced by stochastic methods. Sec. 4.3 shows how to stochastically estimate quark lines with diluted noise vectors within the LapH subspace, followed by how estimates of quark sinks/sources are used to calculate temporal correlators in Sec. 4.4. Finally, Sec. 4.5 involves a brief discussion on the different dilution schemes we consider.

4.1 DISTILLATION AND THE LAPH SUBSPACE

The Dirac matrix is far too large to invert exactly for all but very small lattices. However, recall that we are interested in the low-lying spectrum and the reduction of the couplings of the higher lying modes to our operators was achieved by using smeared quark fields. The usefulness of LapH smearing to the evaluation of quark propagators was introduced in Ref. [50]. In that paper, the smearing operators considered—the so-called *distillation* operators—were constructed to have a rank $N \ll M$, where $M \equiv N_c N_s^3$, to be block-diagonal in time, and not act on the Dirac spin indices. These are projection operators from a vector space of dimension M to a vector space of dimension N. Therefore, if we choose to smear our quark fields with one of these distillation operators, then we need only evaluate quark propagators within the smaller vector space of dimension N as opposed to the full lattice vector space. It is important that the distillation operator is chosen such that as many symmetries of the quark fields remain intact. The LapH smearing matrix is an ideal candidate for such an operator, because it has the same symmetry properties of the covariant Laplacian (*e.g.* transforms as a scalar, is gauge covariant, invariant under parity and charge conjugation, *etc.*). The subspace that the quark fields are projected into by the LapH smearing operator—the so-called LapH subspace—is spanned by the N_v lowest eigenvectors of the covariant Laplacian on each time slice and copied for each Dirac spin index. These eigenvectors form the columns of the matrix $V_s \otimes I_4^d$ (*cf.* Eq. (3.27)).

Hence, when we include LapH smeared quark fields in our hadron operators, the Dirac matrix inverses are replaced with[2]

$$\mathcal{S} M^{-1} \mathcal{S} = V_s (V_s^\dagger M^{-1} V_s) V_s^\dagger, \tag{4.7}$$

using the definition of $\mathcal{S}$ in Eq. (3.27). Thus, we need only determine the elements of the matrix $V_s^\dagger M^{-1} V_s$, which is much smaller than M^{-1}. Now that we have a much smaller matrix to evaluate, we can consider the possibility of obtaining this matrix exactly.

[2]There is a slight abuse in notation here, because $V_s^\dagger$ has $N_s^3 N_t N_c$ columns and M^{-1} has $N_s^3 N_t N_c N_d$ rows, and thus these matrices cannot be multiplied as shown. This could be made more rigorous by replacing V_s with $V_s \otimes I_4^d$, but this notation quickly becomes cumbersome. Instead, it is to be understood that the spin indices remain on M^{-1} and are untouched by V_s. That is, with the indices explicit, $(V_s^\dagger M^{-1})(\alpha, l, t; \beta, b, \boldsymbol{x}, t_0) = V_s^\dagger(l, t; a, \boldsymbol{x}', t') M^{-1}(\alpha, a, \boldsymbol{x}', t'; \beta, b, \boldsymbol{x}, t_0)$, where l is the LapH eigenvector index, and all repeated indices are summed over. Therefore, $V_s^\dagger M^{-1} V_s$ is a $N_v N_t N_d \times N_v N_t N_d$ matrix.

The methods used for inverting a large matrix usually involve solving a collection of linear systems. If one wants to solve for the inverse exactly, then the number of linear systems that must be solved is equal to the dimension of the matrix. Therefore to solve for $V_s^\dagger M^{-1} V_s^\dagger$ exactly would require $N_v N_t N_d$ linear systems to be solved (inverted) on each gauge configuration and for each quark mass. Clearly, the feasibility of this method relies on the size of N_v, which can be shown to grow in proportion to the spatial volume of the lattice [17]. For instance, on our $24^3 \times 128$ and $32^3 \times 256$ lattices we found $N_v = 112$ and $N_v = 264$ levels below the σ_s^2 cutoff (*cf.* Sec. 3.2.2). Thus, the $32^3 \times 256$ requires over $270,000$ inversions per quark mass per gauge configuration, which is far beyond the available computing resources. Therefore, on all but a few small lattices, we need to seek alternative methods.

4.2 STOCHASTIC ESTIMATE OF MATRIX INVERSES

The Dirac matrix M is a large, but sparse, $N \times N$ matrix, where $N = N_s^3 N_t N_c N_d$ (N_s = number of spatial sites in each direction, N_t = number of temporal sites, N_c = number of colors, N_d = number of Dirac spin indices). For some of the larger lattices we use, where $N \sim 100$ million, finding, and even storing, the inverse of M exactly is impractical. Instead, we can perform a stochastic estimate of the inverse of M by introducing random noise vectors η and solving the linear system $MX = \eta$ for each noise vector generated. By choosing noise vectors such that their expected values are given by $E(\eta_i) = 0$ and $E(\eta_i \eta_j^*) = \delta_{ij}$, then

$$\begin{aligned} E(X_i \eta_j^*) &= E\Big(\sum_k M_{ik}^{-1} \eta_k \eta_j^* \Big) \\ &= \sum_k M_{ik}^{-1} E(\eta_k \eta_j^*) \\ &= \sum_k M_{ik}^{-1} \delta_{kj} \\ &= M_{ij}^{-1}. \end{aligned} \tag{4.8}$$

Therefore, by generating N_R random noise vectors, we can give an estimate of M_{ij}^{-1} by

$$M_{ij}^{-1} = \frac{1}{N_R}\sum_{r=1}^{N_R} X_i^{(r)}\eta_j^{(r)*} \pm \sqrt{\frac{V(X_i\eta_j^*)}{N_R}}, \qquad \text{where } MX^{(r)} = \eta^{(r)}, \tag{4.9}$$

where V stands for the variance. For large N_R, this estimate follows from the *law of large numbers*, and the error follows from the *central limit theorem*.

Notice that this approximation only becomes exact in the limit $N_R \to \infty$, yet it would only take N solutions to this linear system, using point sources, to find the inverse of M exactly. Thus, we would like a modification of this stochastic method that becomes exact as the number of solution vectors X calculated approaches N. Such a modification does exist and requires the generation of only one noise vector.

After generating a noise vector η, introduce the set of N noise vectors $\left\{\eta^{[s]}\right\}$ such that every component is equal to zero except the s-th component, which is equal to η_s. That is

$$\eta = \sum_{s=1}^{N} \eta^{[s]}, \qquad \text{where } \eta_j^{[s]} = \eta_j\delta_{js} \quad \text{(no sum over j)}. \tag{4.10}$$

This is an example of *diluting* a noise vector. Having only one non-zero component for each diluted noise vector is known as full dilution. Dilution will be discussed further in the next section.

Next, define the solution vectors $X^{[s]}$ such that

$$MX^{[s]} = \eta^{[s]}, \tag{4.11}$$

which can then be solved, yielding

$$\begin{aligned} X_j^{[s]} &= \sum_k M_{jk}^{-1}\eta_k^{[s]} \\ &= \sum_k M_{jk}^{-1}\eta_k\delta_{ks} \\ &= M_{js}^{-1}\eta_s. \end{aligned} \tag{4.12}$$

Then, we find

$$\begin{aligned}\sum_{s=1}^{N} X_i^{[s]}\eta_j^{[s]*} &= \sum_{s=1}^{N} M_{is}^{-1}\eta_s\eta_j^{[s]*} \\ &= \sum_{s=1}^{N} M_{is}^{-1}\eta_s\eta_j^{*}\delta_{js} \\ &= M_{ij}^{-1}\eta_j\eta_j^{*}, \qquad \text{(no sum over j)}.\end{aligned} \tag{4.13}$$

If we use random noise such that the variance of $\eta_i\eta_j^*$ is given by

$$V(\eta_i\eta_j^*) = 1 - \delta_{ij}, \tag{4.14}$$

then $\eta_j\eta_j^*$ is unity with zero variance, and Eq. (4.13) shows that M_{ij}^{-1} can be determined exactly with the generation of only one noise vector and the calculation of N solution vectors.[3] If it were feasible to calculate N solution vectors, then we would have no need for stochastic estimates and could determine the inverse exactly. All we have done is motivate a modification of our stochastic method that will reduce the error in our estimates.

4.2.1 Variance Reduction through Noise Dilution

We saw in the previous section that introducing a set of diluted noise vectors with only one non-zero component (known as full dilution) allowed for the exact computation of the inverse of M using stochastic estimation methods. This suggests that we may reduce the error in our estimate by introducing a set of diluted noise vectors with anywhere between one and N components chosen to be zero. We start by formalizing this procedure of noise dilution [58, 59] in order to investigate many different possible dilution schemes.

Let us introduce a set of $N \times N$ projection matrices $P^{[a]}$ with the following properties

$$P^{[a]}P^{[b]} = \delta^{ab}P^{[a]}, \qquad \sum_a P^{[a]} = 1, \qquad P^{[a]\dagger} = P^{[a]}. \tag{4.15}$$

Next, define the diluted noise vectors as

$$\eta_k^{[a]} = P_{kk'}^{[a]}\eta_{k'}, \qquad \eta_j^{[a]*} = \eta_{j'}^{*}P_{j'j}^{[a]} = P_{jj'}^{[a]*}\eta_{j'}^{*}, \tag{4.16}$$

[3] Unless otherwise stated, we will always assume that we've chosen noise vectors such that Eq. (4.14) holds.

where it can be seen that $\eta = \sum_a \eta^{[a]}$, as desired. Then, the solution vectors $X^{[a]}$ are defined in the usual way

$$M_{ik} X_k^{[a]} = \eta_i^{[a]}. \tag{4.17}$$

Using these definitions we find,

$$\begin{aligned}
E\Big(\sum_a X_i^{[a]} \eta_j^{[a]*}\Big) &= \sum_a E(X_i^{[a]} \eta_j^{[a]*}) \\
&= M_{ik}^{-1} \sum_a E(\eta_k^{[a]} \eta_j^{[a]*}) \\
&= M_{ik}^{-1} \sum_a E(P_{kk'}^{[a]} \eta_{k'} \ \eta_{j'}^* P_{j'j}^{[a]}) \\
&= M_{ik}^{-1} \sum_a P_{kk'}^{[a]} E(\eta_{k'} \eta_{j'}^*) P_{j'j}^{[a]} \\
&= M_{ik}^{-1} \sum_a P_{kk'}^{[a]} \delta_{k'j'} P_{j'j}^{[a]} \\
&= M_{ik}^{-1} \sum_a P_{kk'}^{[a]} P_{k'j}^{[a]} \\
&= M_{ik}^{-1} \sum_a P_{kj}^{[a]} \\
&= M_{ik}^{-1} \delta_{kj} \\
&= M_{ij}^{-1},
\end{aligned} \tag{4.18}$$

which allows us to estimate the Dirac inverse by generating N_R noise vectors as follows

$$M_{ij}^{-1} = \frac{1}{N_R} \sum_{r=1}^{N_R} \sum_a X_i^{(r)[a]} \eta_j^{(r)[a]*} \pm \sqrt{\frac{V\big(\sum_a X_i^{[a]} \eta_j^{[a]*}\big)}{N_R}}. \tag{4.19}$$

If we choose the set of projection matrices $P^{[a]}$ such that each has only one non-zero element along the diagonal, then we recover the result in Eq. (4.13) by using only one noise vector, which again is referred to as full dilution. But, as was stated above, using full dilution is computationally infeasible on large lattices.

Even if we do not use full dilution, it can be seen that there is an improvement in the variance. One way to see this is by comparing Eqs. (4.8) and (4.18), which shows that diluting the noise vectors involves the following replacement in the determination of M^{-1},

$$\sum_k M_{ik}^{-1} E(\eta_k \eta_j^*) \to \sum_k M_{ik}^{-1} \sum_a E(\eta_k^{[a]} \eta_j^{[a]*}). \tag{4.20}$$

Many of the components of the diluted noise vectors are exactly zero, thus $V(\eta_k^{[a]}\eta_j^{[a]*})$ is zero when either $\eta_k^{[a]}$ or $\eta_j^{[a]}$ is exactly zero. This will never happen for $V(\eta_k\eta_j^*)$, which obeys Eq. (4.14), since neither η_k nor η_j will ever be exactly zero.

4.3 STOCHASTIC ESTIMATE OF QUARK LINES IN THE LAPH SUBSPACE

Our basic building blocks are gauge-covariantly displaced LapH-smeared quark fields. Additionally, the barred quark fields are defined with a γ_4 in order to ensure a Hermitian temporal correlator matrix. Therefore, we are not after the quark propagators directly, which are the inverse matrix elements of the Dirac matrix. Instead, we seek to calculate quark lines defined by

$$\mathcal{Q} = D^{(j)}\mathcal{S}\Omega^{-1}\mathcal{S}D^{(k)\dagger}, \tag{4.21}$$

where $D^{(i)}$ is a displacement operator of type i, and the γ_4 from the barred quark field has been absorbed into $\Omega \equiv \gamma_4 M$. Because our quark fields are LapH smeared, we are able to exploit this by inserting noise vectors only in the LapH subspace, which should produce less error in our final results, as can be seen from Figure 4.2. This is achieved by inserting the noise and dilution projectors in between the rightmost V_s and $V_s^\dagger$ that are used in the definition of $\mathcal{S}$. The noise vectors are denoted by ρ,[4] to distinguish them from the noise vectors used in the full lattice space. As usual, we assume the components are random Z_N noise such that $E(\rho) = 0$ and $E(\rho\rho^\dagger) = I$,[5] and we assume the projection matrices also live only in the LapH subspace.

Now, we move on to how we actually estimate these quark lines stochastically using noise generated within the LapH subspace. Starting from Eq. (4.21), we can insert the noise

[4]Keep in mind that the compound index for these noise vectors in the LapH subspace have spin, time, and Laplacian eigenmode number.

[5]We have now transitioned to a vector notation, rather than including indices on the noise vectors. Therefore, $\rho\rho^\dagger$ is in fact an outer product.

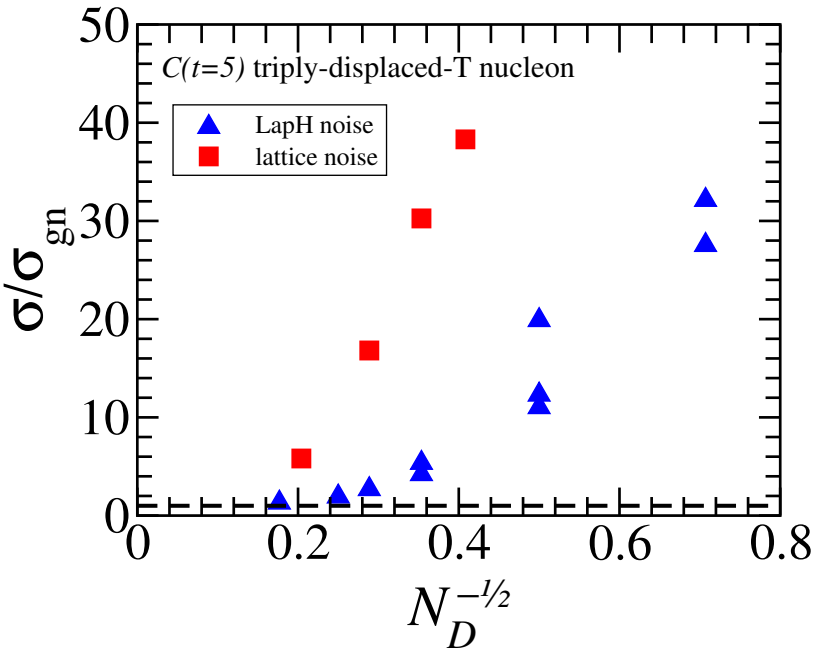

Figure 4.2: The error from the calculation of a correlator $C(t = 5)$ of a TDT nucleon operator on a $16^3 \times 128$ lattice. The error is shown as a ratio over σ_{gn}, which is the error from calculating the correlator exactly; This error arises solely from the gauge configurations, hence the gauge noise (*i.e.* gn). N_D is the number of inversions that were calculated. We see a significant reduction in the error when considering LapH noise vectors. Figure taken from Ref. [17].

vectors as follows,

$$\begin{aligned}
\mathcal{Q} &= D^{(j)}\mathcal{S}\Omega^{-1}\mathcal{S}D^{(k)\dagger} \\
&= D^{(j)}\mathcal{S}\Omega^{-1}V_s V_s^\dagger D^{(k)\dagger} \\
&= \sum_a D^{(j)}\mathcal{S}\Omega^{-1}V_s P^{[a]}P^{[a]\dagger}V_s^\dagger D^{(k)\dagger} \\
&= \sum_a D^{(j)}\mathcal{S}\Omega^{-1}V_s P^{[a]}E(\rho\rho^\dagger)P^{[a]\dagger}V_s^\dagger D^{(k)\dagger} \\
&= \sum_a E(D^{(j)}\mathcal{S}\Omega^{-1}V_s P^{[a]}\rho(D^{(k)}V_s P^{[a]}\rho)^\dagger).
\end{aligned} \tag{4.22}$$

Notice that the quark line has factorized quite nicely. This suggests we should define the

displaced-smeared-diluted quark-source and quark-sink vectors as

$$\varrho_{b\beta k}^{(r)[A_d]}(\boldsymbol{x}, t|U) \equiv \left(D^{(k)} V_s P^{[A_d]} \rho^{(r)}\right)_{b\beta}(\boldsymbol{x}, t|U), \tag{4.23a}$$

$$\varphi_{a\alpha j}^{(r)[A_d]}(\boldsymbol{x}, t|U) \equiv \left(D^{(j)} \mathcal{S}\Omega^{-1} V_s P^{[A_d]} \rho^{(r)}\right)_{a\alpha}(\boldsymbol{x}, t|U), \tag{4.23b}$$

respectively. We use A_d to denote the dilution index (where we had used a previously) to avoid confusion with the color indices, r labels the noise vector, and U represents a particular gauge configuration. Then, we can obtain an estimate for the quark line with

$$\mathcal{Q}_{ij}^{AB}(\boldsymbol{x}, t; \boldsymbol{x}_0, t_0) \approx \frac{1}{N_R} \delta_{AB} \sum_{r=1}^{N_R} \sum_{A_d} \varphi_i^{(r)[A_d]}(\boldsymbol{x}, t) \varrho_j^{(r)[A_d]}(\boldsymbol{x}_0, t_0)^*, \tag{4.24}$$

where A, B are the flavors for the source and sink fields; and the color, spin, displacement type, and gauge configuration dependence have all been compounded into a single latin index.

As has been emphasized earlier, we need these quark line estimates for same time (sink-to-sink and source-to-source) quark propagation on essentially every time slice (these are also referred to as relative quark lines), and this effectively requires some sort of temporal dilution scheme for these quark lines. On the other hand, there are many cases where we need quark line estimates from a source time t_0 to a sink time t, and we can get away with only considering the quark line starting on a manageable set of source times (these are referred to as slice-to-slice or fixed quark lines), which allows us to exploit full time dilution. However, since mesons are made of a quark and an antiquark, then for the contraction shown on the left in Figure 4.3, one quark line begins on the meson source time and ends on the meson sink time, whereas the other quark line begins on the meson sink time and ends on the meson source time.[6] But, we want to be able to use only a handful of source times for

[6] A word of caution: the hadron source/sink times are to be differentiated from the quark line source/sink times. Every quark line begins at a source time and ends at a sink time. And every correlator contains a hadron operator at a source time and a hadron operator at a sink time. The source time for a quark line can be the sink time for a hadron operator (as is the case for one of the quark lines in the contractions shown on the left in Figure 4.3). Or, the quark source/sink time could be the same time (as is the case for the contractions shown on the right in Figure 4.3). When a qualifier for the souce/sink time is not given, it is assumed to be referring to the hadron operator source/sink time.

the quark lines, and to avoid this issue, we can reverse the quark line starting on the meson sink time. This can be done, because an equivalent estimate for the quark line is given by

$$\mathcal{Q}_{ij}^{AB}(\boldsymbol{x}_0, t_0; \boldsymbol{x}, t) \approx \frac{1}{N_R}\delta_{AB}\sum_{r=1}^{N_R}\sum_{A_d}\bar{\varrho}_i^{(r)[A_d]}(\boldsymbol{x}_0, t_0)\bar{\varphi}_j^{(r)[A_d]}(\boldsymbol{x}, t)^*, \tag{4.25}$$

where we have used γ_5-Hermiticity of the Dirac matrix (*i.e.* $M^\dagger = \gamma_5 M \gamma_5$), and we define

$$\bar{\varrho} = -\gamma_5\gamma_4\varrho, \qquad \bar{\varphi} = \gamma_5\gamma_4\varphi. \tag{4.26}$$

4.4 TEMPORAL CORRELATORS

In this section we describe how we use the quark sinks/sources described in Sec. 4.3 to evaluate correlation functions involving meson operators. Generalizations to other correlation functions are straightforward (see Ref. [17] for details on baryon correlation functions). At this point it may seem that our task at hand is straightforward in the sense that once we have estimated the needed quark lines, then the final correlator is just a summation of simple products of these quark lines. However, products of stochastically estimated values can introduce a bias. For example, if a random variable has an expected value of zero, then a Monte Carlo estimate for this quantity will give a value close to zero. If we then use the product of this variable with itself, we will necessarily obtain a positive quantity, and this clearly introduces a bias towards positive values for this product. Hence, we do not use estimates of the quark lines directly, but instead we express our correlators in terms of the quark sinks and quark sources before taking the sums over the dilution indices and noise vectors.

4.4.1 Meson Temporal Correlators

First, recall from Sec. 3.3.3 that our meson annihilation and creation operators are of the form

$$M_l(t) = c^{(l)}_{\alpha\beta}\Phi^{AB}_{\alpha\beta}(\boldsymbol{p},t), \tag{4.27a}$$

$$\overline{M}_l(t) = c^{(l)*}_{\alpha\beta}\overline{\Phi}^{AB}_{\alpha\beta}(\boldsymbol{p},t), \tag{4.27b}$$

respectively, where the elemental meson annihilation and creation operators are of the form

$$\Phi^{AB}_{\alpha\beta}(\boldsymbol{p},t) = \sum_{\boldsymbol{x}} e^{-i\boldsymbol{p}\cdot(\boldsymbol{x}+\frac{1}{2}(\boldsymbol{d}_\alpha+\boldsymbol{d}_\beta))}\delta_{ab}\overline{q}^A_{a\alpha}(\boldsymbol{x},t)q^B_{b\beta}(\boldsymbol{x},t), \tag{4.28a}$$

$$\overline{\Phi}^{AB}_{\alpha\beta}(\boldsymbol{p},t) = \sum_{\boldsymbol{x}} e^{i\boldsymbol{p}\cdot(\boldsymbol{x}+\frac{1}{2}(\boldsymbol{d}_\alpha+\boldsymbol{d}_\beta))}\delta_{ab}\overline{q}^B_{b\beta}(\boldsymbol{x},t)q^A_{a\alpha}(\boldsymbol{x},t), \tag{4.28b}$$

respectively. Then, a meson-to-meson correlation function is given by (following Ref. [17])

$$\begin{aligned} C_{l\bar{l}}(t-t_0) &= \frac{1}{N_t}\sum_{t_0}\langle M_l(t)\overline{M}_{\bar{l}}(t_0)\rangle \\ &= \langle M_l(t)\overline{M}_{\bar{l}}(t_0)\rangle \\ &= c^{(l)}_{\alpha\beta}c^{(\bar{l})*}_{\bar{\alpha}\bar{\beta}}\,\langle\Phi^{AB}_{\alpha\beta}(t)\overline{\Phi}^{\bar{A}\bar{B}}_{\bar{\alpha}\bar{\beta}}(t_0)\rangle \\ &= c^{(l)}_{\alpha\beta}c^{(\bar{l})*}_{\bar{\alpha}\bar{\beta}}\sum_{\boldsymbol{x}\bar{\boldsymbol{x}}} e^{-i\boldsymbol{p}\cdot(\boldsymbol{x}+\frac{1}{2}(\boldsymbol{d}_\alpha+\boldsymbol{d}_\beta))}e^{i\boldsymbol{p}\cdot(\bar{\boldsymbol{x}}+\frac{1}{2}(\boldsymbol{d}_{\bar{\alpha}}+\boldsymbol{d}_{\bar{\beta}}))} \\ &\qquad\times\langle\overline{q}^A_{a\alpha}(\boldsymbol{x},t)q^B_{a\beta}(\boldsymbol{x},t)\overline{q}^{\bar{B}}_{\bar{a}\bar{\beta}}(\bar{\boldsymbol{x}},t_0)q^{\bar{A}}_{\bar{a}\bar{\alpha}}(\bar{\boldsymbol{x}},t_0)\rangle\,, \end{aligned} \tag{4.29}$$

where time translation invariance was used in the 2nd line. Next, we perform the path integral over the quark fields to obtain

$$\begin{aligned} C_{l\bar{l}}(t-t_0) = c^{(l)}_{\alpha\beta}c^{(\bar{l})*}_{\bar{\alpha}\bar{\beta}}\sum_{\boldsymbol{x}\bar{\boldsymbol{x}}} e^{-i\boldsymbol{p}\cdot(\boldsymbol{x}+\frac{1}{2}(\boldsymbol{d}_\alpha+\boldsymbol{d}_\beta))}e^{i\boldsymbol{p}\cdot(\bar{\boldsymbol{x}}+\frac{1}{2}(\boldsymbol{d}_{\bar{\alpha}}+\boldsymbol{d}_{\bar{\beta}}))} \\ \times\langle-\mathcal{Q}^{\bar{A}A}_{\bar{a}\bar{\alpha};a\alpha}\mathcal{Q}^{B\bar{B}}_{a\beta;\bar{a}\bar{\beta}}+\mathcal{Q}^{BA}_{a\beta;a\alpha}\mathcal{Q}^{\bar{A}\bar{B}}_{\bar{a}\bar{\alpha};\bar{a}\bar{\beta}}\rangle_U\,, \end{aligned} \tag{4.30}$$

where we have suppressed the explicit space, time, and gauge configuration labels from the quark lines, and $\langle\rangle_U$ refers to an average over all gauge configurations. Note that the two terms being summed in Eq. (4.30) come from the two possible Wick contractions. This is expressed diagrammatically in Figure 4.3. We then proceed to write the correlator in terms

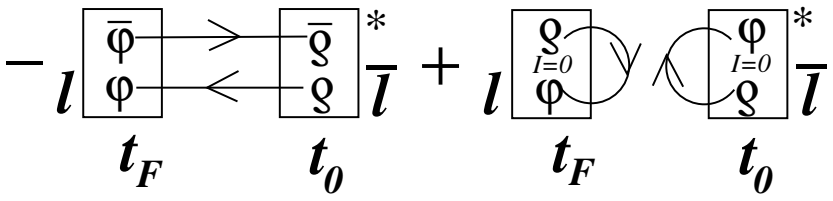

Figure 4.3: A diagrammatic representation of the quark sinks/sources required in the meson sinks/sources for a meson-to-meson correlation function. Figure taken from Ref. [17].

of the quark sinks/sources, but in order to simplify the expressions we introduce a meson function defined by

$$\mathcal{M}^{[A_1A_2]}(\varrho_1,\varphi_2;t) \equiv c^{(l)}_{\alpha\beta}\sum_{\boldsymbol{x}} e^{-i\boldsymbol{p}\cdot(\boldsymbol{x}+\frac{1}{2}(\boldsymbol{d}_\alpha+\boldsymbol{d}_\beta))}\varrho^{(1)[A_1]}_{a\alpha}(\boldsymbol{x},t)^*\varphi^{(2)[A_2]}_{a\beta}(\boldsymbol{x},t), \tag{4.31}$$

where the superscript (i) on ϱ and φ refers to the particular noise vector being used,[7] A_i refers to the dilution indices, and the dependence on the gauge configuration is once again suppressed.

Then, finally, we can write the temporal correlator as

$$\begin{aligned} C_{l\bar{l}}(t-t_0) = \langle &-\delta_{\bar{A}A}\delta_{B\bar{B}}\mathcal{M}^{[A_1A_2]}_l(\bar{\varphi}_1,\varphi_2;t)\mathcal{M}^{[A_1A_2]}_{\bar{l}}(\bar{\varrho}_1,\varrho_2;t_0)^* \\ &+\delta_{AB}\delta_{\bar{A}\bar{B}}\mathcal{M}^{[A_1A_1]}_l(\varrho_1,\varphi_1;t)\mathcal{M}^{[A_2A_2]}_{\bar{l}}(\varphi_2,\varrho_2;t_0)^*\rangle_{U,\rho}, \end{aligned} \tag{4.32}$$

where $\langle\rangle_{U,\rho}$ denotes a summation over all gauge configurations and noise vectors, and a summation over all dilution indices. There are two things to take from this final result: 1) the correlator for each gauge configuration, noise vector, and set of dilution indices factorizes into two functions, one of which is defined on the source time t_0 and the other defined on the sink time t; and 2) the correlator can be represented diagrammatically as seen in Figure 4.3, where each box corresponds to a particular meson function. The meson functions at the source time t_0 are referred to as meson sources, and the meson functions at the sink time t are referred to as meson sinks. The major advantage of this factorization, is that we can

[7] The quark sink and source connected by a quark line must be using the same noise vector, and different quark lines must use different noise vectors in order to avoid any introduction of a bias

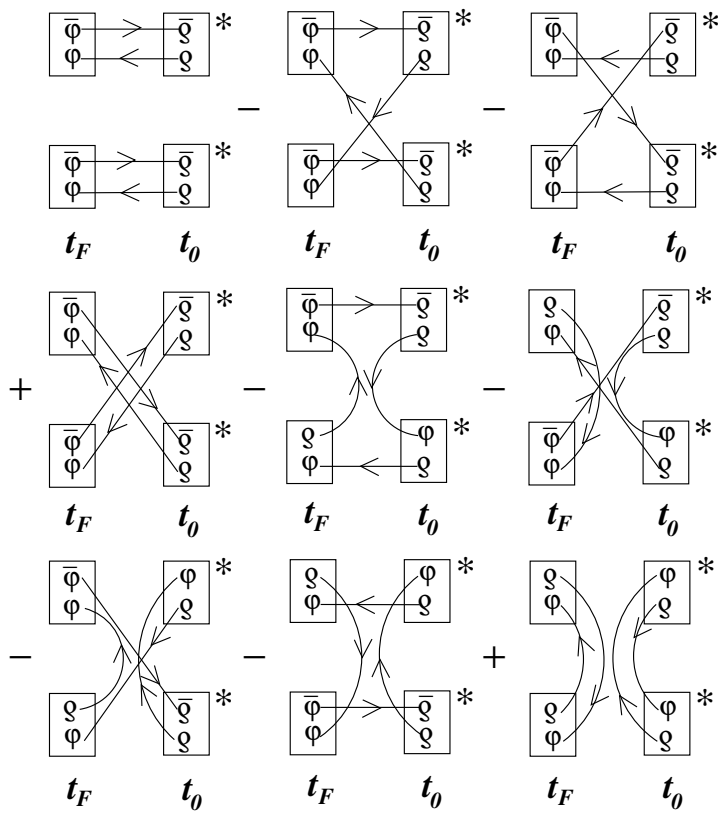

Figure 4.4: A diagrammatic representation of the quark sinks/sources required in the meson sinks/sources for a two-meson to two-meson correlation function. Figure taken from Ref. [17].

easily construct a large set of meson sources/sinks, and then tie them together as needed to form the final correlator.

4.4.2 Multi-Hadron Correlators

Based on the diagrammatic representation of our correlation functions, generalizations to correlators involving multi-hadron operators are quite simple. We need only determine the appropriate diagrams for these more complicated correlators, and then the expressions can be written down immediately. For the case of a two-meson to two-meson correlator, the diagrammatic representation of the correlator is shown in Figure 4.4.

4.5 DILUTION SCHEMES

We end this chapter with a discussion on the different dilution schemes we considered. The dilution projectors live in the LapH subspace, and therefore their index will be treated as a compound index $A = (A_T, A_s, A_L)$, where A_T is dilution index in time, A_s is the dilution index in spin, and A_L is the dilution index in LapH eigenvector mode. Hence, our dilution projectors can be written as

$$P^{[A]}_{t\alpha l;t'\alpha' l'} = P^{[A_T]}_{tt'} P^{[A_s]}_{\alpha\alpha'} P^{[A_L]}_{ll'}. \tag{4.33}$$

The dilution schemes we consider are [17]:

$$P^{[A]}_{ij} = \delta_{ij}, \qquad A = 0, \qquad \text{(no dilution)} \tag{4.34a}$$

$$P^{[A]}_{ij} = \delta_{ij}\delta_{Ai}, \qquad A = 0, \ldots, N-1, \qquad \text{(full dilution)} \tag{4.34b}$$

$$P^{[A]}_{ij} = \delta_{ij}\delta_{A\lfloor Ji/N \rfloor}, \qquad A = 0, \ldots, J-1, \qquad \text{(block-}J\text{)} \tag{4.34c}$$

$$P^{[A]}_{ij} = \delta_{ij}\delta_{A,\, i \bmod J}, \qquad A = 0, \ldots, J-1, \qquad \text{(interlace-}J\text{)} \tag{4.34d}$$

where N is the size of the space being considered (*i.e.* $N = N_t$ for time dilution, $N = N_d = 4$ for spin dilution, and $N = N_v$ for LapH eigenvector dilution). The particular dilution schemes chosen for this work are specified in Ref. [17] where explicit comparisons are made between the different schemes on a 16^3 and 20^3 lattice.

5.0 TETRAQUARK OPERATORS

In this chapter we present an extension of the methods discussed so far to the construction of tetraquark operators. We find that every tetraquark operator can be written in terms of linear combinations of two separate meson-like operators. These differ slightly from the two-meson operators we constructed in Chap. 3, because the separate gauge invariant parts of these tetraquark operators are not constructed to transform irreducibly under any particular symmetry operation. It is only the entire tetraquark operator that must transform irreducibly. We then present the two linearly independent tetraquark operators based on the meson-meson-like operators from which all other tetraquark operators are constructed.

5.1 COLOR STRUCTURE

The color structure for a tetraquark operator is dictated by gauge invariance. Since quarks and antiquarks transform in the $\mathbf{3}$ and $\overline{\mathbf{3}}$ representations of $SU_c(3)$, we consider the different ways of combining four of these representations:

$$\mathbf{3} \otimes \mathbf{3} \otimes \mathbf{3} \otimes \mathbf{3} = \mathbf{15} \oplus \mathbf{15} \oplus \mathbf{15} \oplus \mathbf{15} \oplus \overline{\mathbf{6}} \oplus \overline{\mathbf{6}} \oplus \mathbf{3} \oplus \mathbf{3} \oplus \mathbf{3}, \tag{5.1a}$$

$$\mathbf{3} \otimes \mathbf{3} \otimes \mathbf{3} \otimes \overline{\mathbf{3}} = \mathbf{24} \oplus \overline{\mathbf{15}} \oplus \overline{\mathbf{15}} \oplus \mathbf{6} \oplus \mathbf{6} \oplus \mathbf{6} \oplus \overline{\mathbf{3}} \oplus \overline{\mathbf{3}} \oplus \overline{\mathbf{3}}, \tag{5.1b}$$

$$\mathbf{3} \otimes \mathbf{3} \otimes \overline{\mathbf{3}} \otimes \overline{\mathbf{3}} = \mathbf{27} \oplus \overline{\mathbf{10}} \oplus \mathbf{10} \oplus \mathbf{8} \oplus \mathbf{8} \oplus \mathbf{8} \oplus \mathbf{8} \oplus \mathbf{1} \oplus \mathbf{1}. \tag{5.1c}$$

From these decompositions, we see that the only gauge invariant four quark hadron must be made of two quarks and two antiquarks. We also see that there exists two independent ways to construct a gauge invariant object. Let p, q, r, and s denote color vectors that transform

in the **3**-dimensional representation (**3** vectors). Then, $p^\dagger$, $q^\dagger$, $r^\dagger$, and $r^\dagger$ transform in the $\overline{\mathbf{3}}$-dimensional representation ($\overline{\mathbf{3}}$ vectors). That is, under a local gauge transformation, these color vectors transform as

$$p_a(x) \to \Omega_{aa'}(x) p_{a'}(x), \tag{5.2a}$$

$$p_a^*(x) \to \left(\Omega_{aa'}(x) p_{a'}(x)\right)^* = p_{a'}^*(x) \Omega_{a'a}^\dagger(x), \tag{5.2b}$$

where $\Omega(x)$ is an $SU(3)$ matrix. A color singlet can easily be constructed from contracting a color vector in the **3**-dimensional irrep with a color vector in the $\overline{\mathbf{3}}$-dimensional irrep:

$$\begin{aligned} p_a^*(x) q_a(x) &\to p_{a'}^*(x) \Omega_{a'a}^\dagger(x) \Omega_{aa''}(x) q_{a''}(x) \\ &= p_{a'}^*(x) \delta_{a'a''} q_{a''}(x) \\ &= p_a^*(x) q_a(x), \end{aligned} \tag{5.3}$$

where we have used the unitarity of $\Omega(x)$. This contraction forms the basis for a meson operator. From this result it easy to see that the following linearly independent combinations

$$T_S = (\delta_{ac}\delta_{bd} + \delta_{ad}\delta_{bc}) p_a^*(x) q_b^*(x) r_c(x) s_d(x), \tag{5.4a}$$

$$T_A = (\delta_{ac}\delta_{bd} - \delta_{ad}\delta_{bc}) p_a^*(x) q_b^*(x) r_c(x) s_d(x), \tag{5.4b}$$

are gauge invariant. Thus we have found the two independent gauge invariant combinations expected from the decomposition in Eq. (5.1c). Note that T_S and T_A are simply linear combinations of products of meson-like operators. However, these differ slightly from the two-meson operators described in Chap. 3, because the individual gauge-invariant pieces in Eq. (5.4) are not required to transform irreducibly under any symmetry operation other than gauge symmetry. The final tetraquark operators are, of course, made to transform irreducibly under all appropriate symmetry groups. Regardless, we still expect these operators to have some overlap onto the two-meson states created by our two-meson operators.

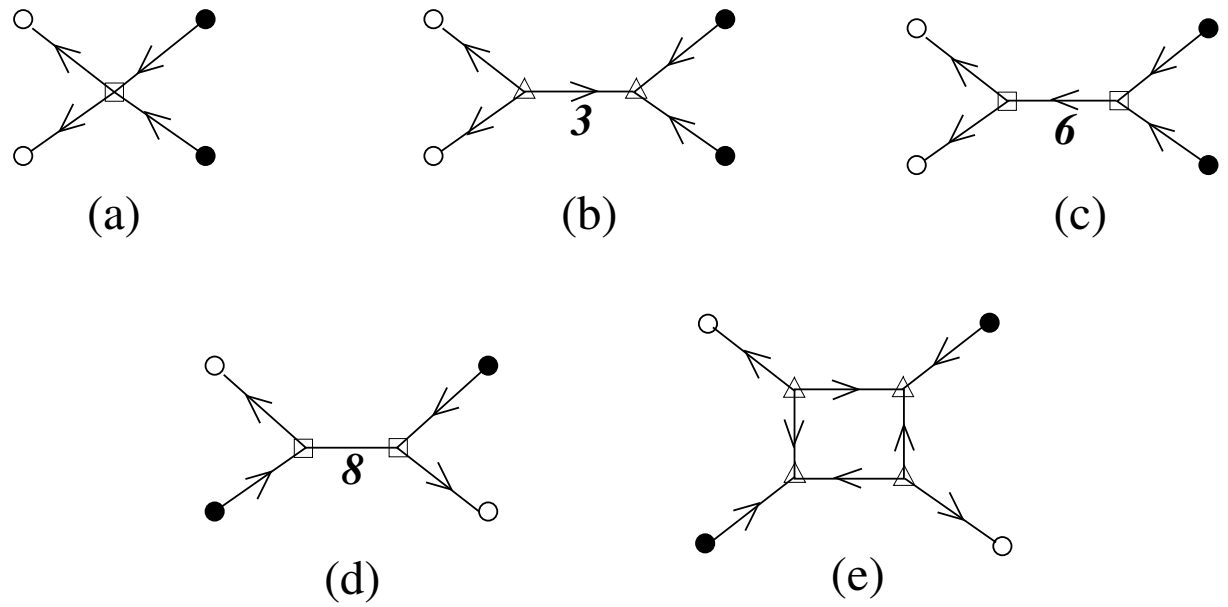

Figure 5.1: The possible tetraquark operators with displacements that we consider. The triangles denote a Levi-Civita coupling, and the squares denote the appropriate Clebsch-Gordan coupling.

5.1.1 More Complicated Color Structure

Here we investigate the possibility of more complicated color structure emerging from the inclusion of gauge links. A quark field has the same structure and transformation properties regardless of its displacement. Thus, the operator shown in Figure 5.1(a) does not give us a new object. But, gauge links can be included in more complicated ways other than simply displacing single quarks, as can be seen in (b), (c), (d), and (e) of Figure 5.1. It is not immediately clear if the different color structures shown in Figure 5.1 can be related in any way. Thus, our goal now is to find any relationships among these different operators.

We begin by considering a diquark-diquark model for the tetraquarks.[1] The possible diquarks can be determined by performing the direct products between pairs of $\mathbf{3}$ and $\overline{\mathbf{3}}$

[1]In the literature, the phrase diquark is generally reserved for two quarks which form an object that transforms in the $\overline{\mathbf{3}}$ representation. Here, we generally refer to any pair of quarks/antiquarks that transforms in some irreducible representation of $SU_c(3)$ as a diquark.

vectors

$$\mathbf{3} \otimes \mathbf{3} = \mathbf{6} \oplus \overline{\mathbf{3}}, \tag{5.5a}$$

$$\overline{\mathbf{3}} \otimes \overline{\mathbf{3}} = \overline{\mathbf{6}} \oplus \mathbf{3}, \tag{5.5b}$$

$$\mathbf{3} \otimes \overline{\mathbf{3}} = \mathbf{8} \oplus \mathbf{1}. \tag{5.5c}$$

Hence, we can construct diquarks transforming in the $\mathbf{8}$, $\mathbf{6}$, $\overline{\mathbf{6}}$, $\mathbf{3}$, or $\overline{\mathbf{3}}$ dimensional representations (the $\mathbf{1}$ representation corresponds to a meson and thus has already been considered above). These diquarks can be written in terms of our basic building blocks (*i.e.* covariantly-displaced LapH-smeared quark fields) in the following way

$$d^{(\overline{3})}_{\alpha}(x) = -\overline{d}^{(3)}_{\alpha}(x) = q^{A}_{a}(x) q^{B}_{b}(x) C(3a; 3b|\overline{3}\alpha), \tag{5.6a}$$

$$d^{(6)}_{\alpha}(x) = -\overline{d}^{(\overline{6})}_{\alpha}(x) = q^{A}_{a}(x) a^{B}_{b}(x) C(3a; 3b|6\alpha), \tag{5.6b}$$

$$d^{(8)}_{\alpha}(x) = \overline{q}^{A}_{a}(x) q^{B}_{b}(x) C(\overline{3}a; 3b|8\alpha), \tag{5.6c}$$

where the C's are the Clebsch-Gordan coefficients shown in Table 5.1, which were determined from the algorithm described in Ref. [60].

Next, we need to see which diquarks can be combined to form a gauge-invariant object. This can again be determined from the direct product decompositions. The only combinations that produce color singlets are

$$\mathbf{3} \otimes \overline{\mathbf{3}} = \mathbf{8} \oplus \mathbf{1}, \tag{5.7a}$$

$$\mathbf{6} \otimes \overline{\mathbf{6}} = \mathbf{27} \oplus \mathbf{8} \oplus \mathbf{1}, \tag{5.7b}$$

$$\mathbf{8} \otimes \mathbf{8} = \mathbf{27} \oplus \overline{\mathbf{10}} \oplus \mathbf{10} \oplus \mathbf{8} \oplus \mathbf{8} \oplus \mathbf{1}. \tag{5.7c}$$

These operators are shown in (b), (c), and (d) of Figure 5.1, respectively.

Now we consider the tetraquark operator formed from diquarks in the $\mathbf{3}$ and $\overline{\mathbf{3}}$ representations, where one of the diquarks is displaced by a gauge link in the $\overline{\mathbf{3}}$ representation

$$\overline{d}^{(\overline{3})}_{\alpha}(x)\ U^{(\overline{3})}_{\mu;\alpha\beta}(x)\ d^{(\overline{3})}_{\beta}(x+\hat{\mu}). \tag{5.8}$$

Table 5.1: The $SU(3)$ Clebsch-Gordan coefficients used for constructing different color structures for tetraquarks. All omitted coefficients are zero. These were computed using the algorithm from Ref. [60].

a	b	α	$C(3a;3b\|\overline{3}\alpha)$
2	3	1	$1/\sqrt{2}$
3	2	1	$-1/\sqrt{2}$
1	3	2	$-1/\sqrt{2}$
3	1	2	$1/\sqrt{2}$
1	2	3	$1/\sqrt{2}$
2	1	3	$-1/\sqrt{2}$

a	b	α	$C(3a;3b\|6\alpha)$
1	1	1	1
2	2	2	1
3	3	3	1
1	2	4	$1/\sqrt{2}$
2	1	4	$1/\sqrt{2}$
2	3	5	$1/\sqrt{2}$
3	2	5	$1/\sqrt{2}$
1	3	6	$1/\sqrt{2}$
3	1	6	$1/\sqrt{2}$

a	b	α	$C(\overline{3}a;3b\|8\alpha)$
1	2	1	$1/\sqrt{2}$
2	1	1	$1/\sqrt{2}$
1	2	2	$-1/\sqrt{2}$
2	1	2	$1/\sqrt{2}$
1	1	3	$1/\sqrt{2}$
2	2	3	$-1/\sqrt{2}$
1	3	4	$1/\sqrt{2}$
3	1	4	$1/\sqrt{2}$
1	3	5	$-1/\sqrt{2}$
3	1	5	$1/\sqrt{2}$
2	3	6	$1/\sqrt{2}$
3	2	6	$1/\sqrt{2}$
2	3	7	$-1/\sqrt{2}$
3	2	7	$1/\sqrt{2}$
1	1	8	$-1/\sqrt{6}$
2	2	8	$-1/\sqrt{6}$
3	3	8	$\sqrt{2/3}$

This operator is as simple as possible without any loss of generality, because the individual quark displacements do not affect the color structure, and we need only consider displacing one of the diquarks (displacing two of the diquarks can always be written in terms of a displacement of just one of the diquarks). For simplicity in what follows, we remove the spatial dependence. Then, we can write this operator as

$$\begin{aligned}
\overline{d}^{(\overline{3})}_{\alpha}\ U^{(\overline{3})}_{\alpha\beta}\ d^{(\overline{3})}_{\beta} &= \overline{q}^{C}_{a}\overline{q}^{D}_{b}\ C(3a;3b|\overline{3}\alpha)U^{(\overline{3})}_{\alpha\beta}\ q^{A}_{a'}q^{B}_{b'}\ C(3a';3b'|\overline{3}\beta) \\
&= \overline{q}^{C}_{a}\overline{q}^{D}_{b}\ C(3a;3b|\overline{3}\alpha)U_{cc'}U_{dd'}\ C(3c;3d|\overline{3}\alpha)C(3c';3d'|\overline{3}\beta)\ q^{A}_{a'}q^{B}_{b'}\ C(3a';3b'|\overline{3}\beta) \\
&= \frac{1}{4}\overline{q}^{C}_{a}\overline{q}^{D}_{b}\ U_{cc'}U_{dd'}\ q^{A}_{a'}q^{B}_{b'}\ (\delta_{ac}\delta_{bd}-\delta_{bc}\delta_{ad})(\delta_{a'c'}\delta_{b'd'}-\delta_{b'c'}\delta_{a'd'}) \\
&= \frac{1}{2}\overline{q}^{C}_{a}U_{aa'}q^{A}_{a'}\ \overline{q}^{D}_{b}U_{bb'}q^{B}_{b'}-\frac{1}{2}\overline{q}^{C}_{a}U_{ab'}q^{B}_{b'}\ \overline{q}^{D}_{b}\ U_{ba'}q^{A}_{a'},
\end{aligned} \tag{5.9}$$

where in the second line we used the identity

$$U^{\overline{3}}_{\alpha\alpha'}=U^{*}_{\alpha\alpha'}=U_{aa'}U_{bb'}\ C(3a;3b|\overline{3}\alpha)C(3a';3b'|\overline{3}\alpha'), \tag{5.10}$$

and in the third line we used the identity

$$C(3a';3b'|\overline{3}\alpha')C(3c;3d|\overline{3}\alpha')=\frac{1}{2}(\delta_{a'c}\delta_{b'd}-\delta_{b'c}\delta_{a'd}). \tag{5.11}$$

Thus, we see that this tetraquark operator is a linear combination of meson-meson-like operators. Notice that Eq. (5.10) relates the gauge links in the $\overline{\mathbf{3}}$ representation $U^{(\overline{3})}$ to the original gauge links U, which are in the $\mathbf{3}$ representation. This is an important identity that is generalized to other representations.

Next, we consider the tetraquark formed from diquarks in the $\mathbf{6}$ and $\overline{\mathbf{6}}$ representations, where one of the diquarks is displaced by a gauge link in the $\mathbf{6}$ representation

$$\overline{d}^{(6)}_{\alpha}(x)\ U^{(6)}_{\mu;\alpha\beta}(x)\ d^{(6)}_{\beta}(x+\mu). \tag{5.12}$$

Again, this operator has no loss of generality, and we suppress the spatial dependence. Then, similarly as before, we find

$$\begin{aligned}
\overline{d}^{(6)}_{\alpha}\ U^{(6)}_{\alpha\beta}\ d^{(6)}_{\beta} &= \overline{q}^{C}_{a}\overline{q}^{D}_{b}\ C(3a;3b|6\alpha)U^{(6)}_{\alpha\beta}\ q^{A}_{a'}q^{B}_{b'}\ C(3a';3b'|6\beta) \\
&= \overline{q}^{C}_{a}\overline{q}^{D}_{b}\ C(3a;3b|6\alpha)U_{cc'}U_{dd'}\ C(3c;3d|6\alpha)C(3c';3d'|6\beta)\ q^{A}_{a'}q^{B}_{b'}\ C(3a';3b'|6\beta) \\
&= \frac{1}{4}\overline{q}^{C}_{a}\overline{q}^{D}_{b}\ U_{cc'}U_{dd'}\ q^{A}_{a'}q^{B}_{b'}\ (\delta_{ac}\delta_{bd}+\delta_{bc}\delta_{ad})(\delta_{a'c'}\delta_{b'd'}+\delta_{b'c'}\delta_{a'd'}) \\
&= \frac{1}{2}\overline{q}^{C}_{a}U_{aa'}q^{A}_{a'}\ \overline{q}^{D}_{b}U_{bb'}q^{B}_{b'}+\frac{1}{2}\overline{q}^{C}_{a}U_{ab'}q^{B}_{b'}\ \overline{q}^{D}_{b}\ U_{ba'}q^{A}_{a'},
\end{aligned} \tag{5.13}$$

where in the second line we used the identity

$$U^{(6)}_{\alpha\beta} = U_{aa'}U_{bb'}\ C(3a;3b|6\alpha)C(3a';3b'|6\beta), \tag{5.14}$$

and in the third line we used the identity

$$C(3a';3b'|6\alpha')C(3c;3d|6\alpha') = \frac{1}{2}(\delta_{a'c}\delta_{b'd}+\delta_{b'c}\delta_{a'd}). \tag{5.15}$$

Again, we see that this tetraquark operator is a linear combination of a meson-meson-like operator.

Lastly, we consider the tetraquark formed from diquarks in the **8**-dimensional representations, where one of the diquarks is displaced by a gauge link in the **8** representation

$$\overline{d}^{(8)}_{\alpha}(x)\ U^{(8)}_{\mu;\alpha\beta}(x)\ d^{(8)}_{\beta}(x+\mu). \tag{5.16}$$

Once more, this operator suffers no loss of generality, and we suppress the spatial dependence. Then, we find

$$\begin{aligned}
\overline{d}^{(8)}_{\alpha}\ U^{(8)}_{\alpha\beta}\ d^{(8)}_{\beta} &= q^{C}_{a}\overline{q}^{D}_{b}\ C(\overline{3}a;3b|8\alpha)U^{(8)}_{\alpha\beta}\ \overline{q}^{A}_{a'}q^{B}_{b'}\ C(\overline{3}a';3b'|8\beta) \\
&= q^{C}_{a}\overline{q}^{D}_{b}\ C(\overline{3}a;3b|8\alpha)U^{*}_{cc'}U_{dd'}\ C(\overline{3}c;3d|8\alpha)C(\overline{3}c';3d'|8\beta)\ \overline{q}^{A}_{a'}q^{B}_{b'}\ C(\overline{3}a';3b'|8\beta) \\
&= q^{C}_{a}\overline{q}^{D}_{b}\ U^{*}_{cc'}U_{dd'}\ \overline{q}^{A}_{a'}q^{B}_{b'}\left(\delta_{ac}\delta_{bd}-\frac{1}{3}\delta_{ab}\delta_{cd}\right)\left(\delta_{c'a'}\delta_{d'b'}-\frac{1}{3}\delta_{c'd'}\delta_{a'b'}\right) \\
&= \overline{q}^{A}_{a'}U^{\dagger}_{a'a}q^{C}_{a}\ \overline{q}^{D}_{b}U_{bb'}q^{B}_{b'}-\frac{1}{3}\overline{q}^{D}_{b}\ U_{bc'}U^{\dagger}_{c'a}q^{C}_{a}\ \overline{q}^{A}_{a'}q^{B}_{a'}-\frac{1}{3}\overline{q}^{D}_{a}q^{C}_{a}\ \overline{q}^{A}_{a'}U^{\dagger}_{a'c}U_{cb'}q^{B}_{b'} \\
&\quad+\frac{1}{9}\overline{q}^{D}_{a}q^{C}_{a}\ U^{\dagger}_{c'c}U_{cc'}\ \overline{q}^{A}_{a'}q^{B}_{a'},
\end{aligned} \tag{5.17}$$

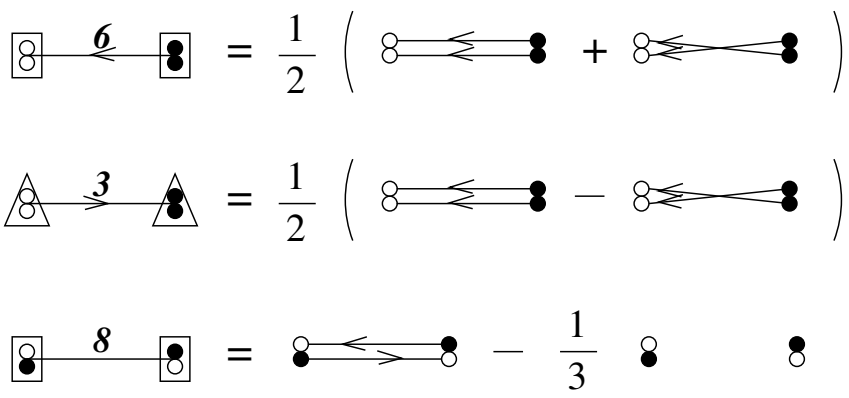

Figure 5.2: The diagrammatic representation of the equivalence between tetraquarks made of displaced diquarks and meson-meson-like operators.

where in the second line we used the identity

$$U^{(8)}_{\alpha\beta} = U^*_{aa'} U_{bb'}(x)\ C(\overline{3}a; 3b|8\alpha) C(\overline{3}a'; 3b'|8\beta), \tag{5.18}$$

and in the third line we used the identity

$$C(\overline{3}a'; 3b' 8\alpha') C(\overline{3}c; 3d|8\alpha') = \delta_{a'c}\delta_{b'd} - \frac{1}{3}\delta_{a'b'}\delta_{cd}. \tag{5.19}$$

Thus, we see, as with the other tetraquarks constructed from diquarks, that this tetraquark operator is a linear combination of a meson-meson-like operator. These results are summarized diagrammatically in Figure 5.2.

The last operator we consider is shown in (e) of Figure 5.1. We again use Eq. (5.10) to show that this operator can also be written as a linear combination of the meson-meson-like operators. Without loss of generality, we may ignore the quark displacements, because these do not affect the color structure. Also, take notice of the Levi-Civita tensors indicated by the triangles. Thus, we consider the operator shown in Figure 5.3, which is given by

$$\begin{aligned} &\varepsilon_{abc}\varepsilon_{a'c'f'}\varepsilon_{def}\varepsilon_{d'b'e'}\ q_a(x) q_d(x+\mu+\nu) \overline{q}_{a'}(x+\nu) \overline{q}_{d'}(x+\mu) \\ &\quad \times U_{\mu;bb'}(x) U_{\nu;cc'}(x) U_{-\mu;ee'}(x+\mu+\nu) U_{-\nu;ff'}(x+\mu+\nu). \end{aligned} \tag{5.20}$$

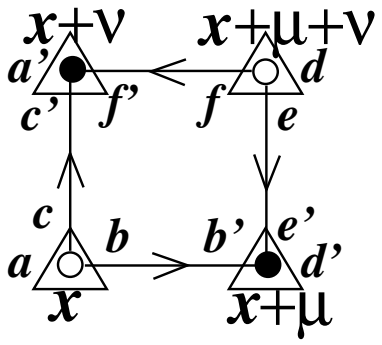

Figure 5.3: The tetraquark 'box' operator without individually displaced quarks.

For simplification, we introduce the following notation: $q_a = q_a(x)$, $p^*_{a'} = \overline{q}_{a'}(x+\nu)$, $s_d = q_d(x+\mu+\nu)$, $r^*_{d'} = \overline{q}_{d'}(x+\mu)$ and $U_{bb'} = U_{\mu;bb'}(x)$, $X_{cc'} = U_{\nu;cc'}(x)$, $V_{ee'} = U_{-\mu;ee'}(x+\mu+\nu)$, and $W_{ff'} = U_{-\nu;ff'}(x+\mu+\nu)$, then this tetraquark operator can be written as

$$\varepsilon_{abc}\varepsilon_{a'c'f'}\varepsilon_{def}\varepsilon_{d'b'e'}\ q_a s_d p^*_{a'} r^*_{d'} U_{bb'} X_{cc'} V_{ee'} W_{ff'}. \tag{5.21}$$

Next, we use the following

$$U_{bb'} = \frac{1}{2}\varepsilon_{bij}\varepsilon_{b'i'j'} U^*_{ii'} U^*_{jj'}, \qquad W_{ff'} = \frac{1}{2}\varepsilon_{fkl}\varepsilon_{f'k'l'} W^*_{kk'} W^*_{ll'}, \tag{5.22}$$

to rewrite this operator in the following form

$$\frac{1}{4}\varepsilon_{abc}\varepsilon_{bij}\,\varepsilon_{d'b'e'}\varepsilon_{b'i'j'}\,\varepsilon_{def}\varepsilon_{fkl}\,\varepsilon_{f'k'l'}\varepsilon_{a'c'f'}\ q_a s_d p^*_{a'} r^*_{d'} U^*_{ii'} U^*_{jj'} X_{cc'} V_{ee'} W^*_{kk'} W^*_{ll'}. \tag{5.23}$$

Finally, rewriting the Levi-Civita symbols in terms of Kronecker deltas gives

$$\begin{aligned}
&\frac{1}{4}(\delta_{ci}\delta_{aj} - \delta_{cj}\delta_{ai})(\delta_{e'i'}\delta_{d'j'} - \delta_{e'j'}\delta_{d'i'})(\delta_{dk}\delta_{el} - \delta_{dl}\delta_{ek})(\delta_{a'k'}\delta_{c'l'} - \delta_{a'l'}\delta_{c'k'}) \\
&\qquad \times q_a s_d p^*_{a'} r^*_{d'} U^*_{ii'} U^*_{jj'} X_{cc'} V_{ee'} W^*_{kk'} W^*_{ll'} \\
&= (r^\dagger U^\dagger q)(p^\dagger W^\dagger s)\mathrm{Tr}(XW^\dagger VU^\dagger) - (r^\dagger U^\dagger q)(p^\dagger W^\dagger VU^\dagger XW^\dagger s) \\
&\qquad - (r^\dagger U^\dagger XW^\dagger VU^\dagger q)(p^\dagger W^\dagger s) + (r^\dagger U^\dagger XW^\dagger s)(p^\dagger W^\dagger VU^\dagger q).
\end{aligned}$$

Thus, we see this tetraquark operator can be decomposed into linear combinations of the meson-meson-like operators and a purely gluonic loop. This decomposition is shown diagrammatically in Figure 5.4.

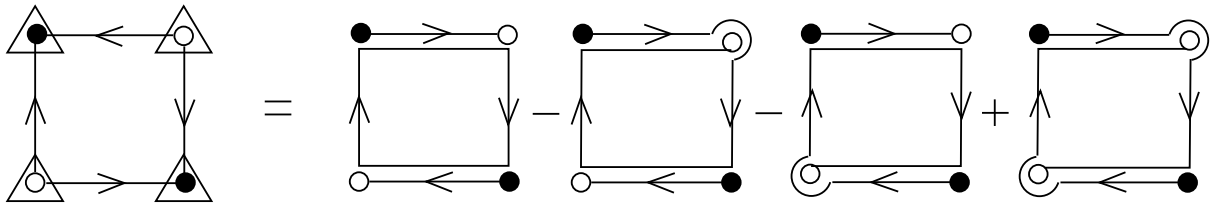

Figure 5.4: Expression of a tetraquark operator with four Levi-Civita couplings in terms of gauge-invariant pieces that are quark-antiquark pairs and a pure gluon loop.

5.1.2 Elemental Operators

Because every tetraquark operator we considered could be written in terms of meson-meson-like operators, we chose to use only tetraquark operators constructed from two displaced quarks and two displaced antiquarks based on the structure in Eq. (5.4). The displacement types we consider are shown in Figure 5.5. These are single-site operators (SS), doubly-displaced operators in an I configuration (DDIa and DDIb), and quadruply-displaced operators configured in a cross (QDXa and QDXb). The letters 'a' and 'b' in the displacement type label indicates different orderings for displacing the quarks and antiquarks. As with the operators discussed in Chap. 3, our tetraquark operators are constructed from covariantly-displaced LapH-smeared quark fields (see Sec. 3.2). Thus, we use tetraquark annihilation operators that are linear combinations of the following elemental operator

$$\Phi^{ABCD(\pm)}_{\alpha\beta\gamma\delta}(t) = \sum_{\boldsymbol{x}} e^{-i\boldsymbol{p}\cdot\boldsymbol{x}}(\delta_{ab}\delta_{cd} \pm \delta_{ad}\delta_{bc})\overline{q}^{A}_{a\alpha}(\boldsymbol{x},t)q^{B}_{b\beta}(\boldsymbol{x},t)\overline{q}^{C}_{c\gamma}(\boldsymbol{x},t)q^{D}_{d\delta}(\boldsymbol{x},t), \tag{5.24}$$

and the corresponding creation operators are linear combinations of the "barred" elemental operator

$$\overline{\Phi}^{ABCD(\pm)}_{\alpha\beta\gamma\delta}(t) = \sum_{\boldsymbol{x}} e^{i\boldsymbol{p}\cdot\boldsymbol{x}}(\delta_{ab}\delta_{cd} \pm \delta_{ad}\delta_{bc})\overline{q}^{D}_{d\delta}(\boldsymbol{x},t)q^{C}_{c\gamma}(\boldsymbol{x},t)\overline{q}^{B}_{b\beta}(\boldsymbol{x},t)q^{A}_{a\alpha}(\boldsymbol{x},t). \tag{5.25}$$

Notice that unlike our meson elemental operators in Eqs. (3.51) and (3.52), these operators do not have the spatial displacements in the phases, even though it was stated previously

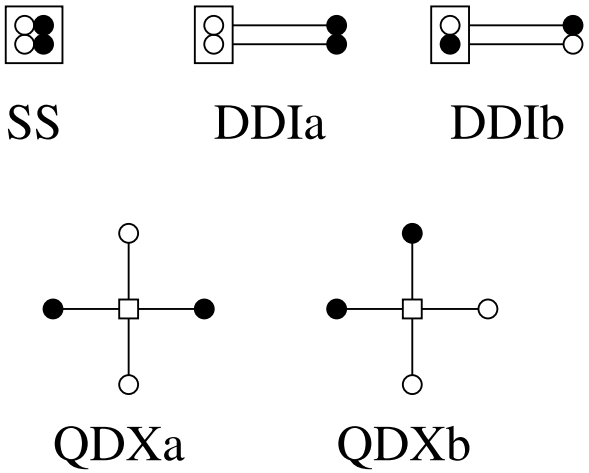

Figure 5.5: The tetraquark displacements we consider.

that the meson operators needed these altered phases in order to transform appropriately under G-parity. However, in the case of mesons, these phases were only necessary, because the antiquark field in the meson was displaced twice as opposed to the quark field which was only displaced once. This different treatment of the fields in the meson operators was the true reason for the altered phases. In our tetraquark operators we do not consider different treatments of the quark fields, and therefore the displacement vectors do not need to be included in the phases. Finally, our tetraquark annihilation and creation operators are of the form

$$T_l^{(\pm)}(t) = c^{(l)}_{\alpha\beta\gamma\delta}\Phi^{ABCD(\pm)}_{\alpha\beta\gamma\delta}(t), \tag{5.26a}$$

$$\overline{T}_l^{(\pm)}(t) = c^{(l)*}_{\alpha\beta\gamma\delta}\overline{\Phi}^{ABCD(\pm)}_{\alpha\beta\gamma\delta}(t). \tag{5.26b}$$

5.2 COMPUTATIONAL DETAILS

The same software used for calculating projection coefficients of the baryon and meson operators, written in MAPLE, was extended to include the calculation of the coefficients for

the operator types shown in Figure 5.5. The software used for operator construction, known as Chroma LapH, was modified to include tetraquark operators constructed from these coefficients. The extra valence quark in these operators posed a noticeable increase in the computational effort, and we parallelized the computation of the tetraquark sources and sinks for each dilution index. When this was done, an appreciable decrease in computational time was observed and began to approach times on the order of the baryon calculations.

6.0 ENERGIES FROM TEMPORAL CORRELATORS

In Chap. 4, it was shown how we stochastically estimate temporal correlation functions, and in this chapter we discuss how these correlation functions can be used to extract the finite-volume spectrum. This chapter opens with an overview on the thermal effects due to our finite temporal extent in Sec. 6.1. Then, the analysis of our temporal correlator matrices is presented in Sec. 6.2, which shows how the lowest N energies can be determined from an $N \times N$ correlator matrix. Finally, we briefly discuss the fit functions we consider for finding best fit curves for our correlators in Sec. 6.3.

6.1 EUCLIDEAN SPACE AND THERMAL EFFECTS

Our calculations are necessarily performed in Euclidean space and with finite temporal extent. Therefore, with the introduction of anti-periodic boundary conditions in time for the quark fields, our path integrals are equivalent to quantum statistical mechanical expectation values with a temperature given by the inverse temporal extent of our lattice. That is[1]

$$\begin{aligned} \mathcal{C}_{ij}(t) &= \left\langle \mathcal{O}_i(t)\overline{\mathcal{O}}_j(0)\right\rangle_T \\ &= \left\langle e^{Ht}\mathcal{O}_i(0)e^{-Ht}\ \overline{\mathcal{O}}_j(0)\right\rangle_T \\ &= \frac{1}{Z_T}\,\mathrm{Tr}\left[e^{-H(T-t)}\mathcal{O}(0)e^{-Ht}\ \overline{\mathcal{O}}(0)\right], \end{aligned} \tag{6.1}$$

where $\langle\rangle_T$ can be interpreted as a quantum statistical mechanical expectation value in a system with temperature $\frac{1}{T}$ or as a correlation function in Euclidean space with finite temporal

[1] The temporal extent is denoted by T, not to be confused with the temperature.

extent T which has a path integral representation. The partition function is defined as

$$\begin{aligned} Z_T &\equiv \operatorname{Tr} e^{-TH} \\ &= \sum_n \langle n| e^{-TH} |n\rangle \\ &= \sum_n e^{-TE_n}. \end{aligned} \tag{6.2}$$

Then, performing the trace in Eq. (6.1) we find

$$\begin{aligned} \mathcal{C}_{ij}(t) &= \frac{1}{Z_T} \sum_m \langle m| e^{-(T-t)H} \mathcal{O}_i(0) e^{-tH} \overline{\mathcal{O}}_j(0) |m\rangle \\ &= \frac{1}{Z_T} \sum_{n,m} \langle m| e^{-(T-t)H} \mathcal{O}_i(0) |n\rangle \langle n| e^{-tH} \overline{\mathcal{O}}_j(0) |m\rangle \\ &= \frac{1}{Z_T} \sum_{n,m} e^{-(T-t)E_m} \langle m| \mathcal{O}_i(0) |n\rangle e^{-tE_n} \langle n| \overline{\mathcal{O}}_j(0) |m\rangle \\ &= \frac{\sum_{n,m} \langle m| \mathcal{O}_i(0) |n\rangle \langle n| \overline{\mathcal{O}}_j(0) |m\rangle e^{-(T-t)E_m} e^{-tE_n}}{\sum_n e^{-TE_n}} \\ &\underset{T\to\infty}{=} \sum_n \langle 0| \mathcal{O}_i(0) |n\rangle \langle n| \overline{\mathcal{O}}_j(0) |0\rangle e^{-tE_n} \\ &= \sum_n \langle 0| e^{-Ht} \mathcal{O}_i(0) e^{-Ht} |n\rangle \langle n| \overline{\mathcal{O}}_j(0) |0\rangle \\ &= \langle 0| \mathcal{O}_i(t) \overline{\mathcal{O}}_j(0) |0\rangle , \end{aligned} \tag{6.3}$$

where $H|n\rangle = E_n|n\rangle$, and we assume the energies have been shifted such that $E_0 = 0$. Therefore, as expected, as the temporal extent is made large, the Euclidean correlation function approaches the vacuum expectation value.

Generally, the thermal effects for the lattices we consider are small. But, for the lightest mesons, ignoring these thermal effects is not always valid. Fortunately, the backward propagating modes from meson correlators have the same energy as the forward propagating modes, and thus operators corresponding to the lightest mesons were constructed to be symmetric under time reversal (see Sec. 3.3.3). Then, in these cases, we can use a fit function that is also symmetric under time reversal to take the thermal effects into consideration. Additionally, adding a constant to our fit function can also help. The specific fit functions we consider are discussed in Sec. 6.3. We have been able to observe thermal effects on our $24^3 \times 128$ lattice, but the spectrum was seen to be independent of the fit forms used on the $32^3 \times 256$ lattice where the temperature is approximately 22.6 MeV.

6.2 TEMPORAL CORRELATOR MATRIX

The temporal correlation matrix contains information on the complete spectrum we are after, but extraction of the finite-volume energy from this matrix directly is impractical and inefficient. Instead, we use the variational methods described in Ref. [20] to extract energies and overlaps of the states created by our operators and the energy eigenstates. In what follows, we assume that the temporal extent of the lattice is large enough such that the temporal wrap-around effects can be ignored and the temporal correlator matrix is well approximated by

$$\mathcal{C}_{ij}(t) = \langle 0 | \, \mathcal{O}_i(t + t_0) \overline{\mathcal{O}}_j(t_0) \, | 0 \rangle \, . \tag{6.4}$$

As a first step, we attempt to remove any normalization differences among our operators by rescaling the correlator matrix. This must be done in such a way as to not affect the stationary-state energies. This can be achieved by rescaling $\mathcal{O}_i$ in the same way as $\overline{\mathcal{O}}_i$. Our choice for rescaling is

$$C_{ij}(t) \equiv \frac{\mathcal{C}_{ij}(t)}{\left(\mathcal{C}_{ii}(\tau_N)\mathcal{C}_{jj}(\tau_N)\right)^{1/2}}, \tag{6.5}$$

where τ_N is chosen to be a very early time, when the errors are small (generally a value of $\tau_N = 3$ is chosen).[2]

Performing a spectral decomposition of this correlator matrix gives (*cf.* Sec. 2.4)

$$C_{ij}(t) = \sum_n \langle 0 | \, \mathcal{O}_i(0) \, | n \rangle \, \langle n | \, \overline{\mathcal{O}}_j(0) \, | 0 \rangle \, e^{-E_n t}. \tag{6.6}$$

We purposefully designed our operators such that the resulting correlator matrices were Hermitian (see Sec. 2.4.1), which implies

$$\langle 0 | \, \mathcal{O}_i(0) \, | n \rangle^* = \langle n | \, \overline{\mathcal{O}}_i(0) \, | 0 \rangle \, . \tag{6.7}$$

Then, defining the overlap factors

$$Z_j^{(n)} \equiv \langle 0 | \, \mathcal{O}_j \, | n \rangle \tag{6.8}$$

[2] We do not continue to carry along the rescaling factors. It is always assumed the operators have been replaced by their rescaled versions.

representing the overlap between the states created by our operators and the energy eigenvalues, we can finally write

$$C_{ij}(t) = \sum_n Z_i^{(n)} Z_j^{(n)*} e^{-E_n t}. \tag{6.9}$$

The normalizations of the energy eigenvectors are set by the spectral decomposition but the phase is not. This can be seen from the invariance of Eq. (6.9) under

$$Z_j^{(n)} \to Z_j^{(n)} e^{i\phi_n}. \tag{6.10}$$

Thus, we can only determine the magnitude $|Z_j^{(n)}|$ of the overlap factors. Given the unlikely occurrences of accidental degeneracies, we assume only non-degenerate energies and that they are ordered (*i.e.* $E_{n+1} > E_n$).

6.2.1 The Generalized Eigenvalue Problem

Sec. 2.4 presented a brief discussion on how a variational approach can be used to extract the ground state energy in a particular channel, and that this approach was equivalent to finding the largest eigenvalue in a generalized eigenvalue problem (GEVP). In what follows, we will present this GEVP and show how its solution can determine many energy eigenstates and not just the ground state. Additionally, these methods allow extraction of the overlap factors defined in Eq. (6.8). First, a theorem from Ref. [19] motivates much of what follows:

> **Theorem.** For every $t \geq 0$, let $\lambda_n(t)$ be the eigenvalue of an $N \times N$ correlation matrix $C(t)$ ordered such that $\lambda_0 \geq \lambda_1 \geq \cdots \geq \lambda_{N-1}$, then
>
> $$\lim_{t\to\infty} \lambda_n(t) = c_n e^{-E_n t}\big[1 + O(e^{-t\Delta_n})\big], \quad c_n > 0, \quad \Delta_n = \min_{m\neq n} |E_n - E_m|. \tag{6.11}$$

This theorem shows that diagonalizing the correlator matrix allows us to extract the N lowest lying energy levels. However, in practice, this is not feasible because the corrections are

$$\mathcal{O}(e^{-t\Delta_n}), \tag{6.12}$$

which require very large values of t to become small. Thus, to reliably extract the spectrum, we must take t out large enough, but since the error on our correlators generally increases

with time this is not a viable option. The authors of Ref. [19] suggest an alternative approach, which they show to give smaller corrections, and instead solve the GEVP

$$C(t)\upsilon_n(t,\tau_0) = \lambda_n(t,\tau_0)C(\tau_0)\upsilon_n(t,\tau_0), \qquad n = 1,\cdots,N-1, \qquad t > \tau_0, \tag{6.13}$$

where N is the dimension of $C(t)$, and τ_0 is referred to as the metric time. They motivate this suggestion by considering the truncated correlator matrix

$$C_{ij}^{(0)}(t) = \sum_{n=0}^{N-1} Z_i^{(n)} Z_j^{(n)*} e^{-E_n t}, \tag{6.14}$$

which gives eigenvalues that are exactly

$$\lambda_n^{(0)}(t,\tau_0) = e^{-E_n(t-\tau_0)} \tag{6.15}$$

when used in the GEVP of Eq. (6.13). Of course, it is not clear whether the contributions from states with $E_n \geq E_N$ can simply be ignored.

To better understand these corrections and how to suppress them, a perturbative expansion of the temporal correlations is considered in Ref. [20]. Their findings are that if $\tau_0 \geq t/2$, then the leading order corrections to $\lambda_n^{(0)}(t,\tau_0)$ are

$$\mathcal{O}(e^{-(E_N - E_n)t}), \tag{6.16}$$

which is a significant improvement from Eq. (6.12) for all but the highest lying states. This result demonstrates the advantage of solving the GEVP over simply diagonalizing $C(t)$. Additionally, we see that keeping N and τ_0 large is more important than having large t in order to reduce the systematic errors in the extraction of energies. Also, since the leading order corrections become larger as $n \to N-1$, it is important to make N much larger than the number of stationary states you wish to reliably extract. We have found that choosing $N \approx \frac{3}{2}n$, where n is the desired number of energies, is a good rule of thumb.

The GEVP can be formed as an eigenvalue problem in the following way

$$\begin{aligned}
&C(t)\upsilon_n(t,\tau_0) = \lambda_n(t,\tau_0)C(\tau_0)\upsilon_n(t,\tau_0) \\
\Rightarrow\ &C^{-1/2}(\tau_0)C(t)C^{-1/2}(\tau_0)C^{1/2}(\tau_0)\upsilon_n(t,\tau_0) = \lambda_n(t,\tau_0)C^{1/2}(\tau_0)\upsilon_n(t,\tau_0) \\
\Rightarrow\ &C^{-1/2}(\tau_0)C(t)C^{-1/2}(\tau_0)\upsilon'_n(t,\tau_0) = \lambda_n(t,\tau_0)\upsilon'_n(t,\tau_0),
\end{aligned} \tag{6.17}$$

where $v'_n(t,\tau_0) \equiv C^{1/2}(\tau_0)v_n(t,\tau_0)$. Therefore, solving the GEVP is equivalent to diagonalizing

$$G(t) \equiv C^{-1/2}(\tau_0)C(t)C^{-1/2}(\tau_0), \tag{6.18}$$

which is the route we choose. To determine $C^{\pm 1/2}(\tau_0)$, we first find the eigenvalues and eigenvectors of $C(\tau_0)$. We put the eigenvectors of $C(\tau_0)$ into the columns of the U_0 (which is unitary since $C(\tau_0)$ is Hermitian) and form a diagonal matrix Λ_0 from the eigenvalues such that

$$C(\tau_0) = U_0\Lambda_0 U_0^\dagger. \tag{6.19}$$

Then,

$$C^{\pm 1/2}(\tau_0) = U_0\Lambda_0^{\pm 1/2}U_0^\dagger. \tag{6.20}$$

After diagonalizing $G(t)$, the eigenvalues obey [20]

$$\lambda_n(t) \to |Z'_n|^2 e^{-E_n t}, \qquad t \to \infty, \tag{6.21}$$

and the overlap factors are approximated by

$$Z_j^{(n)} \approx C_{jk}(\tau_0)^{1/2}V_{kn}(t)Z'_n, \tag{6.22}$$

where $V(t)$ is the unitary matrix that contains the eigenvectors of $G(t)$ in its columns. In the expression for the overlap factors, the term Z'_n can be taken to be the square root of the asymptotic amplitude of $\lambda_n(t)$.

6.2.2 The Correlator Matrix Pivot

In addition to being Hermitian, it has been assumed that $C(t)$ is positive definite. This guarantees that $C(\tau_0)^{\pm 1/2}$ are both Hermitian and positive definite, which further guarantees that $G(t) = C^{-1/2}(\tau_0)C(t)C^{-1/2}(\tau_0)$ is Hermitian and positive definite. The need for these properties can be seen from our assumption that the eigenvalues of $G(t)$ are well approximated by a decaying exponential with a positive coefficient.

In principal, one expects $C(t)$ to be positive definite, because it is a Hermitian correlation matrix in imaginary time. However, in practice, statistical noise and operators that are not sufficiently linearly independent can produce eigenvalues that are statistically zero or

even slightly negative, which can make $C(t)$ become ill-conditioned. To avoid this issue, we initially use some kind of "pruning" procedure to remove operators that are causing the correlator matrix to become ill-conditioned (a more detailed discussion on this is deferred until Sec. 8.2). But, there is always a possibility that our "pruning" procedures cannot produce a well-conditioned correlator matrix for any number of reasons (*e.g.* if a well-conditioned matrix can only be achieved by the removal of operators deemed important). In this case, we can still proceed by using a method based on the singular value decomposition [61]. We refer to this method, and similar methods (see Sec. 6.2.2.1), as a correlator matrix pivot, and we use this method regardless of whether the correlator matrix is ill-conditioned to begin with. In the end, the matrix produces a diagonal matrix that is well-conditioned with eigenvalues that tend to $\lambda_n(t) \propto e^{-E_n t}$.

The method works by first projecting $C(\tau_0)$ onto the space spanned by the eigenvectors associated with eigenvalues that are greater than some small cutoff and using this matrix to form $G(t)$. Then, we do the exact same thing to $G(\tau_D)$. The condition number of a matrix is defined as

$$\xi^{cn} = \left|\frac{\lambda_{max}}{\lambda_{min}}\right|, \tag{6.23}$$

where λ_{max} and λ_{min} are the maximum and minimum eigenvalues of the matrix, respectively. A matrix is said to be ill-conditioned if the condition number is too high and well-conditioned if it is low enough. Generally, in this work, we accept a condition number as high as ≈ 100. We see that there are two ways of improving the condition number: 1) remove the eigenvectors associated with the largest eigenvalues or 2) remove the eigenvectors associated with the smallest eigenvalues. Since we expect the eigenvalues to asymptotically obey $\lambda_n(t) \propto e^{-E_n t}$, we must retain the largest eigenvalues, because these correspond to the lowest energies. It is the smaller eigenvalues that decay according to the largest energies in our system, which we do not care as much about.

For our procedure to begin, we must start by choosing some threshold that will correspond to our smallest allowed eigenvalue. This can of course be expressed as

$$\lambda_{thres} = \frac{\lambda_{max}}{\xi^{cn}_{max}}, \tag{6.24}$$

where ξ^{cn}_{max} is the maximum accepted condition number. Generally, we choose $1/\xi^{cn}_{max}$ to be on the order of the statistical error found in the matrix we are working with. Next, we from a $N \times N_0$ matrix P_0 that contains the $N_0 \leq N$ eigenvectors of $C(\tau_0)$ associated with eigenvalues larger than λ_{thes}. We then define $\widetilde{C}(t)$ as

$$\widetilde{C}(t) = P_0^\dagger C(t) P_0, \tag{6.25}$$

and then use this to form $\widetilde{G}(t)$:

$$\widetilde{G}(t) = \widetilde{C}^{-1/2}(\tau_0)\widetilde{C}(t)\widetilde{C}^{-1/2}(\tau_0). \tag{6.26}$$

Next, we form the $N_0 \times N_p$ matrices $\widetilde{V}(\tau_D)$ containing the $N_p \leq N_0$ eigenvectors of $\widetilde{G}(\tau_D)$ associated with the eigenvalues larger than λ_{thes}, where τ_D is referred to as the diagonalization time that is chosen such that $\tau_0 < \tau_D \leq 2\tau_0$.[3] Finally, we have an $N_p \times N_p$ diagonal matrix

$$\widetilde{D}(t) = \widetilde{V}^\dagger(\tau_D)\widetilde{G}(t)\widetilde{V}(\tau_D), \tag{6.27}$$

which has diagonal elements that tend to $\lambda_n(t) \propto e^{-E_n t}$. There is no guarantee that $\widetilde{D}(t)$ remains diagonal for $t > \tau_D$, and we must inspect the off-diagonal elements to ensure that it does. If it does not remain diagonal, we must adjust our parameters τ_0 and τ_D until it does.

6.2.2.1 Alternative Pivot Methods The approach just described above used a single time slice τ_D for constructing the matrices $\widetilde{V}(\tau_D)$ used for diagonalizing $\widetilde{G}(t)$, and is referred to as the *single pivot* method. This rotation is done on a per configuration basis (*i.e.* we rotated the correlator matrix on each gauge configuration). Alternatively, there are two other approaches one could consider: 1) the *principal axes* method in which a pivot procedure is performed for every time t and on each jackknife or bootstrap resampling; and 2) the *rolling pivot* method in which a pivot procedure is performed for every time t but performing this pivot on each gauge configuration only. Both of these methods require the use of eigenvector pinning, and they can be very cumbersome. The single pivot method is clearly much simpler and so long as $\widetilde{D}(t)$ is shown to remain diagonal, then the results should not differ from these alternative approaches. Therefore, in this work, we have only considered the single pivot method.

[3] This requirement is based on the findings in Ref. [20] in which they found when $\tau_0 \geq t/2$ the leading order corrections to the eigenvalues are given by Eq. (6.16).

6.3 FITTING TO TEMPORAL CORRELATORS

Once we have obtained the matrix $\widetilde{D}(t)$, we need to perform fits to the diagonal elements in order to extract the spectrum. In this section, we discuss the different fit functions we use. For a discussion on our fitting procedure see Appendix B. The simplest fit function we consider, referred to as the time-forward single exponential is,

$$C(t) = Ae^{-Et}. \tag{6.28}$$

It is possible that thermal effects could be significant (especially for the lowest energy states), and in order to observe the effects of backward propagating mesons, we fit to the time-symmetric single exponential:

$$C(t) = A\Big[e^{-Et} + e^{-E(T-t)}\Big], \tag{6.29}$$

where T is the temporal extent of our lattice. For baryons, the backward propagating modes do not have the same mass as the forward propagating modes (see Sec. 3.3.2), and the time-symmetric fit function is not valid. However, we do not expect thermal effects to be significant for baryons, because they generally have much higher energies.

The above fit functions have assumed that the effects from the leading order corrections to the diagonal elements from excited state contamination are negligible. However, this is only true for very large times, and in order to perform fits starting with smaller times, we use a time-forward two exponential fit:

$$C(t) = Ae^{-Et}\Big[1 + Be^{-\Delta^2 t}\Big], \tag{6.30}$$

where we use Δ^2 to ensure the decay constant in the second exponential remains positive. The hope is that the second term in this fit will mock up the effects of the leading order corrections. This fit can also be made to be time symmetric as well. Additionally, it is always possible to add a constant to any of these fit functions. A constant term can be helpful for mocking up the thermal effects, but it is usually only seen to be non-zero for lattices with small temporal extent.

Another fit form that can help mock up the excited state contamination is the time-forward geometric series

$$C(t) = \frac{Ae^{-Et}}{1 - Be^{-\Delta^2 t}}, \tag{6.31}$$

which is equivalent to an infinite sum of decaying exponentials, and since the effects of excited state contamination will be an infinite sum of decaying exponentials then this fit form may work very well in certain cases. As before, we can also use a time-symmetric version of this fit function.

7.0 THE LÜSCHER QUANTIZATION CONDITION

The goal of spectroscopy calculations in lattice QCD is to study the many hadron resonances that experiments have observed. But, so far, all we have done is extract the finite-volume stationary-state energies of QCD. Hadron resonances are not stationary states, and it has not been made clear yet how the finite-volume physics we extract relates to the physical world. In order to better understand these questions, Martin Lüscher sought to study the volume dependence of the spectrum. He started by studying the single-particle stable states and found that the difference between the finite-volume and infinite-volume masses decreased to zero exponentially with the size of the lattice [21], and given a lattice size L sufficiently larger than the range of the interactions, the errors due to the finite volume may safely be ignored. This amounts to requiring L be larger than the correlation length of the system, and since the correlation length of the system is given by the inverse of the lightest mass in the spectrum, then we should at least require $m_\pi L > 1$. In what follows, we always assume that L is large enough such that the exponentially suppressed finite-volume corrections are negligible. Therefore, the finite-volume stationary states that are found to have significant overlap only with single-hadron operators should be expected to have energies that compare well with infinite-volume resonances. The possible exceptions to this are for broad resonances or resonances near a threshold. We can only expect agreement to occur within the decay width of the resonance, and thus if the resonance width is large, then we would not expect the finite-volume energy to agree well with the infinite-volume resonance mass. Near a threshold, we expect the energies near that resonance to have significant mixing with two-hadron states such that the finite-volume energy is shifted away from that of the resonance.

However, stationary states are stable and cannot decay, and the extraction of the single-hadron dominated energies in finite-volume gives us no information about the decay width

of the hadronic resonances we seek to study. Lüscher continued to study the volume dependence of the spectrum for scattering states and determined that the finite-volume corrections for two-particle states fell off much slower as a power series expansion in L^{-1},[1] and that the coefficients in this expansion were related to the elastic scattering amplitudes in infinite-volume for the two stable particles in question [22]. There also exists exponentially decaying dependence on the size of lattice due to interactions "around the world" (*i.e.* due to polarization effects), which are really no different from the single particle case, and therefore we still require that L is large enough to safely ignore these exponential corrections. It is the corrections involving the inverse lattice size that are due to the direct interactions among the scattering particles. This is because the probability for the particles to directly interact is expected to be of the order $1/L^{-3}$. These ideas were then expanded upon in Refs. [23, 24], which formally introduced the relationship between the infinite-volume elastic scattering amplitude and the finite-volume spectrum at rest for a single-decay channel of spinless identical particles. Thus, one could only reliably use energies below the inelastic threshold.

This relationship was then generalized to non-zero total momentum [62, 63, 64]. The main advantage of this generalization is the extra energies that can be extracted from channels with non-zero momentum in order to determine the scattering amplitude at more energies below the inelastic threshold, and generally the resonance can be determined with smaller volumes when using channels with non-zero total momentum. Finally, these results were then generalized further to consider multiple decay channels involving non-identical and non-zero spin particles [65, 66, 67, 68, 69, 70]. The energies we use can now go up to the three-particle threshold or the lowest two-particle threshold not considered (whichever comes first), but now in principal all two-body decay channels can be included and our energy limit is the three-particle threshold (or whichever n-particle threshold opens first, where $n > 2$). Additionally, generalizations that include three-particle scattering have been studied [71], but we do not consider these here.

[1] It is interesting to note, that in principal one could assign stationary states as single- or multi-hadron-dominated by observing this state's dependence on the volume.

7.1 THE QUANTIZATION CONDITION

The relationship between the infinite-volume S-matrix and the finite-volume energies with total momentum $\boldsymbol{P}$ is given by[2]

$$\det[1 + F^{(\boldsymbol{P})}(S - 1)] = 0, \tag{7.1}$$

where $F^{(\boldsymbol{P})}$ is a known function of the finite-volume energies (see Eq. (7.5)). Before this function is formally introduced, a brief discussion, followed by conventions and important quantities are summarized. This equation allows one to extract a condition for the S-matrix at each energy extracted from a correlation matrix, keeping in mind the threshold limitations mentioned above. However, when considering multiple decay channels and/or multiple partial waves, the S-matrix cannot be determined exactly from the quantization condition, because this only gives us one condition on the S-matrix which has multiple independent elements. Hence, some kind of parameterization related to the S-matrix is required. We choose a K-matrix parameterization (see Sec. 7.2).

For a given energy E extracted in the "lab" frame with total momentum $\boldsymbol{P}$ we perform a boost to the center-of-momentum frame by calculating

$$E_{cm} = \sqrt{E^2 - \boldsymbol{P}^2}, \tag{7.2}$$

which requires obtaining the lattice anisotropy $\xi = a_s/a_t$. Due to the periodic boundary conditions imposed in our lattice calculations, the total momentum in the lab frame is discrete and restricted to the values $\boldsymbol{P} = \frac{2\pi}{L}\boldsymbol{d}$, where $\boldsymbol{d}$ is a vector of integers and L^3 is the volume of our lattice. Let the different open two-particle channels be designated by an integer a, and the spins and masses of these scattered particles in a given channel be denoted by s_{ia} and m_{ia}, respectively, where $j = 1, 2$. Then, we introduce the following quantities that are useful for defining $F^{(\boldsymbol{P})}$:

$$u_a^2 = \frac{L^2 \boldsymbol{q}_{cm,a}^2}{(2\pi)^2}, \qquad \boldsymbol{s}_a = \left[1 + \frac{(m_{1a}^2 - m_{2a}^2)}{E_{cm}^2}\right]\boldsymbol{d}, \tag{7.3a}$$

$$\boldsymbol{q}_{cm,a}^2 = \frac{1}{4}E_{cm}^2 - \frac{1}{2}(m_{1a}^2 + m_{2a}^2) + \frac{(m_{1a}^2 - m_{2a}^2)^2}{4E_{cm}^2}. \tag{7.3b}$$

[2]This relationship is commonly referred to as the 'Quantization Condition'.

It is interesting to note that $\boldsymbol{q}_{cm,a}^2$ comes from the solution of

$$E_{cm,a} = \sqrt{\boldsymbol{q}_{cm,a}^2 + m_{1a}^2} + \sqrt{\boldsymbol{q}_{cm,a}^2 + m_{2a}^2}. \tag{7.4}$$

Thus, $\boldsymbol{q}_{cm,a}^2$ mocks up the energy shift due to the interactions.

Next, we choose a JLS basis to write the quantization condition in. Each basis state is represented by $|Jm_JLSa\rangle$, where J is the total angular momentum of the two particles, m_J is the projection of the total angular momentum onto the z-axis, L is the orbital angular momentum in the center-of-momentum frame,[3] S is the total spin of the two scattering particles,[4] and a designates all other necessary labels: the particle species, the intrinsic spins, parities, isospins, isospin projections, G-parities (if applicable) of the scattering particles, *etc.* Finally, we are ready to write the explicit expressions for $F^{(\boldsymbol{P})}$ in this basis:

$$\begin{aligned}\langle J'm_{J'}L'S'a'|\, F^{(\boldsymbol{P})}\, |Jm_JLSa\rangle = \delta_{a'a}\delta_{S'S}\frac{1}{2}\Big[&\delta_{J'J}\delta_{m_{J'}m_J}\delta_{L'L} \\ &+ \langle J'm_{J'}|L'm_{L'}Sm_S\rangle\, \langle Lm_LSm_S|Jm_J\rangle\, W^{(\boldsymbol{P}a)}_{L'm_{L'};Lm_L}\Big],\end{aligned} \tag{7.5}$$

where $\langle j_1m_1j_2m_2|JM\rangle$ are Clebsch-Gordan coefficients. The $W^{(\boldsymbol{P}a)}$ matrix is given by

$$-iW^{(\boldsymbol{P}a)}_{L'm_{L'};Lm_L} = \sum_{l=|L'-L|}^{L'+L}\sum_{m=-l}^{l}\frac{\mathcal{Z}_{lm}(\boldsymbol{s}_a,\gamma,u_a^2)}{\pi^{3/2}\gamma u_a^{l+1}}\sqrt{\frac{(2L'+1)(2l+1)}{(2L+1)}}\,\langle L'0,l0|L0\rangle\,\langle L'm_{L'},lm|Lm_L\rangle\,, \tag{7.6}$$

where $\gamma = \frac{E}{E_{cm}}$, and $\mathcal{Z}_{lm}$ are the Rummukainen-Gottlieb-Lüscher (RGL) shifted zeta functions [23, 62]. Our method of computing these functions is described in Ref. [27].

One other important fact to mention is the extra symmetry under the exchange of identical particles. All of the above results are independent of whether the scattering particles are distinguishable or not. However, since identical bosons (fermions) are required to be (anti-)symmetric under particle exchange, this leads to the requirement that $L+S+I-2I_1$ is even, where I is the total isospin, and $I_1 = I_2$ is the isospin of the identical particles.

[3] Not to be confused with the length L of the lattice.
[4] Not to be confused with the S-matrix.

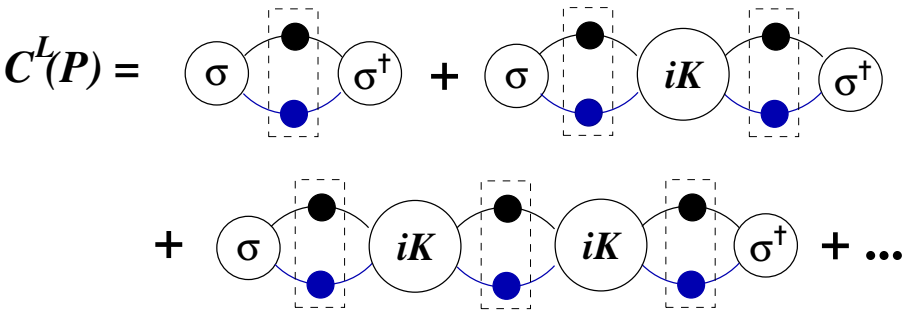

Figure 7.1: A diagrammatic representation of $C^L(P)$ in terms of the Bethe-Salpeter kernel iK connected by fully dressed propagators, and the interpolating operator σ. The dashed rectangle specifies the finite-volume loop momentum sum.

7.1.1 Deriving The Quantization Condition

In this section, an overview of the derivation for the quantization condition is given. We mainly follow the derivation presented in Ref. [63]. First, we introduce a two-body interpolating operator $\sigma(x)$, which couples to all open two-body channels and define

$$C^L(P) = \int_L \mathrm{d}^4x \; e^{i(P\cdot x)} \left\langle 0 \right| \sigma(x)\sigma^\dagger(0) \left| 0 \right\rangle , \tag{7.7}$$

where L is the size of the box we are working in and $P = (E, \boldsymbol{P})$ is the total four-momentum of the system. The quantity $C^\infty(P)$ has branch cuts beginning at each two-particle threshold, but since momentum is discrete due to the periodic boundary conditions in finite volume $C_L(P)$ replaces these branch cuts with a series of poles that correspond to the finite-volume spectrum.[5] To make $C_L(P)$ more useful, we write it in terms of the Bethe-Salpeter kernel iK, which is depicted diagrammatically in Figure 7.1

$$\begin{aligned} C_L(P) =& \frac{1}{L^3} \sum_{\boldsymbol{q}} \int \frac{\mathrm{d}q^0}{2\pi} \sigma_a(q) B_a^L(q) \sigma_a^\dagger(q) \\ &+ \frac{1}{L^6} \sum_{\boldsymbol{q},\boldsymbol{q}'} \int \frac{\mathrm{d}q^0}{2\pi} \frac{\mathrm{d}q'^0}{2\pi} \sigma_a(q) B_a^L(q) iK_{ab}(q,q') B_b^L(q') \sigma_b^\dagger(q') + \cdots, \end{aligned} \tag{7.8}$$

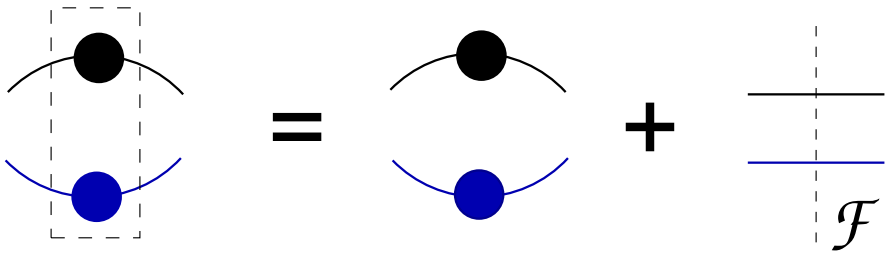

Figure 7.2: The finite-volume loop momentum sum (specified by the dashed rectangle) expressed as the infinite-volume loop momentum integral plus a finite-volume correction $\mathcal{F}$.

where a, b label the two-particle channel, and $\sigma_a(q)$ is the Fourier transform of $\sigma(x)$ which couple to the two-particle channel a. The only requirement on $\sigma_a(q)$ is that it be a regular function of q. The momenta being summed over are the allowed momenta from the periodic boundary conditions $\boldsymbol{q} = (2\pi/L)\boldsymbol{n}$. Let the two hadrons within channel a be of type a_1 and a_2, then

$$B_a^L(q) = \zeta_a[z_{a_1}(q)\Delta_{a1}(q)][z_{a_2}(P-q)\Delta_{a_2}(P-q)], \tag{7.9}$$

where ζ_a is a symmetry factor, and $z_a(q)\Delta_a$ is the fully-dressed propagator for a hadron of type a, *i.e.*

$$z_a(q)\Delta_a(q) = \int \mathrm{d}^4x e^{iq\cdot x} \left\langle \phi_a(x)\phi_a^\dagger(0)\right\rangle, \qquad \text{(no summation over } a\text{)}, \tag{7.10a}$$

$$\Delta_a(q) = \frac{i}{q^2 - m_a^2 + i\epsilon}. \tag{7.10b}$$

The field ϕ_a is an interpolating field for a hadron of type a, which has been chosen such that $z_a = 1$ if the particle is on shell. The most important feature of Eq. (7.8) is that the Bethe-Salpeter kernel iK, and the residues z_a have exponentially decaying finite-volume corrections that we assume are negligible [21, 22]. Hence, these quantities are replaced by their infinite-volume versions. However, the loop momentum summations cannot be replaced by loop

[5]The poles in $C^L(P)$ only correspond to the energies of stationary states that couple to the operator $\sigma(x)$, and not necessarily the entire finite-volume spectrum.

momentum integrals in infinite volume, and the finite-volume corrections follow a power-law dependence in the volume for these momentum sums. Thus, we write $B^L = B^\infty + \mathcal{F}$, where $\mathcal{F}$ contains the finite volume corrections to B^L. This is depicted in Figure 7.2.

Writing $C^L(P)$ in terms of $\mathcal{F}$ and evaluating $C_{sub}(P) \equiv C^L(P) - C^\infty(P)$ gives the expression

$$C_{sub}(P) = A\mathcal{F}\sum_{n=0}^{\infty}(i\mathcal{M}\mathcal{F})^n A', \tag{7.11}$$

where

$$A \equiv \sigma\sum_{n=0}^{\infty}(BiK)^n, \qquad A' = \sum_{n=0}^{\infty}(iKB)^n\sigma^\dagger, \tag{7.12}$$

and $i\mathcal{M}$ is the infinite-volume scattering amplitude defined by

$$i\mathcal{M} \equiv iK\sum_{n=0}^{\infty}(BiK)^n. \tag{7.13}$$

This is all shown diagrammatically in Figure 7.3.

Next, we simplify the expression for $C_{sub}(P)$

$$\begin{aligned} C_{sub}(P) &= A\mathcal{F}\sum_{n=0}^{\infty}(i\mathcal{M}\mathcal{F})^n A' \\ &= A\mathcal{F}(1 - i\mathcal{M}\mathcal{F})^{-1}A' \\ &= A(\mathcal{F}^{-1} - i\mathcal{M})^{-1}A', \end{aligned} \tag{7.14}$$

where we used the geometric series identity in the second line. Now, recall that the poles of $C^L(P)$ correspond to the finite-volume spectrum. These poles are still contained in $C_{sub}(P)$, and they can be used to find the infinite-volume scattering amplitude as a function of the energies in finite volume. We simply find the value of $\mathcal{M}$ that makes C_{sub} singular for each energy in the finite-volume spectrum. Encountering a pole in $C_{sub}(P)$ is equivalent to encountering a zero eigenvalue of $\mathcal{F}^{-1} - i\mathcal{M}$.[6] Therefore, this condition can be expressed as

$$\det[\mathcal{F}^{-1} - i\mathcal{M}] = 0. \tag{7.15}$$

[6]The factors A and A' are not involved, because they do not contain any singularities and have no finite-volume corrections [63].

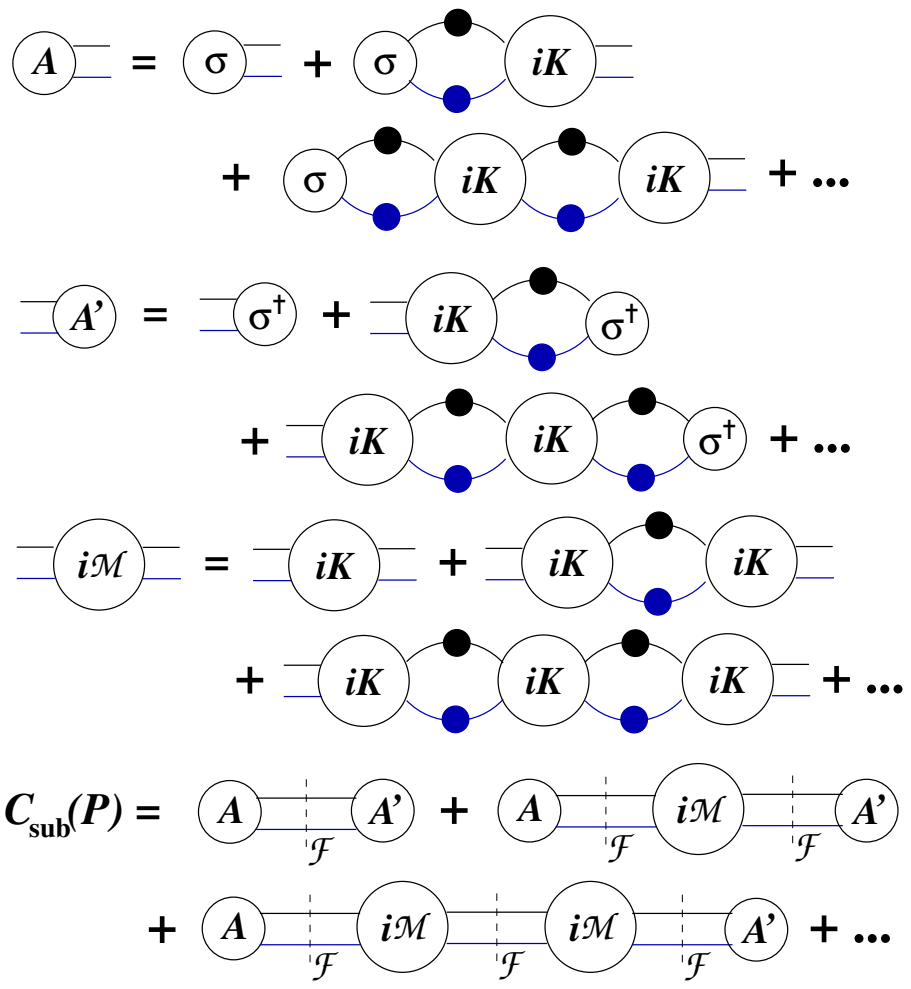

Figure 7.3: The diagrammatic representation of $C_{sub}(P) = C^L(P) - C^\infty(P)$ in terms of $A, A', i\mathcal{M}$, and the $\mathcal{F}$ insertions.

This expression is equivalent to the one shown in Eq. (7.1), where

$$F^{(\boldsymbol{P})} = -\frac{16\pi^2 E_{cm}}{q_{cm}}\mathcal{F} \tag{7.16}$$

and $q_{cm} = \sqrt{\boldsymbol{q}_{cm}^2}$.

Next, to find an expression for $F^{(\boldsymbol{P})}$ involves isolating the finite-volume corrections in the generic form of the loop momentum summation depicted in Figure 7.1:

$$I = \frac{1}{L^3}\sum_{\boldsymbol{k}}\int\frac{dk_0}{2\pi}\frac{f(k_0,\boldsymbol{k})}{(k^2 - m_1^2 + i\varepsilon)((P-k)^2 - m_2^2 + i\varepsilon)}. \tag{7.17}$$

The details of isolating the finite-volume corrections are shown in Ref. [63]. This is achieved by ignoring finite-volume corrections that decay exponentially with the volume by replacing summations with integrals via

$$\frac{1}{L^3}\sum_{\boldsymbol{p}} g_c(\boldsymbol{p}) = \int \frac{d^3k}{(2\pi)^3} g_c(\boldsymbol{k}) + O(e^{-mL}), \qquad (g_c(\boldsymbol{p}) \text{ analytic and spatially contained}), \tag{7.18}$$

which can be derived from the Poisson summation formula, and where m is some mass scale (typically the pion). Hence, whenever a momentum summation over a spatially contained analytic function is encountered, we can replace this with a momentum integration, which is exact up to exponential corrections that are assumed to be negligible. For example, consider the following momentum sum

$$\frac{1}{L^3}\sum_{\boldsymbol{p}} \frac{g(\boldsymbol{p}^2)}{(\boldsymbol{p}^2 - a^2)}, \tag{7.19}$$

where $g(\boldsymbol{p}^2)$ is analytic. We can rewrite this as

$$\frac{1}{L^3}\sum_{\boldsymbol{p}} \frac{g(a^2)}{(\boldsymbol{p}^2 - a^2)} + \frac{1}{L^3}\sum_{\boldsymbol{p}} \frac{g(\boldsymbol{p}^2) - g(a^2)}{(\boldsymbol{p}^2 - a^2)}, \tag{7.20}$$

where the summand in the second term no longer contains a singularity and can be replaced by a momentum integration. Thus, the finite volume contributions in Eq. (7.19) have been isolated in the first term of Eq. (7.20). This approach will be applied to the summation in Eq. (7.17) to put it in the form

$$I = I^{\infty} + I^{FV}. \tag{7.21}$$

Then, it is I^{FV} that can be written in terms of $\mathcal{F}$.

7.2 THE K-MATRIX

Many calculations for the ρ resonance used a 1×1 S-matrix [72, 73, 74]. However, the reduced symmetry of the lattice allows mixing of total angular momentum, which can be seen from the definition of $F^{(\boldsymbol{P})}$. Using a 1×1 S-matrix ignores this mixing. In the case of the ρ resonance, this was justified by the belief that no resonance existed with a mass

near that of the ρ with the same quantum numbers except different spin. One desirable feature of such a simple S-matrix is that its value can be determined exactly for a given energy using the quantization condition, and thus a model-independent parameterization of the S-matrix in terms of a scattering phase shift can be made. Of course, in the end we are interested not in the phase shift but the resonance mass and width, and thus some sort of parameterization cannot be avoided. In most cases, we want to consider a larger S-matrix that includes multiple partial waves and all open coupled channels in the system. But, as we will see, it is much simpler to parameterize the K-matrix [75, 76, 77, 78, 79, 80].

7.2.1 The S-matrix

Before introducing the K-matrix, we present some important properties for the S-matrix. In the JLS basis, the S-matrix is written

$$\langle J' m_{J'} L' S' a' | \, S \, | J m_J L S a \rangle = \delta_{J'J} \delta_{m_{J'} m_J} s^{(J)}_{L'S'a';LSa}(E), \tag{7.22}$$

where $s^{(J)}$ is unitary from conservation of probability, and rotational invariance has been assumed. Rotational invariance leads to the conservation of J and m_J, and ensures $s^{(J)}$ is independent of m_J. Further assuming invariance under parity gives

$$s^{(J)}_{L'S'a';LSa}(E) = 0 \qquad \text{if } \eta^P_{1a'} \eta^P_{1a} \eta^P_{2a'} \eta^P_{2a} (-1)^{L'+L} = -1, \tag{7.23}$$

where η^P_{ia} gives the intrinsic parity of particle i in channel a, and assuming time reversal invariance gives

$$s^{(J)}_{L'S'a';LSa}(E) = s^{(J)}_{LSa;L'S'a'}, \tag{7.24}$$

which just tells us that $s^{(J)}$ is symmetric.

For a single elastic channel involving spinless particles, the S-matrix is typically parameterized by

$$s^{(J)} = s^{(L)} = e^{2i\delta_L(E)}, \tag{7.25}$$

where $\delta_L(E)$ is the scattering phase shift for the L-th partial wave. The scattering phase shifts can be parameterized in terms of a Breit-Wigner to determine the resonance information.

If we now include another channel of spinless particles, then $s^{(L)}$ requires three parameters after using time reversal invariance and unitarity. The conventional parameterization is

$$s^{(L)} = \begin{bmatrix} \eta e^{2i\delta_1^{(L)}} & i\sqrt{1-\eta^2}e^{i(\delta_1^{(L)}+\delta_2^{(L)})} \\ i\sqrt{1-\eta^2}e^{i(\delta_1^{(L)}+\delta_2^{(L)})} & \eta e^{2i\delta_2^{(L)}} \end{bmatrix}, \tag{7.26}$$

where $\delta_i^{(L)}$ is the L-th partial wave for channel j, and $\eta \in [0,1]$ is the inelasticity. To reiterate, the inclusion of multiple waves and/or multiple channels does not allow all the parameters in the S-matrix to be determined exactly from the quantization condition, because it is only one condition involving multiple parameters. Additionally, the parameters used to parameterize the S-matrix (*i.e.* the phase shifts, the inelasticity, *etc.*) are not of significant interest to us. What we seek are the resonance masses and widths. Furthermore, as more and more channels are added, parameterizing a unitary matrix can become tedious.

For these reasons, we seek an approach that offers a simple parameterization in terms of quantities of interest. The K-matrix has the properties we seek:

$$K = (2T^{-1} + i)^{-1}, \tag{7.27}$$

where T is the transition operator defined by

$$S = 1 + iT, \tag{7.28}$$

and it has been assumed that $\det T \neq 0$.[7] The K-matrix is Hermitian, which can be shown to follow from the unitarity of the S-matrix. A Hermitian matrix is generally much simpler to parameterize than a unitary matrix and parameterizing K guarantees unitarity for S. Additionally, the K-matrix is symmetric from time reversal invariance. This follows from the fact that S is symmetric from time reversal invariance, and therefore T must be symmetric. Then, since T is symmetric, K must be symmetric from Eq. (7.27). Thus, K is a real

[7] If there are no interactions than $T = 0$, and thus $\det T = 0$, but in the interacting theory $\det T$ is expected to be nonzero.

symmetric matrix. Through some algebraic manipulations, one can solve for T in terms of K, and then substitute this into Eq. (7.28) to obtain S in terms of K. First,

$$\begin{aligned} T &= TK^{-1}K \\ &= T(2T^{-1} + i)K \\ &= 2K + iTK. \end{aligned} \tag{7.29}$$

Then, rearranging we have

$$T(1 - iK) = 2K, \tag{7.30}$$

which can easily be solved for T

$$T = 2K(1 - iK)^{-1}. \tag{7.31}$$

Finally, substituting this into Eq. (7.28), we have

$$\begin{aligned} S &= 1 + iT \\ &= 1 + 2iK(1 - iK)^{-1} \\ &= \Big[(1 - iK) + 2iK\Big](1 - iK)^{-1} \\ &= (1 + iK)(1 - iK)^{-1}. \end{aligned} \tag{7.32}$$

Additionally, starting with $T = KK^{-1}T$, and following similar steps, it can be shown that

$$S = (1 - iK)^{-1}(1 + iK). \tag{7.33}$$

Similar to the S-matrix, from rotational invariance the K-matrix is written as

$$\langle J' m_{J'} L' S' a' | \, K \, | J m_J L S a \rangle = \delta_{J'J} \delta_{m_{J'} m_J} K^{(J)}_{L'S'a';LSa}(E), \tag{7.34}$$

and from invariance under parity

$$K^{(J)}_{L'S'a';LSa}(E) = 0 \qquad \text{if } \; \eta^P_{1a'} \eta^P_{1a} \eta^P_{2a'} \eta^P_{2a} (-1)^{L'+L} = -1. \tag{7.35}$$

7.2.2 Parameterizing the K-matrix

In the case of a single elastic channel of spinless particles K is diagonal and given by

$$K^{(J)} = K^{(L)} = \tan\delta_L. \tag{7.36}$$

The pole in $K^{(L)}$ at $\delta_L = \pi/2$ is indicative of a resonance. And, for short-ranged interactions the phase shift can be expressed in terms of the effective range expansion

$$q_{cm}^{2L+1} K_L^{(L)-1} = q_{cm}^{2L+1} \cot\delta_L = -\frac{1}{a_L} + \frac{r_L}{2} q_{cm}^2 + O(q_{cm}^2), \tag{7.37}$$

where a_L is known as the scattering length, and r_L is known as the effective range. For convenience and due to the way K^{-1} appears in Eq. (7.37), we define $\widetilde{K}$ by

$$K^{-1}_{L'S'a';LSa}(E_{cm}) = u_{a'}^{-L'-\frac{1}{2}} \widetilde{K}^{-1}_{L'S'a';LSa}(E_{cm}) u_a^{-L-\frac{1}{2}}. \tag{7.38}$$

The benefit of using $\widetilde{K}^{-1}(E_{cm})$ is that it is expected to behave smoothly with energy E_{cm}. Then, through rotational invariance we have

$$\langle J' m_{J'} L' S' a' | \, \widetilde{K} \, | J m_J L S a \rangle = \delta_{J'J} \delta_{m_{J'} m_J} \mathcal{K}^{(J)}_{L'S'a';LSa}(E). \tag{7.39}$$

From the expectation that $\widetilde{K}^{-1}$ is a smooth function of E_{cm}, one clear parameterization is through an expansion in powers of E_{cm}

$$\mathcal{K}^{(J)-1}_{\alpha\beta}(E_{cm}) = \sum_{k=0}^{N_{\alpha\beta}} c^{(Jk)}_{\alpha\beta} E^k_{cm}, \tag{7.40}$$

where α and β are compound indices for L, S, and a; and the $c^{(Jk)}_{\alpha\beta}$ are a set of real symmetric matrices. The more physically relevant and intuitive parameterization one could consider involves a sum of poles with the possibility of a background term parameterized by a sum of powers in E_{cm} [79]

$$\mathcal{K}^{(J)}_{\alpha\beta}(E_{cm}) = \sum_p \frac{g^{(Jp)}_\alpha g^{(Jp)}_\beta}{E^2_{cm} - m^2_{Jp}} + \sum_k d^{(Jk)}_{\alpha\beta} E^k_{cm}, \tag{7.41}$$

where $g^{(Jp)}_\alpha$ are real couplings and $d^{(Jk)}_{\alpha\beta}$ are a set of real symmetric matrices. This parameterization is more interesting, because when extracting information about a particular

resonance, the m_{Jp} correspond to resonance masses and the $g_\alpha^{(Jp)}$ are couplings for the resonance to a particular channel which can be reparameterized in terms of a partial decay width. Thus, we see that not only is the K-matrix amenable to simple parameterizations with arbitrary numbers of partial waves and open channels, but can be simply written in terms of the physically relevant quantities.

7.3 THE BOX MATRIX

We now would like to rewrite the quantization condition in terms of $\widetilde{K}$:

$$\begin{aligned} 0 &= \det\left[1 + F^{(\boldsymbol{P})}(S-1)\right] \\ &= \det\left[1 + iF^{(\boldsymbol{P})}T\right] \\ &= \det\left[1 + 2iF^{(\boldsymbol{P})}K(1-iK)^{-1}\right], \end{aligned} \tag{7.42}$$

where we used the definition of the T matrix in the first line, and Eq. (7.31) in the second line. Next, because $(1-iK)$ is invertible, this implies that $\det(1-iK) \neq 0$, which allows us to write

$$\begin{aligned} 0 &= \det\left[1 + 2iF^{(\boldsymbol{P})}K(1-iK)^{-1}\right]\det(1-iK) \\ &= \det\left[1 - iK + 2iF^{(\boldsymbol{P})}K\right], \end{aligned} \tag{7.43}$$

where we have used the identity $\det(AB) = \det(A)\det(B)$. Thus, the quantization condition can be written as

$$\det\left[1 - \mathcal{B}^{(\boldsymbol{P})}K\right] = 0, \tag{7.44}$$

where

$$\mathcal{B}^{(\boldsymbol{P})} = -2iF^{(\boldsymbol{P})} + i. \tag{7.45}$$

We have now written the quantization condition in terms of the K-matrix, but we would like it in terms of $\widetilde{K}$. From the definition of $\widetilde{K}$ in terms of K in Eq. (7.38), we find the quantization condition to be

$$\det[1 - B^{(\boldsymbol{P})}\widetilde{K}] = 0, \tag{7.46}$$

where $B^{(\boldsymbol{P})}$ is known as the *box matrix* [27] and can be written as

$$\begin{aligned}\langle J'm_{J'}L'S'a'|\, B^{(\boldsymbol{P})}\, |Jm_JLSa\rangle &= u_a^{L'+L+1}\, \langle J'm_{J'}L'S'a'|\, \mathcal{B}^{(\boldsymbol{P})}\, |Jm_JLSa\rangle \\ &= u_a^{L'+L+1}\, \langle J'm_{J'}L'S'a'|\, (-2iF^{(\boldsymbol{P})}+i)\, |Jm_JLSa\rangle \\ &= -i\delta_{a'a}\delta_{S'S}u_a^{L'+L+1}W^{(\boldsymbol{P}a)}_{L'm_{L'};Lm_L}\, \langle J'm_{J'}|L'm_{L'},Sm_S\rangle\, \langle Lm_L,Sm_S|Jm_J\rangle\,.\end{aligned} \tag{7.47}$$

Generally, we parameterize $\widetilde{K}^{-1}$ instead of $\widetilde{K}$ itself. Hence, a more convenient form of the quantization condition is

$$\det[\widetilde{K}^{-1} - B^{(\boldsymbol{P})}] = 0. \tag{7.48}$$

7.4 BLOCK DIAGONALIZATION

The JLS basis in which the quantization condition has been derived is not suitable for our purposes. First, the energies we calculate are in the basis of the lattice symmetry group. Furthermore, the matrix inside the determinant condition is of infinite dimension, and thus evaluating this determinant is very difficult. Instead, we block diagonalize $B^{(\boldsymbol{P})}$ and $\widetilde{K}$ using the irreps of the little group, which allows us to work within the separate blocks. However, each of these blocks is still of infinite dimension, and we impose a maximum orbital angular momentum L_{max} in order to truncate each block. The basis we work with is given by

$$|\Lambda\lambda nJLSa\rangle = \sum_{m_J} c_{m_J}^{J\eta;\Lambda\lambda n}\, |Jm_JLSa\rangle\,, \tag{7.49}$$

where Λ is the little group irrep, λ is the irrep row, n is an integer that identifies the occurrence of the Λ irrep in the JLS basis, and $\eta = (-1)^L$. Further details on how the coefficients $c_{m_J}^{J\eta;\Lambda\lambda n}$ are determined can be found in Ref. [27]. In this basis, the box matrix can be written as

$$\langle \Lambda'\lambda'n'J'L'S'a'|\, B^{(\boldsymbol{P})}\, |\Lambda\lambda nJLSa\rangle = \delta_{\Lambda'\Lambda}\delta_{\lambda'\lambda}\delta_{S'S}\delta_{a'a}B^{(\boldsymbol{P}\Lambda_B Sa)}_{J'L'n';JLn}. \tag{7.50}$$

Note that Λ_B is used in the box matrix, instead of Λ. This arises because the box matrix is independent of the intrinsic parities of the scattering particles, whereas we choose the irrep Λ to involve the intrinsic parities. If $\eta_{1a}^P\eta_{2a}^P = 1$, then $\Lambda_B = \Lambda$. But, if $\eta_{1a}^P\eta_{2a}^P = -1$, then in general $\Lambda_B \neq \Lambda$. The relationship between Λ_B and Λ in this case is shown in Table 7.1.

Table 7.1: The relationship between the irrep of the B-matrix to the irrep of the lattice symmetry group. If $\eta_{1a}^P \eta_{2a}^P = 1$, then $\Lambda_B = \Lambda$. Otherwise, the relationship is shown here. *LG* stands for the "little group". Table taken from Ref. [27].

$\boldsymbol{d}$	LG	Λ_B relationship to Λ when $\eta_{1a}^P \eta_{2a}^P = -1$
$(0,0,0)$	O_h	Subscript $g \leftrightarrow u$
$(0,0,n)$	C_{4v}	$A_1 \leftrightarrow A_2$; $B_1 \leftrightarrow B_2$; E, G_1, G_2 unchanged
$(0,n,n)$	C_{2v}	$A_1 \leftrightarrow A_2$; $B_1 \leftrightarrow B_2$; G unchanged
(n,n,n)	C_{3v}	$A_1 \leftrightarrow A_2$; $F_1 \leftrightarrow F_2$; E, G unchanged

7.5 FITTING STRATEGIES

We now describe two different fitting strategies to determine best fits for the parameterization of the $\widetilde{K}$-matrix. The methods differ in the choice of the residuals to be used in a χ^2 minimization (see Appendix B for a review of fitting with a χ^2 minimization and an introduction to the notation we use). There is an advantage to making sure the model you fit to does not depend on the data (observables). If your model does depend on the observations, then you must calculate the covariance between the residuals which depend on your model parameters. Hence, as the fit proceeds and the fit parameters are adjusted, these covariances need to be updated, and the covariance matrix needs to be inverted. This can be computationally demanding, and we seek models that do not depend on the observables, because then one only needs the covariance between the observables which does not change as the fit proceeds.

7.5.1 The Spectrum Method

In this method, as the fit proceeds, each time the parameters of $\widetilde{K}$ or $\widetilde{K}^{-1}$ are adjusted, we scan the determinant in the quantization condition to find all of its zeros. This provides us

with a set of energies in the center-of-momentum frame predicted from the model $E_{cm,i}^{(mod)}$. Then, the choice of residuals is straightforward

$$r_i = E_{cm,i}^{(obs)} - E_{cm,i}^{(mod)}. \tag{7.51}$$

Naively, it would seem that the model has completely separated from the observations, and we are free to compute the covariances among the $E_{cm,i}^{(obs)}$ once. But, this has completely ignored the fact that the evaluation of the determinant necessarily involves calculating the RGL-shifted zeta functions which depend on the size of our lattice L, the anisotropy of our lattice $\xi = a_s/a_t$, and the masses of the decay products in each channel m_{1a}, m_{2a}. These are themselves observed quantities, and thus the model predictions do in fact depend on our observations, which means we must recompute the covariance between the residuals every time the fit parameters are updated. A clever way around this issue was proposed in Ref. [27], which suggests introducing $L^{(mod)}$, $\xi^{(mod)}$, $m_{1a}^{(mod)}$, and $m_{2a}^{(mod)}$ as fit parameters themselves. Of course, the minimization should give model predictions for these added parameters that are nearly identical to the observed values, but the advantage is that we have completely separated the observables from the model predictions, and we are justified in calculating the covariance matrix once at the beginning of the fit between all the observed quantities. However, the major shortcoming of this procedure is the need for calculating the determinant and scanning it for zeros, which is a significant computational effort. Despite these complications, the method has been used (ignoring the extra residuals and improperly calculating the covariances) in Refs. [81, 82, 83, 84].

7.5.2 The Determinant Residual Method

This method introduced in Ref. [27], is based on using the determinant condition itself as a part of the residuals. In this paper, it is suggested to not use the determinant condition itself as a residual, because the determinant can become very large for certain matrices. Instead, they propose using the function

$$\Omega(\mu, A) \equiv \frac{\det(A)}{\det\left[(\mu^2 + AA^\dagger)^{1/2)}\right]}, \tag{7.52}$$

where $\mu \neq 0$ is a scalar. This function is zero whenever $\det(A)$ is zero, and thus it reproduces the quantization condition. The added advantage of this function, is that it is bounded between -1 and 1 when the determinant is real, and therefore this is a better behaved function to use as a residual. Thus, for the quantization condition, the residual used is

$$r_i = \Omega\Big(\mu, \widetilde{K}^{-1}(E_{cm,i}^{(obs)}) - B^{(\boldsymbol{P})}(E_{cm,i}^{(obs)})\Big), \tag{7.53}$$

but any of the different forms appearing inside the determinant of the quantization condition could be used in place of $\widetilde{K}^{-1}(E_{cm,i}^{(obs)}) - B^{(\boldsymbol{P})}(E_{cm,i}^{(obs)})$. In this case, the model is dependent on the observables, and we must recalculate the covariance matrix as the parameters are adjusted. However, this method has the advantage that the box matrix is only calculated once for each observed energy, whereas the previous method required the box matrix to be recalculated every time the parameters were adjusted. Since computing the box matrix requires evaluating the complicated RGL-shifted zeta functions, this is a significant benefit of determinant residual method. This is the method we exclusively use in this work.

8.0 RESULTS

We now present results on a large $32^3 \times 256$ lattice with $m_\pi \approx 240\,\text{MeV}$. First, the finite-volume spectrum is extracted up to $\sim 2\,\text{GeV}$ from large correlator matrices using the single pivot method (see Sec. 6.2.2) for all bosonic isovector non-strange channels at rest with odd parity and even G-parity (*i.e.* A_{1u}^+, A_{2u}^+, E_u^+, T_{1u}^+, and T_{2u}^+ with $I = 1$, $S = 0$, and $\boldsymbol{P} = 0$). Then, the resonance properties of the $K^*(892)$ are extracted using the determinant residual method (see Sec. 7.5.2) with a 3×3 K-matrix, which is based on the formalism introduced by Lüscher.

8.1 COMPUTATIONAL DETAILS

The gauge configurations used in this work were generated using the Chroma software system for lattice QCD [85] provided by the USQCD collaboration, which used the RHMC algorithm [44] (see Sec. 2.3.2). These calculations were mainly performed on the Jaguar system at Oak Ridge National Laboratory sponsored by the Department of Energy (DOE) and on the Kraken system at the University of Tennessee sponsored by the National Science Foundation (NSF). This required approximately 200 million core-hours.

Software utilizing the Chroma software system, known as Chroma LapH, was written in C++ for calculating the quark sinks/sources (see Sec. 4.3) and then using these to form hadron sinks/sources (see Sec. 4.4). The calculation of the quark sinks involves performing many inversions, which are very computationally expensive. These inversions were done using the biconjugate gradient method and total around 100 million core-hours (run mainly on the Kraken system). This software is heavily parallelized by making use of the Open MPI

and OpenMP libraries.

The last step in the calculation of a temporal correlation function involves summing products of the hadron sinks and sources. The needed products in this summand and their coefficients are determined by the Wick contractions for each correlator. Then, this result is summed over each dilution index and each noise vector to obtain the correlator for each gauge configuration. Serial software to perform this last part of the calculation, known as Last LapH, was written in C++. These calculations require significant I/O, and we have made use of Stampede at the Texas Advanced Computing Center (TACC) made available through the Extreme Science and Engineering Discovery Environment (XSEDE) [86]. This system was chosen because of its use of large lustre partitions, which are very beneficial for our I/O intensive calculations.

Finally, software for analyzing the temporal correlators, known as SigMonD, was also written in C++. All of our software is XML driven, which means that any particular calculation is done by passing an XML file as input that specifies the tasks to be performed and any necessary input parameters. There is usually significant variation in the XML files that are used, and to help with this process, we have developed scripts in Ruby and Python to generate the needed XML.

8.2 OPERATOR SELECTION

Considering the vast number of independent operators that can be constructed, we must consider some way of "pruning" these sets of operators down to a reasonable size. First, operators associated with very large correlator errors were removed. Next, operators whose effective energy appeared to plateau well above $\sim 2\,\mathrm{GeV}$ were also discarded. Finally, the left over operators were used to form a correlator matrix and operators were removed until the condition number of the normalized correlator matrix at some early time separation was smaller than ≈ 100.

This procedure works well for obtaining a small set of single-hadron operators, but the shear number of independent two-hadron operators that can be formed from a given set

of single-hadron operators is far too large to be feasible to work with. To prune the two-hadron operators, as well as to ensure we do not miss any single- or two-hadron dominated stationary states below $\sim 2\,\mathrm{GeV}$, we attempted to choose one or two operators for each stationary state that couple to that state very strongly. To assist in this goal, a list of "expected" energy levels was created for each channel. These levels were determined by assuming no interactions between the individual hadrons. Thus, these energies are not the true interacting energies but should give a rough guide to the states we expect to appear in each channel. The hadrons used in these expected levels were taken directly from the Particle Data Group (PDG) [9]. For each expected level, the set of operators expected to couple strongly to that level is chosen. Then, from this smaller set of operators, we pick the one or two operators which result in the smallest errors in our temporal correlators.

8.3 THE $I = 1, S = 0, P = -1, G = +1$ BOSONIC SPECTRA

For each channel, the operators chosen are first based on the non-interacting energies. For each non-interacting energy below $\sim 2\,\mathrm{GeV}$ one or two operators are chosen based on the expectation of those operators to overlap strongly onto the corresponding interacting energy. Additionally, in order to ensure all levels are extracted, an additional set of operators is added to the correlator matrix. The operators used to form the correlator matrix in each channel are shown in Appendix C.

The energies extracted from our fits to a diagonalized correlator are in units of the temporal lattice spacing (*i.e.* we extract the dimensionless quantity $\hat{m} = a_t m$). Hence, in order to compare our results with experiment, we either need to divide this result by a_t or by some reference energy fit for which the energy in physical units is known. It is simpler and more robust to divide by a reference energy. In what follows, the kaon is used as our reference energy to set the scale, and therefore comparison to experiment will be made with energies as ratios over the kaon mass. The kaon is chosen, because the parameters of the lattice action were specifically tuned such that the kaon mass was near its experimentally measured mass. The fit used is shown in Figure 8.1. The extracted energy in units of the temporal

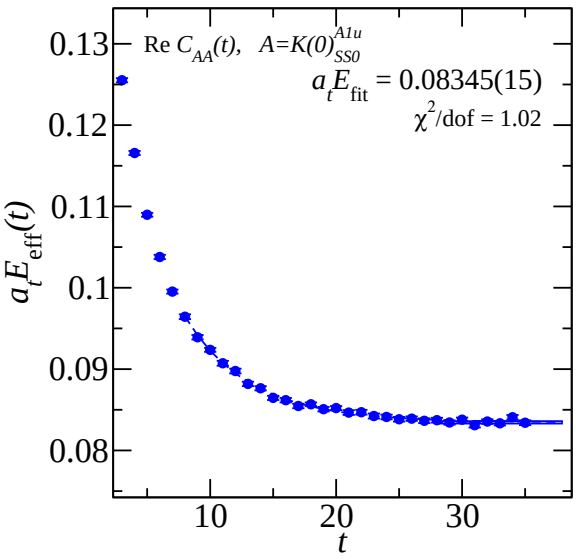

Figure 8.1: A time symmetric geometric series exponential fit with range $(8, 38)$ to the temporal correlator using a kaon single-site operator with $\boldsymbol{P} = (0, 0, 0)$ and transforming in the irrep A_{1u}. This fit will be used as the reference energy for all other fits. The fit was done using jackknife resampling.

lattice spacing is $a_t m_K = 0.08345(15)$. Using the average of the experimentally measured masses for the K^+ and the K^0 from the PDG [9], which is approximately 495.644(11) MeV, we can convert our results to physical units.

One major goal of these finite-volume spectrum extractions is the identification of hadronic resonances. This identification can be done by measuring the overlap factors (6.8) to determine which stationary states appear to be single-hadron dominated. We start by replacing our single-hadron operators with variationally improved single-hadron operators. These are found by first rotating the correlator matrix with only single-hadron operators, and then using the linear combinations of these operators that diagonalized the correlator matrix as our variationally improved single-hadron operators. Using these improved operators helps to remove mixing between the states created by our single-hadron operators. Then, we determine the overlap factors for each variationally-improved single-hadron operator. For each

improved operator, we take the stationary state with the largest overlap and classify this state as single-hadron dominated. We still expect there to be some mixing in the vicinity of this energy, and therefore any stationary states with overlaps larger than 75% of the largest overlap for that operator we classify as 'significant mixing'.

So long as the energy of the single-hadron dominated states are not too near a threshold (where energies are distorted due to avoided level crossings), and the associated resonance is narrow (we can only expect agreement to occur within the size of the decay width), then the finite-volume energy found will have only exponentially decaying corrections to the energy of the corresponding particle in infinite volume.

For each channel we consider, we use jackknife resampling to obtain errors for our fitted energies, and we normalize our correlator matrices using the correlator matrix at a time separation $\tau_N = 3$. As discussed above, the operators are based on the expected levels in Appendix C. We make sure to use $\sim \frac{3}{2}n$ operators, where n is the number of levels we wish to extract (usually we set n to be approximately the number of levels shown in the expected levels tables). The use of $\frac{3}{2}n$ is based on the results discussed in Sec. 6.2.1.

In each section that follows, the fit results for each level are displayed in a table. The effective energies for each level are also shown, with the fit curve for each level overlaid on the plots. The overlap factors are also shown for each operator. And, finally, a so-called staircase plot of energies is displayed, and the stationary states deemed 'single-hadron dominated' and 'significant mixing' are labeled. If we expect any hadronic resonances to appear in the channel in question, a comparison between the stationary states deemed 'single-hadron dominated' and the experimentally observed resonances are made. Additionally, these sections begin with an analysis similar to that described above but using a correlator matrix containing only single-hadron operators.

8.3.1 A_{1u}^+

From the table of expected levels for the A_{1u}^+ channel shown in Table C1 we see that we expect 25 single- and two-hadron levels to appear below the 2 GeV cutoff. We decided on 38 operators that transformed irreducibly under the appropriate symmetry groups for this

channel. Three of these operators were single-hadron operators. Although, experiment tells us that we should not expect to see any resonances in this channel, 3 single-hadron operators were included in order to make sure all states were extracted. However, the noise and quick decay of these operators required a metric time $\tau_0 = 3$, and a diagonalize time $\tau_D = 6$ in order to avoid the errors at small times introduced from the single-hadron operators. The reason that these operators quickly decay is likely due to the fact that if there are any single-hadron states in this channel, then they are probably much higher than the 2 GeV cutoff. The condition number of the $C(\tau_0)$ and $G(\tau_D)$ was 3.18 and 4.45, respectively, which caused us no issues. The lowest 33 levels are shown in Table 8.1. The effective energies for these levels are shown in Figures 8.3 and 8.5 with the fit curves overlaid on the plots. The overlap factors are shown in Figures 8.4 and 8.6, and the spectrum is shown on a staircase plot in Figure 8.2.

Table 8.1: The lowest 33 levels extracted from a 38×38 correlator matrix in the A_{1u}^+ channel.

Level	**Model**	t_{min}	t_{max}	$a_t E_{fit}$	E_{fit}/E_{ref}	χ^2/dof
0	Forward2Exp	3	26	0.211(13)	2.53(16)	1.38
1	Forward2Exp	3	26	0.2346(46)	2.812(56)	1.11
2	ForwardGeomSeriesExp	3	26	0.2504(13)	3.001(17)	1.38
3	Forward2Exp	3	24	0.2633(51)	3.155(61)	1.44
4	Forward2Exp	4	25	0.266(11)	3.18(13)	1.27
5	Forward2Exp	5	26	0.2691(52)	3.224(63)	1.3
6	Forward2Exp	3	26	0.275(13)	3.30(15)	0.81
7	Forward2Exp	3	26	0.2829(18)	3.390(22)	0.89
8	Forward2Exp	3	24	0.2918(70)	3.497(85)	1.44
9	Forward2Exp	3	22	0.3026(58)	3.626(71)	1.26
10	ForwardGeomSeriesExp	3	26	0.3041(10)	3.645(14)	1.0
11	Forward2Exp	3	26	0.3070(39)	3.679(47)	0.95

Table 8.1: (continued)

Level	**Model**	t_{min}	t_{max}	$a_t E_{fit}$	E_{fit}/E_{ref}	χ^2/dof
12	Forward2Exp	3	23	0.3097(70)	3.711(84)	0.92
13	Forward2Exp	3	22	0.314(16)	3.76(19)	1.16
14	Forward2Exp	3	24	0.325(11)	3.89(13)	0.97
15	ForwardGeomSeriesExp	3	26	0.3274(20)	3.924(25)	0.7
16	Forward2Exp	3	24	0.328(15)	3.93(18)	1.4
17	Forward2Exp	3	21	0.332(11)	3.97(13)	1.7
18	Forward2Exp	3	21	0.339(18)	4.07(22)	0.96
19	Forward2Exp	3	19	0.343(23)	4.12(27)	0.77
20	Forward2Exp	3	25	0.345(12)	4.13(15)	1.12
21	Forward2Exp	3	24	0.347(11)	4.15(14)	1.14
22	Forward2Exp	3	26	0.348(18)	4.17(22)	1.03
23	Forward2Exp	3	17	0.349(32)	4.18(38)	0.79
24	ForwardExp	6	18	0.356(15)	4.26(18)	0.5
25	Forward2Exp	3	23	0.363(12)	4.35(14)	1.38
26	ForwardExp	7	18	0.371(23)	4.45(27)	1.66
27	ForwardExp	6	18	0.378(11)	4.54(13)	1.69
28	Forward2Exp	3	24	0.396(22)	4.74(27)	0.81
29	Forward2Exp	3	14	0.406(21)	4.86(25)	1.34
30	Forward2Exp	3	21	0.410(17)	4.91(21)	1.04
31	Forward2Exp	3	21	0.4325(92)	5.18(11)	1.28
32	ForwardExp	6	22	0.4326(98)	5.18(12)	1.2

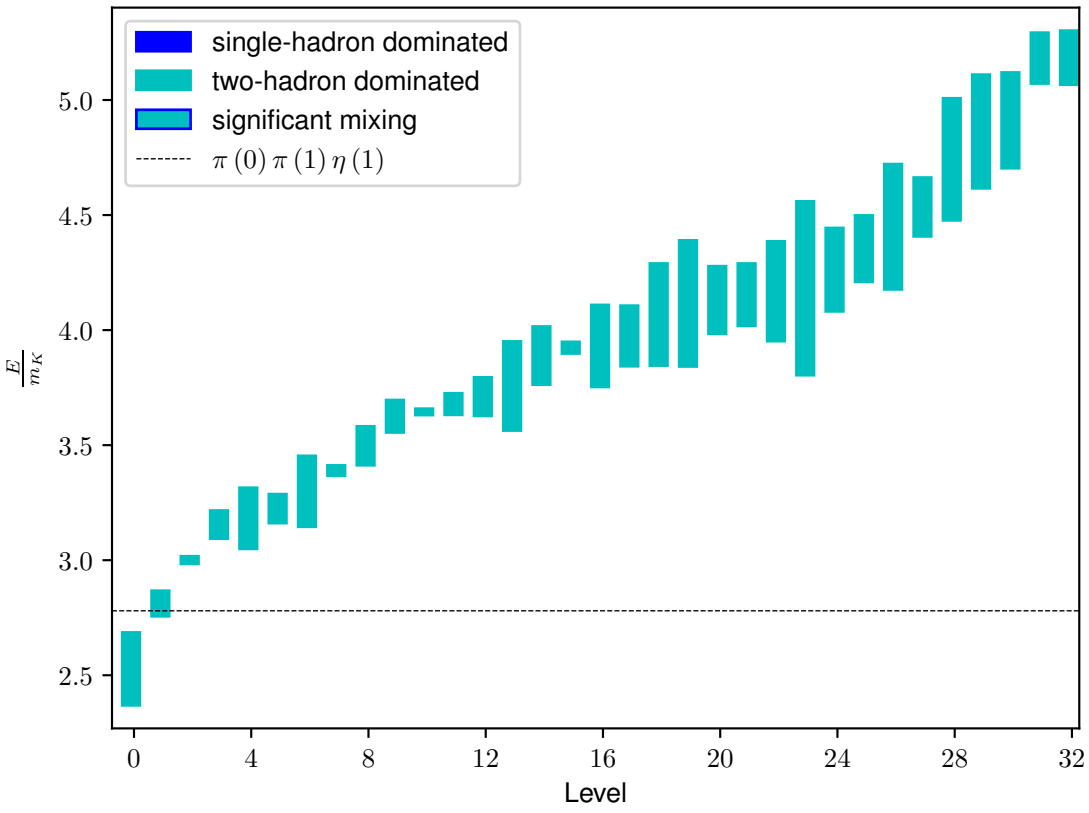

Figure 8.2: The staircase plot, which shows the lowest 33 levels extracted in the A_{1u}^{+} channel.

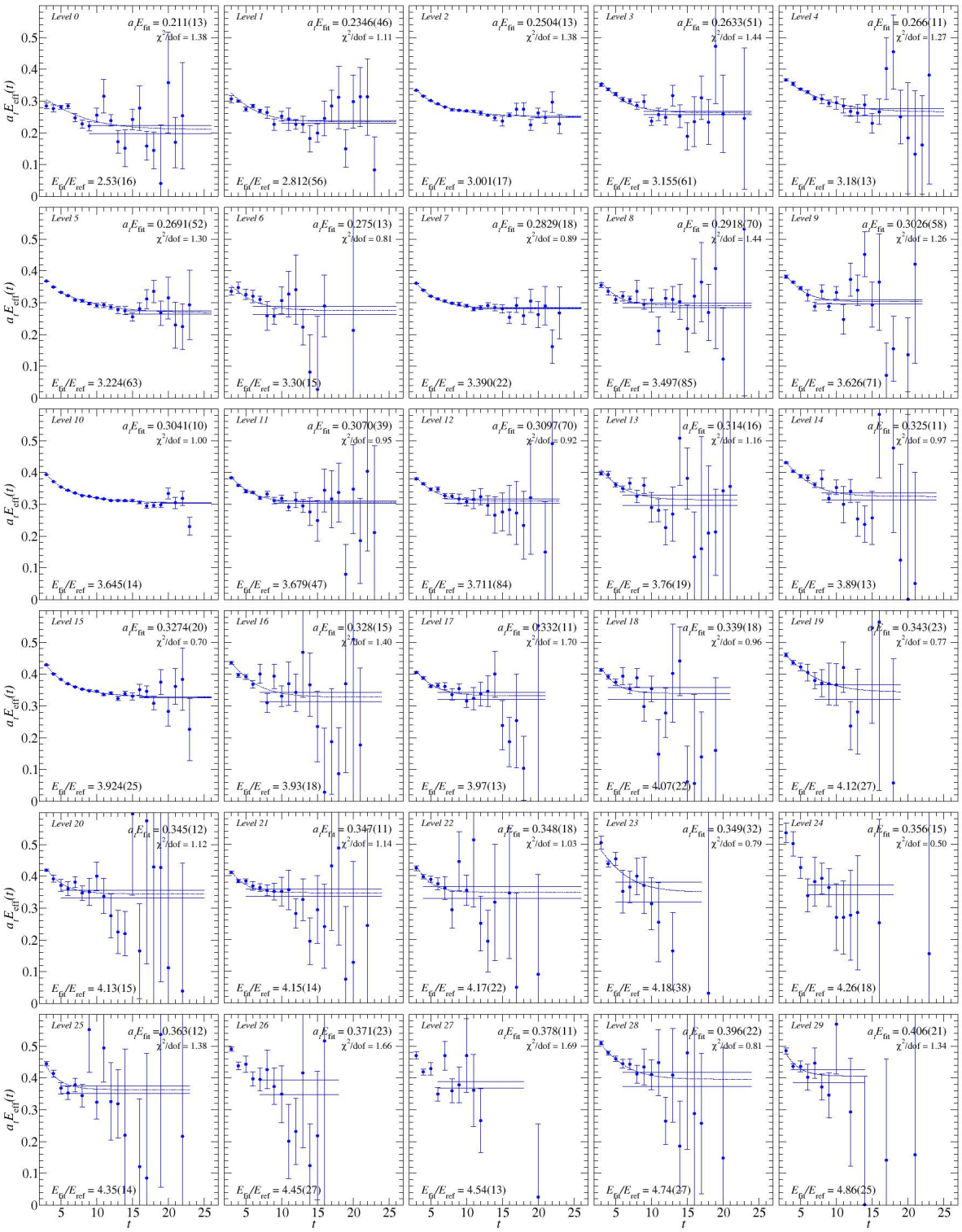

Figure 8.3: The effective energies for the lowest 30 levels in the A_{1u}^+ channel with the fits overlaid on the plots.

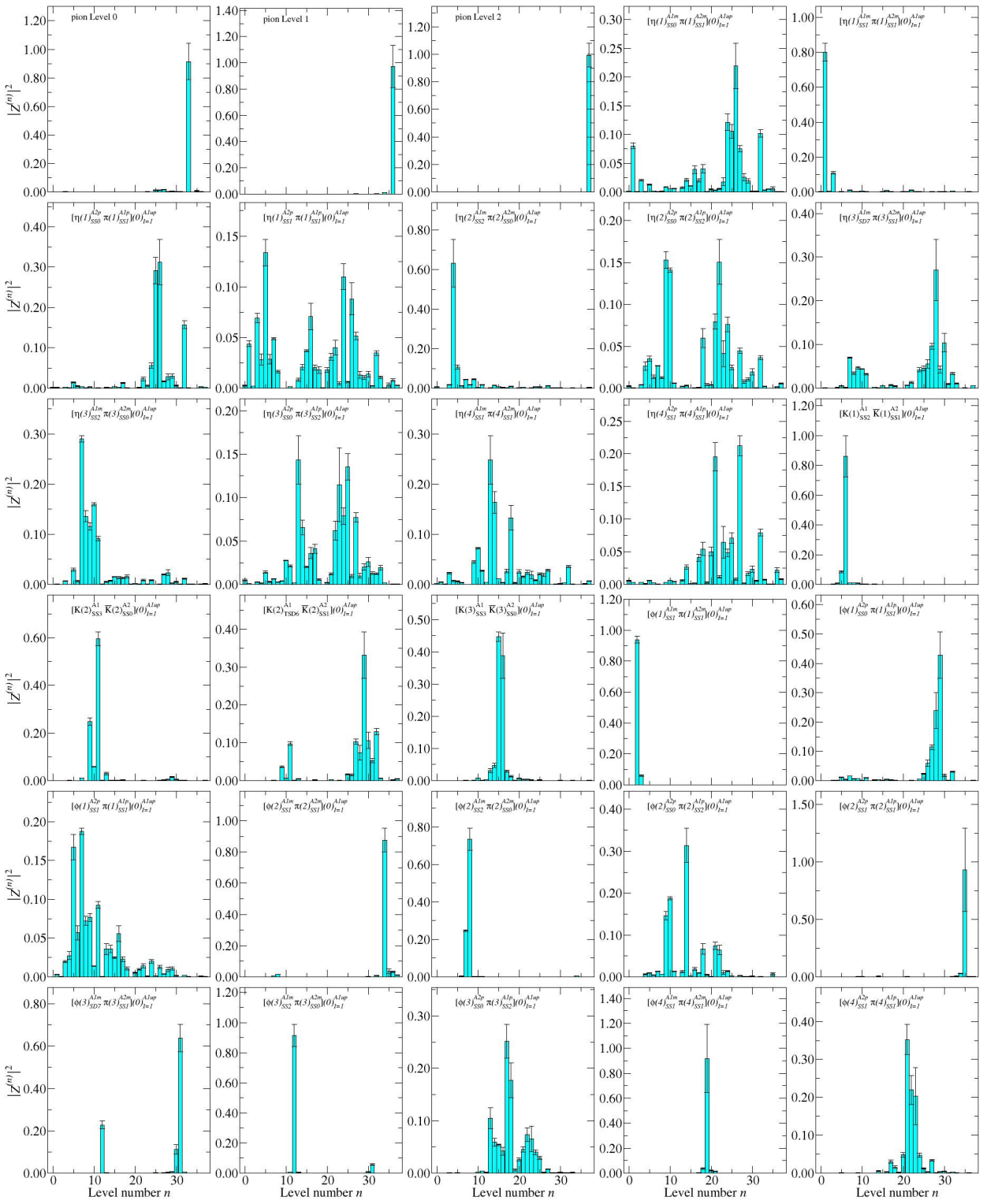

Figure 8.4: The overlap factors for the first 30 operators considered in the A_{1u}^+ channel.

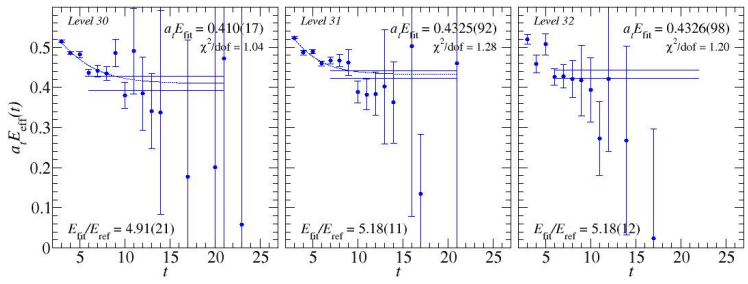

Figure 8.5: The effective energies for levels $30 - 32$ in the A_{1u}^+ channel with the fits overlaid on the plots.

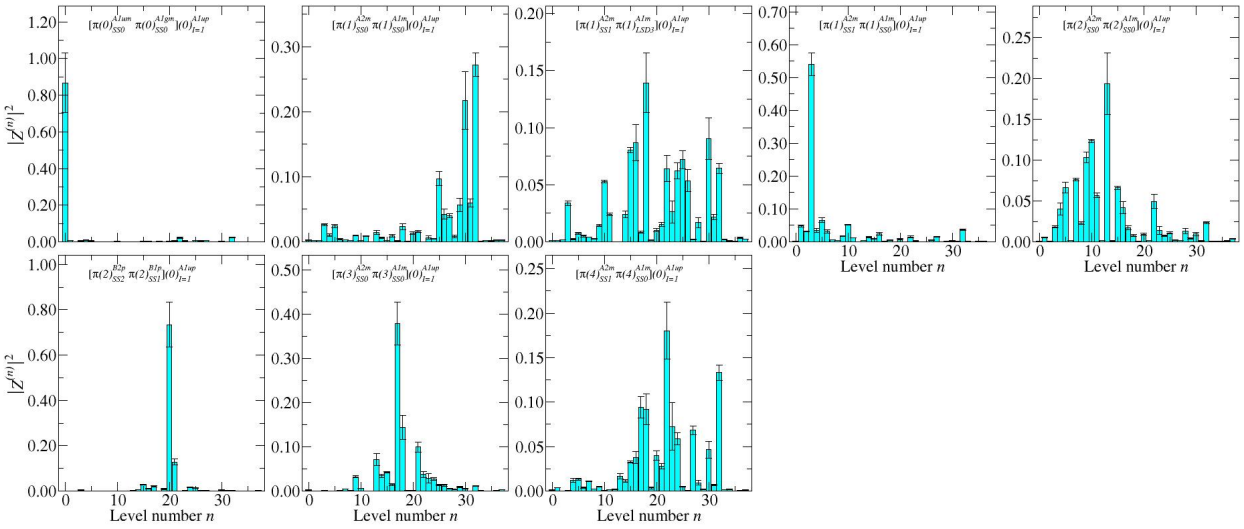

Figure 8.6: The overlap factors for last 8 operators considered in the A_{1u}^+ channel.

8.3.2 A_{2u}^+

From the expected levels table for the A_{2u}^+ channel shown in Table C3, we see that we expect 14 single- and two-hadron levels, including the $\rho_3(1690)$, to appear below the 2 GeV cutoff. We decided on 26 operators that transformed irreducibly under the appropriate symmetry groups for this channel, 3 of which were single hadron operators. The metric time and diagonalization time were chosen to be $\tau_0 = 4$ and $\tau_D = 8$, respectively. The condition number of the $C(\tau_0)$ and $G(\tau_D)$ was 3.36 and 4.81, respectively, which means our correlator matrix is reasonably well-conditioned.

8.3.2.1 Single Hadron Operators In this channel, we expect the $\rho_3(1690)$ and $\rho_3(1990)$ resonances to appear. Therefore, we start with an analysis of just the single-hadron operators. The 3 levels extracted from the correlator matrix consisting of 3 single-hadron operators are shown in Table 8.2.

Table 8.2: The levels extracted from a 3×3 correlator matrix consisting of single-hadron operators in the A_{2u}^+ channel.

Level	**Model**	t_{min}	t_{max}	$a_t E_{fit}$	E_{fit}/E_{ref}	χ^2/dof
0	Forward2Exp	3	21	0.296(22)	3.55(27)	0.79
1	ForwardExp	5	17	0.478(17)	5.73(20)	0.5
2	ForwardExp	5	15	0.564(98)	6.8(1.2)	1.31

8.3.2.2 All operators, Single Hadron Improved Operators The lowest 18 levels are shown in Table 8.3. The effective energies for these levels are shown in Figure 8.12 with the fit curves overlaid on the plots. The overlap factors are shown in Figure 8.13, and the spectrum is shown on a staircase plot in Figure 8.10. There is a clear discrepancy between the extracted levels and experiment as can be seen in Figure 8.11 (notice the significant decrease in error in the lowest single-hadron dominated state after including two-hadron

operators). This suggests that either the $\rho_3(1690)$ or the $\rho_3(1990)$ may not be a quark-antiquark excitation.

Table 8.3: The lowest 18 levels extracted from a 26×26 correlator matrix in the A_{2u}^+ channel. The bolded level is single-hadron dominated.

Level	**Model**	t_{min}	t_{max}	$a_t E_{fit}$	E_{fit}/E_{ref}	χ^2/dof
0	Forward2Exp	3	26	0.2234(35)	2.677(43)	1.32
1	Forward2Exp	4	26	0.2675(18)	3.205(22)	1.29
2	Forward2Exp	3	26	0.2682(33)	3.214(40)	1.12
3	ForwardGeomSeriesExp	4	26	0.27971(93)	3.352(12)	1.42
4	Forward2Exp	3	21	0.296(12)	3.55(15)	1.55
5	Forward2Exp	3	26	0.3039(74)	3.642(88)	1.17
6	**Forward2Exp**	**3**	**26**	**0.3085(22)**	**3.697(27)**	**0.63**
7	Forward2Exp	3	22	0.315(12)	3.77(14)	0.92
8	Forward2Exp	3	26	0.324(28)	3.88(34)	1.74
9	Forward2Exp	3	24	0.332(14)	3.98(17)	1.01
10	Forward2Exp	3	23	0.3333(89)	3.99(11)	0.87
11	Forward2Exp	3	22	0.338(12)	4.05(14)	0.76
12	Forward2Exp	3	24	0.3427(99)	4.11(12)	1.32
13	Forward2Exp	3	21	0.346(18)	4.15(21)	1.02
14	Forward2Exp	3	24	0.355(17)	4.26(20)	1.31
15	Forward2Exp	3	25	0.3559(62)	4.265(74)	1.27
16	Forward2Exp	3	24	0.380(19)	4.55(23)	1.25
17	Forward2Exp	3	18	0.394(34)	4.73(41)	1.12

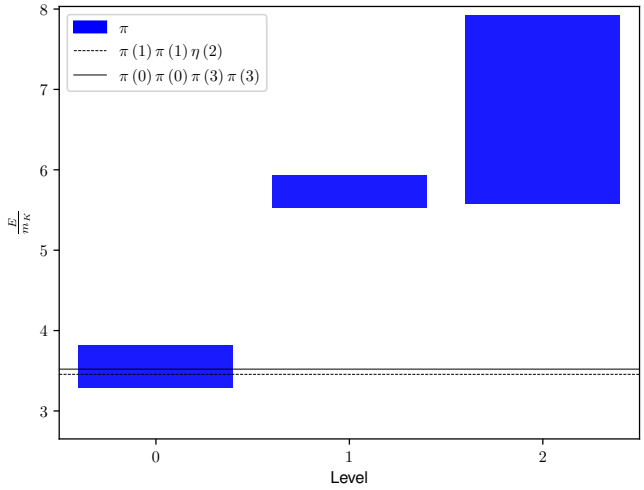

Figure 8.7: The staircase plot for the levels extracted in the A_{2u}^+ channel using only single-hadron operators.

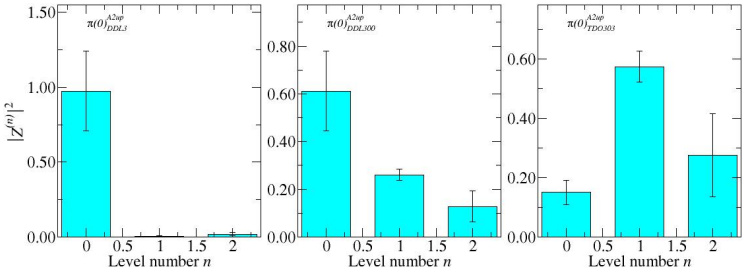

Figure 8.8: The overlap factors for the 3 single-hadron operators considered in the A_{2u}^+ channel.

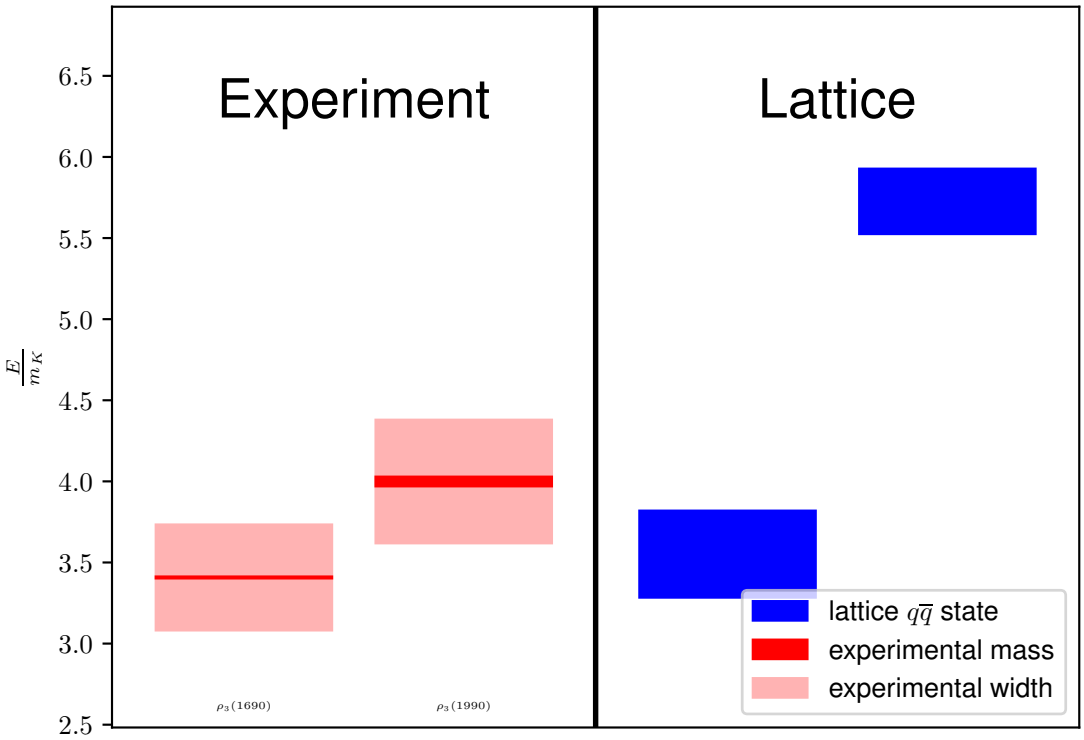

Figure 8.9: A comparison between the experimental resonances expected to appear in the A_{2u}^+ channel and the levels extracted by only considering the 3 single-hadron operators.

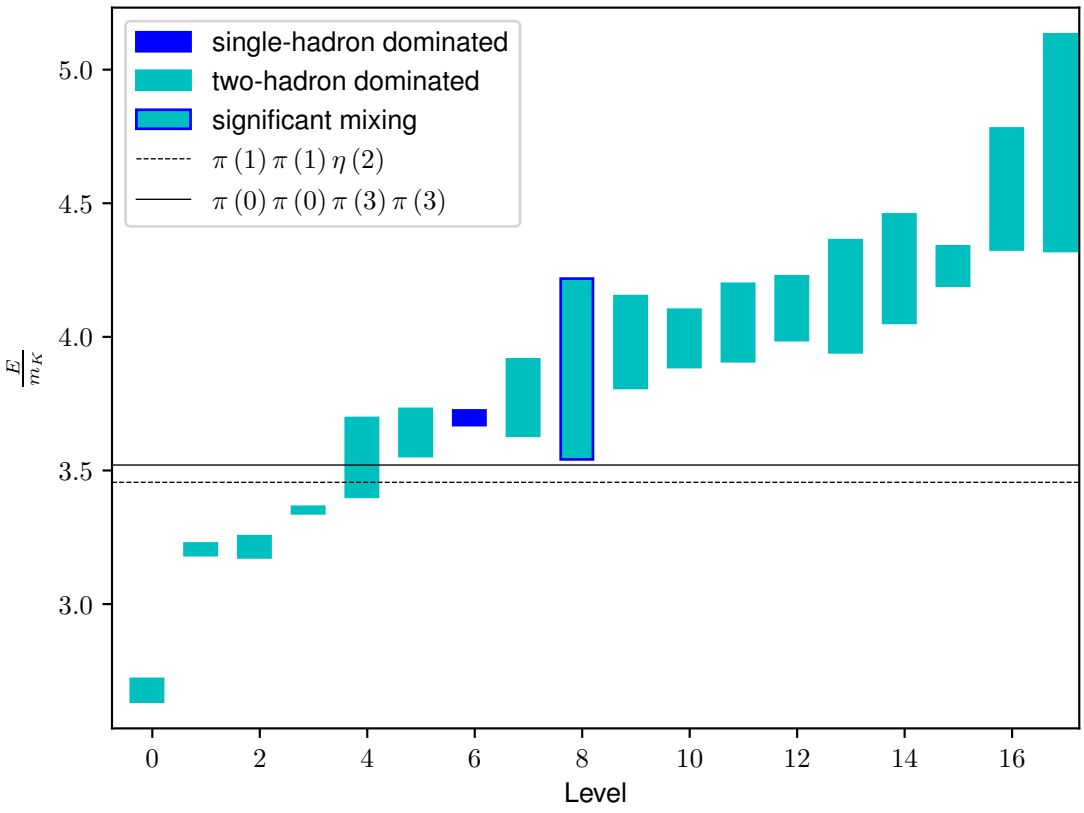

Figure 8.10: The staircase plot, which shows the lowest 18 levels extracted in the A_{2u}^{+} channel.

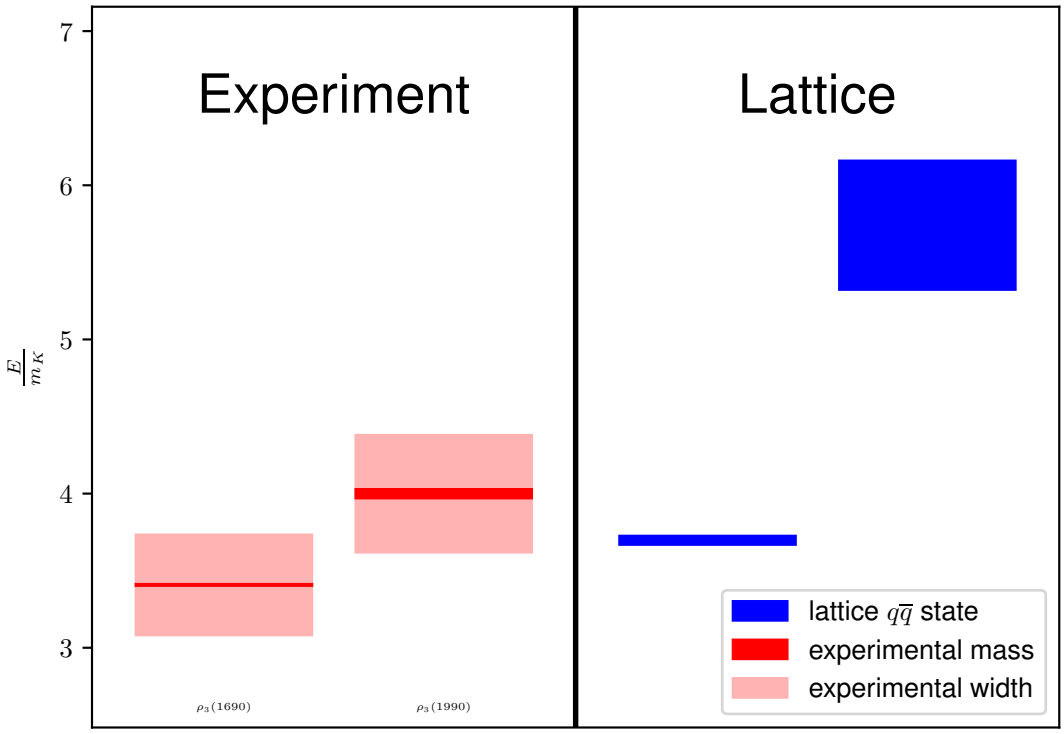

Figure 8.11: A comparison between the experimental resonances expected to appear in the A_{2u}^+ channel and the levels that were determined to be single-hadron dominated.

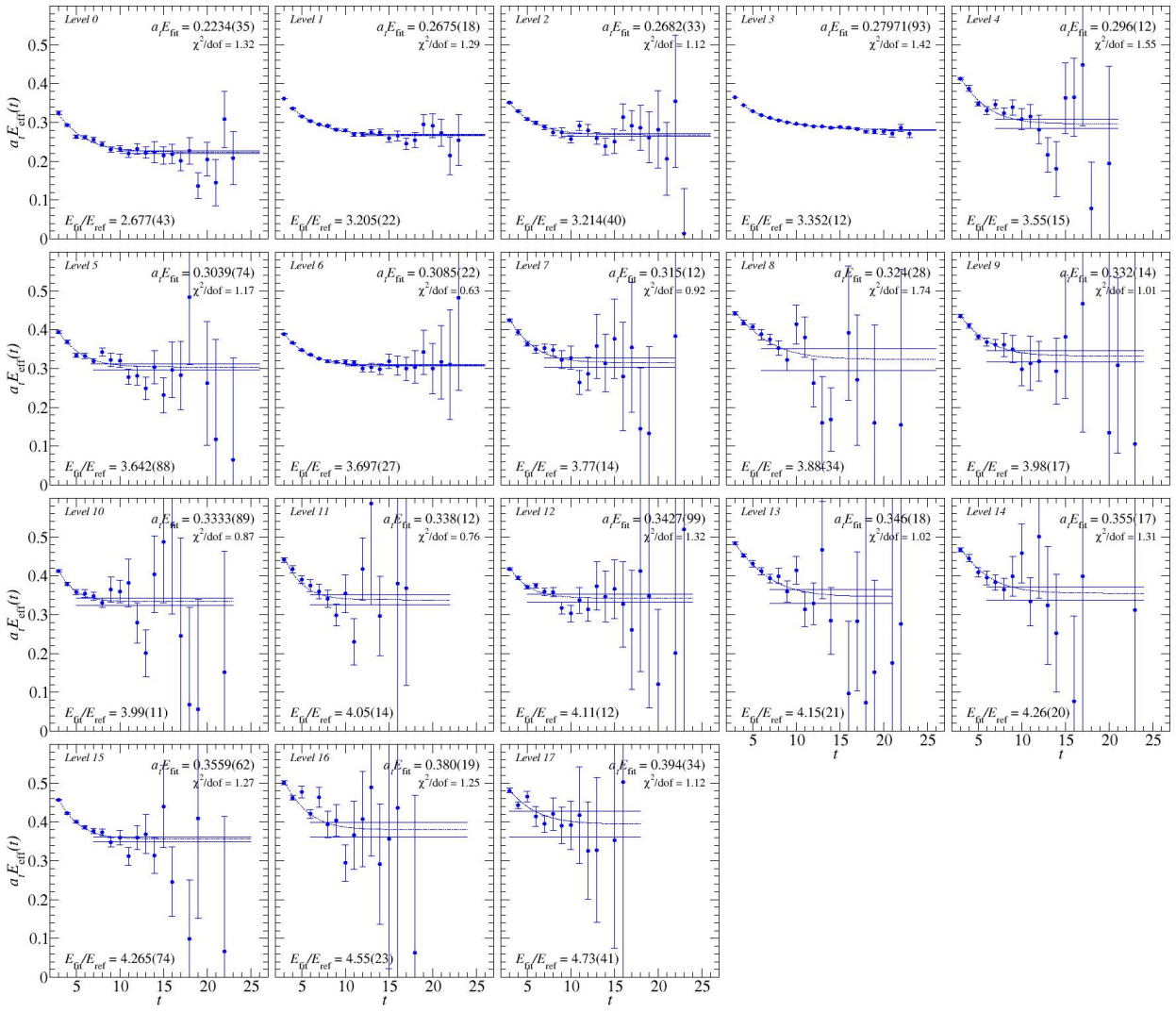

Figure 8.12: The effective energies for the lowest 18 levels in the A_{2u}^+ channel with the fits overlaid on the plots.

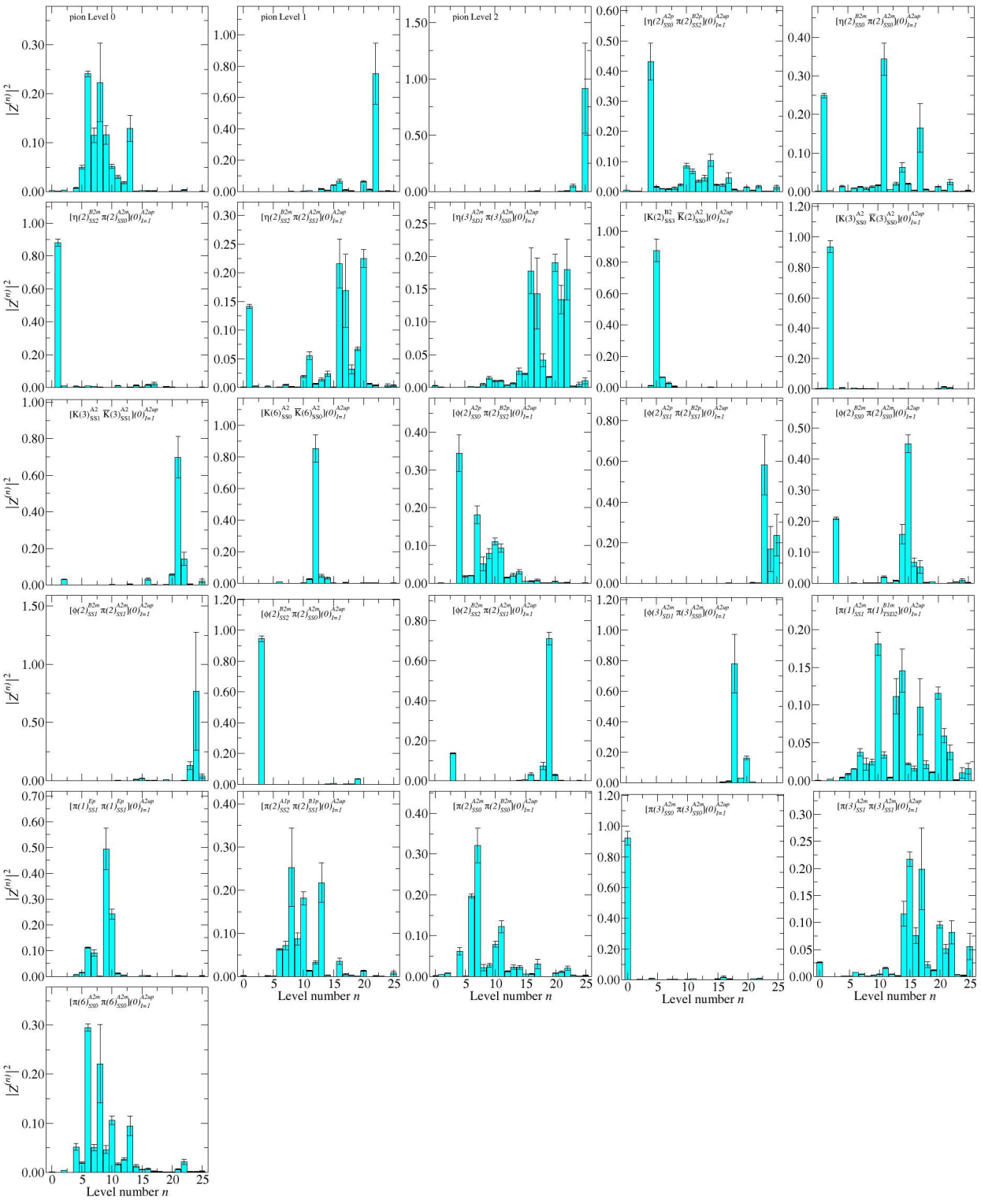

Figure 8.13: The overlap factors for operators considered in the A_{2u}^+ channel.

8.3.3 E_u^+

From the table of expected levels for the E_u^+ channel shown in Table C5 we see that we expect 28 single- and two-hadron levels to appear below the 2 GeV cutoff. We decided on 46 operators that transformed irreducibly under the appropriate symmetry groups for this channel. Two of these operators were single-hadron operators. Although, experiment tells us that we should not expect to see any resonances in this channel, 2 single-hadron operators were included in order to make sure all states were extracted. The metric time and diagonalization time were chosen to be $\tau_0 = 4$ and $\tau_D = 8$, respectively. The condition number of the $C(\tau_0)$ and $G(\tau_D)$ was 3.56 and 3.45, respectively, which caused us no issues. The lowest 36 levels are shown in Tables 8.4. The effective energies for these levels are shown in Figures 8.15 and 8.17 with the fit curves overlaid on the plots. The overlap factors are shown in Figures 8.16 and 8.18, and the spectrum is shown on a staircase plot in Figure 8.14. Although we did not expect any resonances in this channel, the overlap factors identify level 12 as being single-hadron dominated. This may be an indication of the existence of a spin-2 resonance in this channel.

Table 8.4: The lowest 36 levels extracted from a 46×46 correlator matrix in the E_u^+ channel. The bolded level is single-hadron dominated.

Level	**Model**	t_{min}	t_{max}	$a_t E_{fit}$	E_{fit}/E_{ref}	χ^2/dof
0	Sym2Exp	3	24	0.2409(77)	2.887(92)	1.13
1	Forward2Exp	3	25	0.259(11)	3.10(13)	1.5
2	Forward2Exp	3	25	0.2697(32)	3.232(39)	1.03
3	Forward2Exp	3	24	0.2766(66)	3.315(79)	1.05
4	Forward2Exp	3	26	0.2805(67)	3.362(81)	1.38
5	ForwardGeomSeriesExp	3	26	0.28104(90)	3.368(13)	1.52
6	ForwardGeomSeriesExp	3	26	0.2817(15)	3.376(19)	1.41
7	Forward2Exp	3	26	0.2885(41)	3.458(50)	1.47
8	Forward2Exp	3	24	0.295(11)	3.53(13)	0.89

Table 8.4: (continued)

Level	**Model**	t_{min}	t_{max}	$a_t E_{fit}$	E_{fit}/E_{ref}	χ^2/dof
9	Forward2Exp	3	22	0.2959(90)	3.55(11)	1.53
10	Forward2Exp	4	22	0.303(20)	3.63(24)	2.71
11	**Forward2Exp**	**3**	**24**	**0.306(10)**	**3.66(12)**	**1.22**
12	Forward2Exp	3	26	0.3065(39)	3.672(47)	0.98
13	Forward2Exp	3	24	0.3099(99)	3.71(12)	1.47
14	Forward2Exp	3	25	0.3117(68)	3.735(82)	1.48
15	Forward2Exp	3	26	0.3170(28)	3.799(34)	1.73
16	Forward2Exp	3	24	0.3172(53)	3.801(65)	0.93
17	Forward2Exp	3	22	0.3214(72)	3.852(87)	2.37
18	Forward2Exp	3	26	0.3223(63)	3.862(76)	0.91
19	Forward2Exp	3	25	0.3277(58)	3.927(70)	0.62
20	Forward2Exp	3	24	0.330(14)	3.95(17)	0.95
21	Forward2Exp	3	24	0.333(18)	3.99(21)	1.22
22	Forward2Exp	3	20	0.334(12)	4.00(14)	0.76
23	Forward2Exp	3	25	0.3339(56)	4.002(68)	1.55
24	Forward2Exp	3	24	0.335(13)	4.02(16)	1.04
25	Forward2Exp	3	25	0.3358(19)	4.024(24)	1.27
26	Forward2Exp	3	24	0.3363(71)	4.030(86)	0.49
27	Forward2Exp	3	22	0.3388(82)	4.059(99)	0.99
28	Forward2Exp	3	22	0.3408(72)	4.084(86)	1.01
29	Forward2Exp	3	19	0.349(28)	4.18(33)	1.26
30	Forward2Exp	3	21	0.3499(86)	4.19(10)	0.86
31	Forward2Exp	3	26	0.352(21)	4.21(25)	1.21
32	ForwardExp	8	18	0.356(16)	4.26(20)	0.8
33	Forward2Exp	3	22	0.359(13)	4.30(16)	1.03
34	ForwardExp	8	20	0.361(13)	4.33(16)	1.0

Table 8.4: (continued)

Level	**Model**	t_{min}	t_{max}	$a_t E_{fit}$	E_{fit}/E_{ref}	χ^2/dof
35	ForwardExp	7	21	0.372(12)	4.46(14)	1.82

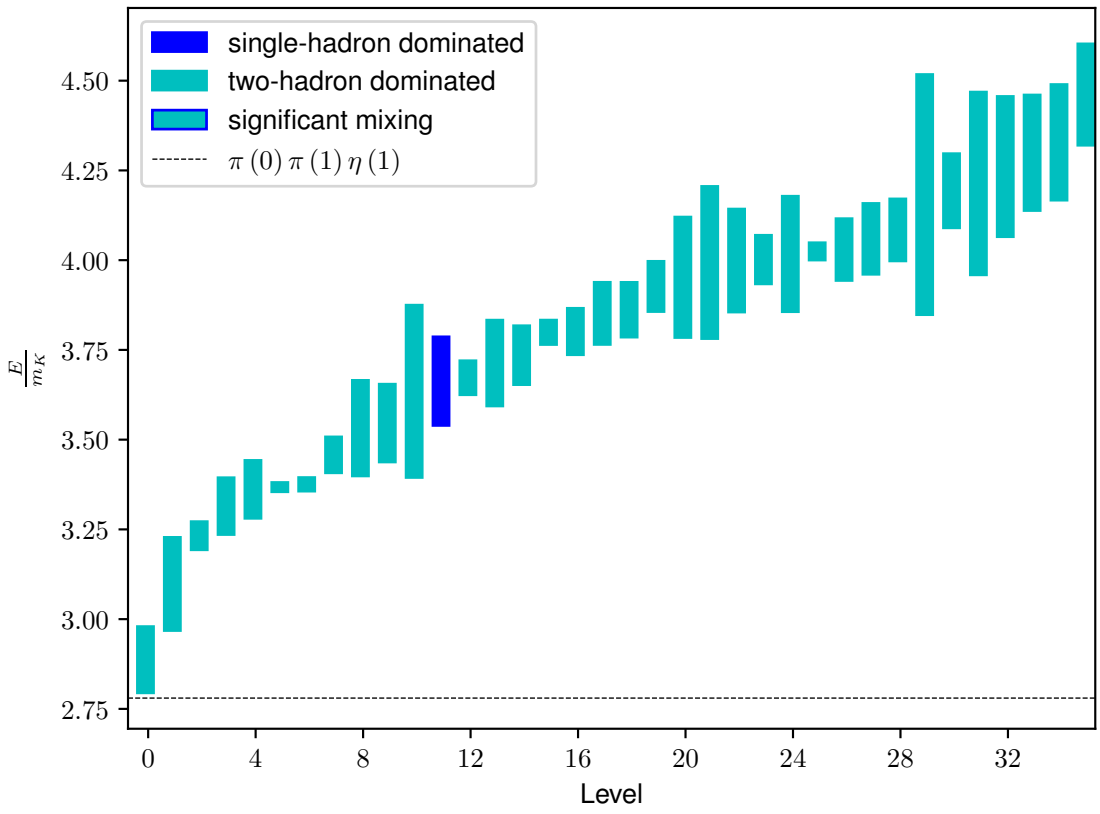

Figure 8.14: The staircase plot, which shows the lowest 36 levels extracted in the E_u^+ channel.

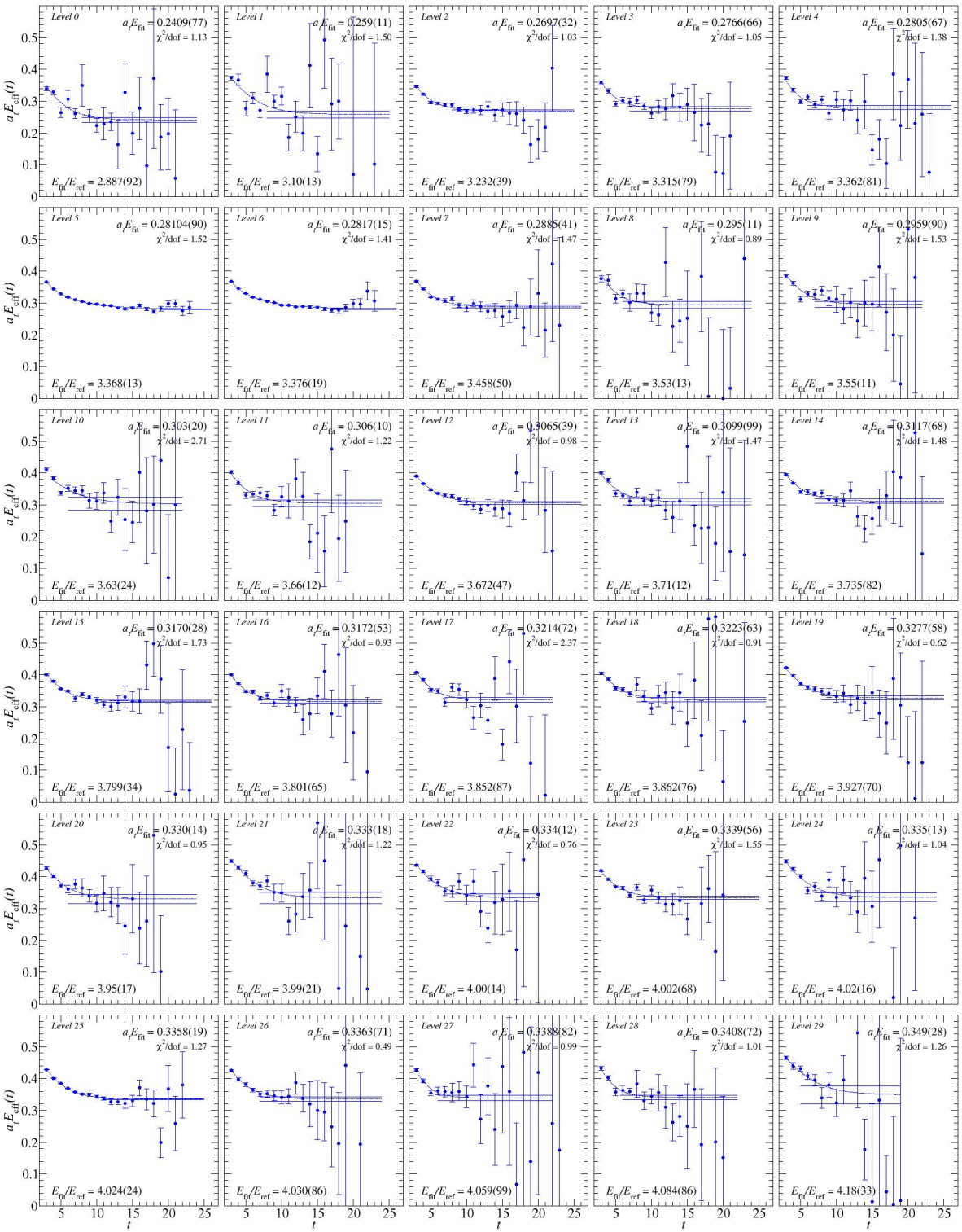

Figure 8.15: The effective energies for the lowest 30 levels in the E_u^+ channel with the fits overlaid on the plots.

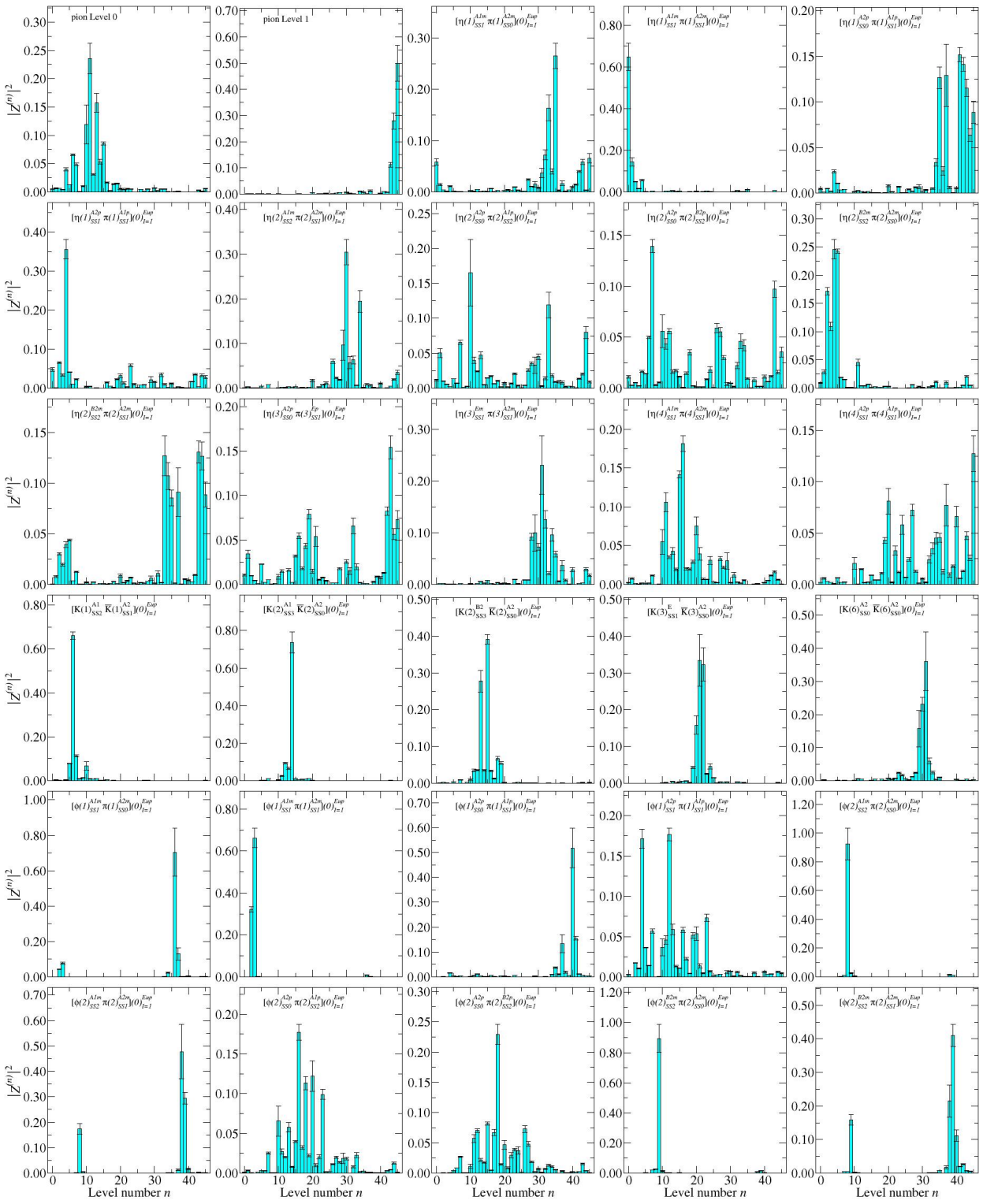

Figure 8.16: The overlap factors for first 30 operators considered in the E_u^+ channel.

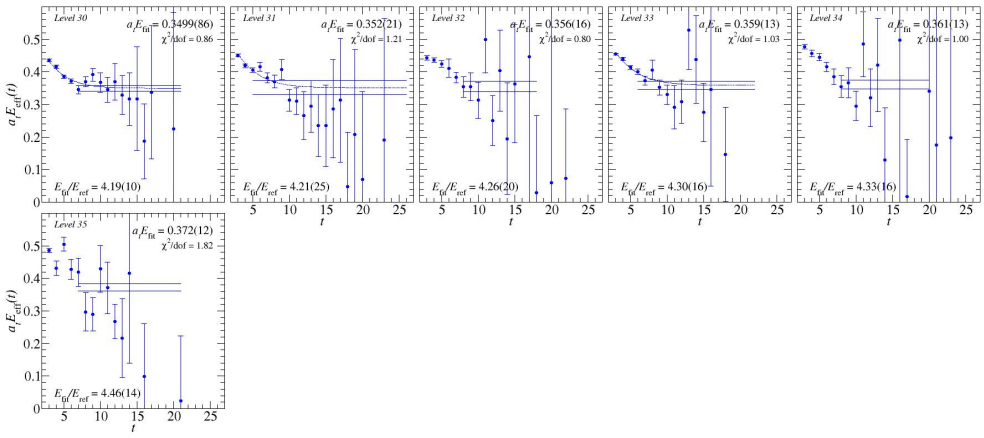

Figure 8.17: The effective energies for levels $30 - 35$ levels in the E_u^+ channel with the fits overlaid on the plots.

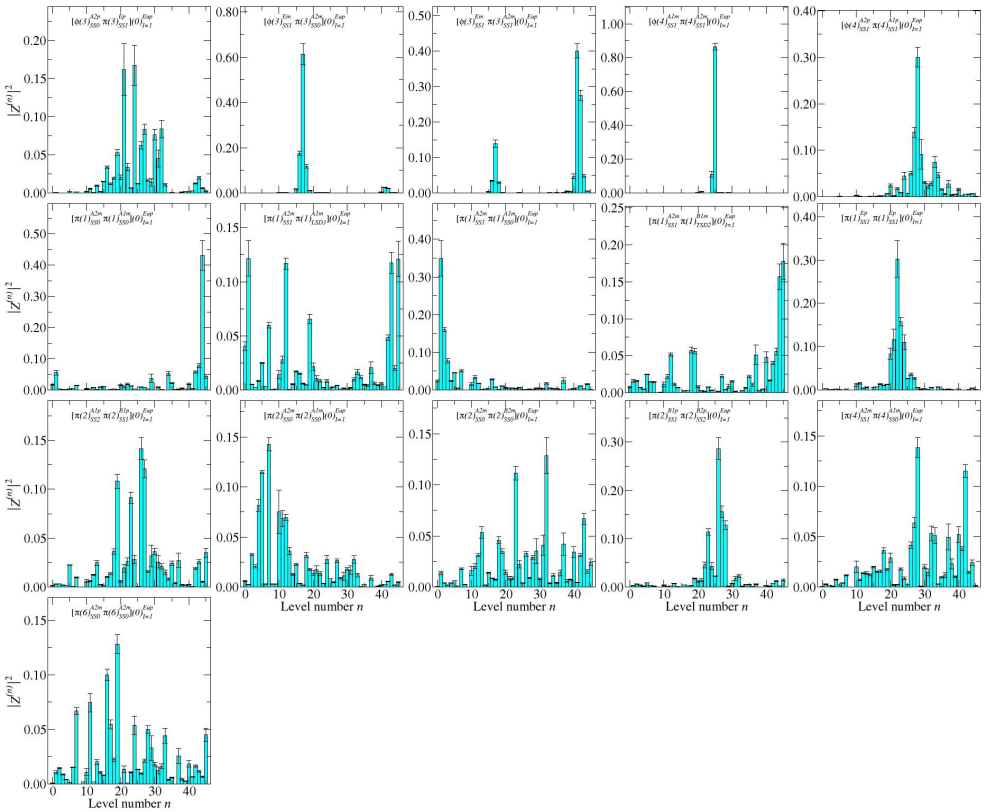

Figure 8.18: The overlap factors for last 16 operators considered in the E_u^+ channel.

8.3.4 T_{1u}^{+}

From the expected levels table for the T_{1u}^{+} channel shown in Table C7 we see that we expect 43 single- and two-hadron levels, including the $\rho(770)$, $\rho(1450)$, $\rho(1570)$, $\rho_3(1690)$, $\rho(1700)$, to appear below the 2 GeV cutoff. We decided on 73 operators that transformed irreducibly under the appropriate symmetry groups for this channel, 9 of which were single hadron operators. The metric time and diagonalization time were chosen to be $\tau_0 = 5$ and $\tau_D = 8$, respectively. The condition number of the $C(\tau_0)$ and $G(\tau_D)$ was 15.36 and 6.58, respectively, which means our correlator matrix is reasonable well-conditioned. These condition numbers occurred after one level was dropped via the procedure described in Sec. 6.2.2.

8.3.4.1 Single Hadron Operators In this channel, we expect multiple resonances to appear. Therefore, we start with an analysis of just the single-hadron operators. The 9 levels extracted from the correlator matrix consisting of 9 single-hadron operators are shown in Table 8.5.

Table 8.5: The levels extracted from a 9×9 correlator matrix consisting of single-hadron operators in the T_{1u}^{+} channel.

Level	**Model**	t_{min}	t_{max}	$a_t E_{fit}$	E_{fit}/E_{ref}	χ^2/dof
0	SymGeomSeriesExp	3	26	0.1335(16)	1.600(20)	1.06
1	Forward2Exp	3	24	0.262(16)	3.14(19)	1.25
2	Forward2Exp	3	26	0.2961(78)	3.548(94)	1.19
3	Forward2Exp	3	18	0.338(37)	4.05(45)	0.73
4	Forward2Exp	3	21	0.364(18)	4.36(22)	0.74
5	ForwardExp	6	23	0.473(35)	5.67(42)	1.19
6	ForwardExp	5	12	0.495(30)	5.94(35)	0.74
7	ForwardExp	5	11	0.565(34)	6.77(40)	0.71
8	ForwardExp	5	9	0.566(81)	6.78(97)	3.06

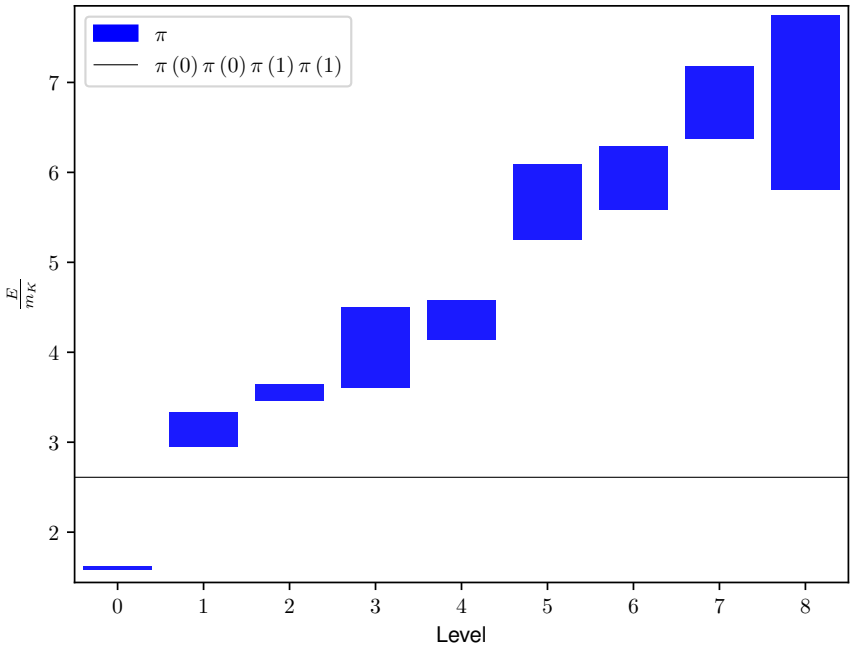

Figure 8.19: The staircase plot for the levels extracted in the T_{1u}^{+} channel using only single-hadron operators.

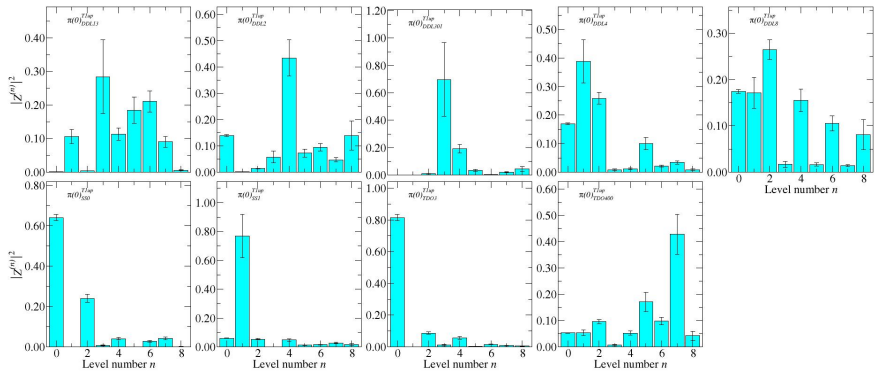

Figure 8.20: The overlap factors for the 9 single-hadron operators considered in the T_{1u}^{+} channel.

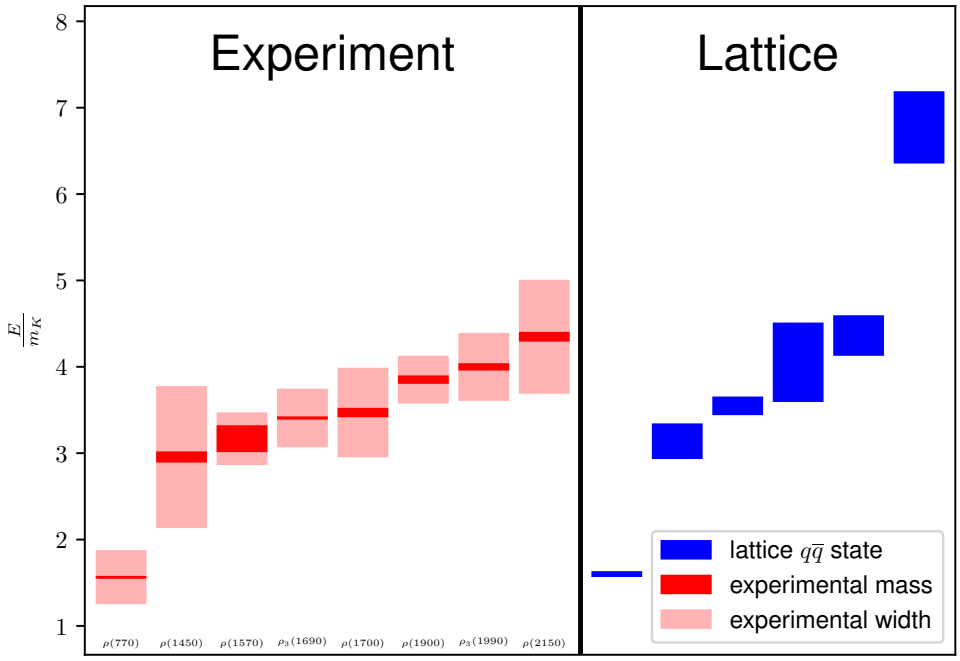

Figure 8.21: A comparison between the experimental resonances expected to appear in the T_{1u}^{+} channel and the levels extracted by only considering the 9 single-hadron operators.

8.3.4.2 All operators, Single Hadron Improved Operators The lowest 64 levels are shown in Table 8.6. The effective energies for these levels are shown in Figures 8.24 8.26 and 8.28, with the fit curves overlaid on the plots. The overlap factors are shown in Figures 8.25, 8.27, and 8.29. The spectrum is shown on a staircase plot in Figure 8.22. Once again, as can be seen in Figure 8.23, we see a clear discrepancy between the states deemed to be single-hadron dominated and the expected experimental references (notice the significant decrease in error in the lowest single-hadron dominated state after including two-hadron operators). The experimental spectrum has at least one extra state that may not be a quark-antiquark excitation.

Table 8.6: The lowest 64 levels extracted from a 73×73 correlator matrix consisting of single-hadron operators in the T_{1u}^{+} channel. The levels in bold are single-hadron dominated.

Level	**Model**	t_{min}	t_{max}	$a_t E_{fit}$	E_{fit}/E_{ref}	χ^2/dof
0	**SymGeomSeriesExp**	**4**	**26**	**0.1295(13)**	**1.551(16)**	**1.37**
1	Sym2Exp	5	26	0.1559(70)	1.868(84)	1.39
2	Sym2Exp	3	22	0.198(11)	2.38(13)	1.12
3	Forward2Exp	3	26	0.2026(61)	2.427(73)	2.04
4	Forward2Exp	3	26	0.206(16)	2.47(19)	2.43
5	Forward2Exp	3	26	0.2249(24)	2.695(29)	1.43
6	Forward2Exp	3	26	0.2546(52)	3.051(62)	1.95
7	Forward2Exp	3	25	0.2590(63)	3.103(76)	1.56
8	Forward2Exp	3	25	0.2617(77)	3.136(92)	1.86
9	Forward2Exp	3	24	0.2663(62)	3.191(74)	1.49
10	Forward2Exp	3	26	0.2664(25)	3.192(30)	1.39
11	Forward2Exp	4	25	0.2741(43)	3.285(53)	1.72
12	Forward2Exp	3	26	0.2763(57)	3.311(69)	1.17
13	Forward2Exp	3	24	0.276(13)	3.31(15)	1.56
14	Forward2Exp	3	25	0.277(13)	3.32(15)	1.84
15	Forward2Exp	3	25	0.2777(56)	3.328(67)	1.33
16	**Forward2Exp**	**3**	**26**	**0.2834(59)**	**3.396(70)**	**1.48**
17	Forward2Exp	3	24	0.2854(69)	3.421(84)	1.31
18	Forward2Exp	3	24	0.289(11)	3.47(13)	1.29
19	Forward2Exp	3	26	0.2905(80)	3.481(96)	1.75
20	Forward2Exp	3	26	0.2918(14)	3.497(17)	2.37
21	Forward2Exp	4	25	0.2946(65)	3.530(78)	1.16
22	Forward2Exp	3	25	0.2963(55)	3.550(66)	1.39
23	Forward2Exp	3	25	0.2972(36)	3.562(43)	1.76

Table 8.6: (continued)

Level	**Model**	t_{min}	t_{max}	$a_t E_{fit}$	E_{fit}/E_{ref}	χ^2/dof
24	Forward2Exp	4	25	0.297(23)	3.56(28)	1.81
25	Forward2Exp	3	23	0.3020(87)	3.62(10)	1.43
26	**Forward2Exp**	**3**	**22**	**0.3033(52)**	**3.635(62)**	**1.67**
27	Forward2Exp	3	21	0.304(13)	3.64(15)	1.62
28	Forward2Exp	3	23	0.304(21)	3.64(26)	1.21
29	Forward2Exp	4	25	0.3054(73)	3.660(88)	2.13
30	Forward2Exp	3	22	0.3062(100)	3.67(12)	1.6
31	Forward2Exp	3	22	0.308(18)	3.69(22)	1.64
32	Forward2Exp	3	21	0.313(20)	3.75(24)	1.98
33	Forward2Exp	3	24	0.3149(99)	3.77(12)	0.96
34	Forward2Exp	3	25	0.3162(34)	3.789(41)	1.03
35	Forward2Exp	3	23	0.3173(79)	3.802(95)	0.93
36	Forward2Exp	6	21	0.318(32)	3.81(39)	1.76
37	Forward2Exp	3	24	0.3184(75)	3.816(90)	0.96
38	Forward2Exp	3	24	0.3207(60)	3.843(73)	1.41
39	Forward2Exp	3	20	0.3242(59)	3.885(71)	1.72
40	Forward2Exp	3	22	0.324(19)	3.89(22)	1.01
41	Forward2Exp	3	24	0.325(13)	3.90(16)	1.81
42	Forward2Exp	3	26	0.326(11)	3.91(14)	1.58
43	Forward2Exp	3	24	0.3288(91)	3.94(11)	0.99
44	Forward2Exp	3	25	0.3288(71)	3.940(86)	1.66
45	Forward2Exp	3	20	0.329(23)	3.95(27)	1.28
46	Forward2Exp	3	22	0.3302(94)	3.96(11)	0.6
47	Forward2Exp	3	26	0.331(12)	3.97(14)	1.36
48	Forward2Exp	3	24	0.3328(63)	3.988(75)	2.28
49	Forward2Exp	3	26	0.333(19)	4.00(22)	1.85

Table 8.6: (continued)

Level	**Model**	t_{min}	t_{max}	$a_t E_{fit}$	E_{fit}/E_{ref}	χ^2/dof
50	**Forward2Exp**	**3**	**20**	**0.333(23)**	**4.00(28)**	**1.98**
51	Forward2Exp	3	24	0.334(15)	4.00(18)	0.79
52	Forward2Exp	3	25	0.3374(88)	4.04(11)	0.93
53	Forward2Exp	3	23	0.3427(94)	4.11(11)	0.89
54	Forward2Exp	3	24	0.3436(85)	4.12(10)	0.86
55	Forward2Exp	3	24	0.351(61)	4.20(73)	1.11
56	Forward2Exp	3	20	0.352(12)	4.22(14)	1.31
57	**Forward2Exp**	**3**	**21**	**0.353(21)**	**4.23(25)**	**1.01**
58	Forward2Exp	3	20	0.3530(83)	4.229(99)	0.88
59	Forward2Exp	3	23	0.356(63)	4.27(76)	0.76
60	Forward2Exp	3	24	0.361(34)	4.32(41)	2.55
61	Forward2Exp	3	26	0.363(21)	4.35(26)	1.75
62	Forward2Exp	7	24	0.3650(79)	4.374(96)	1.49
63	**Forward2Exp**	**3**	**21**	**0.377(15)**	**4.52(18)**	**0.85**

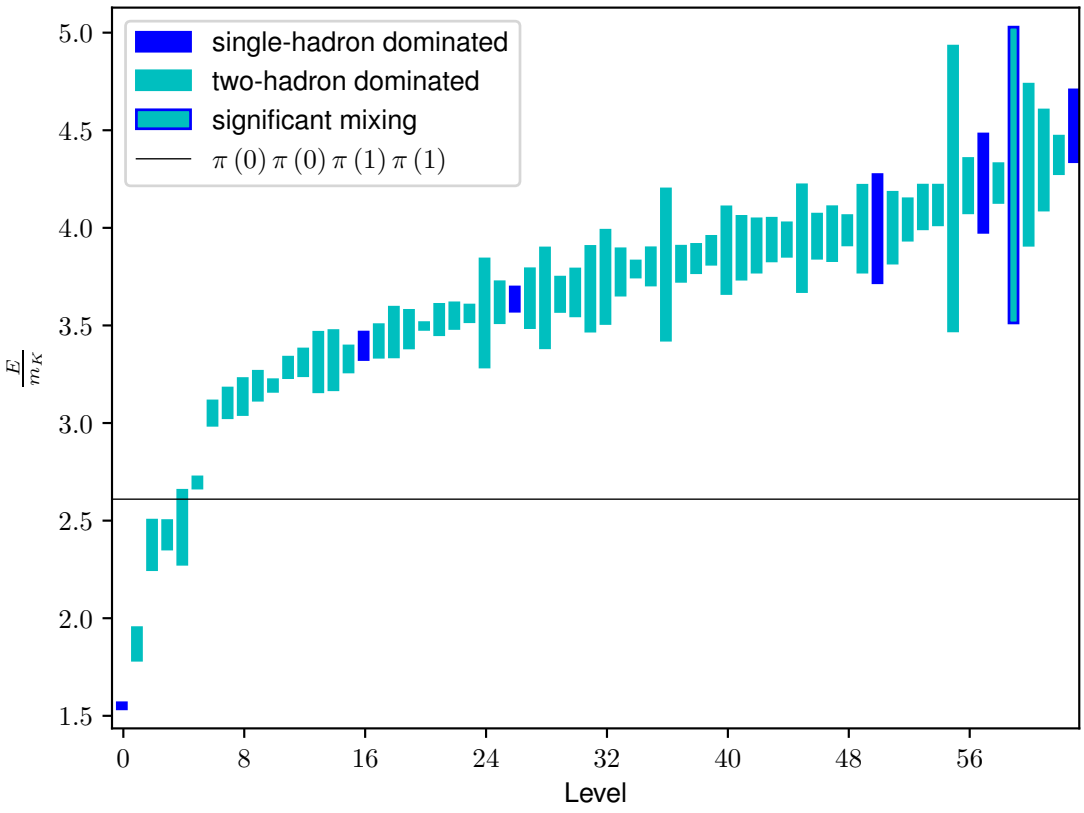

Figure 8.22: The staircase plot, which shows the lowest 64 levels extracted in the T_{1u}^{+} channel.

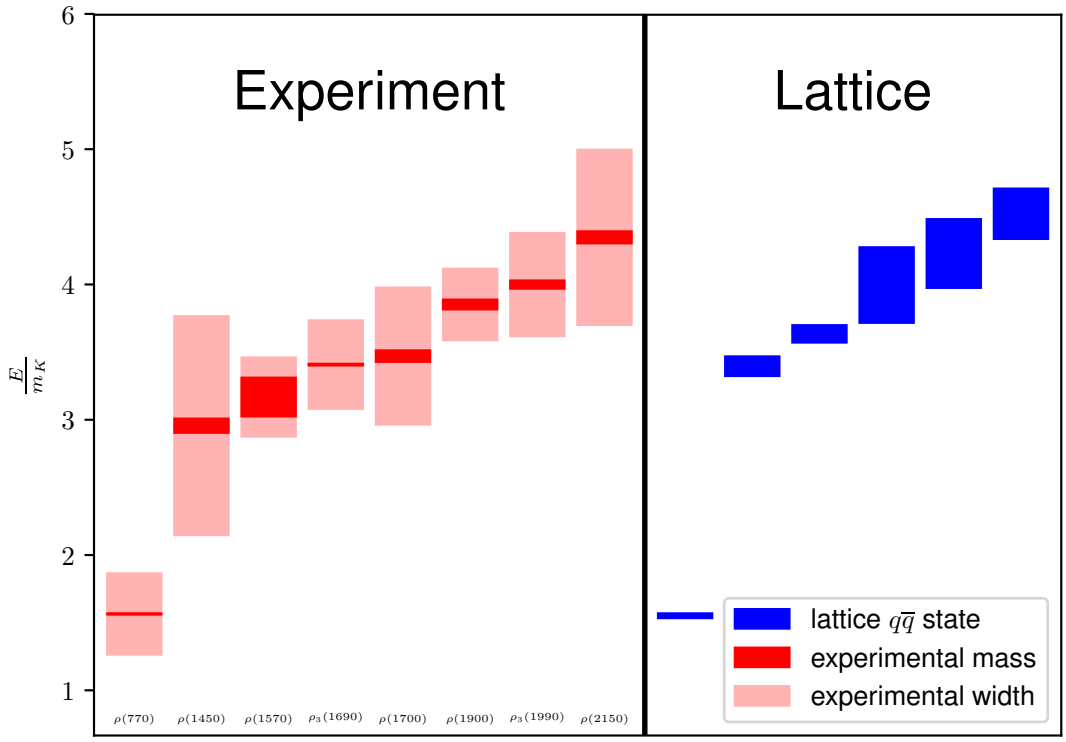

Figure 8.23: A comparison between the experimental resonances expected to appear in the T_{1u}^{+} channel and the levels that were determined to be single-hadron dominated.

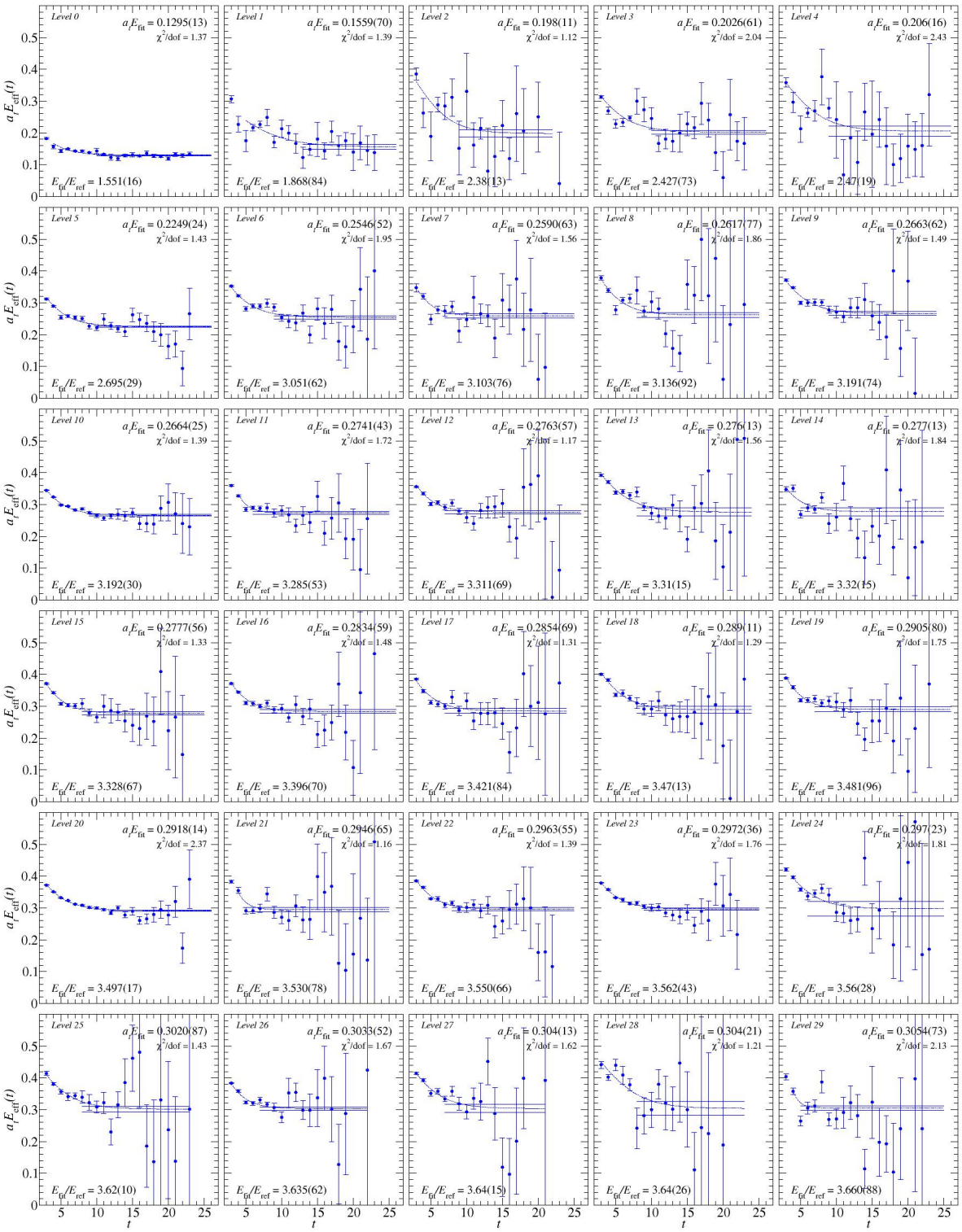

Figure 8.24: The effective energies for the lowest 30 levels in the T_{1u}^{+} channel with the fits overlaid on the plots.

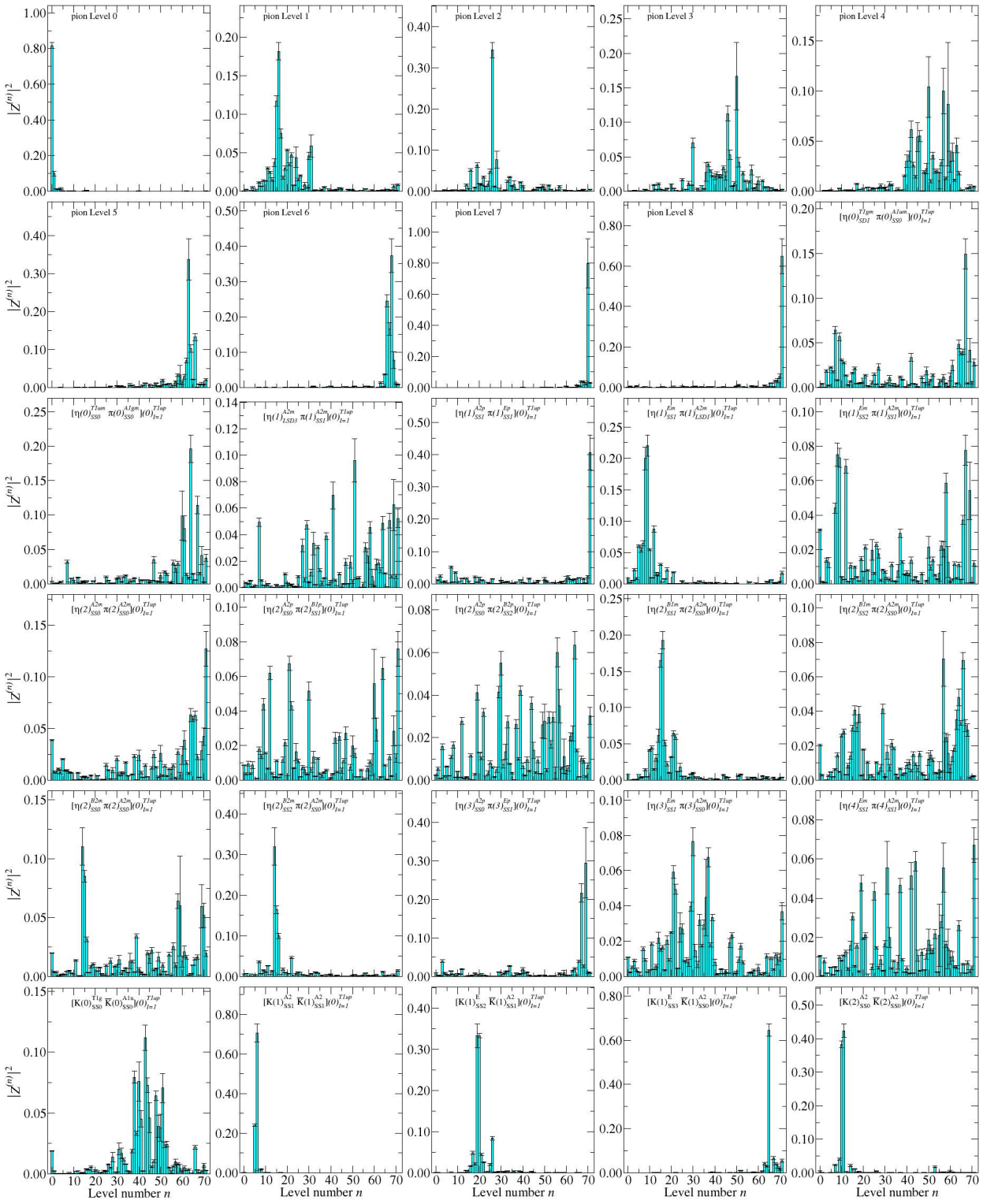

Figure 8.25: The overlap factors for the first 30 operators considered in the T_{1u}^+ channel.

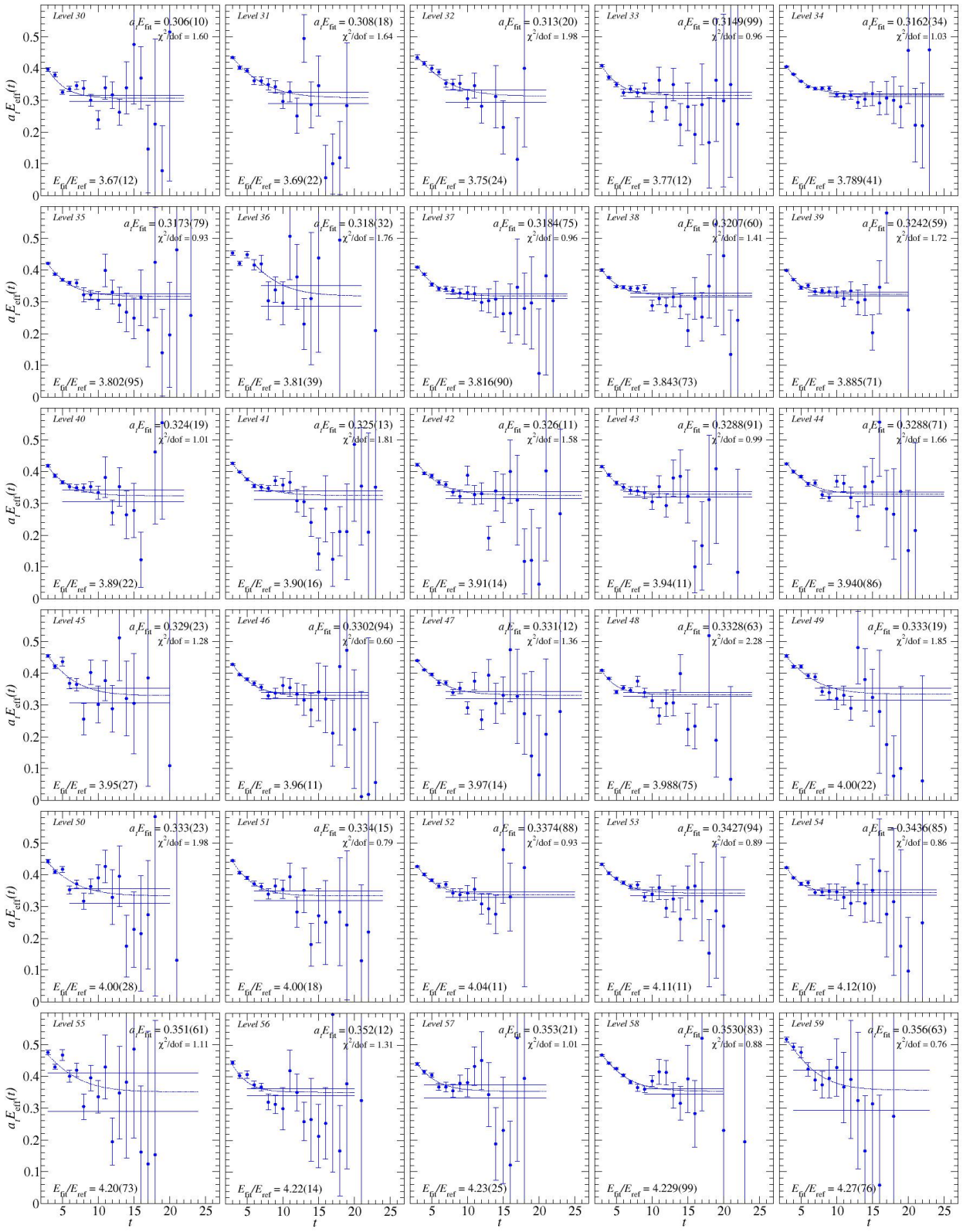

Figure 8.26: The effective energies for next lowest 30 levels in the T_{1u}^{+} channel with the fits overlaid on the plots.

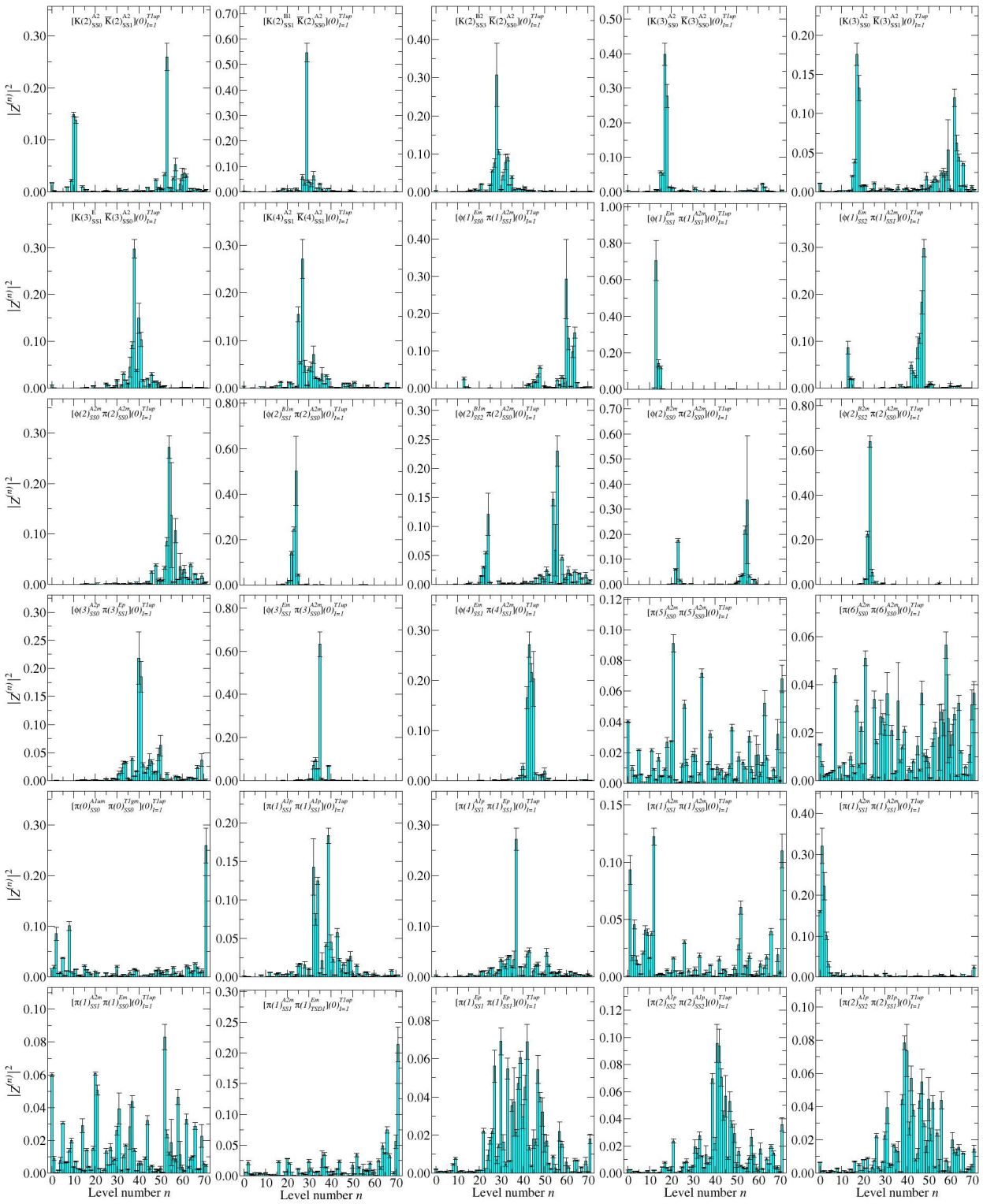

Figure 8.27: The overlap factors for the next 30 operators considered in the T_{1u}^+ channel.

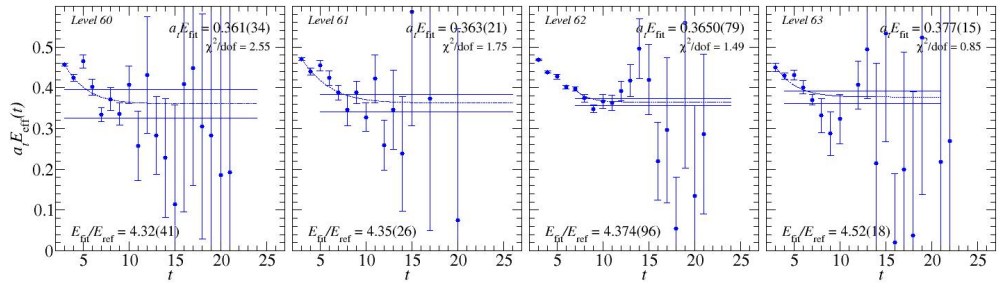

Figure 8.28: The effective energies for next lowest 4 levels in the T_{1u}^+ channel with the fits overlaid on the plots.

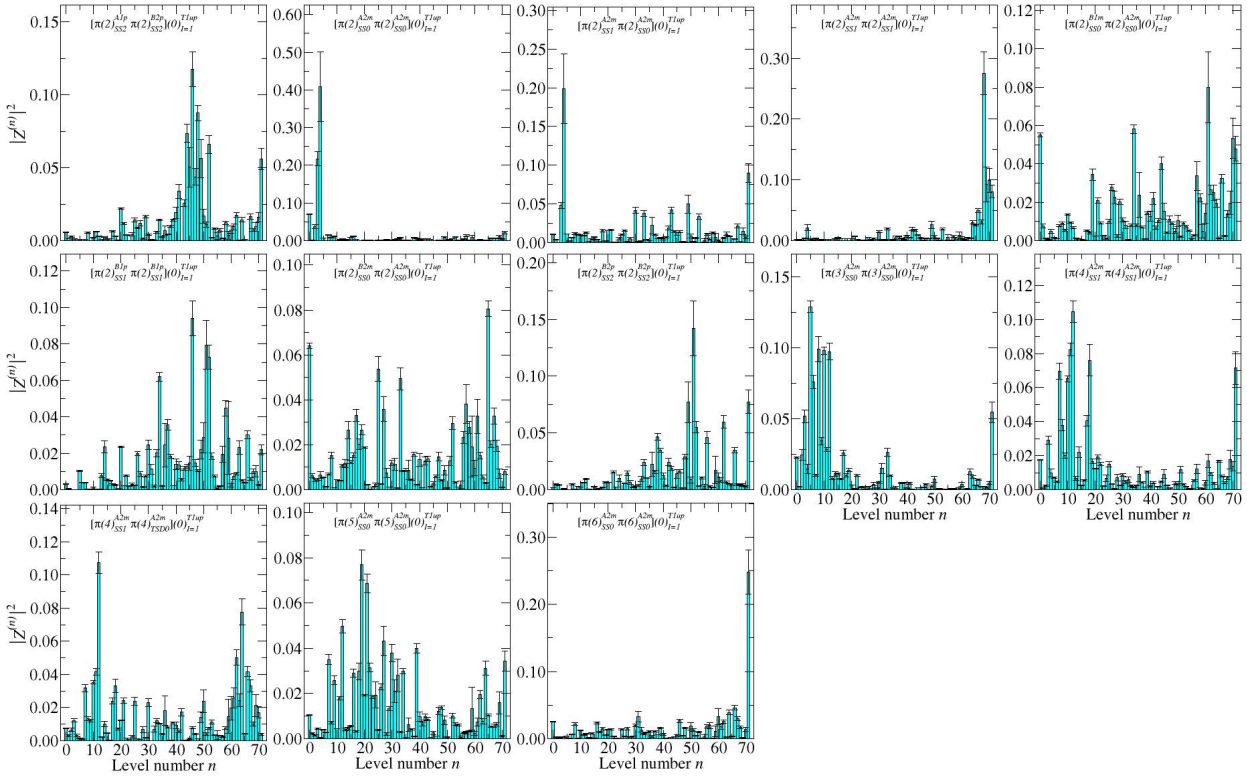

Figure 8.29: The overlap factors for the last 12 operator considered in the T_{1u}^+ channel.

8.3.5 T_{2u}^{+}

From the expected levels table for the T_{2u}^{+} channel shown in Table C9 we see that we expect 34 single- and two-hadron levels, including the $\rho_3(1690)$, to appear below the 2 GeV cutoff. We decided on 57 operators that transformed irreducibly under the appropriate symmetry groups for this channel, 4 of which were single hadron operators. The metric time and diagonalization time were chosen to be $\tau_0 = 5$ and $\tau_D = 8$, respectively. The condition number of the $C(\tau_0)$ and $G(\tau_D)$ was 10.74 and 4.82, respectively, which means our correlator matrix is reasonably well-conditioned.

8.3.5.1 Single Hadron Operators In this channel, we expect the $\rho_3(1690)$ and $\rho_3(1990)$ resonances to appear. Therefore, we start with an analysis of just the single-hadron operators. The 4 levels extracted from the correlator matrix consisting of 4 single-hadron operators are shown in Table 8.7.

Table 8.7: The levels extracted from a 4×4 correlator matrix consisting of single-hadron operators in the T_{2u}^{+} channel.

Level	**Model**	t_{min}	t_{max}	$a_t E_{fit}$	E_{fit}/E_{ref}	χ^2/dof
0	Sym2Exp	3	26	0.301(24)	3.61(28)	2.0
1	Sym2Exp	3	21	0.341(20)	4.09(24)	1.2
2	Forward2Exp	3	13	0.34(12)	4.1(14)	0.27
3	Forward2Exp	3	17	0.47(12)	5.6(14)	1.38

8.3.5.2 All operators, Single Hadron Improved Operators The lowest 47 levels are shown in Table 8.8. The effective energies for these levels are shown in Figures 8.35 and 8.37, with the fit curves overlaid on the plots. The overlap factors are shown in Figures 8.36 and 8.38. The spectrum is shown on a staircase plot in Figure 8.33. There appears to be clear agreement between the experimental resonances expected to appear in this channel and

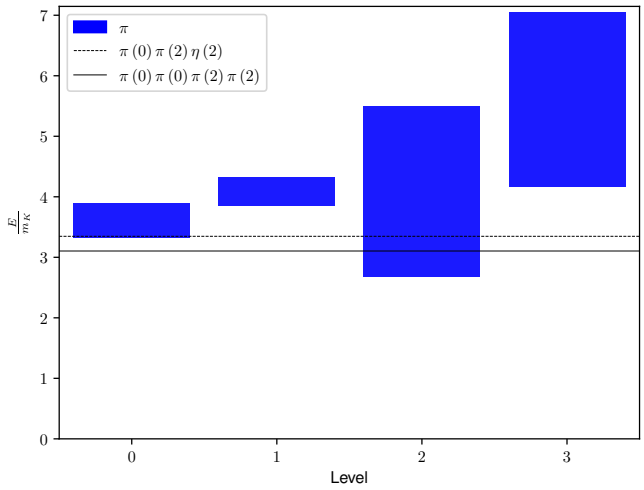

Figure 8.30: The staircase plot for the levels extracted in the T_{2u}^+ channel using only the single-hadron operators.

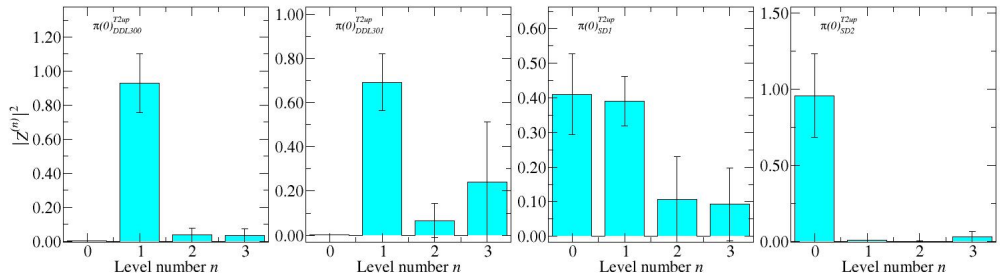

Figure 8.31: The overlap factors for the 4 single-hadron operators considered in the T_{2u}^+ channel.

the lattice stationary states deemed single-hadron dominated (see Figure 8.34). However, since we did not see agreement in the A_{2u}^+ channel, and we saw an unexpected state in the E_u^+ channel spectrum that could also appear here, it makes more sense to identify one of these single-hadron dominated states as the degenerate partner to the single-hadron dominated state found in the E_u^+ channel.

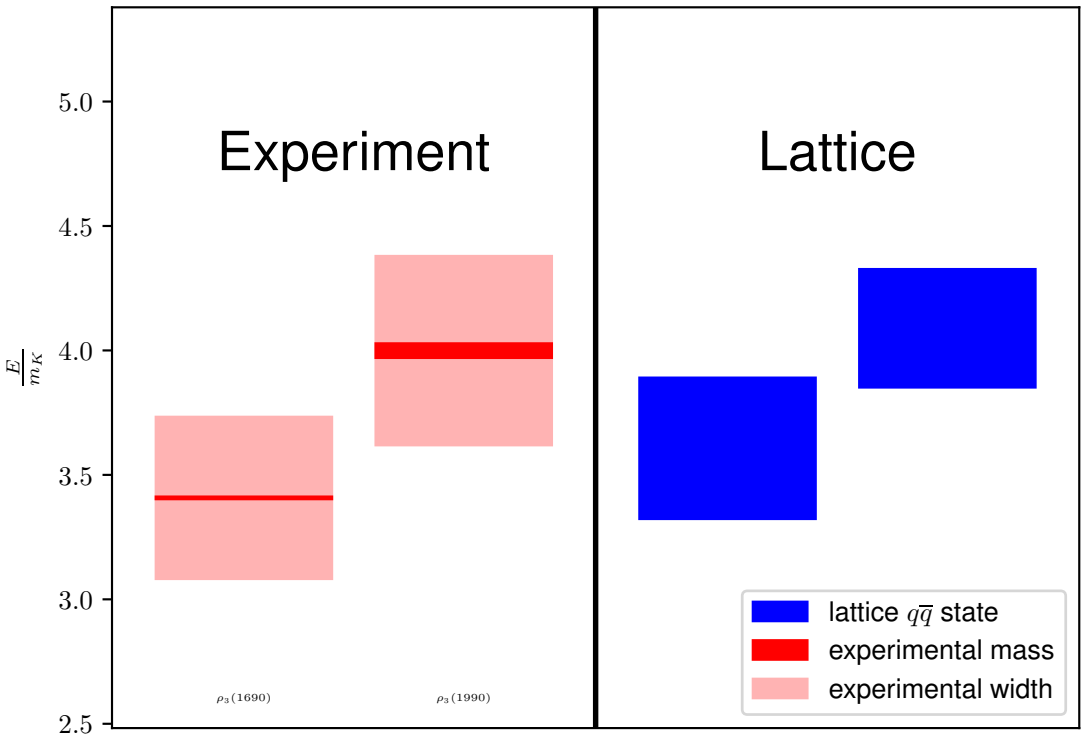

Figure 8.32: A comparison between the experimental resonances expected to appear in the T_{2u}^+ channel and the levels extracted by only considering the 4 single-hadron operators.

Table 8.8: The lowest 47 levels extracted from a 57×57 correlator matrix in the T_{2u}^+ channel. The levels in bold are single-hadron dominated.

Level	**Model**	t_{min}	t_{max}	$a_t E_{fit}$	E_{fit}/E_{ref}	χ^2/dof
0	Sym2Exp	4	26	0.1848(32)	2.214(38)	1.95
1	Sym2Exp	3	25	0.2420(62)	2.900(74)	1.85
2	Sym2Exp	4	26	0.2430(20)	2.912(25)	1.74

Table 8.8: (continued)

Level	**Model**	t_{min}	t_{max}	$a_t E_{fit}$	E_{fit}/E_{ref}	χ^2/dof
3	SymGeomSeriesExp	3	26	0.2500(14)	2.995(17)	1.56
4	Sym2Exp	3	25	0.2629(92)	3.15(11)	2.52
5	Sym2Exp	3	25	0.277(22)	3.32(27)	1.35
6	Sym2Exp	3	25	0.280(11)	3.36(13)	1.29
7	SymGeomSeriesExp	3	26	0.2811(62)	3.368(74)	1.76
8	Sym2Exp	3	24	0.2865(54)	3.433(65)	1.95
9	SymGeomSeriesExp	3	26	0.2865(36)	3.434(44)	1.18
10	Sym2Exp	3	23	0.295(14)	3.54(17)	1.83
11	Sym2Exp	3	26	0.2965(40)	3.553(48)	1.95
12	Sym2Exp	3	26	0.299(12)	3.59(14)	1.47
13	Sym2Exp	3	26	0.301(10)	3.61(12)	1.74
14	Sym2Exp	3	26	0.3057(74)	3.664(90)	1.38
15	**Sym2Exp**	**3**	**24**	**0.3059(65)**	**3.665(79)**	**1.47**
16	Sym2Exp	3	22	0.3066(87)	3.67(10)	0.77
17	Sym2Exp	3	25	0.307(11)	3.68(13)	1.57
18	Sym2Exp	3	26	0.3075(61)	3.685(73)	1.52
19	Sym2Exp	3	26	0.3090(48)	3.703(58)	1.4
20	Forward2Exp	3	24	0.312(10)	3.74(13)	0.97
21	Sym2Exp	3	24	0.3132(87)	3.75(10)	2.51
22	Forward2Exp	3	26	0.3145(54)	3.769(65)	1.24
23	Sym2Exp	3	25	0.3152(30)	3.777(37)	1.96
24	Sym2Exp	3	26	0.3166(93)	3.79(11)	1.32
25	**Sym2Exp**	**3**	**25**	**0.3174(61)**	**3.804(74)**	**1.35**
26	Forward2Exp	3	25	0.319(14)	3.82(17)	1.37
27	Forward2Exp	3	23	0.3208(67)	3.844(81)	0.93
28	Sym2Exp	3	23	0.3212(69)	3.849(83)	1.04

Table 8.8: (continued)

Level	**Model**	t_{min}	t_{max}	$a_t E_{fit}$	E_{fit}/E_{ref}	χ^2/dof
29	Forward2Exp	3	25	0.3213(71)	3.850(85)	1.38
30	Forward2Exp	3	25	0.325(22)	3.89(26)	0.77
31	Forward2Exp	3	24	0.3251(80)	3.896(96)	0.81
32	Forward2Exp	3	22	0.3284(67)	3.935(81)	0.79
33	Forward2Exp	3	22	0.328(15)	3.94(18)	0.85
34	Forward2Exp	3	22	0.3343(84)	4.01(10)	1.1
35	Forward2Exp	4	26	0.3361(21)	4.028(26)	1.07
36	Forward2Exp	3	19	0.338(12)	4.05(15)	1.27
37	Forward2Exp	3	25	0.3379(54)	4.049(65)	0.56
38	Forward2Exp	3	25	0.339(20)	4.06(24)	1.48
39	Forward2Exp	3	23	0.3397(68)	4.071(82)	1.01
40	Forward2Exp	3	26	0.3403(21)	4.078(26)	1.63
41	Forward2Exp	3	25	0.3443(61)	4.126(74)	0.82
42	Forward2Exp	3	19	0.344(15)	4.13(18)	0.92
43	Forward2Exp	3	20	0.345(16)	4.13(19)	2.1
44	Forward2Exp	3	21	0.353(13)	4.23(16)	1.45
45	Forward2Exp	3	18	0.374(43)	4.49(52)	0.93
46	Forward2Exp	3	26	0.384(15)	4.60(18)	1.46

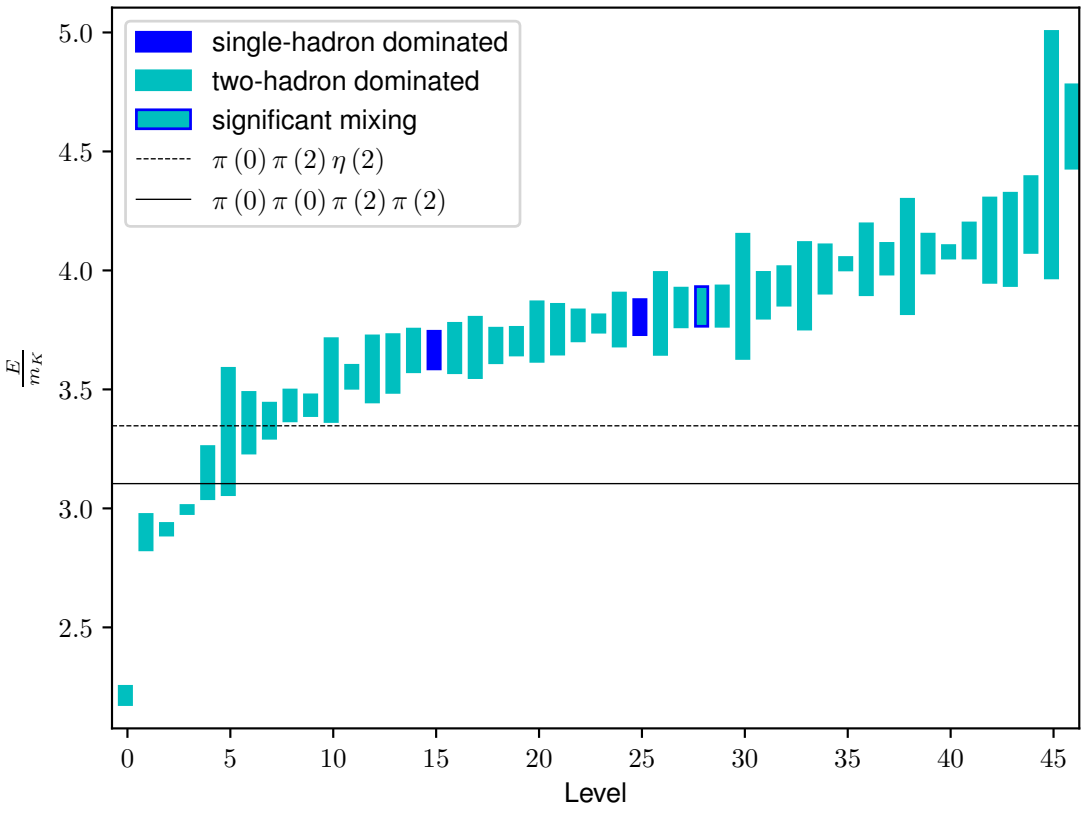

Figure 8.33: The staircase plot, which shows the lowest 47 levels extracted in the T_{2u}^{+} channel.

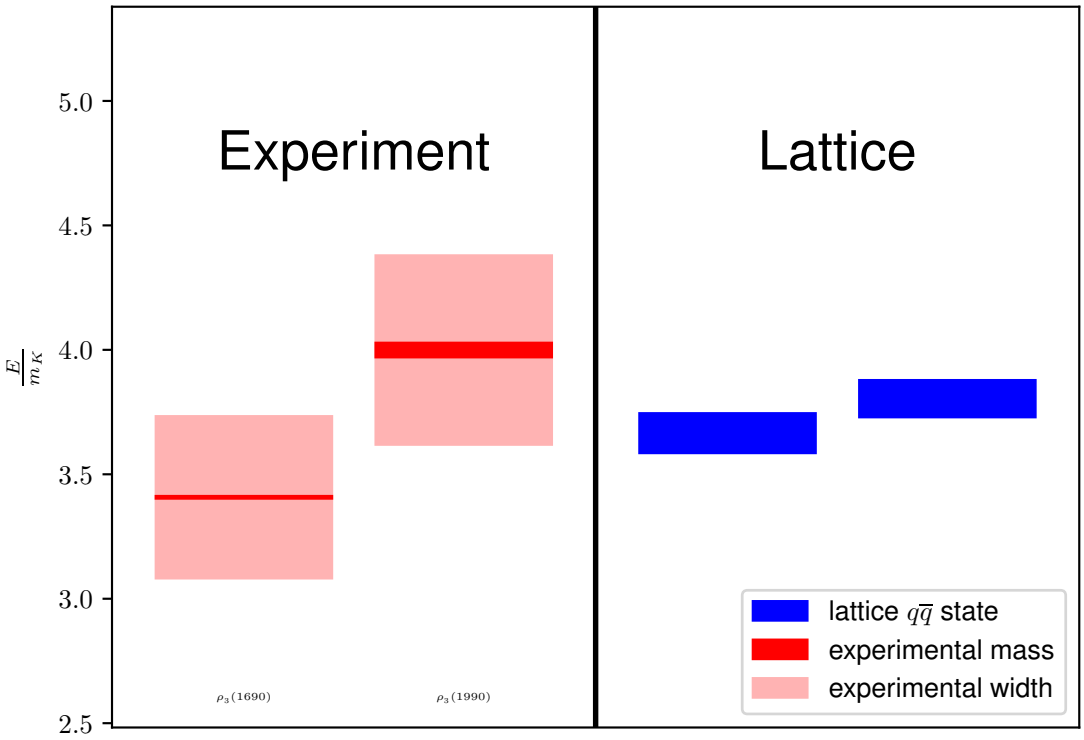

Figure 8.34: A comparison between the experimental resonances expected to appear in the T_{2u}^{+} channel and the levels that were determined to be single-hadron dominated.

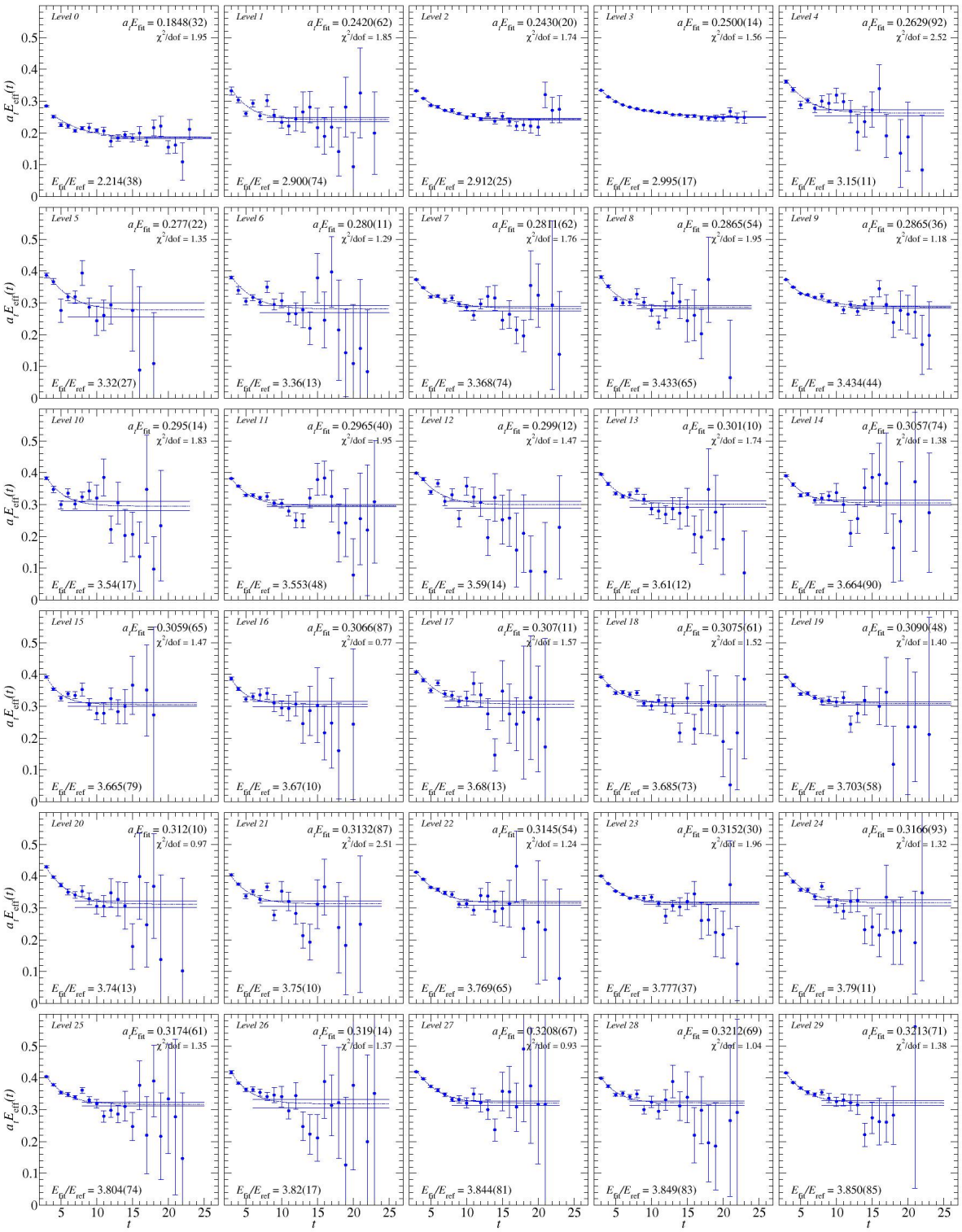

Figure 8.35: The effective energies for the lowest 30 levels in the T_{2u}^{+} channel with the fits overlaid on the plots.

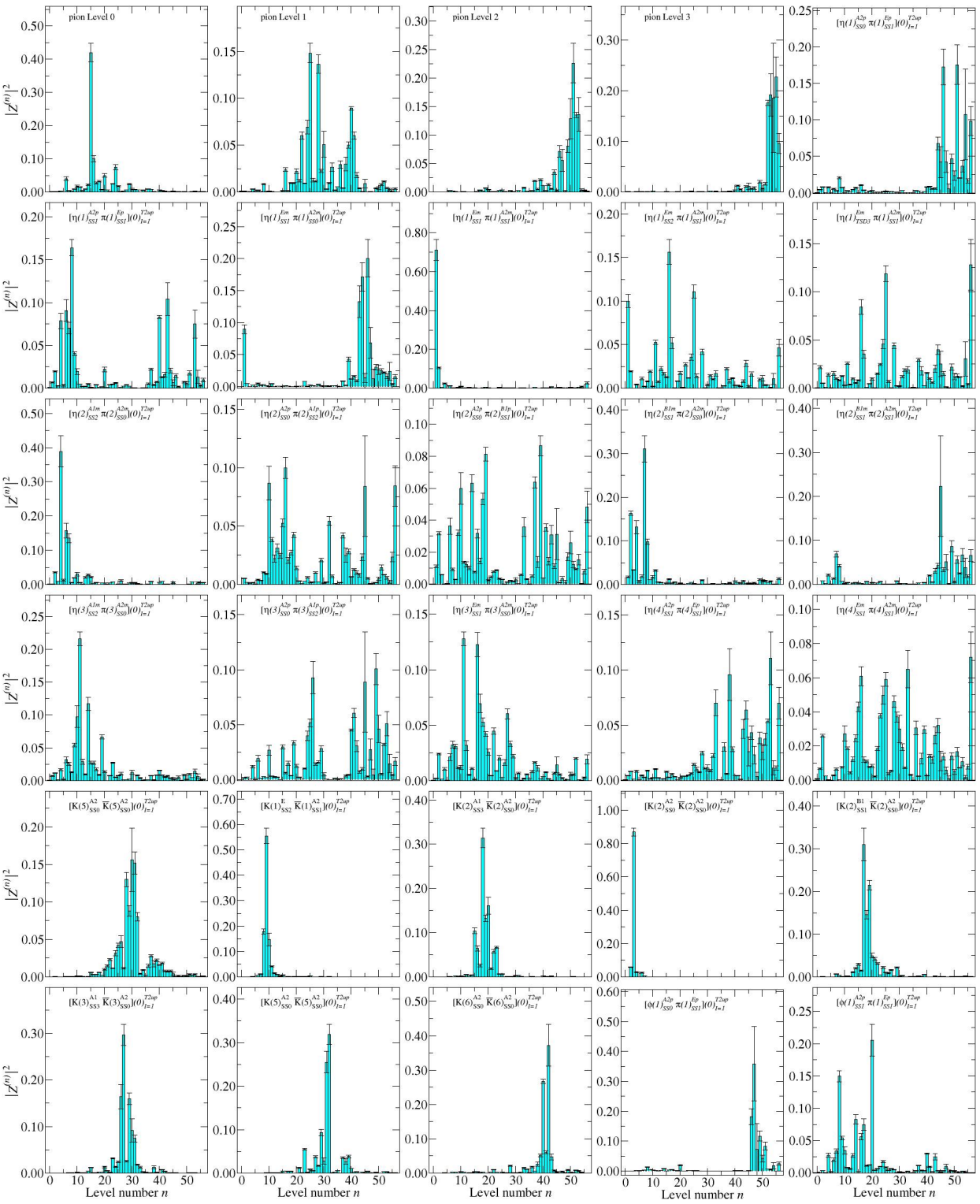

Figure 8.36: The overlap factors for the first 30 operators considered in the T_{2u}^+ channel.

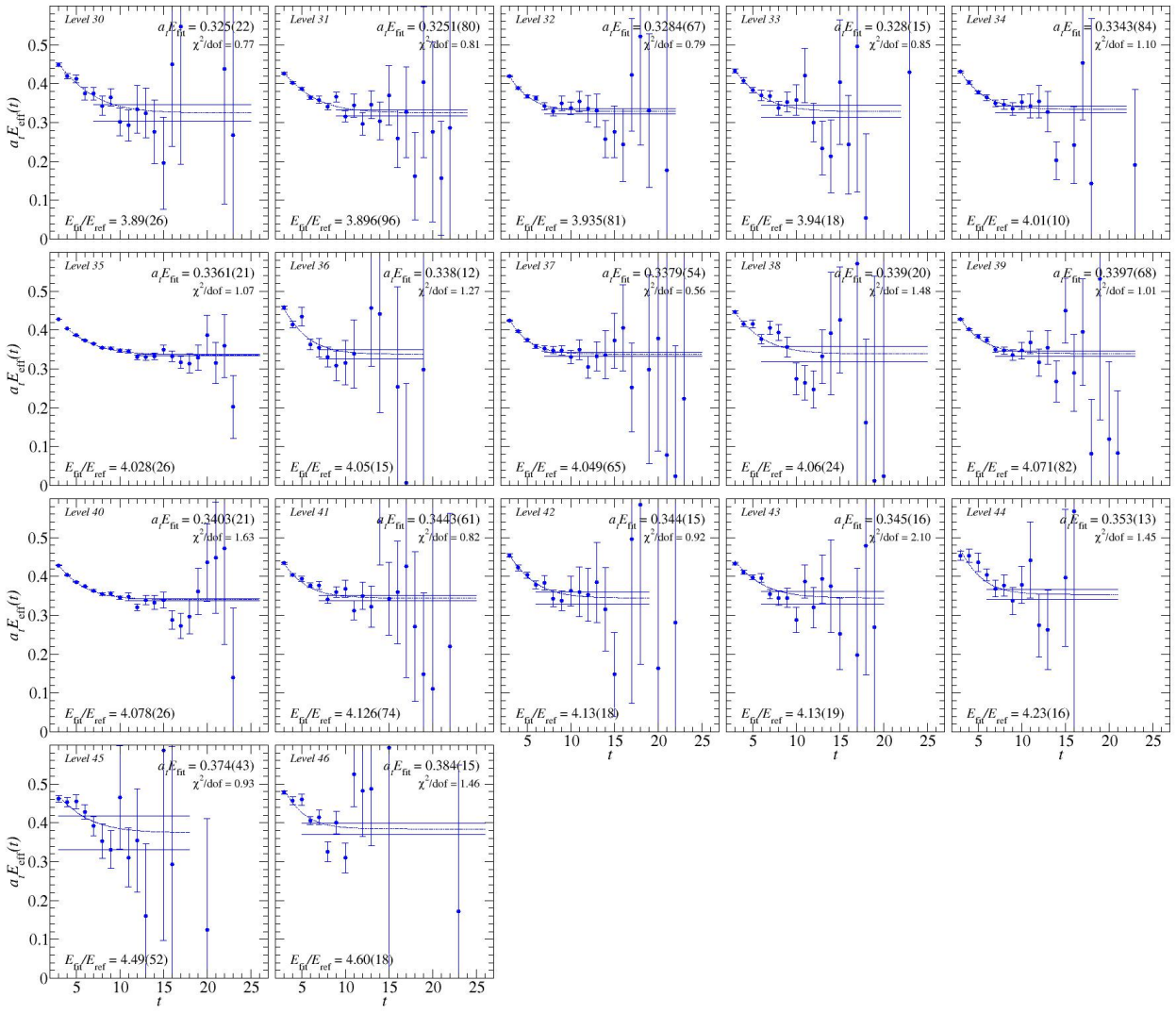

Figure 8.37: The effective energies for next lowest 17 levels in the T_{2u}^{+} channel with the fits overlaid on the plots.

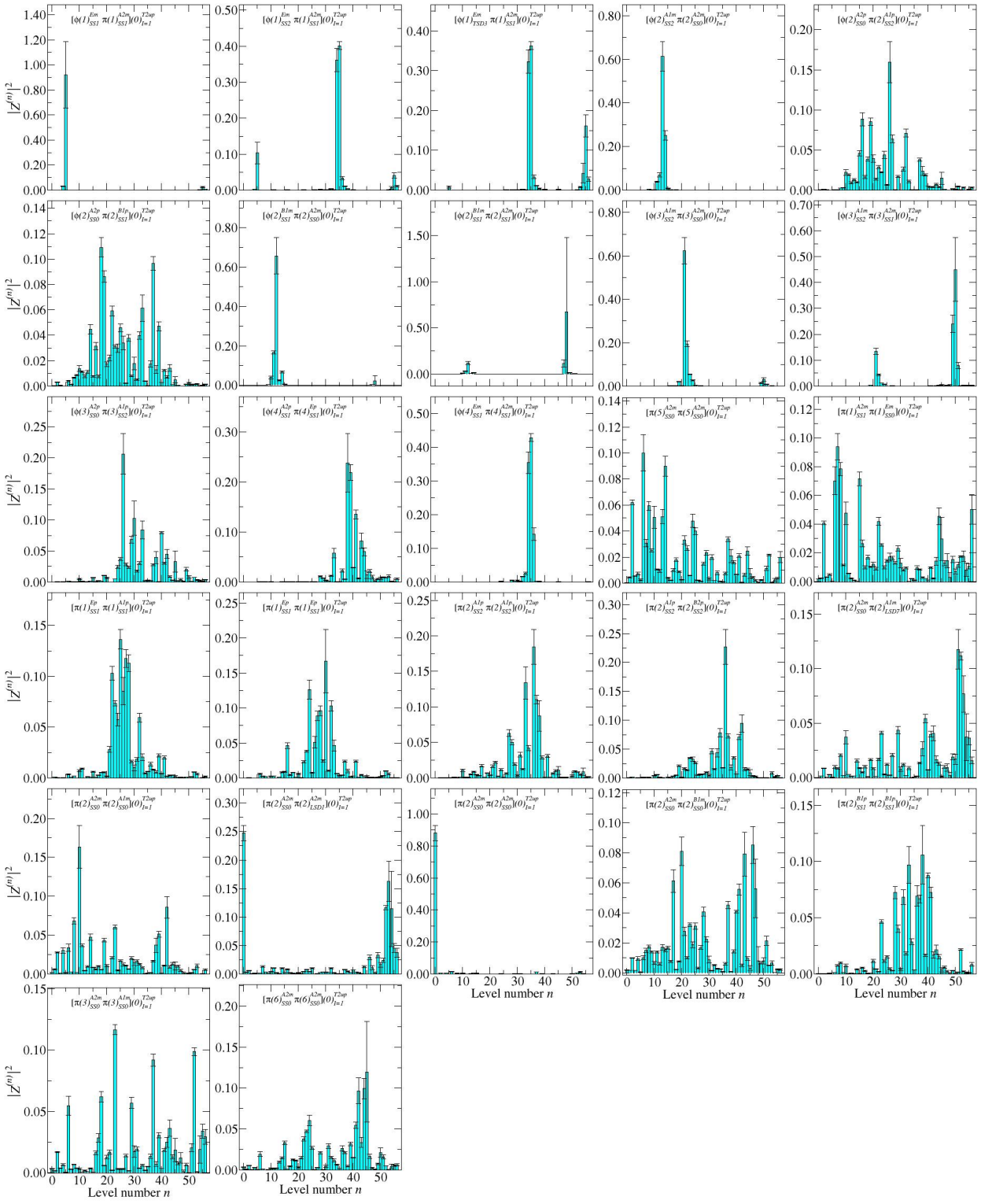

Figure 8.38: The overlap factors for the next 27 operators considered in the T_{2u}^+ channel.

8.3.6 Finite-volume Spectrum Conclusions

In a series of papers [87, 88, 26], the Hadron Spectrum Collaboration (HSC) presented their results for the isoscalar and isovector spectrum on a much smaller $24^3 \times 128$ lattice with a much heavier pion $\approx 391\,\text{MeV}$, and no two-hadron operators were included in the analysis. Their final results were collected into a single figure from Ref. [26], which is shown in Figure 8.39. For comparison to our results shown above, we focus on the isovectors (in blue) with $J^{PC} = 1^{--}, 3^{--}$, which shows 4 levels below 2.0 GeV and 2 levels between 2 GeV and 2.5 GeV. This then does compare well with the single-hadron resonances we extracted in the T_{1u}^+ channel (see Figure 8.23), which is the only channel that will contain both $J = 1, 3$. Additionally, we might expect to see spin-4 states in the T_{1u}^+ channel, and the 4^{--} isovector meson in Figure 8.39 agrees with the highest state shown in T_{1u}^+. Furthermore, the results in Figure 8.39 show 2^{--} isovector meson that can explain the unexpected single-hadron state found in the E_u^+ channel. This state also lends support for our suggestion that one of the single-hadron dominated states in the T_{2u}^+ channel spectrum was in fact the degenerate partner to the single-hadron dominated state found in the E_u^+ channel.

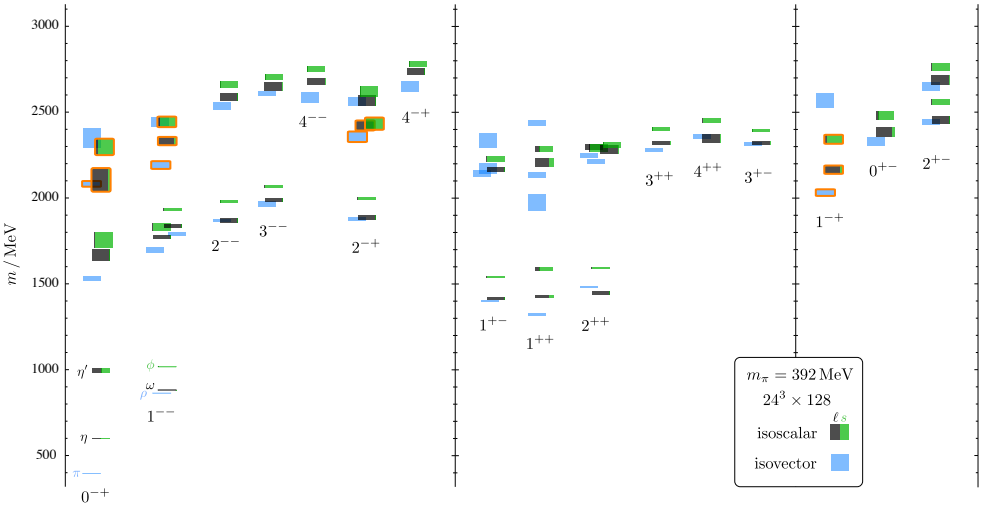

Figure 8.39: The isoscalar and isovector meson spectrum results from the Hadron Spectrum Collaboration on a $24^3 \times 128$ lattice with $m_\pi \approx 391\,\text{MeV}$. Continuum spin identification has been used to label the states by J^{PC}. Figure take from Ref. [26].

8.4 THE $K^*(892)$ RESONANCE

The approach used in the previous section to identify resonances from the finite-volume spectrum was based on the use of the overlap factors. This identification is somewhat qualitative and is not expected to reproduce resonance energies with a high accuracy, especially when near a decay threshold or if the resonance has a large width. In order to reliably extract properties of hadron resonances, we must resort to other methods. The most widely used and successful approach is based on the Lüscher formalism introduced in Chap. 7. In that chapter, we described a newly developed approach to extracting resonance information from the Lüscher quantization condition, which includes multiple partial waves and/or decay channels. We use that method here for the inclusion of the $l = 0$, $l = 1$, and the $l = 2$ partial waves.

The $K^*(892)$ represents an interesting test case for the inclusion of multiple partial waves because there is no symmetry preventing the mixing of the s- and p-wave when $\boldsymbol{P} \neq 0$, and the s-wave is expected to be non-negligible [81], which may be due to the κ resonance. This partial wave mixing can be avoided if one only uses irreps of the little group that do not mix with $l = 0$ as was done in Ref. [89]. But, we will not restrict ourselves in that way here. The relevant channels are listed in Table 8.9. Notice that this table includes the A_{1g} irrep which would not contain the $K^*(892)$, but we include this channel to pick up the s-wave since we are considering multiple partial waves in our analysis.

We do not consider coupled channels here, and therefore we can only consider energies below the inelastic threshold given by $\frac{E_{cm}}{m_\pi} = 2 + \frac{m_K}{m_\pi} \approx 4.12$. All energies extracted below this cutoff are shown in Table 8.10. Notice that the phase shift is sometimes shown in one or both of the last two columns. These values are calculated by assuming no partial wave mixing, where the phase shift can be determined exactly from the quantization condition. That is, in the case of a single channel and only considering one partial wave, the K-matrix is then a 1×1 matrix and the quantization condition in Eq. (7.46) is easily solved by $\widetilde{K}^{-1} = B^{(\boldsymbol{P})}$,

Table 8.9: The list of irreps of the little group we will consider for $K\pi$ scattering. The last column shows the lowest partial waves that each irrep includes.

d^2	Λ	l
0	A_{1g}	0, 4, ...
	T_{1u}	1, 3, ...
1	A_1	0, 1, 2, ...
	E	1, 2, 3, ...
2	A_1	0, 1, 2, ...
	B_1	1, 2, 3, ...
	B_2	1, 2, 3, ...
3	A_1	0, 1, 2, ...
	E	1, 2, 3, ...
4	A_1	0, 1, 2, ...

which gives

$$\begin{aligned} q_{cm}^{2l+1} \cot \delta_l &= q_{cm}^{2l+1} K_l^{-1} \\ &= \left(\frac{2\pi}{L}\right)^{2l+1} \widetilde{K}_l^{-1} \\ &= \left(\frac{2\pi}{L}\right)^{2l+1} B^{(\boldsymbol{P})}. \end{aligned} \tag{8.1}$$

Therefore, in this case, the phase shift can be determined exactly from calculating $B^{(\boldsymbol{P})}$.

We started with a simple fit focusing on the dominant p-wave and ignoring the mixing with the other partial waves. In this first fit we also ignore the irreps that mix with the s-wave. We expect the $K^*(892)$ to be well described by the relativistic Breit-Wigner parameterization of the T-matrix

$$T = \frac{-E_{cm}\Gamma(E_{cm})}{E_{cm}^2 - m_{K^*}^2 + iE_{cm}\Gamma(E_{cm})}. \tag{8.2}$$

We could then write this in terms of $\widetilde{K}^{-1}$ and use the result as our parameterization of the K-matrix. However, the width is strongly dependent on the unphysically large pion mass due

Table 8.10: The extracted energies relevant for the channels used in our analysis.

d^2	Λ	#	E_{cm}/m_π	$a_t\Delta E_{lab}$	$(q_{cm}/m_\pi)\cot\delta_0$	$(q_{cm}/m_\pi)^3\cot\delta_1$
0	A_{1g}	0	3.091(11)	-0.00134(37)	3.8(1.1)	---
0	T_{1u}	0	3.776(25)	-0.02151(83)	---	0.057(56)
1	A_1	0	3.214(12)	-0.00165(35)	2.02(42)	1.33(24)
		1	3.533(16)	-0.00224(41)	0.50(19)	1.63(38)
		2	3.832(23)	0.00875(69)	-0.460(63)	-1.651(82)
1	E	0	3.836(22)	-0.02367(63)	---	0.050(45)
2	A_1	0	3.303(13)	-0.00236(38)	1.16(19)	1.26(20)
		1	3.667(22)	-0.00466(66)	0.56(19)	-0.23(13)
		2	3.777(18)	-0.00083(48)	4.3(1.6)	1.44(45)
		3	3.919(20)	0.00099(54)	-4.4(1.6)	-11.8(5.6)
2	B_1	0	3.818(21)	-0.02757(59)	---	-0.109(33)
2	B_2	0	3.676(17)	-0.00434(45)	---	2.20(29)
		1	3.998(19)	0.00688(48)	---	-3.67(19)
3	A_1	0	3.404(14)	-0.00193(48)	1.32(31)	1.82(45)
		1	3.768(33)	-0.0067(10)	0.68(24)	-0.64(16)
		2	3.871(23)	-0.00335(57)	1.98(34)	0.09(15)
3	E	0	3.755(26)	-0.00716(75)	---	1.22(22)
		1	4.045(20)	0.00244(43)	---	-5.4(1.8)
4	A_1	0	3.184(15)	-0.00040(42)	2.4(1.4)	1.12(55)
		1	3.473(19)	-0.00240(64)	0.50(27)	1.48(48)
		2	3.737(62)	0.0057(19)	-0.71(34)	-1.81(52)

to a decrease in the phase space available for the decay. We instead choose to parameterize the decay width in terms of the $K^*(892) \to K\pi$ coupling g, which has been shown to have

little dependence on the pion mass [90]. The coupling is defined by

$$\Gamma(E_{cm}) = \frac{q_{cm}^3}{6\pi E_{cm}^2} g^2. \tag{8.3}$$

Next, substituting the decay width into the Breit-Wigner parameterization gives

$$q_{cm}^3 \cot \delta_1 = \frac{6\pi E_{cm}}{g^2}(m_{K^*}^2 - E_{cm}^2), \tag{8.4}$$

where we used the definition of the scattering phase shift $S_l = e^{2i\delta_l}$. Then, we write $\cot \delta_1$ in terms of $\widetilde{K}^{-1}$

$$\begin{aligned} \widetilde{K}^{-1} &= \frac{6\pi L^3 E_{cm}}{(2\pi)^3 g^2}(m_{K^*}^2 - E_{cm}^2) \\ &= \frac{6\pi (m_\pi L)^3 E_{cm}}{(2\pi)^3 m_\pi g^2}\left(\frac{m_{K^*}^2}{m_\pi^2} - \frac{E_{cm}^2}{m_\pi^2}\right). \end{aligned} \tag{8.5}$$

Finally, defining $k_0 \equiv \frac{2\pi}{m_\pi L}$, we have

$$\widetilde{K}_1^{-1} = \frac{6\pi E_{cm}}{k_0^3 m_\pi g^2}\left(\frac{m_{K^*}^2}{m_\pi^2} - \frac{E_{cm}^2}{m_\pi^2}\right), \tag{8.6}$$

which is the fit form we use to parameterize the p-wave. The result of this fit is

$$\frac{m_{K^*}}{m_\pi} = 3.814(19), \qquad g = 5.52(19), \qquad \chi^2/dof = 0.96. \tag{8.7}$$

A plot of this fit is shown in Figure 8.40. In this fit, and all subsequent fits, we used 1000 bootstrap resamplings and the Ω function defined in Eq. (7.52) with $\mu = 30$. For some fits we also used the determinant condition itself as a residual with nearly identical results to those using the Ω function. But, it becomes especially important to use the Ω function as more partial waves are included. Converting to physical units gives a mass $m_{K^*} = 893.0(2.8)$ MeV, which agrees very well with the experimental value. We also note the $K^*(892) \to K\pi$ coupling is in agreement with the experimental value of $g^{(exp)} = 5.720(60)$. These results suggest the d-wave contribution is in fact negligible. The results from Ref. [89] were found using the same irreps. Their value of $g = 5.7(1.6)$ has a mean value much closer to the experimental value, but their error is an order of magnitude larger than our error.

To show the importance of including multiple partial waves, we next performed a fit using only the s-wave. Because we expect a broad s-wave resonance, the effective range expansion was used for our model in this case

$$\widetilde{K}_0^{-1} = -\frac{1}{k_0 m_\pi a_0} + \frac{m_\pi r_0}{k_0}\left(\frac{E_{cm}}{m_\pi}\right)^2. \tag{8.8}$$

The result of this fit is shown in Figure 8.41, and has a $\chi^2/dof = 4.92$. As expected, the s-wave phase shift is poorly determined due to higher partial wave mixing.

Next, we included all irreps and allowed mixing between the s-, p-, and d-wave. Since we do not expect the d-wave contributions to be large, we parameterized this partial wave by

$$\widetilde{K}_2^{-1} = \frac{1}{k_0^5 m_\pi^5 a_2}, \tag{8.9}$$

which should result in $a_2 \approx 0$ if the d-wave is negligible. The result of this fit is

$$\begin{gathered}\frac{m_{K^*}}{m_\pi} = 3.785(15), \qquad g = 5.50(18), \qquad m_\pi a_0 = -0.36(26), \qquad m_\pi r_0 = -0.12(15), \\ m_\pi^5 a_2 = -0.0092(48), \qquad \chi^2/dof = 1.36,\end{gathered} \tag{8.10}$$

which shows that the d-wave contribution is very small. In light of this, we also performed a fit with all irreps and only included the s- and p-wave. The result of this fit is

$$\begin{gathered}\frac{m_{K^*}}{m_\pi} = 3.775(11), \qquad g = 5.48(18), \qquad m_\pi a_0 = -0.34(20), \\ m_\pi r_0 = -0.13(14), \qquad \chi^2/dof = 1.48.\end{gathered} \tag{8.11}$$

Only one previous calculation has included multiple partial waves in the extraction of the $K^*(892)$ resonance parameters [81]. But, they used a small $24^3 \times 128$ lattice, a much heavier pion around 390 MeV, and assumed the $l = 2$ partial wave was negligible without explicitly showing that this was the case. Although the stochastic LapH method was introduced for qualitative studies of the QCD excitation spectrum, these results show that the method has sufficient precision for application of the Lüscher method to study scattering phase shifts.

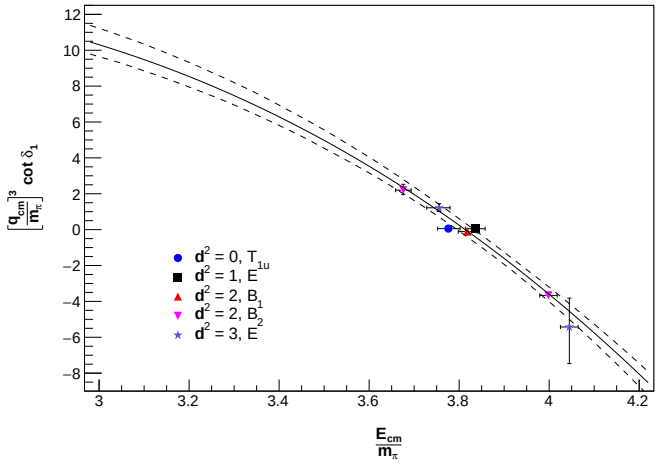

Figure 8.40: $(\frac{q_{cm}}{m_\pi})^3 \cot \delta_1$ plotted as a function of $\frac{E_{cm}}{m_\pi}$, where δ_1 is the $K\pi$ p-wave scattering phase shift. Each data point corresponds to an extracted energy, and the legend denotes the irrep and momentum for that energy. This fit assumed no partial wave mixing and only included the irreps that do not mix with $l = 0$.

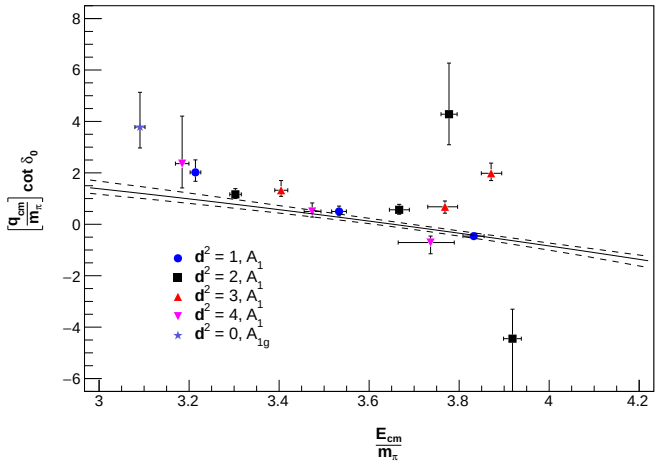

Figure 8.41: $\frac{q_{cm}}{m_\pi} \cot \delta_0$ plotted as a function of $\frac{E_{cm}}{m_\pi}$, where δ_0 is the $K\pi$ s-wave scattering phase shift. Each data point corresponds to an extracted energy, and the legend denotes the irrep and momentum for that energy. This fit assumed no partial wave mixing and resulted in $\chi^2/dof = 4.92$, which indicates this assumption is not valid.

9.0 CONCLUSIONS AND OUTLOOKS

The finite-volume single- and two-particle spectra were extracted in five symmetry channels which contain the $\rho(770)$ and its excitations. Qualitative identifications of the single-hadron dominated states were used in a comparison with the expected resonances in each channel. There we found a single-hadron dominated state that could be identified with either the $\rho_3(1690)$ or the $\rho_3(1990)$ suggesting one of these states may not be a quark-antiquark excitation. We also found a single-hadron dominated state with an energy $E = 1.814(59)\,\text{GeV}$ that is best described as a spin-2 resonance. This is in agreement with results from a smaller lattice and heavier pion [26]. Further, the resonances expected to appear in the T_{1u}^{+} channel were not all reproduced, which suggests at least one of these states is not a quark-antiquark excitation.

To identify resonances in a rigorous manner, we rely on the formalism introduced by Lüscher which relates finite-volume energies to infinite-volume scattering amplitudes. Recent developments in the inclusion of multiple partial waves and/or decay channels introduced in Ref. [27] were used for extracting the resonance parameters of the $K^*(892)$ including $l = 0$, $l = 1$, and $l = 2$ partial waves.

Finally, tetraquark operators were described, and we were able to show that every tetraquark operator we considered could be expressed as linear combinations of meson-meson-like operators. These meson-meson-like operators differ from our two-meson operators described in Chap. 3 in that each individual gauge-invariant object does not transform irreducibly under the usual symmetry groups and only the structure as a whole is made to transform appropriately. Although local operators like these were considered in Sec. 3.6.1 and discarded due to significant excited-state contamination, it may occur that the effective energy does in fact plateau much quicker for some of these tetraquark operators, which would

be a significant finding.

These methods have laid the ground work for future extensions aiming to clear up controversy surrounding the $\Lambda(1405)$, the Roper resonance, Jaffe's inverted spectrum [13], and the XYZ mesons.

APPENDIX A

RESAMPLING

Here we summarize the methods used for error calculation of so-called non-simple observables via resampling. A simple observable is one that can be defined on a single configuration (*i.e.* the observable must coincide with the integrand of a single path integral). Simple observables can therefore be estimated with errors using the Monte Carlo method. Examples of simple observables are the real or imaginary part of a temporal correlator for one time separation, and the real or imaginary part of the vacuum expectation value of a single operator. Consider a set of simple observables $\{d_i\}$, where $d_i^{(C)}$ is the value of the observable d_i on the configuration U_C, then the sample mean and covariance are given by

$$\langle d_i \rangle = \frac{1}{N_C} \sum_{C=0}^{N_C-1} d_i^{(C)}, \tag{A.1a}$$

$$\mathrm{cov}(d_i, d_j) = \frac{1}{N_C - 1} \langle (d_i - \langle d_i \rangle)(d_j - \langle d_j \rangle) \rangle = \frac{\langle d_i d_j \rangle - \langle d_i \rangle \langle d_j \rangle}{N_C - 1}, \tag{A.1b}$$

where N_C is the number of configurations, and it is assumed that autocorrelations can be ignored.[1]

A non-simple observable is any observable that is not simple. And, therefore, the methods for estimating these quantities from the Monte Carlo method in Eq. (A.1) cannot be used.

[1] Sometimes the covariance is defined with a factor of $\frac{1}{N_C}$ instead of $\frac{1}{N_C-1}$, but using the latter removes the bias from the estimate for the sample mean. The difference is usually not noticeable, though. You may wonder why this factor is there at all. The more commonly seen equation for the variance is: $\mathrm{cov}(d_i, d_i) = \langle (d_i - \langle d_i \rangle)(d_i - \langle d_i \rangle) \rangle$. This quantity is the variance of d_i itself, but what we really want is the variance in our estimate of d_i. That is, we want the variance for *our* estimate of d_i, not the variance of d_i itself. This is the difference between the population mean/covariance and the sample mean/covariance.

Examples of non-simple quantities are energies and the lattice anisotropy. Of course, a value for these quantities can still be determined, because these non-simple observables are obtained from other simple observables. For example, the effective energy (2.78) at a particular time is determined from the estimate of the correlator at two different time separations. In this case, one could use simple propagation of uncertainty to determine the error. But, it is not as clear how one could estimate the error of parameters from a fit. And, in the case of highly non-linear functions of the observables, simple propagation of uncertainty will introduce a bias in the error estimate.

Instead, the approach we advocate is to use statistical resampling schemes. Each scheme involves determining a set of resamplings for some observable, where each resampling contains an estimate for that observable. In order to determine the value of a non-simple observable on a particular resampling, we must first determine the values of the simple observables used in calculating the non-simple observable on that particular resampling. Then, we can compute the non-simple observable on each resampling of the simple observables. This allows the covariance to be determined for non-simple observables from their values on each resampling. For a discussion on how resampling is used to determine the error in best-fit parameters for a χ^2 minimization, see App. B. The two resampling schemes we consider are the jackknife and the bootstrap.

A.1 JACKKNIFE

The jackknife resamplings for a simple observable are determined by removing one configuration for each resampling. That is, the estimate on the J-th resampling for a simple observable is given by

$$\langle d_i \rangle_J = \frac{1}{N_C - 1} \sum_{C \neq J} d_i^{(C)} = \frac{1}{N_C - 1} \sum_{C=0}^{N_C - 1} d_i^{(C)} (1 - \delta_{CJ}). \tag{A.2}$$

From this definition, it can be shown that $\langle d_i \rangle = \langle d_i \rangle^{(J)}$ and $\mathrm{cov}(d_i, d_j) = \mathrm{cov}^{(J)}(d_i, d_j)$, where[2]

$$\langle d_i \rangle^{(J)} = \frac{1}{N_C} \sum_{J=0}^{N_C-1} \langle d_i \rangle_J \,, \tag{A.3a}$$

$$\mathrm{cov}^{(J)}(d_i, d_j) = \frac{N_C - 1}{N_C} \sum_{J=0}^{N_C-1} (\langle d_i \rangle_J - \langle d_i \rangle^{(J)})(\langle d_j \rangle_J - \langle d_j \rangle^{(J)}), \tag{A.3b}$$

which can be determined using only the values of an observable on each resampling, and hence for both simple and non-simple observables.

A.2 BOOTSTRAP

Each bootstrap resampling for a simple observable is determined from the values of that observable on N_C randomly chosen configurations where each configuration can be selected multiple times. The number N_B of bootstrap resamplings used can be set to anything, but of course, if too few are chosen then we would not expect a very good estimate for the covariance. So, this number should be set high enough such that any further bootstrap resamplings added do not effect the results significantly. Let $C_\alpha^{(B)}$ be the α-th randomly selected configuration for the B-th bootstrap resampling. Then, the estimate for the simple observable on the B-th resampling is

$$\langle d_i \rangle_B = \frac{1}{N_C} \sum_{\alpha=0}^{N_C-1} d_i^{(C_\alpha^{(B)})}. \tag{A.4}$$

[2]Note that the (J) in the superscript of these quantities does not refer to a particular jackknife resampling but is just a reminder that the jackknife scheme is being used.

Once the value of an observable, simple or non-simple, on each bootstrap resampling has been determined, an estimate for the mean and covariance is given by[3]

$$\langle d_i \rangle^{(B)} = \frac{1}{N_B} \sum_{b=0}^{N_B-1} \langle d_i \rangle_B \,, \tag{A.5a}$$

$$\mathrm{cov}^{(B)}(d_i, d_j) = \frac{1}{N_B - 1} \sum_{b=0}^{N_B-1} (\langle d_i \rangle_B - \langle d_i \rangle^{(B)})(\langle d_j \rangle_B = \langle d_j \rangle^{(B)}). \tag{A.5b}$$

[3]Note that, unlike with jackknife resampling, these estimates for the mean and covariance using the bootstrap resampling do not in general exactly equal $\langle d_i \rangle$ and $\mathrm{cov}(d_i, d_j)$, respectively, for non-simple observables. But, we do expect the values to be close.

APPENDIX B

FITTING

Here we present the general framework for performing a χ^2 minimization in order to determine estimates for best-fit parameters. Let the set of observables that you wish to describe by some model be arranged into a vector $\boldsymbol{R}$, and let the set of best-fit parameters be arranged into a vector $\boldsymbol{\alpha}$. Then, let the model function be denoted by a vector $\boldsymbol{M}(\boldsymbol{\alpha}, \boldsymbol{R})$. As a concrete example, suppose we want to fit a temporal correlator $C(t)$ to the function Ae^{-Et}, where A and E are the fit parameters, with a fit range of $t = (3, 20)$. Then, we would have:

$$\boldsymbol{R} = \begin{bmatrix} C(3) \\ C(4) \\ \vdots \\ C(20) \end{bmatrix}, \qquad \boldsymbol{M} = \begin{bmatrix} \alpha_0 e^{-3\alpha_1} \\ \alpha_0 e^{-4\alpha_1} \\ \vdots \\ \alpha_0 e^{-20\alpha_1} \end{bmatrix}, \qquad \boldsymbol{\alpha} = \begin{bmatrix} A \\ E \end{bmatrix}. \tag{B.1}$$

In this example, the model function $\boldsymbol{M}$ does not depend on the observables $\boldsymbol{R}$, but this will not always be the case. Below, we will see a great simplification that is achieved when the model does not depend on the observables.

Additionally, let us define the vector of residuals by

$$\boldsymbol{r}(\boldsymbol{R}, \boldsymbol{\alpha}) = \boldsymbol{R} - \boldsymbol{M}(\boldsymbol{\alpha}, \boldsymbol{R}). \tag{B.2}$$

Then, the best fit parameters in $\boldsymbol{\alpha}$ can be determined by minimizing the correlated χ^2 given by

$$\chi^2 = \sum_{i,j} \langle r_i \rangle \, \sigma_{ij}^{-1} \, \langle r_j \rangle \,, \tag{B.3}$$

where $\sigma_{ij} = \mathrm{cov}(r_i, r_j)$. The need for a correlated χ^2 is due to the data in general not being statistically independent. This is because the observables are determined from the same ensemble of configurations. However, we do assume that autocorrelations are negligible. If the model does not depend on the observables, then one can show that $\mathrm{cov}(r_i, r_j) = \mathrm{cov}(R_i, R_j)$. This greatly simplifies the minimization, because then the covariance matrix need only be calculated once before the minimization begins. If instead the model does depend on the observables, then every time one of the fit parameters in $\boldsymbol{\alpha}$ is changed, σ^{-1} must be recalculated and this can be computationally costly.

We will use a resampling scheme for our χ^2 minimizations (see App. A), and there are two cases to consider: 1) the observables are simple and 2) the observables are non-simple. If the observables are simple, then we can obtain best-fit estimates by using the standard Monte Carlo formulas (A.1) for χ^2 and performing the minimization. Then, to obtain error estimates on the fit parameters, we perform a χ^2 minimization for each resampling. This is still done by exploiting the same Monte Carlo formulas, but the summations are now only over the configurations included in the particular resampling being considered. Once the fit parameters have been determined for each resampling, the covariances for these parameters can be obtained using the covariance formulas specific to the resampling scheme (*i.e.* Eq. (A.3b) for jackknife resampling and Eq. (A.5b) for bootstrap resampling). For many cases, it may turn out that calculating the covariance matrix using the Monte Carlo formulas for each resampling has little effect on the final results. If this is the case, then one can "freeze" the covariance matrix by using the original set of configurations for each resampling. Of course, it will still be important to use the means obtained on each resampling.

Now, if the observables are non-simple, we can no longer use the Monte Carlo formulas. It will be assumed that these non-simple observables have been determined on each resampling, and the covariance matrix used in the χ^2 minimization of each resampling will be given by covariance formulas specific to that resampling scheme. Then, once a best fit value has been determined on each resampling, we can again use the formulas specific to that resampling scheme to obtain the means and covariances for each fit parameter. It is sometimes possible to use the procedure described for simple observables on non-simple observables if the observables are available on each configuration. For example, this can be

done for vacuum-subtracted temporal correlators, which are non-simple observables.

APPENDIX C

OPERATOR CHOICES

The operators we use are detailed in the tables below. For each type of operator (*e.g.* single site (SS), singly-displaced (SD), *etc.*) the numerical suffix is simply a convenient identifier. The definitions of these operators have been stored in files that our program reads. They are not given here but are available upon request.

C.1 A_{1u}^+

Table C1: The operator choices for the A_{1u}^+ channel corresponding to each level of free particle states up to 2.00 m_N. The multiplicity n is indicated in the second column. The operators in bold were chosen to be included in the correlator matrix. The operators colored red or blue were not included because they were considered too noisy or too linearly dependent on another operator, respectively. Other operators were found to be unnecessary.

E/m_N	n	Particle content	Available Operator(s)
1.299	1	$\pi(0)\ a_0[980](0)$	$\boldsymbol{\pi(0)\ A_{1u}^-\ SS0\ -\ \pi(0)\ A_{1g}^-\ SS0}$
1.330	1	$\pi(1)\ \omega(1)$	$\boldsymbol{\pi(1)\ A_2^-\ SS1\ -\ \eta(1)\ A_1^-\ SS1}$
1.361	1	$\pi(0)\ \pi(1)\ \eta(1)$	N/A
1.514	1	$\pi(2)\ \omega(2)$	$\boldsymbol{\pi(2)\ A_2^-\ SS0\ -\ \eta(2)\ A_1^-\ SS2}$
1.527	1	$\pi(1)\ a_0[980](1)$	$\boldsymbol{\pi(1)\ A_2^-\ SS1 - \pi(1)\ A_1^-\ SS0}$
1.567	1	$\pi(1)\ \phi[1020](1)$	$\boldsymbol{\pi(1)\ A_2^-\ SS1\ -\ \phi(1)\ A_1^-\ SS1}$
1.572	1	$\rho(1)\ \eta(1)$	$\boldsymbol{\pi(1)\ A_1^+\ SS1\ -\ \eta(1)\ A_2^+\ SS1}$ $\boldsymbol{\pi(1)\ A_1^+\ SS1\ -\ \phi(1)\ A_2^+\ SS1}$
1.642	1	$\overline{K}(1)\ K^*[892](1)$	$\boldsymbol{\overline{K}(1)\ A_2\ SS1\ -\ K(1)\ A_1\ SS2}$
1.673	1	$\pi(3)\ \omega(3)$	$\boldsymbol{\pi(3)\ A_2^-\ SS1\ -\ \eta(3)\ A_1^-\ SD7}$
1.701	1	$\pi(2)\ a_0[980](2)$	$\boldsymbol{\pi(2)\ A_2^-\ SS0\ -\ \pi(2)\ A_1^-\ SS0}$
1.718	1	$\rho(2)\ \eta(2)$	$\boldsymbol{\pi(2)\ A_1^+\ SS2\ -\ \eta(2)\ A_2^+\ SS0}$ $\boldsymbol{\pi(2)\ A_1^+\ SS2\ -\ \phi(2)\ A_2^+\ SS0}$
1.739	1	$\pi(2)\ \phi[1020](2)$	$\boldsymbol{\pi(2)\ A_2^-\ SS0\ -\ \phi(2)\ A_1^-\ SS2}$
1.787	1	$\overline{K}(2)\ K^*[892](2)$	$\boldsymbol{\overline{K}(2)\ A_2\ SS0\ -\ K(2)\ A_1\ SS3}$
1.811	1	$\pi(0)\ \pi(0)\ \pi(0)\ a_0[980](0)$	N/A
1.814	1	$\pi(4)\ \omega(4)$	$\boldsymbol{\pi(4)\ A_2^-\ SS1\ -\ \eta(4)\ A_1^-\ SS1}$
1.826	1	$\pi(0)\ a_0[1450](0)$	$\pi(0)\ A_{1u}^-\ TDO1\ -\ \pi(0)\ A_{1g}^-\ SD2$
1.850	1	$\pi(3)\ a_0[980](3)$	$\boldsymbol{\pi(3)\ A_2^-\ SS0\ -\ \pi(3)\ A_1^-\ SS0}$

Table C1: (continued)

E/m_N	n	Particle content	Available Operator(s)
1.852	1	$\rho(3)$ $\eta(3)$	$\boldsymbol{\pi(3)\ A_1^+\ SS2\ -\ \eta(3)\ A_2^+\ SS0}$
			$\boldsymbol{\pi(3)\ A_1^+\ SS2\ -\ \phi(3)\ A_2^+\ SS0}$
1.874	1	$\pi(1)$ $a_2[1320](1)$	$\boldsymbol{\pi(1)\ A_2^-\ SS1\ -\ \pi(1)\ A_1^-\ LSD3}$
1.887	1	$\pi(3)$ $\phi[1020](3)$	$\boldsymbol{\pi(3)\ A_2^-\ SS1\ -\ \phi(3)\ A_1^-\ SD7}$
1.911	1	$\pi(1)$ $\pi_1[1400](1)$	$\boldsymbol{\pi(1)\ A_2^-\ SS0\ -\ \pi(1)\ A_1^-\ SS0}$
1.917	1	$\rho(2)$ $\rho(2)$	$\boldsymbol{\pi(2)\ B_2^+\ SS2\ -\ \pi(2)\ B_1^+\ SS1}$
1.919	1	$\overline{K}(3)$ $K^*[892](3)$	$\boldsymbol{\overline{K}(3)\ A_2\ SS0\ -\ K(3)\ A_1\ SS3}$
1.944	2	$\pi(5)$ $\omega(5)$	N/A
1.971	1	$\rho(1)$ $\eta'(1)$	$\boldsymbol{\pi(1)\ A_1^+\ SS1\ -\ \eta(1)\ A_2^+\ SS0}$
			$\boldsymbol{\pi(1)\ A_1^+\ SS1\ -\ \phi(1)\ A_2^+\ SS0}$
1.977	1	$\rho(4)$ $\eta(4)$	$\boldsymbol{\pi(4)\ A_1^+\ SS1\ -\ \eta(4)\ A_2^+\ SS1}$
			$\boldsymbol{\pi(4)\ A_1^+\ SS1\ -\ \phi(4)\ A_2^+\ SS1}$
1.984	1	$\pi(4)$ $a_0[980](4)$	$\boldsymbol{\pi(4)\ A_2^-\ SS1\ -\ \pi(4)\ A_1^-\ SS0}$
1.985	1	$\pi(1)$ $\omega[1420](1)$	$\boldsymbol{\pi(1)\ A_2^-\ SS1\ -\ \eta(1)\ A_1^-\ SS0}$

Table C2: Additional available A_{1u}^+ operators. The operators in bold were chosen to be included in the correlator matrix. The operators colored red or blue were not included because they were considered too noisy or too linearly dependent on another operator, respectively. Other operators were found to be unnecessary.

Available Operators
$\boldsymbol{\pi(0)\ A_{1u}^+\ TDO400}$
$\boldsymbol{\pi(0)\ A_{1u}^+\ TDO0}$
$\boldsymbol{\pi(0)\ A_{1u}^+\ TDO5}$

Table C2: (continued)

Available Operators
$\pi(0)\ A_{1u}^{+}\ TDO3$
$\pi(0)\ A_{1u}^{+}\ SD0$
$\pi(0)\ A_{1u}^{+}\ TDU0$
$\pi(0)\ A_{1u}^{+}\ TDU1$
$\pi(0)\ A_{1u}^{-}\ SS0\ -\ \pi(0)\ A_{1g}^{-}\ SD2$
$\pi(0)\ A_{1u}^{-}\ TDO1\ -\ \pi(0)\ A_{1g}^{-}\ SS0$
$\pi(1)\ A_{2}^{-}\ SS0\ -\ \pi(1)\ A_{1}^{-}\ LSD3$
$\pi(1)\ A_{2}^{-}\ SS1\ -\ \pi(1)\ A_{1}^{-}\ TSD1$
$\pi(1)\ A_{2}^{-}\ TSD2\ -\ \pi(1)\ A_{1}^{-}\ SS0$
$\pi(2)\ B_{1}^{+}\ SS1\ -\ \pi(2)\ B_{2}^{+}\ SS2$
$\pi(2)\ A_{2}^{-}\ SS1\ -\ \pi(2)\ A_{1}^{-}\ TSD1$
$\pi(2)\ A_{2}^{-}\ SS0\ -\ \pi(2)\ A_{1}^{-}\ LSD7$
$\pi(1)\ A_{2}^{-}\ SS0\ -\ \eta(1)\ A_{1}^{-}\ SS0$
$\pi(1)\ A_{1}^{+}\ SS2\ -\ \eta(1)\ A_{2}^{+}\ SS0$
$\pi(2)\ A_{2}^{-}\ SS1\ -\ \eta(2)\ A_{1}^{-}\ SS1$
$\pi(2)\ A_{1}^{+}\ SS0\ -\ \eta(2)\ A_{2}^{+}\ TSD2$
$\boldsymbol{\pi(3)\ A_{2}^{-}\ SS0\ -\ \eta(3)\ A_{1}^{-}\ SS2}$
$\pi(1)\ A_{1}^{+}\ SS2\ -\ \phi(1)\ A_{2}^{+}\ SS0$
$\pi(1)\ A_{2}^{-}\ SS0\ -\ \phi(1)\ A_{1}^{-}\ SS0$
$\pi(1)\ A_{2}^{-}\ SS1\ -\ \phi(1)\ A_{1}^{-}\ SS0$
$\boldsymbol{\pi(2)\ A_{2}^{-}\ SS1\ -\ \phi(2)\ A_{1}^{-}\ SS1}$
$\boldsymbol{\pi(3)\ A_{2}^{-}\ SS0\ -\ \phi(3)\ A_{1}^{-}\ SS2}$
$\boldsymbol{\pi(4)\ A_{2}^{-}\ SS1\ -\ \phi(4)\ A_{1}^{-}\ SS1}$
$\boldsymbol{\pi(4)\ A_{1}^{+}\ SS1\ -\ \phi(4)\ A_{2}^{+}\ SS1}$
$\overline{K}(1)\ A_{2}\ SS0\ -\ K(1)\ A_{1}\ SS0$

Table C2: (continued)

Available Operators
$\overline{\boldsymbol{K}}(\mathbf{2})\ \boldsymbol{A_2}\ \boldsymbol{SS1}\ -\ \boldsymbol{K}(\mathbf{2})\ \boldsymbol{A_1}\ \boldsymbol{TSD6}$

C.2 A_{2u}^+

Table C3: The operator choices for the A_{2u}^+ channel corresponding to each level of free particle states up to 2.00 m_N. The multiplicity n is indicated in the second column. The operators in bold were chosen to be included in the correlator matrix. The operators colored red or blue were not included because they were considered too noisy or too linearly dependent on another operator, respectively. Other operators were found to be unnecessary.

E/m_N	n	Particle content	Available Operator(s)
1.296	1	$\pi(3)\ \pi(3)$	$\boldsymbol{\pi(3)\ A_2^-\ SS0\ -\ \pi(3)\ A_2^-\ SS0}$
1.514	1	$\pi(2)\ \omega(2)$	$\boldsymbol{\pi(2)\ A_2^-\ SS1\ -\ \eta(2)\ B_2^-\ SS2}$
1.592	1	$\overline{K}(3)\ K(3)$	$\boldsymbol{\overline{K}(3)\ SS0\ A_2\ -\ K(3)\ A_2\ SS0}$
1.617	1	$\pi(1)\ \pi(1)\ \eta(2)$	N/A
1.718	1	$\rho(2)\ \eta(2)$	$\boldsymbol{\pi(2)\ B_2^+\ SS2\ -\ \eta(2)\ A_2^+\ SS0}$
			$\boldsymbol{\pi(2)\ B_2^+\ SS2\ -\ \phi(2)\ A_2^+\ SS0}$
1.739	1	$\pi(2)\ \phi[1020](2)$	$\boldsymbol{\pi(2)\ A_2^-\ SS1\ -\ \phi(2)\ B_2^-\ SS2}$
1.761	1	$\pi(6)\ \pi(6)$	$\boldsymbol{\pi(6)\ A_2^-\ SS0\ -\ \pi(6)\ A_2^-\ SS0}$
1.787	1	$\overline{K}(2)\ K^*[892](2)$	$\boldsymbol{\overline{K}(2)\ A_2\ SS0\ -\ K(2)\ B_2\ SS3}$
1.789	1	$\rho(1)\ \rho(1)$	$\boldsymbol{\pi(1)\ E^+\ SS1\ -\ \pi(1)\ E^+\ SS1}$
1.799	1	$\rho_3[1690]$	$\boldsymbol{\pi(0)\ A_{2u}^+\ DDL3}$
1.808	1	$\pi(0)\ \pi(0)\ \pi(3)\ \pi(3)$	N/A
1.874	1	$\pi(1)\ a_2[1320](1)$	$\boldsymbol{\pi(1)\ A_2^-\ SS1\ -\ \pi(1)\ B_1^-\ TSD2}$
1.887	1	$\pi(2)\ h_1[1170](2)$	$\boldsymbol{\pi(2)\ A_2^-\ SS0\ -\ \eta(2)\ B_2^-\ SS2}$
			$\boldsymbol{\pi(2)\ A_2^-\ SS0\ -\ \phi(2)\ B_2^-\ SS2}$
1.917	1	$\rho(2)\ \rho(2)$	$\boldsymbol{\pi(2)\ A_1^+\ SS2\ -\ \pi(2)\ B_1^+\ SS1}$
1.944	2	$\pi(5)\ \omega(5)$	N/A
1.947	1	$\pi(2)\ a_1[1260](2)$	$\boldsymbol{\pi(2)\ A_2^-\ SS0\ -\ \pi(2)\ B_2^-\ SS0}$
1.988	1	$\overline{K}(6)\ K(6)$	$\boldsymbol{\overline{K}(6)\ A_2\ SS0\ -\ K(6)\ A_2\ SS0}$

Table C4: Additional available A_{2u}^+ operators. The operators in bold were chosen to be included in the correlator matrix. The operators colored red or blue were not included because they were considered too noisy or too linearly dependent on another operator, respectively. Other operators were found to be unnecessary.

Available Operators
$\boldsymbol{\pi(0)\ A_{2u}^+\ DDL300}$
$\boldsymbol{\pi(0)\ A_{2u}^+\ TDO303}$
$\pi(0)\ A_{2u}^+\ TDO4$
$\pi(0)\ A_{2u}^+\ DDL301$
$\pi(0)\ A_{2u}^+\ TDO302$
$\pi(0)\ A_{2u}^+\ TDO300$
$\pi(0)\ A_{2u}^+\ TDO2$
$\pi(0)\ A_{2u}^+\ TDO3$
$\pi(0)\ A_{2u}^+\ DDL2$
$\pi(0)\ A_{2u}^+\ DDL5$
$\pi(0)\ A_{2u}^+\ TDO301$
$\pi(0)\ A_{2u}^+\ DDL0$
$\pi(1)\ E^+\ SS2\ -\ \pi(1)\ E^+\ SS2$
$\pi(1)\ A_2^-\ SS0\ -\ \pi(1)\ B_1^-\ TSD3$
$\pi(2)\ B_1^+\ SS1\ -\ \pi(2)\ A_1^+\ SS2$
$\pi(2)\ A_2^-\ SS0\ -\ \pi(2)\ B_2^-\ LSD7$
$\boldsymbol{\pi(3)\ A_2^-\ SS1\ -\ \pi(3)\ A_2^-\ SS1}$
$\boldsymbol{\pi(2)\ A_2^-\ SS0\ -\ \eta(2)\ B_2^-\ SS0}$
$\pi(2)\ A_2^-\ SS1\ -\ \eta(2)\ B_2^-\ SS1$
$\pi(2)\ B_2^+\ SS1\ -\ \eta(2)\ A_2^+\ SS1$
$\boldsymbol{\pi(3)\ A_2^-\ SS0\ -\ \eta(3)\ A_2^-\ SD1}$
$\boldsymbol{\pi(2)\ A_2^-\ SS0\ -\ \phi(2)\ B_2^-\ SS0}$
$\boldsymbol{\pi(2)\ B_2^+\ SS1\ -\ \phi(2)\ A_2^+\ SS1}$

Table C4: (continued)

Available Operators
$\boldsymbol{\pi(2)\ A_2^-\ SS1\ -\ \phi(2)\ B_2^-\ SS1}$
$\boldsymbol{\pi(3)\ A_2^-\ SS0\ -\ \phi(3)\ A_2^-\ SD1}$
$\overline{K}(2)\ A_2\ SS1\ -\ K(2)\ B_2\ SS2$
$\boldsymbol{\overline{K}(3)\ A_2\ SS1\ -\ K(3)\ A_2\ SS1}$

C.3 E_u^+

Table C5: The operator choices for the E_u^+ channel corresponding to each level of free particle states up to 2.00 m_N. The multiplicity n is indicated in the second column. The operators in bold were chosen to be included in the correlator matrix. The operators colored red or blue were not included because they were considered too noisy or too linearly dependent on another operator, respectively. Other operators were found to be unnecessary.

E/m_N	n	Particle content	Available Operator(s)
1.330	1	$\pi(1)\ \omega(1)$	$\boldsymbol{\pi(1)\ A_2^-\ SS0\ -\ \eta(1)\ A_1^-\ SS1}$
1.361	1	$\pi(0)\ \pi(1)\ \eta(1)$	N/A
1.514	2	$\pi(2)\ \omega(2)$	$\boldsymbol{\pi(2)\ A_2^-\ SS1\ -\ \eta(2)\ A_1^-\ SS2}$
			$\boldsymbol{\pi(2)\ A_2^-\ SS1\ -\ \eta(2)\ B_2^-\ SS2}$
1.527	1	$\pi(1)\ a_0[980](1)$	$\boldsymbol{\pi(1)\ A_2^-\ SS1\ -\ \pi(1)\ A_1^-\ SS0}$
1.567	1	$\pi(1)\ \phi[1020](1)$	$\boldsymbol{\pi(1)\ A_2^-\ SS0\ -\ \phi(1)\ A_1^-\ SS1}$
1.572	1	$\rho(1)\ \eta(1)$	$\boldsymbol{\pi(1)\ A_1^+\ SS1\ -\ \eta(1)\ A_2^+\ SS0}$
			$\boldsymbol{\pi(1)\ A_1^+\ SS1\ -\ \phi(1)\ A_2^+\ SS0}$
1.642	1	$\overline{K}(1)\ K^*[892](1)$	$\boldsymbol{\overline{K}(1)\ A_2\ SS1\ -\ K(1)\ A_1\ SS2}$
1.660	1	$\pi(0)\ a_2[1320](0)$	$\pi(0)\ A_{1u}^-\ SS0\ -\ \pi(0)\ E_g^-\ TDU4$
1.673	1	$\pi(3)\ \omega(3)$	$\boldsymbol{\pi(3)\ A_2^-\ SS1\ -\ \eta(3)\ E^-\ SS1}$
1.701	1	$\pi(2)\ a_0[980](2)$	$\boldsymbol{\pi(2)\ A_2^-\ SS0\ -\ \pi(2)\ A_1^-\ SS0}$
1.718	2	$\rho(2)\ \eta(2)$	$\boldsymbol{\pi(2)\ A_1^+\ SS2\ -\ \eta(2)\ A_2^+\ SS0}$
			$\boldsymbol{\pi(2)\ A_1^+\ SS2\ -\ \phi(2)\ A_2^+\ SS0}$
			$\boldsymbol{\pi(2)\ B_2^+\ SS2\ -\ \eta(2)\ A_2^+\ SS0}$
			$\boldsymbol{\pi(2)\ B_2^+\ SS2\ -\ \phi(2)\ A_2^+\ SS0}$
1.739	2	$\pi(2)\ \phi[1020](2)$	$\boldsymbol{\pi(2)\ A_2^-\ SS1\ -\ \phi(2)\ A_1^-\ SS2}$
			$\boldsymbol{\pi(2)\ A_2^-\ SS1\ -\ \phi(2)\ B_2^-\ SS2}$
1.761	1	$\pi(6)\ \pi(6)$	$\boldsymbol{\pi(6)\ A_2^-\ SS0\ -\ \pi(6)\ A_2^-\ SS0}$

Table C5: (continued)

E/m_N	n	Particle content	Available Operator(s)
1.787	2	$\overline{K}(2)$ $K^*[892](2)$	$\boldsymbol{\overline{K}(2)\ A_2\ SS0\ -\ K(2)\ A_1\ SS3}$
			$\boldsymbol{\overline{K}(2)\ A_2\ SS0\ -\ K(2)\ B_2\ SS3}$
1.789	1	$\rho(1)$ $\rho(1)$	$\boldsymbol{\pi(1)\ E^+\ SS1\ -\ \pi(1)\ E^+\ SS1}$
1.814	1	$\pi(4)$ $\omega(4)$	$\boldsymbol{\pi(4)\ A_2^-\ SS1\ -\ \eta(4)\ A_1^-\ SS1}$
1.841	1	$\pi(0)$ $\pi(0)$ $\pi(1)$ $\omega(1)$	N/A
1.852	1	$\rho(3)$ $\eta(3)$	$\boldsymbol{\pi(3)\ E^+\ SS1\ -\ \eta(3)\ A_2^+\ SS0}$
			$\boldsymbol{\pi(3)\ E^+\ SS1\ -\ \phi(3)\ A_2^+\ SS0}$
1.874	2	$\pi(1)$ $a_2[1320](1)$	$\boldsymbol{\pi(1)\ A_2^-\ SS0\ -\ \pi(1)\ A_1^-\ SS0}$
			$\boldsymbol{\pi(1)\ A_2^-\ SS1\ -\ \pi(1)\ B_1^-\ TSD2}$
1.887	1	$\pi(3)$ $\phi[1020](3)$	$\boldsymbol{\pi(3)\ A_2^-\ SS1\ -\ \phi(3)\ E^-\ SS1}$
1.887	1	$\pi(2)$ $h_1[1170](2)$	$\boldsymbol{\pi(2)\ A_2^-\ SS0\ -\ \eta(2)\ B_2^-\ SS2}$
			$\boldsymbol{\pi(2)\ A_2^-\ SS0\ -\ \phi(2)\ B_2^-\ SS2}$
1.911	1	$\pi(1)$ $\pi_1[1400](1)$	$\boldsymbol{\pi(1)\ A_2^-\ SS1\ -\ \pi(1)\ A_1^-\ LSD3}$
1.917	2	$\rho(2)$ $\rho(2)$	$\boldsymbol{\pi(2)\ A_1^+\ SS2\ -\ \pi(2)\ B_1^+\ SS1}$
			$\boldsymbol{\pi(2)\ B_1^+\ SS1\ -\ \pi(2)\ B_2^+\ SS1}$
1.919	1	$\overline{K}(3)$ $K^*[892](3)$	$\boldsymbol{\overline{K}(3)\ A_2\ SS0\ -\ K(3)\ E\ SS1}$
1.944	4	$\pi(5)$ $\omega(5)$	N/A
1.947	1	$\pi(2)$ $a_1[1260](2)$	$\boldsymbol{\pi(2)\ A_2^-\ SS0\ -\ \pi(2)\ B_2^-\ SS0}$
1.971	1	$\rho(1)$ $\eta'(1)$	$\boldsymbol{\pi(1)\ A_1^+\ SS1\ -\ \eta(1)\ A_2^+\ SS1}$
			$\boldsymbol{\pi(1)\ A_1^+\ SS1\ -\ \phi(1)\ A_2^+\ SS1}$
1.977	1	$\rho(4)$ $\eta(4)$	$\boldsymbol{\pi(4)\ A_1^+\ SS1\ -\ \eta(4)\ A_2^+\ SS1}$
			$\boldsymbol{\pi(4)\ A_1^+\ SS1\ -\ \phi(4)\ A_2^+\ SS1}$
1.984	1	$\pi(4)$ $a_0[980](4)$	$\boldsymbol{\pi(4)\ A_2^-\ SS1\ -\ \pi(4)\ A_1^-\ SS0}$
1.985	1	$\pi(1)$ $\omega[1420](1)$	$\boldsymbol{\pi(1)\ A_2^-\ SS1\ -\ \eta(1)\ A_1^-\ SS1}$
1.988	1	$\overline{K}(6)$ $K(6)$	$\boldsymbol{\overline{K}(6)\ A_2\ SS0\ -\ K(6)\ A_2\ SS0}$

Table C6: Additional available E_u^+ operators. The operators in bold were chosen to be included in the correlator matrix. The operators colored red or blue were not included because they were considered too noisy or too linearly dependent on another operator, respectively. Other operators were found to be unnecessary.

Available Operators
$\boldsymbol{\pi(0)\ E_u^+\ SD0}$
$\pi(0)\ E_u^+\ DDL5$
$\pi(0)\ E_u^+\ TDU0$
$\pi(0)\ E_u^+\ DDL4$
$\boldsymbol{\pi(0)\ E_u^+\ TDO5}$
$\pi(0)\ E_u^+\ DDL3$
$\pi(0)\ E_u^+\ TDO400$
$\pi(0)\ E_u^+\ DDL1$
$\pi(0)\ E_u^+\ TDO2$
$\pi(0)\ A_{1u}^-\ TDO1\ -\ \pi(0)\ E_g^-\ TDU4$
$\pi(1)\ A_2^-\ SS1\ -\ \pi(1)\ A_1^-\ LSD0$
$\pi(1)\ A_2^-\ SS1\ -\ \pi(1)\ A_1^-\ TSD1$
$\pi(2)\ A_2^-\ SS0\ -\ \pi(2)\ B_2^-\ LSD7$
$\pi(2)\ A_2^-\ SS0\ -\ \pi(2)\ A_1^-\ LSD7$
$\pi(1)\ A_2^-\ SS1\ -\ \eta(1)\ A_1^-\ SS0$
$\pi(2)\ A_2^-\ SS0\ -\ \eta(2)\ A_1^-\ SS2$
$\pi(2)\ A_2^-\ SS0\ -\ \eta(2)\ B_2^-\ SS0$
$\pi(3)\ A_2^-\ SS0\ -\ \eta(3)\ E^-\ SS1$
$\pi(3)\ A_2^-\ SS0\ -\ \eta(3)\ E^-\ SS2$
$\boldsymbol{\pi(1)\ A_2^-\ SS1\ -\ \phi(1)\ A_1^-\ SS1}$
$\pi(1)\ A_1^+\ SS0\ -\ \phi(1)\ A_2^+\ SS0$
$\pi(1)\ A_2^-\ SS1\ -\ \phi(1)\ A_1^-\ SS0$
$\boldsymbol{\pi(2)\ A_2^-\ SS0\ -\ \phi(2)\ A_1^-\ SS2}$

Table C6: (continued)

Available Operators
$\pi(2)\ A_2^-\ SS0\ -\ \phi(2)\ B_2^-\ SS0$
$\boldsymbol{\pi(3)\ A_2^-\ SS0\ -\ \phi(3)\ E^-\ SS1}$
$\pi(3)\ A_2^-\ SS1\ -\ \phi(3)\ E^-\ SS2$
$\boldsymbol{\pi(4)\ A_2^-\ SS1\ -\ \phi(4)\ A_1^-\ SS1}$
$\overline{K}(1)\ A_2\ SS0\ -\ K(1)\ A_1\ SS0$

C.4 T_{1u}^{+}

Table C7: The operator choices for the T_{1u}^{+} channel corresponding to each level of free particle states up to 2.00 m_N. The multiplicity n is indicated in the second column. The operators in bold were chosen to be included in the correlator matrix. The operators colored red or blue were not included because they were considered too noisy or too linearly dependent on another operator, respectively. Other operators were found to be unnecessary.

E/m_N	n	Particle content	Available Operator(s)
0.826	1	ρ	$\boldsymbol{\pi(0)\ T_{1u}^{+}\ TDO3}$
0.857	1	$\pi(1)\ \pi(1)$	$\boldsymbol{\pi(1)\ A_2^-\ SS1\ -\ \pi(1)\ A_2^-\ SS1}$
1.099	1	$\pi(2)\ \pi(2)$	$\boldsymbol{\pi(2)\ A_2^-\ SS0\ -\ \pi(2)\ A_2^-\ SS0}$
1.260	1	$\overline{K}(1)\ K(1)$	$\boldsymbol{\overline{K}(1)\ A_2\ SS1\ -\ K(1)\ A_2\ SS1}$
1.296	1	$\pi(3)\ \pi(3)$	$\boldsymbol{\pi(3)\ A_2^-\ SS0\ -\ \pi(3)\ A_2^-\ SS0}$
1.330	1	$\pi(1)\ \omega(1)$	$\boldsymbol{\pi(1)\ A_2^-\ LSD1\ -\ \eta(1)\ E^-\ SS1}$
1.337	1	$\pi(0)\ \pi(0)\ \rho(0)$	N/A
1.368	1	$\pi(0)\ \pi(0)\ \pi(1)\ \pi(1)$	N/A
1.436	1	$\overline{K}(2)\ K(2)$	$\boldsymbol{\overline{K}(2)\ A_2\ SS0\ -\ K(2)\ A_2\ SS0}$
1.467	1	$\pi(4)\ \pi(4)$	$\boldsymbol{\pi(4)\ A_2^-\ SS1\ -\ \pi(4)\ A_2^-\ SS1}$
1.502	1	$\pi(0)\ h_1[1170](0)$	$\boldsymbol{\pi(0)\ A_{1u}^-\ SS0\ -\ \eta(0)\ T_{1g}^-\ SD1}$
1.514	2	$\pi(2)\ \omega(2)$	$\boldsymbol{\pi(2)\ A_2^-\ SS0\ -\ \eta(2)\ B_1^-\ SS1}$ $\boldsymbol{\pi(2)\ A_2^-\ SS0\ -\ \eta(2)\ B_2^-\ SS2}$
1.560	1	$\rho[1450]$	$\boldsymbol{\pi(0)\ T_{1u}^{+}\ SS1}$
1.566	1	$\pi(0)\ a_1[1260](0)$	$\boldsymbol{\pi(0)\ A_{1u}^-\ SS0\ -\ \pi(0)\ T_{1g}^-\ SS0}$
1.567	1	$\pi(1)\ \phi[1020](1)$	$\boldsymbol{\pi(1)\ A_2^-\ SS1\ -\ \phi(1)\ E^-\ SS1}$
1.572	1	$\rho(1)\ \eta(1)$	$\boldsymbol{\pi(1)\ E^+\ SS1\ -\ \eta(1)\ A_2^+\ SS1}$
1.592	1	$\overline{K}(3)\ K(3)$	$\boldsymbol{\overline{K}(3)\ A_2\ SS0\ -\ K(3)\ A_2\ SS0}$
1.621	2	$\pi(5)\ \pi(5)$	$\boldsymbol{\pi(5)\ A_2^-\ SS0\ -\ \pi(5)\ A_2^-\ SS0}$

Table C7: (continued)

E/m_N	n	Particle content	Available Operator(s)
			$\boldsymbol{\pi(5)\ A_2^-\ SS0\ -\ \pi(5)\ A_2^-\ SS0\ [CG1]}$
1.642	1	$\overline{K}(1)\ K^*[892](1)$	$\boldsymbol{\overline{K}(1)\ A_2\ SS1\ -\ K(1)\ E\ SS2}$
1.672	1	$\rho[1570]$	$\boldsymbol{\pi(0)\ T_{1u}^+\ SS0}$
1.673	1	$\pi(3)\ \omega(3)$	$\boldsymbol{\pi(3)\ A_2^-\ SS0\ -\ \eta(3)\ E^-\ SS1}$
1.718	2	$\rho(2)\ \eta(2)$	$\boldsymbol{\pi(2)\ B_1^+\ SS1\ -\ \eta(2)\ A_2^+\ SS0}$
			$\boldsymbol{\pi(2)\ B_1^+\ SS2\ -\ \eta(2)\ A_2^+\ SS0}$
1.721	2	$\pi(1)\ h_1[1170](1)$	$\boldsymbol{\pi(1)\ A_2^-\ SS1\ -\ \eta(1)\ A_2^-\ LSD3}$
			$\boldsymbol{\pi(1)\ A_2^-\ SS1\ -\ \eta(1)\ E^-\ SS2}$
			$\boldsymbol{\pi(1)\ A_2^-\ SS1\ -\ \phi(1)\ E^-\ SS2}$
1.734	1	$\overline{K}(4)\ K(4)$	$\boldsymbol{\overline{K}(4)\ A_2\ SS1\ -\ K(4)\ A_2\ SS1}$
1.739	2	$\pi(2)\ \phi[1020](2)$	$\boldsymbol{\pi(2)\ A_2^-\ SS0\ -\ \phi(2)\ B_1^-\ SS1}$
			$\boldsymbol{\pi(2)\ A_2^-\ SS0\ -\ \phi(2)\ B_2^-\ SS2}$
1.761	2	$\pi(6)\ \pi(6)$	$\boldsymbol{\pi(6)\ A_2^-\ SS0\ -\ \pi(6)\ A_2^-\ SS0}$
			$\boldsymbol{\pi(6)\ A_2^-\ SS0\ -\ \pi(6)\ A_2^-\ SS0\ [CG1]}$
1.783	2	$\pi(1)\ a_1[1260](1)$	$\boldsymbol{\pi(1)\ A_2^-\ SS1\ -\ \pi(1)\ A_2^-\ SS0}$
			$\boldsymbol{\pi(1)\ A_2^-\ SS1\ -\ \pi(1)\ E^-\ SS0}$
1.787	2	$\overline{K}(2)\ K^*[892](2)$	$\boldsymbol{\overline{K}(2)\ A_2\ SS0\ -\ K(2)\ B_1\ SS1}$
			$\boldsymbol{\overline{K}(2)\ A_2\ SS0\ -\ K(2)\ B_2\ SS3}$
1.789	3	$\rho(1)\ \rho(1)$	$\boldsymbol{\pi(1)\ A_1^+\ SS1\ -\ \pi(1)\ A_1^+\ SS1}$
			$\boldsymbol{\pi(1)\ A_1^+\ SS1\ -\ \pi(1)\ E^+\ SS1}$
			$\boldsymbol{\pi(1)\ E^+\ SS1\ -\ \pi(1)\ E^+\ SS1}$
1.799	1	$\rho_3[1690]$	$\boldsymbol{\pi(0)\ T_{1u}^+\ DDL13}$
1.814	1	$\pi(4)\ \omega(4)$	$\boldsymbol{\pi(4)\ A_2^-\ SS1\ -\ \eta(4)\ E^-\ SS1}$
1.832	1	$\rho[1700]$	$\boldsymbol{\pi(0)\ T_{1u}^+\ DDL2}$
1.852	1	$\rho(3)\ \eta(3)$	$\boldsymbol{\pi(3)\ E^+\ SS1\ -\eta(3)\ A_2^+\ SS0}$

Table C7: (continued)

E/m_N	n	Particle content	Available Operator(s)
			$\boldsymbol{\pi(3)\ E^+\ SS1\ -\phi(3)\ A_2^+\ SS0}$
1.855	1	$\pi(1)\ \pi[1300](1)$	$\pi(1)\ A_2^-\ TSD2\ -\ \pi(1)\ A_2^-\ TSD1$
1.865	2	$\overline{K}(5)\ K(5)$	N/A
1.874	1	$\pi(1)\ a_2[1320](1)$	$\boldsymbol{\pi(1)\ A_2^-\ SS1\ -\ \pi(1)\ E^-\ TSD1}$
1.877	1	$a_0[980](0)\ \omega(0)$	$\boldsymbol{\pi(0)\ A_{1g}^-\ SS0\ -\ \eta(0)\ T_{1u}^-\ SS0}$
1.880	1	$\rho(0)\ f_0[980](0)$	N/A
1.883	1	$\overline{K}(0)\ K_1[1270](0)$	$\boldsymbol{\overline{K}(0)\ A_{1u}\ SS0\ -\ K(0)\ T_{1g}\ SS0}$
1.887	1	$\pi(3)\ \phi[1020](3)$	$\boldsymbol{\pi(3)\ A_2^-\ SS0\ -\ \phi(3)\ E^-\ SS1}$
1.887	3	$\pi(2)\ h_1[1170](2)$	$\boldsymbol{\pi(2)\ A_2^-\ SS0\ -\ \eta(2)\ A_2^-\ SS0}$
			$\boldsymbol{\pi(2)\ A_2^-\ SS0\ -\ \phi(2)\ A_2^-\ SS0}$
			$\boldsymbol{\pi(2)\ A_2^-\ SS0\ -\ \eta(2)\ B_1^-\ SS2}$
			$\boldsymbol{\pi(2)\ A_2^-\ SS0\ -\ \phi(2)\ B_1^-\ SS2}$
			$\boldsymbol{\pi(2)\ A_2^-\ SS0\ -\ \eta(2)\ B_2^-\ SS0}$
			$\boldsymbol{\pi(2)\ A_2^-\ SS0\ -\ \phi(2)\ B_2^-\ SS0}$
1.893	1	$b_1[1235](0)\ \eta(0)$	$\pi(0)\ T_{1g}^+\ SS0\ -\ \eta(0)\ A_{1u}^+\ SS0$
1.911	1	$\pi(1)\ \pi_1[1400](1)$	$\pi(1)\ A_2^-\ SS1\ -\ \pi(1)\ E^-\ LSD1$
1.917	5	$\rho(2)\ \rho(2)$	$\boldsymbol{\pi(2)\ A_1^+\ SS2\ -\ \pi(2)\ A_1^+\ SS2}$
			$\boldsymbol{\pi(2)\ A_1^+\ SS2\ -\ \pi(2)\ B_1^+\ SS1}$
			$\boldsymbol{\pi(2)\ A_1^+\ SS2\ -\ \pi(2)\ B_2^+\ SS2}$
			$\boldsymbol{\pi(2)\ B_1^+\ SS1\ -\ \pi(2)\ B_1^+\ SS1}$
			$\boldsymbol{\pi(2)\ B_2^+\ SS2\ -\ \pi(2)\ B_2^+\ SS2}$
1.919	1	$\overline{K}(3)\ K^*[892](3)$	$\boldsymbol{\overline{K}(3)\ A_2\ SS0\ -\ K(3)\ E\ SS1}$
1.944	4	$\pi(5)\ \omega(5)$	N/A
1.947	3	$\pi(2)\ a_1[1260](2)$	$\boldsymbol{\pi(2)\ A_2^-\ SS1\ -\ \pi(2)\ A_2^-\ SS0}$
			$\boldsymbol{\pi(2)\ A_2^-\ SS0\ -\ \pi(2)\ B_1^-\ SS0}$

Table C7: (continued)

E/m_N	n	Particle content	Available Operator(s)
			$\boldsymbol{\pi(2)\ A_2^-\ SS0\ -\ \pi(2)\ B_2^-\ SS0}$
1.971	1	$\rho(1)\ \eta'(1)$	N/A
1.977	1	$\rho(4)\ \eta(4)$	N/A
1.985	1	$\pi(1)\ \omega[1420](1)$	$\pi(1)\ A_2^-\ SS1\ -\ \eta(1)\ E^-\ SS0$
1.988	2	$\overline{K}(6)\ K(6)$	N/A

Table C8: Additional available T_{1u}^+ operators. The operators in bold were chosen to be included in the correlator matrix. The operators colored red or blue were not included because they were considered too noisy or too linearly dependent on another operator, respectively. Other operators were found to be unnecessary.

Available Operators
$\pi(0)\ T_{1u}^+\ TDO15$
$\pi(0)\ T_{1u}^+\ DDL3$
$\boldsymbol{\pi(0)\ T_{1u}^+\ DDL8}$
$\boldsymbol{\pi(0)\ T_{1u}^+\ DDL4}$
$\pi(0)\ T_{1u}^+\ DDL1$
$\pi(0)\ T_{1u}^+\ TDO300$
$\pi(0)\ T_{1u}^+\ TDO303$
$\boldsymbol{\pi(0)\ T_{1u}^+\ TDO400}$
$\pi(0)\ T_{1u}^+\ DDL300$
$\boldsymbol{\pi(0)\ T_{1u}^+\ DDL301}$
$\pi(0)\ T_{1u}^+\ TDO302$
$\pi(0)\ T_{1u}^+\ TDO22$

Table C8: (continued)

Available Operators
$\pi(0)\ T_{1u}^{+}\ DDL12$
$\pi(0)\ T_{1u}^{+}\ TDO7$
$\pi(0)\ T_{1u}^{+}\ TDO301$
$\pi(0)\ T_{1u}^{+}\ DDL0$
$\pi(0)\ T_{1u}^{+}\ TDU0$
$\pi(0)\ T_{1u}^{+}\ TDO10$
$\pi(0)\ A_{1u}^{-}\ TDO1\ -\ \pi(0)\ T_{1g}^{-}\ SS0$
$\pi(1)\ A_{2}^{-}\ SS1\ -\ \pi(1)\ A_{2}^{-}\ TSD0$
$\boldsymbol{\pi(2)\ A_2^-\ SS1\ -\ \pi(2)\ A_2^-\ SS1}$
$\boldsymbol{\pi(4)\ A_2^-\ SS1\ -\ \pi(4)\ A_2^-\ TSD0}$
$\pi(8)\ A_{2}^{-}\ SS0\ -\ \pi(8)\ A_{2}^{-}\ SS0$
$\pi(0)\ A_{1u}^{-}\ SS0\ -\ \eta(0)\ T_{1g}^{-}\ SS0$
$\pi(3)\ A_{2}^{-}\ SS0\ -\ \eta(3)\ E^{-}\ SD6$
$\boldsymbol{\pi(1)\ A_2^-\ SS1\ -\ \phi(1)\ E^-\ SS0}$
$\boldsymbol{\pi(4)\ A_2^-\ SS1\ -\ \phi(4)\ E^-\ SS1}$
$\boldsymbol{\overline{K}(1)\ A_2\ SS0\ -\ K(1)\ E\ SS3}$
$\boldsymbol{\overline{K}(2)\ A_2\ SS1\ -\ K(2)\ A_2\ SS0}$
$\boldsymbol{\overline{K}(3)\ A_2\ SS1\ -\ K(3)\ A_2\ SS0}$

C.5 T_{2u}^{+}

Table C9: The operator choices for the T_{2u}^{+} channel corresponding to each level of free particle states up to 2.00 m_N. The multiplicity n is indicated in the second column. The operators in bold were chosen to be included in the correlator matrix. The operators colored red or blue were not included because they were considered too noisy or too linearly dependent on another operator, respectively. Other operators were found to be unnecessary.

E/m_N	n	Particle content	Available Operator(s)
1.099	1	$\pi(2)\ \pi(2)$	$\boldsymbol{\pi(2)\ A_2^-\ SS0\ -\ \pi(2)\ A_2^-\ SS0}$
1.330	1	$\pi(1)\ \omega(1)$	$\boldsymbol{\pi(1)\ A_2^-\ SS1\ -\ \eta(1)\ E^-\ SS1}$
1.436	1	$\overline{K}(2)\ K(2)$	$\boldsymbol{\overline{K}(2)\ A_2\ SS0\ -\ K(2)\ A_2\ SS0}$
1.514	2	$\pi(2)\ \omega(2)$	$\boldsymbol{\pi(2)\ A_2^-\ SS0\ -\ \eta(2)\ A_1^-\ SS2}$
			$\boldsymbol{\pi(2)\ A_2^-\ SS1\ -\ \eta(2)\ B_1^-\ SS1}$
1.565	1	$\pi(0)\ \pi(2)\ \eta(2)$	N/A
1.567	1	$\pi(1)\ \phi[1020](1)$	$\boldsymbol{\pi(1)\ A_2^-\ SS1\ -\ \phi(1)\ E^-\ SS2}$
1.572	1	$\rho(1)\ \eta(1)$	$\boldsymbol{\pi(1)\ E^+\ SS1\ -\ \eta(1)\ A_2^+\ SS0}$
			$\boldsymbol{\pi(1)\ E^+\ SS1\ -\ \phi(1)\ A_2^+\ SS1}$
1.610	1	$\pi(0)\ \pi(0)\ \pi(2)\ \pi(2)$	N/A
1.621	2	$\pi(5)\ \pi(5)$	$\pi(5)\ A_2^-\ SS0\ -\ \pi(5)\ A_2^-\ SS0$
			$\boldsymbol{\pi(5)\ A_2^-\ SS0\ -\ \pi(5)\ A_2^-\ SS0\ [CG1]}$
1.642	1	$\overline{K}(1)\ K^*[892](1)$	$\boldsymbol{\overline{K}(1)\ A_2\ SS1\ -\ K(1)\ E\ SS2}$
1.660	1	$\pi(0)\ a_2[1320](0)$	$\pi(0)\ A_{1u}^-\ SS0\ -\ \pi(0)\ T_{2g}^-\ TDO24$
1.673	1	$\pi(3)\ \omega(3)$	$\boldsymbol{\pi(3)\ A_2^-\ SS0\ -\ \eta(3)\ E^-\ SS1}$
1.701	1	$\pi(2)\ a_0[980](2)$	$\boldsymbol{\pi(2)\ A_2^-\ SS0\ -\ \pi(2)\ A_1^-\ SS0}$
1.718	2	$\rho(2)\ \eta(2)$	$\boldsymbol{\pi(2)\ A_1^+\ SS2\ -\ \eta(2)\ A_2^+\ SS0}$
			$\boldsymbol{\pi(2)\ A_1^+\ SS2\ -\ \phi(2)\ A_2^+\ SS0}$
			$\boldsymbol{\pi(2)\ B_1^+\ SS1\ -\ \eta(2)\ A_2^+\ SS0}$

Table C9: (continued)

E/m_N	n	Particle content	Available Operator(s)
			$\boldsymbol{\pi(2)\ B_1^+\ SS1\ -\ \phi(2)\ A_2^+\ SS0}$
1.721	2	$\pi(1)\ h_1[1170](1)$	$\boldsymbol{\pi(1)\ A_2^-\ SS0\ -\ \eta(1)\ E^-\ SS1}$
			$\boldsymbol{\pi(1)\ A_2^-\ SS1\ -\ \phi(1)\ E^-\ SS1}$
1.739	2	$\pi(2)\ \phi[1020](2)$	$\boldsymbol{\pi(2)\ A_2^-\ SS0\ -\ \phi(2)\ A_1^-\ SS2}$
			$\boldsymbol{\pi(2)\ A_2^-\ SS1\ -\ \phi(2)\ B_1^-\ SS1}$
1.761	2	$\pi(6)\ \pi(6)$	$\boldsymbol{\pi(6)\ A_2^-\ SS0\ -\ \pi(6)\ A_2^-\ SS0}$
1.783	2	$\pi(1)\ a_1[1260](1)$	$\boldsymbol{\pi(1)\ A_2^-\ SS1\ -\ \pi(1)\ E^-\ SS0}$
1.787	2	$\overline{K}(2)\ K^*[892](2)$	$\boldsymbol{\overline{K}(2)\ A_2\ SS0\ -\ K(2)\ A_1\ SS3}$
			$\boldsymbol{\overline{K}(2)\ A_2\ SS0\ -\ K(2)\ B_1\ SS1}$
1.789	3	$\rho(1)\ \rho(1)$	$\boldsymbol{\pi(1)\ A_1^+\ SS1\ -\ \pi(1)\ E^+\ SS1}$
			$\boldsymbol{\pi(1)\ E^+\ SS1\ -\ \pi(1)\ E^+\ SS1}$
1.799	1	$\rho_3[1690]$	$\boldsymbol{\pi(0)\ T_{2u}^+\ SD2}$
1.814	1	$\pi(4)\ \omega(4)$	$\boldsymbol{\pi(4)\ A_2^-\ SS1 - \eta(4)\ E^-\ SS1}$
1.850	1	$\pi(3)\ a_0[980](3)$	$\boldsymbol{\pi(3)\ A_2^-\ SS0\ -\ \pi(3)\ A_1^-\ SS0}$
1.852	1	$\rho(3)\ \eta(3)$	$\pi(3)\ E^+\ SS1\ -\eta(3)\ A_2^+\ SS0$
			$\pi(3)\ E^+\ SS1\ -\phi(3)\ A_2^+\ SS0$
1.865	2	$\overline{K}(5)\ K(5)$	$\boldsymbol{\overline{K}(5)\ A_2\ SS0\ -\ K(5)\ A_2\ SS0}$
			$\boldsymbol{\overline{K}(5)\ A_2\ SS0\ -\ K(5)\ A_2\ SS0\ [CG1]}$
1.874	1	$\pi(1)\ a_2[1320](1)$	$\pi(1)\ A_2^-\ SS1\ -\ \pi(1)\ E^-\ LSD1$
1.887	1	$\pi(3)\ \phi[1020](3)$	$\pi(3)\ A_2^-\ SS0\ -\ \phi(3)\ E^-\ SS1$
1.887	3	$\pi(2)\ h_1[1170](2)$	$\pi(2)\ A_2^-\ SS0\ -\ \eta(2)\ A_2^-\ SS0$
			$\pi(2)\ A_2^-\ SS0\ -\ \phi(2)\ A_2^-\ SS0$
			$\boldsymbol{\pi(2)\ A_2^-\ SS0\ -\ \eta(2)\ B_1^-\ SS1}$
			$\boldsymbol{\pi(2)\ A_2^-\ SS0\ -\ \phi(2)\ B_1^-\ SS1}$
1.911	1	$\pi(1)\ \pi_1[1400](1)$	$\pi(1)\ A_2^-\ SS1 -\ \pi(1)\ E^-\ TSD1$

Table C9: (continued)

E/m_N	n	Particle content	Available Operator(s)
1.917	5	$\rho(2)$ $\rho(2)$	$\boldsymbol{\pi(2)\ A_1^+\ SS2\ -\ \pi(2)\ A_1^+\ SS2}$
			$\boldsymbol{\pi(2)\ A_1^+\ SS2\ -\ \pi(2)\ B_2^+\ SS2}$
			$\boldsymbol{\pi(2)\ B_1^+\ SS1\ -\ \pi(2)\ B_1^+\ SS1}$
			$\pi(2)\ B_1^+\ SS1\ -\ \pi(2)\ B_2^+\ SS2$
			$\pi(2)\ B_2^+\ SS2\ -\ \pi(2)\ B_2^+\ SS2$
1.919	1	$\overline{K}(3)$ $K^*[892](3)$	$\overline{K}(3)\ A_2\ SS0\ -\ K(3)\ E\ SS1$
1.944	4	$\pi(5)$ $\omega(5)$	N/A
1.947	3	$\pi(2)$ $a_1[1260](2)$	$\boldsymbol{\pi(2)\ A_2^-\ SS0\ -\ \pi(2)\ A_2^-\ LSD1}$
			$\boldsymbol{\pi(2)\ A_2^-\ SS0\ -\ \pi(2)\ B_1^-\ SS0}$
1.971	1	$\rho(1)$ $\eta'(1)$	$\pi(1)\ E^+\ SS1\ -\ \eta(1)\ A_2^+\ SS1$
			$\boldsymbol{\pi(1)\ E^+\ SS1\ -\ \phi(1)\ A_2^+\ SS0}$
1.977	1	$\rho(4)$ $\eta(4)$	$\boldsymbol{\pi(4)\ E^+\ SS1\ -\ \eta(4)\ A_2^+\ SS1}$
			$\boldsymbol{\pi(4)\ E^+\ SS1\ -\ \phi(4)\ A_2^+\ SS1}$
1.985	1	$\pi(1)$ $\omega[1420](1)$	$\boldsymbol{\pi(1)\ A_2^-\ SS1\ -\ \eta(1)\ E^-\ SS2}$
1.988	1	$\overline{K}(6)$ $K(6)$	$\boldsymbol{\overline{K}(6)\ A_2\ SS0\ -\ K(6)\ A_2\ SS0}$

Table C10: Additional available T_{2u}^+ operators. The operators in bold were chosen to be included in the correlator matrix. The operators colored red or blue were not included because they were considered too noisy or too linearly dependent on another operator, respectively. Other operators were found to be unnecessary.

Available Operators
$\boldsymbol{\pi(0)\ T_{2u}^+\ SD1}$
$\boldsymbol{\pi(0)\ T_{2u}^+\ DDL300}$

Table C10: (continued)

Available Operators
$\boldsymbol{\pi(0)\ T_{2u}^{+}\ DDL301}$
$\pi(0)\ T_{2u}^{+}\ TDU7$
$\pi(0)\ T_{2u}^{+}\ TDO303$
$\pi(0)\ T_{2u}^{+}\ TDU5$
$\pi(0)\ T_{2u}^{+}\ TDO302$
$\pi(0)\ T_{2u}^{+}\ TDO300$
$\pi(0)\ T_{2u}^{+}\ SD0$
$\pi(0)\ T_{2u}^{+}\ TDO400$
$\pi(0)\ T_{2u}^{+}\ TDO5$
$\pi(0)\ T_{2u}^{+}\ TDO4$
$\pi(0)\ T_{2u}^{+}\ DDL0$
$\pi(0)\ T_{2u}^{+}\ TDO301$
$\pi(0)\ T_{2u}^{+}\ TDO7$
$\pi(0)\ A_{1u}^{-}\ TDO1\ -\ \pi(0)\ T_{2g}^{-}\ TDO24$
$\pi(1)\ E^{+}\ SS1\ -\ \pi(1)\ A_{1}^{+}\ SS1$
$\pi(1)\ A_{2}^{-}\ SS1\ -\ \pi(2)\ B_{2}^{-}\ TSD1$
$\pi(2)\ B_{1}^{+}\ SS1\ -\ \pi(2)\ B_{2}^{+}\ SS2$
$\pi(2)\ A_{2}^{-}\ SS1\ -\ \pi(2)\ A_{2}^{-}\ SS1$
$\boldsymbol{\pi(2)\ A_{2}^{-}\ SS0\ -\ \pi(2)\ A_{1}^{-}\ LSD7}$
$\pi(2)\ A_{2}^{-}\ SS0\ -\ \pi(2)\ A_{2}^{-}\ SS1$
$\pi(2)\ B_{2}^{+}\ SS2\ -\ \pi(2)\ A_{1}^{+}\ SS2$
$\pi(2)\ A_{2}^{-}\ SS0\ -\ \pi(2)\ B_{1}^{-}\ LSD4$
$\pi(2)\ B_{2}^{+}\ SS2\ -\ \pi(1)\ B_{2}^{+}\ SS2$
$\boldsymbol{\pi(1)\ E^{+}\ SS1\ -\ \eta(1)\ A_{2}^{+}\ SS1}$
$\boldsymbol{\pi(1)\ A_{2}^{-}\ SS1\ -\ \eta(1)\ E^{-}\ TSD3}$
$\pi(1)\ E^{+}\ SS2\ -\ \eta(1)\ A_{2}^{+}\ SS1$

Table C10: (continued)

Available Operators
$\pi(2)\ A_2^-\ SS1\ -\ \eta(2)\ A_1^-\ SS2$
$\pi(2)\ A_2^-\ SS0\ -\ \eta(2)\ B_1^-\ SS2$
$\pi(2)\ A_2^-\ SS0\ -\ \eta(2)\ A_2^-\ SS0$
$\pi(3)\ A_2^-\ SS1\ -\ \eta(3)\ A_1^-\ SS2$
$\boldsymbol{\pi(3)\ A_2^-\ SS0\ -\ \eta(3)\ A_1^-\ SS2}$
$\boldsymbol{\pi(3)\ A_1^+\ SS2\ -\ \eta(3)\ A_2^+\ SS0}$
$\pi(3)\ A_2^-\ SS0\ -\ \eta(3)\ E^-\ SS2$
$\boldsymbol{\pi(1)\ A_2^-\ SS1\ -\ \phi(1)\ E^-\ TSD3}$
$\pi(1)\ A_2^-\ SS0\ -\ \phi(1)\ E^-\ SS1$
$\pi(1)\ E^+\ SS2\ -\ \phi(1)\ A_2^+\ SS1$
$\pi(2)\ A_2^-\ SS1\ -\ \phi(2)\ A_1^-\ SS2$
$\pi(2)\ A_2^-\ SS0\ -\ \phi(2)\ B_1^-\ SS2$
$\boldsymbol{\pi(3)\ A_1^+\ SS2\ -\ \phi(3)\ A_2^+\ SS0}$
$\pi(3)\ A_2^-\ SS0\ -\ \phi(3)\ E^-\ SS2$
$\boldsymbol{\pi(3)\ A_2^-\ SS0\ -\ \phi(3)\ A_1^-\ SS2}$
$\boldsymbol{\pi(3)\ A_2^-\ SS1\ -\ \phi(3)\ A_1^-\ SS2}$
$\boldsymbol{\pi(4)\ A_2^-\ SS1\ -\ \phi(4)\ E^-\ SS1}$
$\overline{K}(2)\ A_2\ SS1\ -\ K(2)\ A_2\ SS1$
$\boldsymbol{\overline{K}(3)\ A_2\ SS0\ -\ K(3)\ A_1\ SS3}$

BIBLIOGRAPHY

[1] M. Gell-Mann, "A schematic model of baryons and mesons," *Physics Letters*, vol. 8, no. 3, pp. 214 – 215, 1964.

[2] G. Zweig, "An $SU(3)$ model for strong interaction symmetry and its breaking," tech. rep., CM-P00042884, 1964.

[3] O. W. Greenberg, "Spin and Unitary-Spin Independence in a Paraquark Model of Baryons and Mesons," *Phys. Rev. Lett.*, vol. 13, pp. 598–602, Nov 1964.

[4] M. Y. Han and Y. Nambu, "Three-Triplet Model with Double SU(3) Symmetry," *Phys. Rev.*, vol. 139, pp. B1006–B1010, Aug 1965.

[5] H. Fritzsch, M. Gell-Mann, and H. Leutwyler, "Advantages of the color octet gluon picture," *Physics Letters B*, vol. 47, no. 4, pp. 365 – 368, 1973.

[6] D. J. Gross and F. Wilczek, "Ultraviolet Behavior of Non-Abelian Gauge Theories," *Phys. Rev. Lett.*, vol. 30, pp. 1343–1346, Jun 1973.

[7] H. D. Politzer, "Reliable Perturbative Results for Strong Interactions?," *Phys. Rev. Lett.*, vol. 30, pp. 1346–1349, Jun 1973.

[8] S. Capstick and W. Roberts, "Quark models of baryon masses and decays," *Progress in Particle and Nuclear Physics*, vol. 45, pp. S241 – S331, 2000.

[9] C. Patrignani *et al.*, "Review of Particle Physics," *Chin. Phys.*, vol. C40, no. 10, p. 100001, 2016.

[10] R. Dalitz and S. Tuan, "The phenomenological representation of K-nucleon scattering and reaction amplitudes," *Annals of Physics*, vol. 10, no. 3, pp. 307 – 351, 1960.

[11] R. H. Dalitz, T. C. Wong, and G. Rajasekaran, "Model Calculation for the $Y_0^*(1405)$ Resonance State," *Phys. Rev.*, vol. 153, pp. 1617–1623, Jan 1967.

[12] J. M. M. Hall, W. Kamleh, D. B. Leinweber, B. J. Menadue, B. J. Owen, A. W. Thomas, and R. D. Young, "Lattice QCD Evidence that the $\Lambda(1405)$ Resonance is an Antikaon-Nucleon Molecule," *Phys. Rev. Lett.*, vol. 114, p. 132002, Apr 2015.

[13] R. Jaffe, "Exotica," *Physics Reports*, vol. 409, no. 1, pp. 1 – 45, 2005.

[14] S.-K. Choi *et al.*, "Observation of a Narrow Charmoniumlike State in Exclusive $B^{\pm} \to K^{\pm}\pi^{+}\pi^{-}J/\psi$ Decays," *Phys. Rev. Lett.*, vol. 91, p. 262001, Dec 2003.

[15] X. Liu, "An overview of XYZ new particles," *Chinese Science Bulletin*, vol. 59, pp. 3815–3830, Oct 2014.

[16] K. G. Wilson, "Confinement of quarks," *Phys. Rev. D*, vol. 10, pp. 2445–2459, Oct 1974.

[17] C. Morningstar, J. Bulava, J. Foley, K. J. Juge, D. Lenkner, *et al.*, "Improved stochastic estimation of quark propagation with Laplacian Heaviside smearing in lattice QCD," *Phys. Rev.*, vol. D83, p. 114505, 2011.

[18] C. Michael, "Adjoint sources in lattice gauge theory," *Nuclear Physics B*, vol. 259, no. 1, pp. 58 – 76, 1985.

[19] M. Lüscher and U. Wolff, "How to calculate the elastic scattering matrix in two-dimensional quantum field theories by numerical simulation," *Nuclear Physics B*, vol. 339, no. 1, pp. 222 – 252, 1990.

[20] A. collaboration, B. Blossier, M. D. Morte, G. von Hippel, T. Mendes, and R. Sommer, "On the generalized eigenvalue method for energies and matrix elements in lattice field theory," *Journal of High Energy Physics*, vol. 2009, no. 04, p. 094, 2009.

[21] M. Lüscher, "Volume dependence of the energy spectrum in massive quantum field theories," *Communications in Mathematical Physics*, vol. 104, pp. 177–206, Jun 1986.

[22] M. Lüscher, "Volume dependence of the energy spectrum in massive quantum field theories," *Communications in Mathematical Physics*, vol. 105, pp. 153–188, Jun 1986.

[23] M. Lüscher, "Two-particle states on a torus and their relation to the scattering matrix," *Nuclear Physics B*, vol. 354, no. 2, pp. 531 – 578, 1991.

[24] M. Lüscher, "Signatures of unstable particles in finite volume," *Nuclear Physics B*, vol. 364, no. 1, pp. 237 – 251, 1991.

[25] L. Maiani and M. Testa, "Final state interactions from euclidean correlation functions," *Physics Letters B*, vol. 245, no. 3, pp. 585 – 590, 1990.

[26] J. J. Dudek, R. G. Edwards, P. Guo, and C. E. Thomas, "Toward the excited isoscalar meson spectrum from lattice QCD," *Phys. Rev. D*, vol. 88, p. 094505, Nov 2013.

[27] C. Morningstar, J. Bulava, B. Singha, R. Brett, J. Fallica, A. Hanlon, and B. Hörz, "Estimating the two-particle K-matrix for multiple partial waves and decay channels from finite-volume energies," *Nuclear Physics B*, 2017.

[28] H. Nielsen and M. Ninomiya, "A no-go theorem for regularizing chiral fermions," *Physics Letters B*, vol. 105, no. 2, pp. 219 – 223, 1981.

[29] Z. Fodor and C. Hoelbling, "Light Hadron Masses from Lattice QCD," *Rev.Mod.Phys.*, vol. 84, p. 449, 2012.

[30] M. Lüscher, "Construction of a selfadjoint, strictly positive transfer matrix for euclidean lattice gauge theories," *Communications in Mathematical Physics*, vol. 54, pp. 283–292, Oct 1977.

[31] M. Lüscher and P. Weisz, "Definition and general properties of the transfer matrix in continuum limit improved lattice gauge theories," *Nuclear Physics B*, vol. 240, no. 3, pp. 349 – 361, 1984.

[32] C. J. Morningstar and M. Peardon, "Efficient glueball simulations on anisotropic lattices," *Phys. Rev. D*, vol. 56, pp. 4043–4061, Oct 1997.

[33] C. J. Morningstar and M. Peardon, "Glueball spectrum from an anisotropic lattice study," *Phys. Rev. D*, vol. 60, p. 034509, Jul 1999.

[34] K. Symanzik, "Continuum limit and improved action in lattice theories," *Nuclear Physics B*, vol. 226, no. 1, pp. 187 – 204, 1983.

[35] G. P. Lepage and P. B. Mackenzie, "Viability of lattice perturbation theory," *Phys. Rev. D*, vol. 48, pp. 2250–2264, Sep 1993.

[36] M. Lüscher and P. Weisz, "On-shell improved lattice gauge theories," *Communications in Mathematical Physics*, vol. 97, no. 1, pp. 59–77, 1985.

[37] M. Lüscher and P. Weisz, "Computation of the action for on-shell improved lattice gauge theories at weak coupling," *Physics Letters B*, vol. 158, no. 3, pp. 250 – 254, 1985.

[38] R. G. Edwards, B. Joó, and H.-W. Lin, "Tuning for three flavors of anisotropic clover fermions with stout-link smearing," *Phys. Rev. D*, vol. 78, p. 054501, Sep 2008.

[39] H.-W. Lin, S. D. Cohen, J. Dudek, R. G. Edwards, B. Joó, D. G. Richards, J. Bulava, J. Foley, C. Morningstar, E. Engelson, S. Wallace, K. J. Juge, N. Mathur, M. J. Peardon, and S. M. Ryan, "First results from $2 + 1$ dynamical quark flavors on an anisotropic lattice: Light-hadron spectroscopy and setting the strange-quark mass," *Phys. Rev. D*, vol. 79, p. 034502, Feb 2009.

[40] P. Chen, "Heavy quarks on anisotropic lattices: The charmonium spectrum," *Phys. Rev. D*, vol. 64, p. 034509, Jul 2001.

[41] N. Metropolis, A. W. Rosenbluth, M. N. Rosenbluth, A. H. Teller, and E. Teller, "Equation of State Calculations by Fast Computing Machines," *The Journal of Chemical Physics*, vol. 21, no. 6, pp. 1087–1092, 1953.

[42] S. Duane, A. Kennedy, B. J. Pendleton, and D. Roweth, "Hybrid Monte Carlo," *Physics Letters B*, vol. 195, no. 2, pp. 216 – 222, 1987.

[43] J. M. Bulava, R. G. Edwards, E. Engelson, J. Foley, B. Joó, A. Lichtl, H.-W. Lin, N. Mathur, C. Morningstar, D. G. Richards, and S. J. Wallace, "Excited state nucleon spectrum with two flavors of dynamical fermions," *Phys. Rev. D*, vol. 79, p. 034505, Feb 2009.

[44] M. Clark, A. Kennedy, and Z. Sroczynski, "Exact 2+1 Flavour RHMC Simulations," *Nuclear Physics B - Proceedings Supplements*, vol. 140, pp. 835 – 837, 2005. LATTICE 2004.

[45] S. Basak, R. G. Edwards, G. T. Fleming, U. M. Heller, C. Morningstar, D. Richards, I. Sato, and S. Wallace, "Group-theoretical construction of extended baryon operators in lattice QCD," *Phys. Rev. D*, vol. 72, p. 094506, Nov 2005.

[46] C. Morningstar, J. Bulava, B. Fahy, J. Foley, Y. C. Jhang, K. J. Juge, D. Lenkner, and C. H. Wong, "Extended hadron and two-hadron operators of definite momentum for spectrum calculations in lattice QCD," *Phys. Rev. D*, vol. 88, p. 014511, Jul 2013.

[47] M. Albanese, F. Costantini, G. Fiorentini, F. Flore, M. Lombardo, R. Tripiccione, P. Bacilieri, L. Fonti, P. Giacomelli, E. Remiddi, M. Bernaschi, N. Cabibbo, E. Marinari, G. Parisi, G. Salina, S. Cabasino, F. Marzano, P. Paolucci, S. Petrarca, F. Rapuano, P. Marchesini, and R. Rusack, "Glueball masses and string tension in lattice QCD," *Physics Letters B*, vol. 192, no. 1, pp. 163 – 169, 1987.

[48] C. Morningstar and M. Peardon, "Analytic smearing of SU(3) link variables in lattice QCD," *Phys. Rev. D*, vol. 69, p. 054501, Mar 2004.

[49] M. Alford, T. Klassen, and P. Lepage, "The D234 action for light quarks," *Nuclear Physics B - Proceedings Supplements*, vol. 47, no. 1, pp. 370 – 373, 1996.

[50] M. Peardon, J. Bulava, J. Foley, C. Morningstar, J. Dudek, R. G. Edwards, B. Joó, H.-W. Lin, D. G. Richards, and K. J. Juge, "Novel quark-field creation operator construction for hadronic physics in lattice QCD," *Phys. Rev. D*, vol. 80, p. 054506, Sep 2009.

[51] G. W. Mackey, "Induced representations of locally compact groups," *Ann. Math.*, vol. 55, pp. 101–139, 1952.

[52] G. W. Mackey, "Induced Representations of Locally Compact Groups II. The Frobenius Reciprocity Theorem," *Ann. Math.*, vol. 58, no. 2, pp. 193–221, 1953.

[53] G. W. Mackey, "Unitary representations of group extensions. I," *Acta. Math.*, vol. 99, pp. 265–311, 1958.

[54] G. W. MacKey, *Induced representations of groups and quantum mechanics.* New York, NY: Benjamin, 1968. Based on 4 lectures given in Pisa, at the Scuola Normale, during spring 1967.

[55] E. Wigner, "On Unitary Representations of the Inhomogeneous Lorentz Group," *Ann. Math.*, vol. 40, no. 1, pp. 149–204, 1939.

[56] R. S. Mulliken, "Report on Notation for the Spectra of Polyatomic Molecules," *The Journal of Chemical Physics*, vol. 23, no. 11, pp. 1997–2011, 1955.

[57] R. S. Mulliken, "Erratum : Report on Notation for the Spectra of Polyatomic Molecules," *The Journal of Chemical Physics*, vol. 24, no. 5, pp. 1118–1118, 1956.

[58] J. Foley, K. Jimmy Juge, A. O'Cais, M. Peardon, S. M. Ryan, and J.-I. Skullerud, "Practical all-to-all propagators for lattice QCD," *Comput. Phys. Commun.*, vol. 172, pp. 145–162, 2005.

[59] S. Bernardson, P. McCarty, and C. Thron, "Monte Carlo methods for estimating linear combinations of inverse matrix entries in lattice QCD," *Computer Physics Communications*, vol. 78, no. 3, pp. 256 – 264, 1994.

[60] A. Alex, M. Kalus, A. Huckleberry, and J. von Delft, "A numerical algorithm for the explicit calculation of SU(N) and SL(N,C) Clebsch-Gordan coefficients," *Journal of Mathematical Physics*, vol. 52, no. 2, p. 023507, 2011.

[61] W. H. Press, S. A. Teukolsky, W. T. Vetterling, and B. P. Flannery, *Numerical Recipes 3rd Edition: The Art of Scientific Computing.* New York, NY, USA: Cambridge University Press, 3 ed., 2007.

[62] K. Rummukainen and S. Gottlieb, "Resonance scattering phase shifts on a non-rest-frame lattice," *Nuclear Physics B*, vol. 450, no. 1, pp. 397 – 436, 1995.

[63] C. Kim, C. Sachrajda, and S. R. Sharpe, "Finite-volume effects for two-hadron states in moving frames," *Nuclear Physics B*, vol. 727, no. 1, pp. 218 – 243, 2005.

[64] N. H. Christ, C. Kim, and T. Yamazaki, "Finite volume corrections to the two-particle decay of states with nonzero momentum," *Phys. Rev. D*, vol. 72, p. 114506, Dec 2005.

[65] T. Luu and M. J. Savage, "Extracting scattering phase shifts in higher partial waves from lattice QCD calculations," *Phys. Rev. D*, vol. 83, p. 114508, Jun 2011.

[66] Z. Fu, "Rummukainen-Gottlieb formula on a two-particle system with different masses," *Phys. Rev. D*, vol. 85, p. 014506, Jan 2012.

[67] L. Leskovec and S. Prelovsek, "Scattering phase shifts for two particles of different mass and nonzero total momentum in lattice QCD," *Phys. Rev. D*, vol. 85, p. 114507, Jun 2012.

[68] M. T. Hansen and S. R. Sharpe, "Multiple-channel generalization of Lellouch-Lüscher formula," *Phys. Rev. D*, vol. 86, p. 016007, Jul 2012.

[69] M. Göckeler, R. Horsley, M. Lage, U.-G. Meißner, P. E. L. Rakow, A. Rusetsky, G. Schierholz, and J. M. Zanotti, "Scattering phases for meson and baryon resonances on general moving-frame lattices," *Phys. Rev. D*, vol. 86, p. 094513, Nov 2012.

[70] R. A. Briceño, "Two-particle multichannel systems in a finite volume with arbitrary spin," *Phys. Rev. D*, vol. 89, p. 074507, Apr 2014.

[71] M. T. Hansen and S. R. Sharpe, "Expressing the three-particle finite-volume spectrum in terms of the three-to-three scattering amplitude," *Phys. Rev. D*, vol. 92, p. 114509, Dec 2015.

[72] J. Bulava, B. Fahy, B. Hörz, K. J. Juge, C. Morningstar, and C. H. Wong, "$I = 1$ and $I = 2$ $\pi\pi$ scattering phase shifts from $N_f = 2 + 1$ lattice QCD," *Nuclear Physics B*, vol. 910, pp. 842 – 867, 2016.

[73] J. J. Dudek, R. G. Edwards, and C. E. Thomas, "Energy dependence of the ρ resonance in $\pi\pi$ elastic scattering from lattice QCD," *Phys. Rev. D*, vol. 87, p. 034505, Feb 2013.

[74] X. Feng, K. Jansen, and D. B. Renner, "Resonance parameters of the ρ meson from lattice QCD," *Phys. Rev. D*, vol. 83, p. 094505, May 2011.

[75] E. P. Wigner, "Resonance Reactions and Anomalous Scattering," *Phys. Rev.*, vol. 70, pp. 15–33, Jul 1946.

[76] E. P. Wigner and L. Eisenbud, "Higher Angular Momenta and Long Range Interaction in Resonance Reactions," *Phys. Rev.*, vol. 72, pp. 29–41, Jul 1947.

[77] R. Dalitz and S. Tuan, "The phenomenological representation of $\overline{K}$-nucleon scattering and reaction amplitudes," *Annals of Physics*, vol. 10, no. 3, pp. 307 – 351, 1960.

[78] A. Badalyan, L. Kok, M. Polikarpov, and Y. Simonov, "Resonances in coupled channels in nuclear and particle physics," *Physics Reports*, vol. 82, no. 2, pp. 31 – 177, 1982.

[79] S. U. Chung, J. Brose, R. Hackmann, E. Klempt, S. Spanier, and C. Strassburger, "Partial wave analysis in K-matrix formalism," *Annalen der Physik*, vol. 507, no. 5, pp. 404–430, 1995.

[80] K. J. Peters, "A Primer on partial wave analysis," *Int. J. Mod. Phys.*, vol. A21, pp. 5618–5624, 2006.

[81] D. J. Wilson, J. J. Dudek, R. G. Edwards, and C. E. Thomas, "Resonances in coupled $\pi K, \eta K$ scattering from lattice QCD," *Phys. Rev. D*, vol. 91, p. 054008, Mar 2015.

[82] J. J. Dudek, R. G. Edwards, and D. J. Wilson, "An a_0 resonance in strongly coupled $\pi\eta$, $K\overline{K}$ scattering from lattice QCD," *Phys. Rev. D*, vol. 93, p. 094506, May 2016.

[83] D. J. Wilson, R. A. Briceño, J. J. Dudek, R. G. Edwards, and C. E. Thomas, "Coupled $\pi\pi$, $K\overline{K}$ scattering in P-wave and the ρ resonance from lattice QCD," *Phys. Rev. D*, vol. 92, p. 094502, Nov 2015.

[84] D. Guo, A. Alexandru, R. Molina, and M. Döring, "Rho resonance parameters from lattice QCD," *Phys. Rev. D*, vol. 94, p. 034501, Aug 2016.

[85] R. G. Edwards and B. Joó, "The Chroma Software System for Lattice QCD," *Nuclear Physics B - Proceedings Supplements*, vol. 140, pp. 832 – 834, 2005. LATTICE 2004.

[86] J. Towns, T. Cockerill, M. Dahan, I. Foster, K. Gaither, A. Grimshaw, V. Hazlewood, S. Lathrop, D. Lifka, G. D. Peterson, R. Roskies, J. R. Scott, and N. Wilkins-Diehr, "XSEDE: Accelerating Scientific Discovery," *Computing in Science & Engineering*, vol. 16, no. 5, pp. 62–74, 2014.

[87] J. J. Dudek, R. G. Edwards, N. Mathur, and D. G. Richards, "Charmonium excited state spectrum in lattice QCD," *Phys. Rev. D*, vol. 77, p. 034501, Feb 2008.

[88] J. J. Dudek, R. G. Edwards, M. J. Peardon, D. G. Richards, and C. E. Thomas, "Toward the excited meson spectrum of dynamical QCD," *Phys. Rev. D*, vol. 82, p. 034508, Aug 2010.

[89] S. Prelovsek, L. Leskovec, C. B. Lang, and D. Mohler, "$K\pi$ scattering and the K^* decay width from lattice QCD," *Phys. Rev. D*, vol. 88, p. 054508, Sep 2013.

[90] J. Nebreda and J. R. Peláez, "Strange and nonstrange quark mass dependence of elastic light resonances from SU(3) unitarized chiral perturbation theory to one loop," *Phys. Rev. D*, vol. 81, p. 054035, Mar 2010.